Unipolar quantum devices for high-speed mid-IR optoelectronics on InP

Thomas Bonazzi

Université Paris Cité

ED n°564 : Physique en Île de France

Laboratoire de Physique de l'Ecole Normale Supérieure

Unipolar quantum devices for high-speed mid-IR optoelectronics on InP

Thomas BONAZZI

Thèse de doctorat de Physique

Dirigée par Angela VASANELLI

Présentée et soutenue publiquement le 12/06/2023

Jury:

Gottfried STRASSER, Full Professor, TU Wien, Rapporteur

Eric TOURNIE, Professeur, Université de Montpellier, Rapporteur

Ileana-Cristina BENEA-CHELMUS, Assistant Professor, ETH Zurich, Examinatrice

Giuseppe LEO, Professeur, Université Paris Cité, Président

Angela VASANELLI, Professeur, Université Paris Cité, Directrice de thèse

Isabelle SAGNES, Directrice de recherche, C2N, Invitée

Carlo SIRTORI, Professeur, Ecole Normale Supérieure, Invité

Mots clés : Couplage lumière-matiere, Transition Intersousbande, Métamateriaux, Modulateur à effet Stark, Infrarouge, Dispositifs optoélectroniques, Détecteur à cascade quantique, Communications en espace libre

Des systèmes optoélectroniques ultra-sensibles et ultrarapides dans l'infrarouge moyen sont nécessaires pour les communications en espace libre, la télédétection par laser (LIDAR), la spectroscopie à haute résolution et l'astronomie d'observation. Les transitions intrabandes dans les puits quantiques des matériaux III-V offrent une plateforme complète pour la conception et la fabrication de dispositifs optoélectroniques dans cette gamme d'énergie. Ce travail se concentre sur l'étude, la conception et la démonstration expérimentale d'un modulateur d'amplitude ainsi que d'un détecteur à 9 µm, fonctionnant à haute fréquences et à température ambiante, sur InP. Le modulateur externe est un élément crucial et manquant pour la réalisation de plateformes optoélectroniques complètes dans l'infrarouge moyen. Ce modulateur tire profit de l'effet Stark, où un champ électrique externe est utilisé pour déplacer l'énergie d'absorption de la transition optique. Afin de tirer parti du très court temps de relaxation des transitions optiques intrabandes, un soin particulier a été apporté à la fabrication d'un dispositif compatible avec les radiofréquences, capable de fonctionner jusqu'à plusieurs GHz. Le dispositif résultant a permis la réalisation expérimentale d'une ligne de transmission de données optique en espace libre à température ambiante, avec un débit de 10 Gbit/s. La limite de la bande passante du dispositif est essentiellement fixée par sa taille. Afin de proposer une seconde génération de modulateurs plus performants, la géométrie du résonateur patch est étudiée, afin de fournir un environnement électromagnétique plus avantageux et améliorer l'interaction lumière-matière tout en réduisant la taille des nouveaux modulateurs en métamatériaux. Une attention particulière a été accordée aux défis de nanofabrication soulevés par les le choix de materiaux ainsi que les faibles tailles en jeu. Les progrès réalisés dans la compréhension et la modélisation de ces métamateriaux ont également été mis à profit pour dimensionner des photo-détecteurs infrarouges quantiques efficaces et rapides. En combinant des détecteurs et modulateurs en métamateriaux, une seconde une ligne de transmission optique en espace libre est démontrée, cette fois avec un débit record de 60 Gbit/s.

Key words: Light-matter coupling, Intersubband, Metamaterial, Stark Modulator, Infrared, Optoelectonic Devices, quantum cascade detectors, free space telecommunication

Highly sensitive and ultrafast mid-infrared (MIR) optoelectronic systems are required for free-space communications, light detection and ranging (LIDAR), high resolution spectroscopy and in observational astronomy. Intraband transitions in quantum wells of III-V materials offer a comprehensive platform for engineering optoelectronic devices in the MIR energy range. This work focuses on the study, the conception and the experimental demonstration of high-speed, room temperature InP-based amplitude modulator and detector at 9 µm, which are crucial and building blocks for a complete optoelectronic platform in the MIR. The proposed modulator takes advantage of the Stark effect, in which an external electric field shifts the absorption energy of the optical transition. In order to exploit the intrinsically fast relaxation times of the optical transitions, special care was taken to process this modulator into an RF-compatible device, able to operate up to several GHz. The resulting device allowed free space optical communications at room temperature with a bitrate of 10 Gbit/s. This electrical bandwidth is mostly set by the size of the device itself. In order to bring forward a second, more performing generation of modulators, patch antenna resonator geometry was studied in the framework of the Coupled Mode Theory. This provides an advantageous electromagnetic environment to enhance light matter interaction while reducing the overall physical size of the resonant metamaterial modulators. A particular attention was given to the nanofabrication challenges raised by material issues and reduced sizes. The progress on the comprehension and modelling of these metamaterials was also used to design efficient high-speed quantum MIR photodetectors. Using the new metamaterial detectors and modulators, a second free space optical link was demonstrated with a record capacity of 60 Gbit/s.

Résumé

La gamme spectrale du moyen infrarouge (MIR) suscite depuis quelques dizaines d'année l'intéret d'une large communauté dans de nombreux domaines allant du médical aux applications liées aux télécommunications et la sécurité. Pour permettre le développement de telles applications, des sources et des détecteurs compacts et efficaces sont nécessaires. Les structures basées sur les puits quantiques dans des semiconducteurs III-V permettent de créer une multitude de fonctions optoélectroniques, de par la possibilité qu'ils offrent de contrôler la longueur d'onde d'absorption ou d'emission de lumière dans cette gamme de longueur d'énergie. De plus, la dynamique intrinsèque des phénomènes en jeu dans ces structures leur confère un potentiel inégalé pour les applications à plusieurs dizaines voire centaines de GHz dans le MIR. A titre d'exemple, les lasers à cascade quantique (QCL) ont, depuis leur démonstration technique en 1994, grandement amélioré leur efficacité. Des températures cryogéniques, les QCLs MIR fonctionnent de nos jours a températures ambiante. De même les détecteurs infrarouges à puits quantiques (QWIP) ou même les détecteurs à cascade quantique (QCD) ont récemment atteint un niveau de maturité suffisant pour permettre leur utilisation à température ambiante, augmentant encore l'intérêt porté à leur égard. Un élément central dans l'amélioration récente des détecteurs est l'intégration des hétérostructures semiconducteurs dans des metamatériaux résonants, permettant l'augmentation significative de la longueur d'interaction de la lumière avec les puits quantiques.

Certaines applications et tout particulièrement les telécommunications en espace libre requièrent, au delà des sources et des détecteurs, un modulateur d'amplitude. Un objectif de cette thèse est la conception, la réalisation et la démonstration d'un tel modulateur dans la seconde fenêtre de transparence de l'atmosphère, autour de 9 µm. L'hétérostructure proposée consiste en deux puits assymétriques en InGaAs couplés et séparé d'une fine barrière en InAlAs, déposés par épitaxie sur InP. L'asymétrie de la structure rend l'énergie de la transition optique entre les deux premiers niveaux (espacés de la longueur d'onde visée) sensible au champ électrique appliqué aux bornes de la structure par effet Stark confiné (Fig.2.1 (a)).

La structure proposé a été épitaxiée au C2N et présente un Stark shift de 0.35 meV.cm.kV^{-1}. Fig.2.1 (b) présente les spectres de transmission de la région active à 78 K pour différentes polarisations DC appliquées à ses bornes. La valeur du Stark shift est proche de la prévision théorique et permet de tirer pleinement profit de la structure et d'atteindre une profondeur de modulation de 47%, limitée par l'absorption de la structure. Afin d'exploiter la vitesse intrinsèque de la structure, les mesas sont connectés à des lignes coplanaire via des pont en

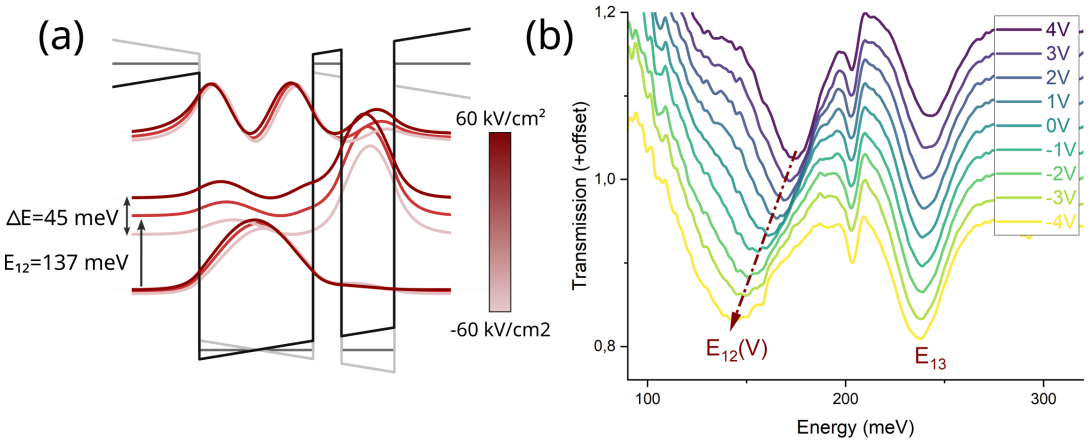

Fig. 0.1 *(a) Structure de bande du modulateur Stark pour trois bias différent. L'énergie de la transition 1-2 varie significativement. (b) Spectre de transmission à 78 K du modulateur Stark pour différent bias, avec un offset. L'énergie de la transition 1-2 varie mais la 1-3 reste quasi consante.*

or afin de limiter les inductances liées aux connections via des fils en or (Fig.0.2 (a)).

La caractérisations de mésas de tailles differentes entre 80x80 cm^2 et 25x25 cm^2 a permis d'établir que la surface des dispositif était le facteur principal limitant la bande passante, mais qu'il semble exister un temps caractéristique à la structure, de l'ordre de quelques picosecondes assurant un possible fonctionnement de cette structure jusqu'à au moins 40 GHz. Couplée à un QCL commercial et un QCD intégré de la même façon, ce modulateur a servi à fabriquer une ligne de transmission optique à 9 µm permettant la transmission de données à un débit record pour cette longueur d'onde de 10 Gbit·s^{-1}. L'alignement des trois dispositifs opoelectroniques est représenté sur la Fig.0.2 (b). Les diagrammes de l'oeil pour les transmissions de 7 et 10 Gbit·s^{-1} sont visibles sur les Fig.0.2 (c) et (d). Si la transmission à 7 Gbit·s^{-1} est strictement sans erreur, celle à 10 Gbit·s^{-1} présente un taux d'erreur non nul mais corrigeable à l'aide de code correcteur d'erreurs et est donc satisfaisante.

Afin de pousser les performances de ce dispositif encore plus loin, ces dispositifs ont eu vocation à être intégrés dans des résonateurs patchs (Fig. 3.5 (a)). Ces structures se sont montrées très avantageuses dans la littérature pour les détecteurs, permettant de confiner le champ electrique incident dans des volumes sub-longeur d'onde et permettant de réduire drastiquement la surface électrique des dispositifs (et donc de gagner en bande passante), tout en augmentant l'intéraction et donc l'absorption de la lumière par les puits quantiques. Cette interaction est modélisée ici grâce à la théorie des modes couplés (CMT), modélisant le système comme deux oscillateurs: le mode optique confiné dans la cavité et la polarisation intersousbande. Seul le mode de cavité est couplé au rayonnement incident et le mode ISB n'est couplé que via le premier, à la fréquence de Rabi. Ce modèle permet de séparer les contributions de la cavité et de l'ISB dans la dissipation de l'énergie.

Tout l'enjeu pour la paramétrisation des dispositifs en métamateriau est le lien entre les paramètres géométriques et les couplage lumière matière. Une étude paramétrique réalisée

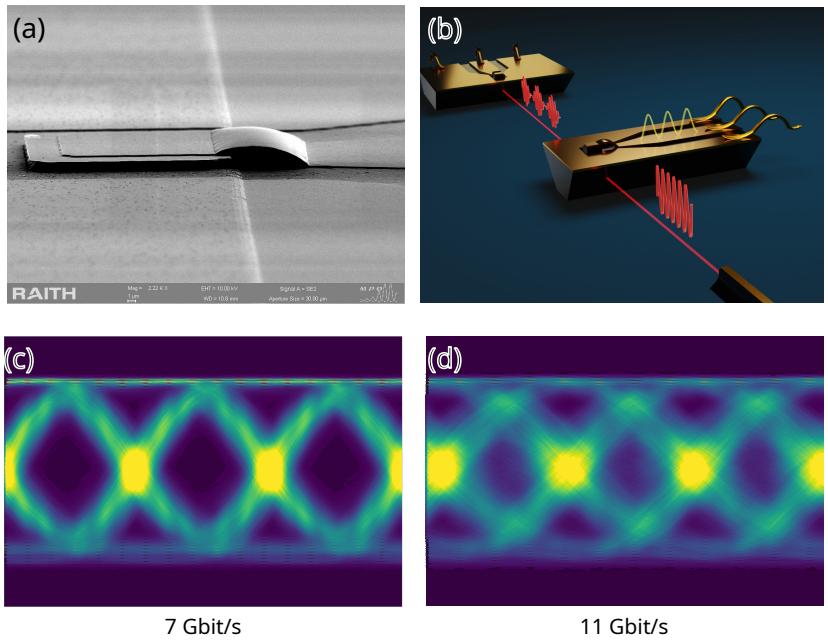

Fig. 0.2 *(a) Image MEB d'un mesa haute fréquence de modulateur Stark (b) Représentation du système de transmission de données avec les dispositif ISB haute fréquence (c) Diagramme de l'oeil de la transmission 7 Gbit·s^{-1}, sans erreur. (d) Diagramme de l'oeil de la transmission 10 Gbit·s^{-1}, avec un taux d'erreur acceptable pour une transmission corrigée.*

avec des résonateurs remplis de GaAs sans transition électronique dans cette gamme d'énergie, de trois épaisseurs (570 nm, 1020 nm et 1710 nm), et portant sur periodicité des résonateurs, a permis d'évaluer les paramètres propres aux cavités ainsi que leur évolution avec la géométrie. Couplés avec la caractérisation des hétérostructures, il devient dès lors possible de simuler les performances attendues pour le modulateur à effet Stark en métamatériau en fonction de la géométrie. L'objectif est alors la maximisation du contraste dans la réflectivité en fonction du champ électrique aux bornes du dispositif (3.5 (b)). La même démarche peut être menée pour les détecteurs, optimisant cette fois l'absorption dans les puits quantiques.

Une fois le dimensionnement approximatif des dispositif terminé, un procédé de fabrication, combinant fabrication des résonateurs micrométriques et les guides d'ondes pour les hautes fréquences comme dans le cas des mésas a été mis au point.3.5 (c).

Avant de procéder à la fabrication des dispositifs finaux, un nouveau QCD sur InP, basé sur une absorption diagonale, est dessiné et optimisé à l'aide d'un logiciel résolvant de l'équation de Schrödinger dans les hétérostructures et déterminant les taux de transitions entre les niveaux. De plus un détecteur QWIP réalisé dans un matériau quaternaire adapté pour une détection à 9 µm est aussi conçu. Une nouvelle structure de modulateur Stark, plus fine, est aussi réalisée pour être compatible avec le procédé de fabrication.

Chaque région active est ensuite étudiée selon le même processus: un spectre d'absorption en mesa est mesuré, et un éventail de paramètres de métamateriaux (taille de résonateurs, périodicité) non connecté électriquement est ensuite fabriqué, puis étudié en refléctivité à

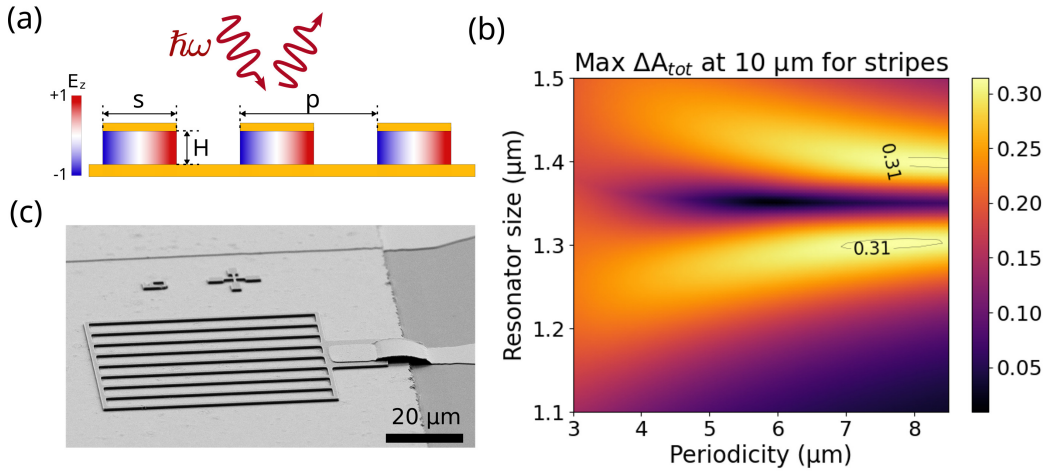

Fig. 0.3 *(a) Schéma d'un réseau de résonateurs double-métal et du mode de cavité en leur sein. (b) Optimisation du fonctionnement du modulateur Stark en cavité à l'aide de la théorie des modes couplés. (c) Image MEB d'un modulateur Stark en cavité.*

l'aide d'un FTIR couplé à un objectif Cassegrain. Le fit de l'ensemble des spectres de réflectivité permet la détermination de chaque des paramètres de CMT et la détermination précise des paramètres géométriques appropriés pour chaque dispositif.

Chacun des dispositifs en cavité finaux est caractérisé. Pour le modulateur, la présence de l'absorption de la cavité, insensible au champ éléctrique appliqué, oblige à repenser le fonctionnement du modulateur et à tendre vers un fonctionnement en couplage fort: dans ce cas, l'absorption à lieu à l'énergie des polaritons. L'application du champ electrique permet alors de obtenir un contraste interessant en changeant l'absorption du système dans son ensemble. Le modulateur proposé à finalement démontré une profondeur de modulation de 28 %, plus faible que dans le cas du mesa, mais réduisant en revanche significativement les pertes d'insertion. La bande passante électrique est elle de 10 GHz.

Du coté du QCD, la région active proposé démontre une faible responsivité à 10 µm, de l'ordre de 3 mA/W à température ambiante. L'optimisation de cette responsivité en cavité est plus simple et se fait en couplage faible lumière-matière. Le meilleur dispositif en cavité permet d'atteindre une responsivité près de 10 fois supérieure à la même longeure d'onde, de 27 mA/W. La bande passante électrique est de 11 GHz. Couplé avec le modulateur et un laser à 10 µm, ces dispositifs ont permis de créer une nouvelle ligne de transmission de données en espace libre (bandes passante in Fig. 0.4 (a)), permettant cette fois d'atteindre le nouveau débit record de 25 Gbit·s^{-1} sans erreur as shown in Fig. 0.4 (b). Aidé par des spécialistes des télécommunications, ce débit est porté à 60 Gbit·s^{-1} grâce à des méthodes de pré- et post-processing des données. Pour les détecteurs, la possibilité de faire varier l'absorption à l'aide des tailles de cavité a aussi permis de remonter à une fonction de transport liant absorption par la polarisation ISB et photocourant. Dans le cas du QCD, cette fonction ressemble à une lorentzienne, piquée à l'énergie du premier niveau de la cascade. Une étude de la variation de cette fonction avec le champ éléctrique appliqué permettrait de confirmer cette intuition.

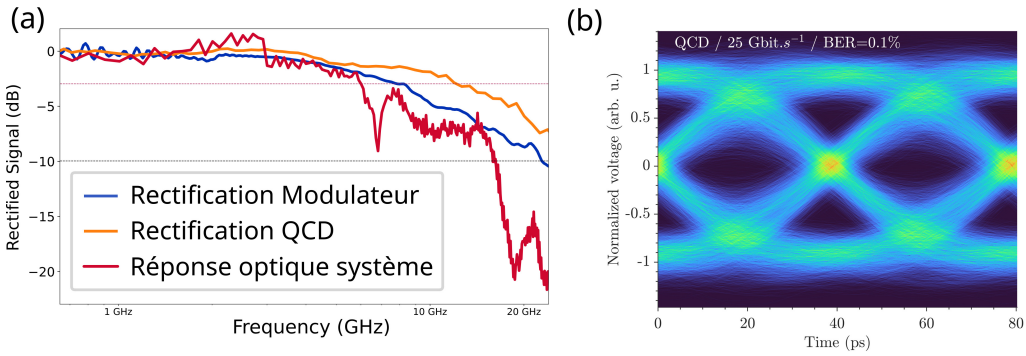

Fig. 0.4 *(a) Réponse électrique du modulateur et du QCD en cavité, et réponse optique en fréquence du systeme de transmission de donnée complet. (b) Diagramme de l'oeil de la transmission 25 Gbit·s^{-1} avec les métamatériaux, avec un taux d'erreur acceptable pour une transmission corrigée.*

Dans le cas du QWIP, deux types de dispositifs ont été fabriqué. D'un côté des dispositifs en couplage faible, afin d'optimiser leur réponse, et de l'autre des dispostifs en couplage fort, notamment pour étudier le transport dans ce cas. Les QWIPs en couplage faible ont une responsivité très élevé à 9 µ et à température ambiante, dépassant 500 mA/W lorsque 1.5 V est appliqué aux bornes du dispositif (Fig. 0.5 (b)). Leur bande passante, <7.5 GHz, ainsi que leur plus important courant d'obscurité, les rend malgré tout moins performants que les QCD pour la transmission de données. Enfin, les QWIP en couplage fort lumière matière ont rendu possible l'observation de photocourant à température ambiante de photocourant à l'énergie du polariton de basse energie jusqu'à 40 meV en dessous de la barrière du puit quantique. L'observation des spectres de photocourant en fonction de la température (Fig. 0.5 (a)) indique que ce photocourant est thermiquement activé (Fig. 0.5 (c)) (avec une énergie d'activation de l'ordre de 40 meV), faisant penser à une interaction avec des phonons du cristal.

Cette thèse, articulée autour de la mise au point de modulateurs et de détecteurs ISB pour le MIR et fonctionnant à température ambiante, a permis l'étude approfondie du couplage lumière matière dans les résonateurs double métal. Les degrés de liberté apporté par les métamateriaux, outre l'optimisation du fonctionnement de chaque dispositif, ont aussi permis de remonter à des informations quant au transport dans les QCDs. Une responsivité record pour les QWIP à température ambiante est aussi démontrée. Du point de vue de la transmission de données en espace libre, le débit record pour cette longeur d'onde de 60 Gbit·s^{-1} a été démontré.

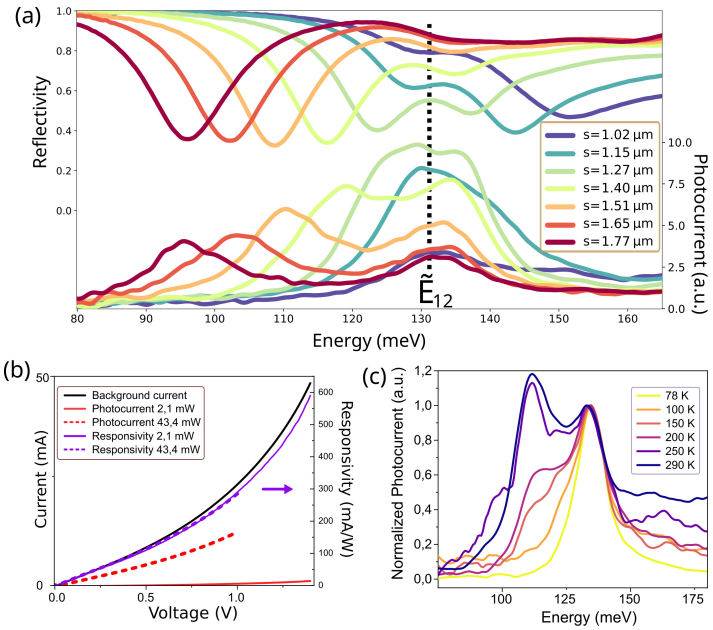

Fig. 0.5 *(a) Spectre de reflexion et de photocourant des QWIPs en couplage fort pour différentes tailles de cavité. (b) Courant d'obscurité, photocourant et responsivité du QWIp en couplage faible pour deux puissance de laser (2.1 mW et 43 mW) (c) Evolmution du spectre de photocourant avec la température d'un QWIP en coulage fort.*

Contents

Introduction

The mid-infrared (MIR) domain is the region of the electromagnetic spectrum spanned by wavelengths from 3 to 30 μm. At these wavelengths, the typical photon energy is a few tens to hundreds of meVs. The ever more precise growth of semiconductor crystals permitted the emergence of low dimensional structures [1] and optoelectronic devices in this energy range: MIR light can be absorbed by electronic transitions between quantum confined states within the conduction band of doped semiconductor nanostructures. These devices are known as intraband devices and are unipolar, as they only rely on electrons for their operation.

Semiconductor quantum wells offer a precise platform to engineer optoelectronic devices interacting with MIR light. Quantum wells, realized by confining a thin layer of a semiconductor between two layers of a second semiconductor with a larger gap energy, serve as building blocks from which efficient devices can be designed. The transitions among confined states can be exploited to engineer devices of various functionality, allowing one to envision a complete optoelectronic platform for the MIR. Electroluminescent devices and lasers [2], amplifiers [3], or amplitude and phase modulators [4] have already been demonstrated. The control of light absorption and the transport of electrons in the heterostructure is essential to the function of all of these optoelectronic devices. A particularly attractive aspect of intersubband devices is the fast characteristic electron relaxation time, on the picosecond timescale, which enables tens and even hundreds of GHz of bandwidth to become accessible.

The tremendous progress in the design and fabrication of the lasers and detectors has made room temperature operation possible. This development has opened this technology to more widespread applications, including free space optical telecommunications. Continuing in this direction, in this work we focus on the development of high-speed devices operating at room temperature. In particular, we develop a crucial missing component for MIR optoelectronics, an efficient amplitude modulator.

The manuscript is structured as follows.
In Chapter 1, after a general introduction and context on the MIR and potential applications, the basic physical principles underlying the intersubband device operation are recalled.
In Chapter 2, we review the Stark effect in asymmetric coupled quantum wells [5], in which an applied external electric field modifies the absorption energy. We exploit this effect to realize a unipolar Stark-effect optoelectronic modulator. We first characterize the optical properties

of the epitaxially grown heterostructure. Then, we detail the fabrication of a device capable of working up to several GHz. We set up a free space optical link using exclusively unipolar quantum optoelectronic devices working at room temperature and demonstrate a high-speed data transmission optical link.
In Chapter 3, in order to design a new generation of efficient and faster modulators, we embed the semiconductor heterostructure in photonic resonators, acting as patch antennas. We proceed to analyze the properties of these metamaterials in the framework of coupled mode theory, in which we consider the exchange of energy between the cavity optical mode and the intersubband transition. We quantify the absorption rate of the electronic transition within the resonator and the loss rates of other dissipation channels as a function of the metamaterial geometry. From these studies we establish parameters to optimize our modulators and detectors.
In Chapter 4, we apply the findings of the previous chapter to the Stark modulator and to intersubband detectors to realize room temperature devices with enhanced performances. We characterize the devices, and consider their improved performances in the context of optical telecommunications. Finally, we demonstrate record high capacity transmission at 9 μm wavelength, pushed even further with digital processing.

All the unipolar devices developed in this work are consistently designed in III-V materials and grown on Indium Phosphide (InP) substrate. This choice contributed a great deal of complexity to the device processing with respect to the well-established GaAs platform, but was made with the future possibility in mind of integrating the modulators on the same platform as the best lasers and detectors. On-chip integration of multiple functions such as what has been demonstrated with silicon photonics in the near infrared represents long term goal towards more widespread implementation of this technology.

Chapter 1

Intraband devices for infrared quantum opto-electronics

1.1 Applications of Mid IR devices

a) The infrared spectrum

The infrared (IR) is the range of the electromagnetic spectrum between the edge of the visible range ($\lambda = 750$ nm) and the microwave range ($\lambda = 1$ mm). For optics and photonics, three spectral regions are defined: the near infrared (NIR) with wavelength between 780 nm and 3 µm, the mid infrared (MIR) between 3 µm and 30 µm and the far-infrared (FIR, known also as terahertz domain) between 30 µm and 1 mm. Two sub-regions of the MIR are particularly interesting because the absorption of these wavelengths by the atmosphere is low: the Mid-Wavelength InfraRed (MWIR) from 3 to 5 µm, and the Long Wave InfraRed (LWIR), from 8 to 14 µm. MWIR and LWIR also belong to the so called 'thermal infrared' range.

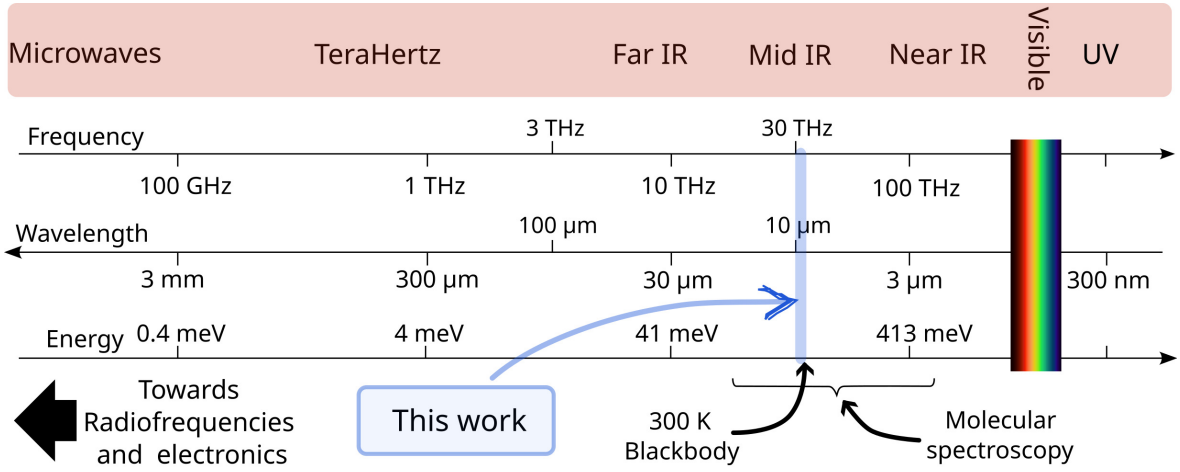

Fig. 1.1 *Electromagnetic spectrum with useful units. Transparency windows of the atmosphere are highlighted.*

These radiations, invisible to the human eye, were identified for the first time in 1800 as a source of heat by Herschel who dispersed sunlight through a prism and placed a thermometer at the location of each color, and further than the red [6]. Infrared invisible radiations were

progressively modelled by scientists like Kirchhoff [7], Stephan, Wien [8], and Planck [9]. In particular the introduced the concept of blackbody, linking the temperature of a body and its emitted radiations. The blackbody models a system that absorbs all the radiation it receives and heats, radiating in turn. At equilibrium, those fluxes balance and the net emission spectrum is simply a function of the temperature. It was while working out a way around limits in contemporary thermodynamical models of the blackbody that Planck introduced his now famous and eponym constant h, as a link between the frequency and the energy of a radiation.

b) Detection of infrared radiation

If a mercury thermometer was enough for Herschel to prove the existence of infrared light, more precise methods of detection have emerged since. A broad variety of platforms exist today to address this part of the electromagnetic spectrum. Thermal detectors are sensitive to the temperature variation of a physical quantity: the bolometer for instance, invented in 1878 [10], is sensitive to the variation of the electrical resistance with the heat generated by IR light. Pyroelectric detectors take advantage of the generation of voltage in polar crystals (for instance gallium nitride (GaN)) when they are heated [11].

In the seventies, when crystalline growth of semiconductors started to be mastered and enabled the creation of new quantum objects with low dimensionality [1], photonic detectors started to be investigated. The impinging infrared photons are detected after causing electronic transitions in the crystal. The first semiconductor detectors that appeared were interband detector, based on transitions occurring between the valence and the conduction band of semiconductors. The most common interband detectors for thermal infrared are semiconductor alloys of HgCdTe (also known as MCT for Mercure Cadmium Telluride) or InGaAs (Indium Gallium Arsenide). The detection energy of these detectors depends on the gap energy between the valence and conduction bands of the material, that can be tuned by changing the composition of the alloy.

The detectors that we will use in this work take advantage of optical transitions between electronic states induced by size confinement in the conduction band of a thin semiconductor layer embedded between two layers with a larger gap. These optical transitions that occur in the conduction band are called intersubband transitions. As we will see in the next section, the detection energy is not fixed by the alloy anymore but by the thickness of the quantum wells, i.e. the thickness of the semiconductor layers. The relaxation of the carriers in those detectors rely mainly on longitudinal optical (LO) phonon emission, an extremely fast process ($\simeq 10^{-12}$ s) that makes ultra-high speed operation possible.

The detection of IR radiation is motivated by several potential applications.

- Wien's displacement law tells that 300 K blackbodies radiate mainly in those wavelengths, meaning that all room temperature objects emit IR light peaked in this part of the spectrum. Heat detection can used for night vision or guiding of missiles but also

for civilian applications such as agriculture [12], leakage detection in industry and to determine heat losses in buildings that need insulation.

- Most functional chemical groups have stretching or bending modes in this spectral region, that will absorb light in specific lines. Gas spectroscopy of these covalent bonds is useful for air control (CO_2 concentration evaluation, SO_x/NO_x detection in industry waste for instance), or for chemical reaction monitoring.

- In astronomy, this part of the spectrum raises interest for its capacity to image through dust that blinds visible/UV telescopes and see older galaxies (cf the images from the James Webb telescope [13]). For interferometer arrays, using IR imaging could also be beneficial compared to the radiofrequencies technology used today (VLTI project in Chile for instance). The angular resolution of such system scales as the wavelength over the distance between the antenna. Using infrared would benefit from the reduced wavelength and the system could reach better resolution without kilometer-large infrastructures like today's projects [14, 15].

c) Free space optical communication

Mid-IR is a promising frequency domain for free space telecommunications [16], where databits are encoded on the amplitude or phase of a laser. Optical telecommunications are investigated as an alternative to wired communications or radiofrequencies (RF) in specific situations.

Today's solutions mainly rely on wired networks for long distance communication, thanks to the optical fibers (working at 1.55 µm), with networks extending between all continents. The most recent fiber deployed underneath the Atlantic ocean by Alphabet has a capacity of 250 terabits per second (Tbit·s^{-1}). Short range networks are, at the end of the line, mainly using radiofrequencies (WiFi, cellular networks). The bridging of the two, for instance between base stations could advantageously be done optically using the 8-14 μm mid-IR transparency window instead of bringing the optical fiber to each user which proves very costly if not prohibitive in remote or sparse area. The use of radiofrequencies during the 'last mile' limits the throughputs because of the ultimate upper limit of the bandwidth fixed by the frequency of the carrier ($\simeq$ 5 GHz for RF, $\simeq$ 30 THz for MIR).

Fig.1.2 presents the atmosphere attenuation as a function of the wavelength, showing transparency windows, i.e. spectral regions where the absorption is low enough to allow efficient propagation and remote detection. At low frequency on the figure lies the RF spectrum, and in the MIR, as stated earlier, the LWIR window between 8 and 14 µm shows a good transparency, fit for free space communications.

An advantage of longer wavelength like 10 µm over shorter NIR wavelengths for laser communication is their lower scattering by microscopic aerosols (Mie and Rayleigh scattering) [17]. Ground-ground long-range ($\simeq$1 km) studies showed the superiority of MIR wavelength over the shorter NIR ones [18, 16], especially during low-visibility episodes. A second advantage is their lesser sensitivity to atmospheric wavefront distortion, particularly relevant for even longer transmission. The increased divergence of a laser operating at MIR wavelength

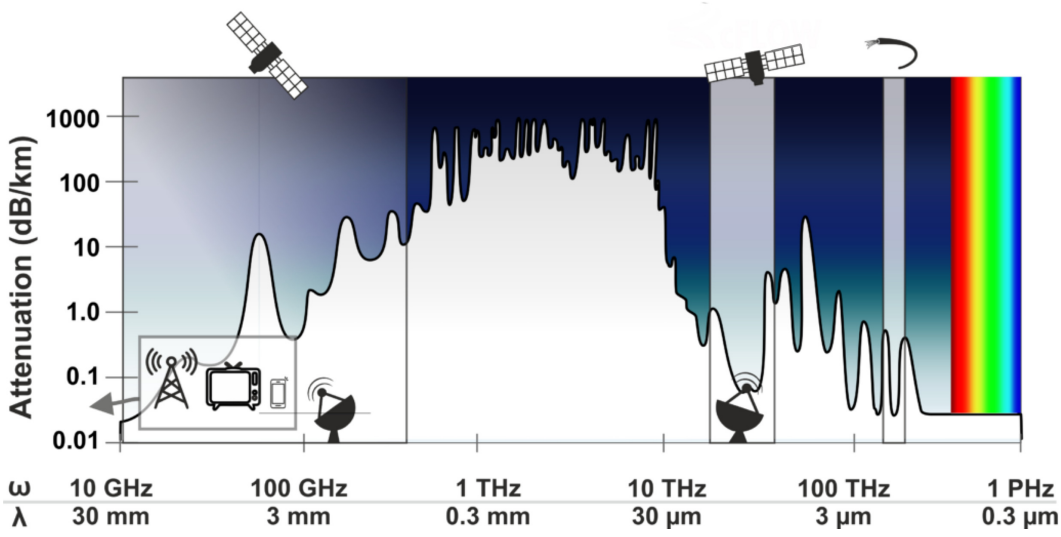

Fig. 1.2 *Attenuation of the atmosphere, from radiofrequencies to visible light. Apart from visible light, three transparency windows are interesting for data transmission: radiofrequencies to millimeter waves used for short-range communications solutions, near-infrared (1.5 µm) and the 8 to 14 µm mid-IR transparency window. Taken from www.cflow-project.eu.*

nevertheless balances those benefits by reducing the power in a given remote collector area. The divergence of a MIR beam is however still orders of magnitude smaller than that of RF. On top of making higher datarates possible, the directionality of free-space optical communications is of great interest for military application because it offers protection regarding the security of the link, extremely difficult to intercept and unjammable. For telecom operators, it also removes interferences between signals and therefore the need for bandwidth sharing regulations as it is the case today in radiofrequencies. On the flip side, this directivity adds a difficulty to the realization of a stable link since aiming must be significantly more precise than with radiofrequencies.

Adverse atmospheric conditions are still problematic and likely prevent ground-to-space links with very high availability. Applications where time delivery of the data is not critical could still benefit from high throughput optical communications (Earth observing satellites for instance) [19].

Regarding communications in space, NIR solutions are already implemented between satellites (there is no atmosphere attenuation and line of sight in space is simple because there aren't any obstacle). Ground-space telecommunications (with low earth orbit satellite constellation) rely mainly on radiofrequencies, but growing needs of throughput could eventually be hindered by this choice of frequency for the carrier. As a sign that the paradigm of RF-only telecommunications might be shifting, companies putting on orbit constellations of satellites (SpaceX, OneWeb, Telesat), equip their newest satellites with laser communication terminals. The ESA and Airbus launched a program for optical telecommunications ('SpaceDataHighway', [20]), while the American defense launched its low Earth orbit constellation (the 'Transport Layer', [21]), equipped among others for Near IR laser telecommunications.

For optical telecommunications, apart from a laser and a detector, there is a need for a modulation scheme to imprint the information on the laser. Two solutions exist: direct modulation of the laser amplitude via a current modulation, or the addition of an external optical modulator on the link. Direct modulation is simpler to implement but the bandwidth is limited by the laser physics and geometry, leading to more restricted bandwidths, often in the GHz range maximum. Moreover, while modulating the current of the laser, the frequency of the laser is also changed and that can lead to transmission errors. The electrical power that is needed can also be higher. On the other hand, external modulation, that requires a supplementary device and therefore high frequency circuitry, uses the laser in continuous wave (CW) operation: the complexity of the message implementation is transferred to the external modulator, which enables larger bandwidth. Though more expensive and harder to implement, this second possibility is preferred for communication application because of the increased throughput.

Different types of external modulators exist for optical modulation in the NIR wavelengths, that illustrate the variety of possible approaches :

- Using the Pockels effect, the refractive index of a material can be changed by applying an electric field on it. If processed into a tuned waveguide or waveplate, the phase of the light can be changed, creating a phase modulation that can carry the information. Used in a Mach-Zender interferometer, it can be recombined with the original beam to produce interferences and carry the desired information *via* amplitude modulation.

- Electro-absorption modulator exploit either the Quantum confined Stark effect (QCSE) or the Franz–Keldysh effect, and use an external electric field to modify the absorption of light at a given wavelength and make amplitude modulation possible.

- Acousto optic modulators (AOM) modulate the intensity of a laser using a sound wave to manipulate the refractive index of a crystal or glass material. An AOM system includes an acousto-transducer piezoelectric that generates the modulated sound wave. This longitudinal wave scatters some of the light and decreases the intensity of the transmitted and measured signal, resulting in amplitude modulation.

These solutions fit well the NIR where optical fibers are particularly efficient and light is guided from the laser output to the modulator. In the LWIR, around 10 µm, fiber solutions are not mature yet because the losses are too high in the available materials.

The lack of efficient modulation schemes at MIR wavelengths compared to smaller wavelength is illustrated in the review [22] where we see that the fastest optical link implemented only allowed for several Gbit·s^{-1} with direct modulation. Unipolar devices based on quantum wells are a suitable candidate to fill this gap: exploiting the very high relaxation rate between levels could lead to devices performing at frequencies of tens of GHz, which is the state of the art for bitrates per channel in c telecommunication.

The first goal of this work is to demonstrate the feasibility of a unipolar amplitude modulator based on the Stark effect in asymmetric coupled quantum wells [5]. Before presenting

the structure and its design in Chapter 2, we present in the next sections the necessary physical toolkit useful for the design of unipolar devices.

1.2 Semiconductor quantum wells and intersubband transitions

The optoelectronic devices studied in this work rely on confined electronic states in semiconductor quantum wells. The key technologies that enabled the emergence of this field are the methods for crystalline growth that made possible, starting in the seventies, the fabrication of semiconductor crystals with thicknesses controlled at the monolayer level [1]. A vast zoology of semiconductor crystals can be grown, with alloys encompassing elements from the second to the sixth column of the periodic table: III-V alloys like GaAs, InP or GaN, IV alloys (SiGe) or II-VI alloys (HgTe, ZnS). For optoelectronic applications, III-V crystals are the most widespread.
By growing a succession of thin layers of semiconductors with different gap energies (but same lattice constant), artificial materials known as heterostructures can be fabricated. From the size confinement in the growth direction stems the quantization of the electronic levels in the conduction and valence bands. In the following, we will describe the building block of the optoelectronic devices based on semiconductor heterostructures: the quantum well. We will briefly introduce the model to compute the electronic wavefunctions in a semiconductor heterostructure, and insist on its resolution in the simple case of the infinite quantum well. Finally, we will see how light can be absorbed by electrons in a quantum well.

1.2.1 Schrödinger equation in a semiconductor heterostructure

We consider a heterostructure made of semiconductors with same lattice constant and different gap.

Assuming that the potential in the crystal is the sum of a periodic crystal potential, with the periodicity of the crystal lattice, and a slowly varying potential due to the heterostructure, the envelope function approximation [23] allows writing the wavefunctions $\Psi_i(\mathbf{r},\mathbf{k})$ as the product between the Bloch function $u(\mathbf{r})$ (with the periodicity of the crystal), and a slowly varying envelope function $f_i(\mathbf{r},\mathbf{k})$:

$$\Psi_i(\mathbf{r},\mathbf{k}) = f_i(\mathbf{r},\mathbf{k})u_i(\mathbf{r}) \tag{1.1}$$

The integer i indexes the band number in the Brillouin zone and k the wavenumber. Casting the wavefunction into such products, allows writing a Schrödinger-like equation for the envelope function:

$$\frac{-\hbar^2}{2}\vec{\nabla}\left(\frac{1}{m^*(z)}\vec{\nabla}\right) f_i(\mathbf{r},\mathbf{k}) + V_{het}(z)f_i(\mathbf{r},\mathbf{k}) = E_i f_i(\mathbf{r},\mathbf{k}) \tag{1.2}$$

The effective mass $m^*(z)$ in this expression replaces the free electron mass m_0, and carries the influence of the crystal potential on the free electron. It can be expressed as $\frac{1}{m^*} = \frac{1}{\hbar}\frac{d^2E}{dk^2}$.

In particular, if the dispersion relation is quadratic, the effective mass is constant.

The problem can be separated between the z-component and the in-plane one:

$$f_i(\mathbf{r}) = \frac{1}{\sqrt{A}}\phi_i(z)\exp(\mathbf{k}_\perp \mathbf{r}_\perp) \tag{1.3}$$

Where A is the area of the sample. The in-plane equation describes free electrons of mass m^*, with a parabolic dispersion. In the growth direction, the energy is set by the heterostructure. The corresponding eigenenergies for the different levels read:

$$E_{i,k_\perp} = E_i + \frac{\hbar^2 \mathbf{k}_\perp^2}{2m^*(z)} \tag{1.4}$$

1.2.2 Electronic states in a quantum well

By confining a thin layer of one semiconductor (InGaAs, or GaAs for instance) between two layers of a second semiconductor (AlInAs or AlGaAs respectively) with a larger energy gap E_g, the difference in Conduction Band Offset (CBO) creates a quantum well in the conduction band in the direction of the growth z. Fig.1.3 (a) shows a Transmission Electronic Microscope (TEM) image of an InAlAs/InGaAs/InAlAs heterostructure, taken by Konstantinos Pantzas. On top of it are schematically represented the top of the valence band and the bottom of the conduction bands for both crystals.

The 1-D Schrödinger equation for a conduction band electron in the well simply writes (by considering a constant effective mass):

$$\left(\frac{\mathbf{p}^2}{2m^*} + V(z)\right)\phi_i(z) = E_i\phi_i(z) \tag{1.5}$$

Where $V(z) = 0$ in the well from $-L/2$ to $L/2$ and is for now set infinite elsewhere. The simplifying infinite potential imposes $\phi_i(-L/2) = \phi_i(L/2) = 0$. The solutions in the well and their energies, indexed by the level number n, are then:

$$\phi_{i,n}^{\infty}(z) = \begin{cases} \sqrt{\frac{2}{L}}\cos\left(\frac{n\pi z}{L}\right) & \text{if n is odd} \\ \sqrt{\frac{2}{L}}\sin\left(\frac{n\pi z}{L}\right) & \text{if n is even} \end{cases}$$
$$E_{i,n}^{\infty} = \frac{\hbar^2\pi^2 n^2}{2m^* L^2} \tag{1.6}$$

Interestingly, the spacing between the electronic levels is proportional to $1/L^2$: the width of the well will define the energy difference between the states.

Solutions for a finite potential must be calculated numerically. Fig.1.3 (b) shows the square moduli of the wavefunctions (i.e. the probability density of an electron) obtained numerically for a 6.5-nm large, 520 meV deep quantum well (simulating an InGaAs/InAlAs QW). The in-plane dispersion of those states, the subbands, are shown in in Fig.1.3 (c). The energies and wavefunctions in heterostructures in this work are calculated with a QUAD group developed program. The numerical method solving the Schrödinger equation (under

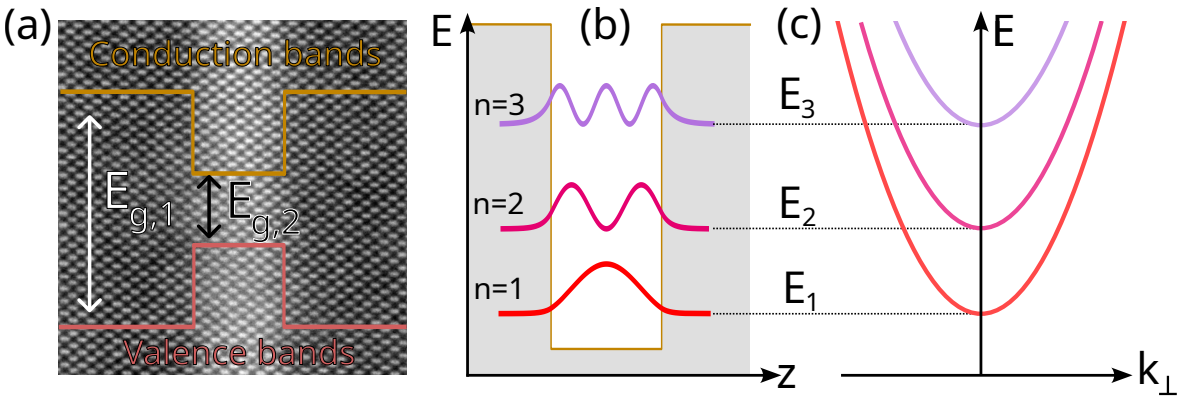

Fig. 1.3 *(a) TEM image of an InAlAs/InGaAs/InAlAs quantum well, taken by Konstantinos Pantzas. (b) Conduction band and square moduli of the wavefunctions plotted at the corresponding energies. (c) In-plane dispersion of the levels in the quantum well.*

an applied bias if necessary) is a shooting method, an iterative method for calculating point by point differential equations. On top of the model presented earlier, the program includes an effective mass calculated with a 3-band Kane model [24], making the effective mass dependent on the energy.

1.2.3 Intersubband absorption

Assuming that the semiconductor is n-doped, and that the first subband of the conduction band is populated, we are interested in the excitation of the electrons by the absorption of a photon. This section follows ref. [25].

The Hamiltonian of an electron interacting with an external electromagnetic field of frequency ω and wavevector $\mathbf{q}$, $\boldsymbol{\mathcal{E}} = E_0 \cos(\omega t - \mathbf{q}.\mathbf{r})\mathbf{e}$ characterized by a vector potential $\mathbf{A}$ is:

$$\mathcal{H} = \frac{(\mathbf{p} - e\mathbf{A})^2}{2m^*} + V(z) = \frac{\mathbf{p}^2}{2m^*} - \frac{e}{2m^*}(\mathbf{A}\cdot\mathbf{p} + \mathbf{p}\cdot\mathbf{A}) + \frac{e^2\mathbf{A}^2}{2m^*} + V(z) \tag{1.7}$$

In the Coulomb gauge, $\mathbf{A}$ and $\mathbf{p}$ commute. For the infrared radiations, we can neglect the spatial dependence of $\mathbf{A}$ since $1/\lambda \ll 1/a$ (a being the lattice constant of the crystal). Furthermore, for weak fields we can neglect the $\mathbf{A}^2$ term. We find:

$$\mathcal{H} = \mathcal{H}_0 + \mathcal{H}_{int} = \frac{\mathbf{p}^2}{2m^*} - \frac{e}{m^*}\mathbf{A}\cdot\mathbf{p} + V(z) \tag{1.8}$$

With $\mathcal{H}_0 = \dfrac{\mathbf{p}^2}{2m^*} + V(z)$ the bare Hamiltonian and $\mathcal{H}_{int} = -\dfrac{e}{m^*}\mathbf{A}\cdot\mathbf{p}$ the interaction potential. The transition rate Γ_{if} between an initial state i and a final state f can be calculated using the Fermi golden rule:

$$\Gamma_{if} = \frac{2\pi}{\hbar}\frac{e^2E_0^2}{4m^{*2}\omega^2}\left|\langle i\left|\mathbf{e}\cdot\mathbf{p}\right|f\rangle\right|^2 \delta\left(E_f - E_i - \hbar\omega\right) \tag{1.9}$$

For intersubband (ISB) transitions, we can calculate the matrix element of the previous expression using the envelope functions, which are issued from the solutions of $\mathcal{H}_0$:

$$\begin{aligned}\langle i\,|\mathbf{e}\cdot\mathbf{p}|\,f\rangle &= \langle f_i\,|\mathbf{e}\cdot\mathbf{p}|\,f_f\rangle \\ &= \int d^3r\,\exp(-j\mathbf{k}_\perp\mathbf{r})\phi_i^*(z)(\mathbf{e}\cdot\mathbf{p})\exp(j\mathbf{k}_\perp\mathbf{r})\phi_f(z) \\ &= \int dz\,\phi_i^*(z)p_z\phi_f(z) \\ &= \langle\phi_i\,|p_z|\,\phi_f\rangle \end{aligned} \tag{1.10}$$

Here we see that only a field with a polarization along the confinement direction z can induce an electronic transition. This *polarization selection rule* will dictate the future geometry of optoelectronic devices.

It is then helpful to define the oscillator strength f_{if} as:

$$f_{if} = \frac{2}{m^*\hbar\omega_{if}}\left|\langle\phi_i\,|p_z|\,\phi_f\rangle\right|^2 = \frac{2m^*\omega_{if}}{\hbar}|\langle\phi_i|z|\phi_f\rangle|^2 \tag{1.11}$$

This quantity verifies what is called the sum rule: $\sum_k f_{nk} = 1$ for a given initial state n and all the final states k. This quantity reflects a second selection rule regarding the parity of the wavefunctions: for a quantum well with a mirror symmetry, only transitions between opposite-parity subbands are significant. In the case of the infinite quantum well, $f_{12} = 0.96$ and $f_{14} = 0.03$. Almost all the oscillator strength is thus concentrated in the 1-2 transition.

Finally, we evaluate the absorption coefficient of a QW, α_{3D}, defined as the ratio between the absorbed electromagnetic energy per unit time and volume $\hbar\omega_{if}\Gamma_{if}/V$ and the energy of the incident radiation $\frac{\varepsilon_0 cnE_0^2}{2}$, (with n the material index) and taking into account all occupied initial states in the subband i and all empty final states in the subband f using the Fermi Dirac distribution f_{FD} for the occupancy of the electrons in the subband. It is convenient for calculations to define the 2D absorption $\alpha_{2D} = \alpha_{3D}\cdot L_{eff}$. L_{eff} is the length over which the electromagnetic wave is effectively absorbed by the quantum well [26]. A first approximation is to consider $L_{eff} \simeq L$. The 2D absorption can be expressed as:

$$\begin{aligned}\alpha_{2D} = \frac{\pi e^2}{\varepsilon_0 cn\omega m^{*2}}\sum_{if}\frac{2}{(2\pi)^2}\int d^2k_\perp\left|\langle i\,|p_z|\,f\rangle\right|^2\left[f_{FD}\left(E_{i,k_\perp}\right) - f_{FD}\left(E_{f,k_\perp}\right)\right] \\ \times\,\delta\left(E_{f,k_\perp} - E_{i,k_\perp} - \hbar\omega\right)\end{aligned} \tag{1.12}$$

Assuming the parabolic dispersion along $k_\perp$, the Fermi Dirac distributions can be integrated (with E_F the Fermi energy and k_B the Boltzmann's constant):

$$\alpha_{2D} = \frac{e^2k_BT}{2\varepsilon_0 cn\hbar}\sum_{i,f}f_{if}\ln\left[\frac{1+\exp\left(\left(E_F-E_i\right)/k_BT\right)}{1+\exp\left(\left(E_F-E_f\right)/k_BT\right)}\right]\frac{\gamma/\pi}{\left(E_f-E_i-\hbar\omega\right)^2+\gamma^2} \tag{1.13}$$

In this final expression, we replaced the Dirac functions by Lorentzian of width γ and

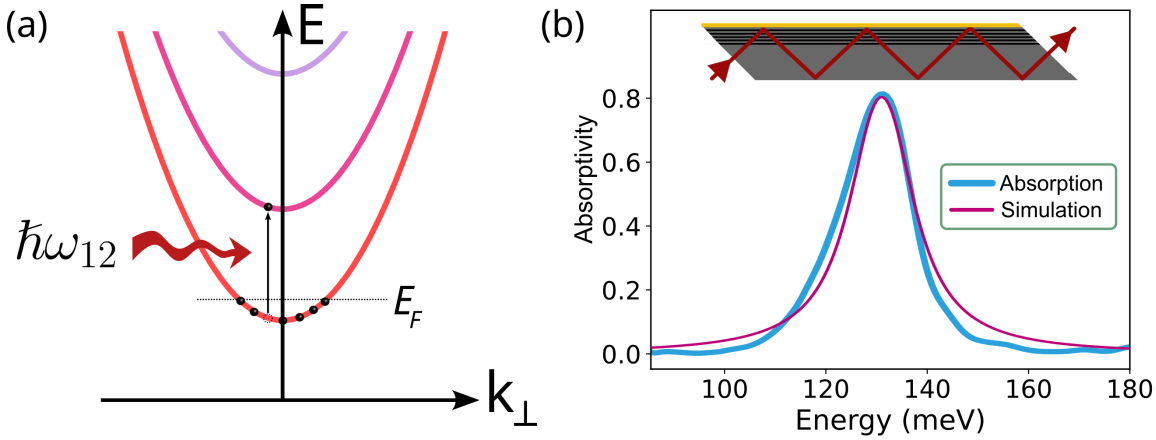

Fig. 1.4 *(a) Optical transition at energy E_{12} by an electron in the first subband of a quantum well. (b) Absorptivity of multipass sample with 13 6.5 nm-large InGaAs/InAlAs quantum wells and absorption simulation assuming 8 passes.*

exploited the fact that the absorption takes non zero values only for energies close to $\hbar\omega_{if}$. Because of the sum rule, it is reasonable in practice to restrict the sum to only the few final states with significant oscillator strength. Finally, the geometry of the light interaction with the active region should be added with a coupling factor, C, related to the polarization selection rules. The absorption of a sample with N_{qw} wells will read, according to Beer Lambert law, $A = 1 - \exp(-N_{qw}\alpha_{2D} \cdot C)$ as long as the absorption remains weak. Fig.1.4 (a) shows the schematic vertical absorption (since we neglected the momentum of the photon) by an electron in the first subband of a QW. Panel (b) presents in blue an example of absorption spectrum of 13 8 nm-large InAlGaAs/InGaAs quantum wells doped at 5.10^{17}cm^{-3} at room temperature in a multipass configuration (as sketched above the spectrum). In purple is plotted the simulation assuming a Lorentzian shape and 8 passes through the active region, reproducing closely the observed absorption with a width of 20 meV.

Depolarization shift

When a QW is highly doped (typically $n_{2D} > 10^{11}$ cm^{-2}), the electron is sensitive to the A.C. Coulomb interaction generated by the electron gas oscillating in the well on top of the external electromagnetic field. This additional contribution will lead to a slightly blue-shifted absorption energy [27]. The plasma shifted absorption frequency $\tilde{\omega}_{12}$ reads:

$$\tilde{\omega}_{12}^2 = \omega_{12}^2 + \omega_p^2 \tag{1.14}$$

Where $\omega_p = \sqrt{\dfrac{f_{12} n_{2D} e^2}{m^* \varepsilon_0 \varepsilon_r L_{eff}}}$ is known as the plasma frequency.

1.2.4 Coupled quantum wells

Epitaxial growth allows engineering more complicated profiles than single quantum wells. By growing two quantum wells separated by a thin barrier, one can exploit the tunnel coupling. Most of the unipolar quantum devices in this work are based on tunnel coupled quantum

wells. Stark Modulators, described in Chapter 2, are based on asymmetric coupled quantum wells, as shown in Fig.1.5 (a).

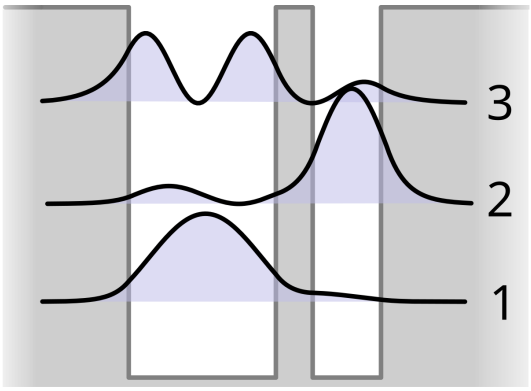

Fig. 1.5 *Asymmetric coupled quantum wells conduction band profile and wavefunction square moduli.*

The wavefunctions resulting from such system are different from the single quantum well: they are delocalized over the two wells, and their symmetry is changed. Due to the lack of symmetry, all transitions are allowed and the oscillator strength can be tailored over the various transitions by changing barriers and wells widths. In particular the 1-3 transition is not forbidden anymore.

This new degree of freedom can even be used to create a situation where $E_{12} = E_{23}$, with also close oscillator strengths. This potential can also be used for second harmonic generation [28, 29], as the second order susceptibility can become very large with *ad hoc* optimization:

$$\chi^{(2)}(2\omega) = \frac{e^3}{\varepsilon_0} N_{qw} \frac{\langle z_{12}\rangle\langle z_{23}\rangle\langle z_{31}\rangle}{(\hbar\omega - \Delta E_{12} - i\gamma_{12})(2\hbar\omega - \Delta E_{13} - i\gamma_{13})}$$
$$\text{with} \quad \langle z_{ij}\rangle = \langle \phi_i \mid z \mid \phi_j \rangle \tag{1.15}$$

Fine tuning of the energies to have them equally spaced and maximize $\chi^{(2)}(2\omega)$ can furthermore be done using an external electric field. Indeed, the spatial separation of the centroids of the second wavefunction with respect to the others make its energy sensitive to external bias. This is the very property that will be used to fabricate the modulator in Chapter 2.

Finally, the transport between coupled wells, essential for the Quantum Cascade Detectors and Lasers was described in [30] with a tight binding approach. The net particular current I_T between levels i and j reads in the first order

$$I_T = \Omega_T^2 \frac{\gamma}{(\omega_i - \omega_j)^2 + \gamma^2}(n_i - n_j) \tag{1.16}$$

n_i is the population in level i, ω_i its frequency, and the tunnel coupling constant $2\Omega_T$ is the minimum frequency splitting between the levels of the coupled wells when they are at resonance, reflecting the mutual interactions of the subbands. The larger the barrier separating the two wells the smaller the coupling constant will be. For levels separated by an

energy $\hbar\omega_{ij} > \Omega_T$, the description of the transport can be directly computed with the Fermi golden rule from the spatial representation of the wavefunctions and considering the various scattering processes that can occur in the crystal, that we will list in the next section for the transport in the QCD.

1.3 Mid Infrared optoelectronic devices based on ISB transitions

Intersubband radiative transitions are exploited to realize mid IR optoelectronic devices. Absorbing QW can be exploited to realize detectors if the photoexcited electrons are extracted in an electronic circuit. Two types of photodetectors are used in this work: the Quantum Well Infrared Photodetector (QWIP), first ISB photodetector invented, dating from 1987 [31], and the Quantum Cascade Detector (QCD). We will see how they are designed and expected to work, their figures of merit and their architecture respecting the polarization selection rule for ISB transitions. Regarding light emission, luminescence can be observed if electrons are injected on an excited level. Careful quantum and electromagnetic engineering led to the realization of lasers: the Quantum Cascade Lasers (QCL). In the last section, we will briefly present how these well-established devices are designed, and the ingredients necessary to their realization.

1.3.1 Quantum well photodetectors

Unlike photodiodes based on valence to conduction band transitions, QWIPs and QCDs being unipolar devices, only one type of carrier is involved in the optical transition and in transport (always electrons, that have a better mobility). They are thus unipolar devices. The transport involves tunneling and scattering mechanisms and the carriers are characterized by a short lifetime and transit time in the order of few ps.

a) Design and principle of operation

a).1 QWIP

Fig.1.6 shows (a) the bandstructures of two periods of a QWIP. The QWIP is a succession of doped (typically 10^{11} cm^{-2}) wells with two confined levels, the second one close to the top of the well, separated by large barriers. At both ends of the structure lie highly doped contact layers, acting as reservoirs of electrons. While operating, the QWIP is biased with a DC voltage, bending the band structure.

Dark Current

Without any illumination and under bias, a current J flows in the structure between the contacts because of the applied electric field F:

$$J(F) = en_{3D} \cdot v_d(F) \tag{1.17}$$

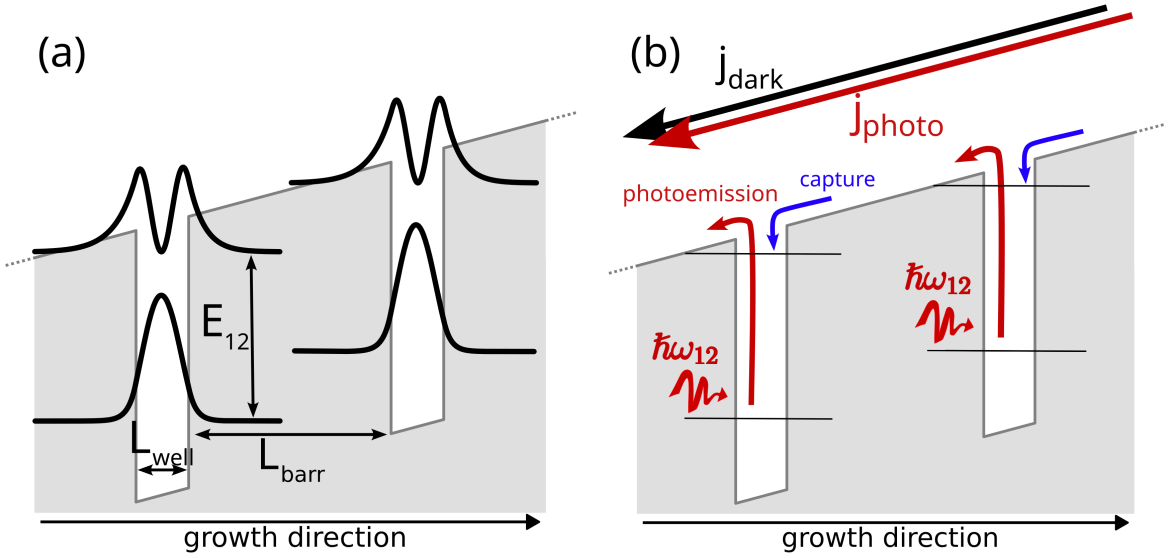

Fig. 1.6 *(a) Schematic representation of a QWIP with the quantities important for the design of one period of an active region: the size of the wells and of the barrier. Square moduli of the wavefunctions localized in the well are also represented. (b) Schematic representation of capture and emission of electrons under illumination. Dark current and photocurrent add up in the structure. The photocurrent results from photoemission from the wells, minus the photoelectrons recaptured in wells.*

where n_{3D} is the electron density above the barrier, in the continuum, and v_d is the drift velocity, defined as $v_d = L_p/\tau_{trans}$. L_p is the length of a period (well and barrier) and τ_{trans} the time necessary to go through it. In steady state, a second mechanism completes the dark transport picture: the emission and capture of electrons in the wells. Electrons can leave the well by thermal activation, and generate an escape dark current j_e^{dark}. On the other hand, electrons traversing a well have a probability p_c to be captured. These phenomena must balance and $J^{dark} = j_e^{dark} + (1-p_c)J^{dark} \rightarrow j_e^{dark} = p_c J^{dark}$.

The capture probability can be written in terms of the capture rate τ_{capt}^{-1} from the excited state in the well and the inverse transit time τ_{trans}^{-1} :

$$p_c = \frac{1/\tau_{capt}}{1/\tau_{capt} + 1/\tau_{trans}} = \frac{\tau_{trans}}{\tau_{trans} + \tau_{capt}} \tag{1.18}$$

j_e^{dark} describes the current due to the thermally excited electrons that populate the excited subband, scattering into the 3D states in the continuum. It can therefore be written as $j_e^{dark} = e n_{2D} \cdot \tau_{scatt}^{-1}$ where τ_{scatt} is the characteristic time necessary for the scattering to the continuum from the localized states in the well. n_{2D}, here the density of electron above the barrier V_b, is calculated with the Fermi Dirac distribution:

$$n_{2D} = \frac{m^*}{\pi\hbar^2} \int_{E_1}^{\infty} dE \frac{T(E,F)}{1 + \exp\left((E - E_F)/k_B T\right)} \tag{1.19}$$

T(E,F) is a function describing the probability of the electron in the second level to tunnel

through the barrier to the continuum. It is a function of the energy and the shape of the barrier, bent by the field. We will consider its value to be 1 when the energy is above the barrier, 0 else. We can finally derive

$$J^{dark} = \frac{j_e^{dark}}{p_c} = \frac{m^*}{\pi\hbar^2}\frac{\tau_{capt}+\tau_{trans}}{\tau_{scatt}\tau_{trans}} k_B T \exp\left(-E_{act}/k_B T\right) \tag{1.20}$$

The dark current is a thermally activated process, exponentially increasing with temperature. The activation energy is $E_{act} = V_b - E_F - FL_{qw}/2$, the difference of energy between the Fermi level and the top of the well, lowered by the electric field F.

Current under illumination

Under illumination, a new process comes in play: electrons in the well can be promoted to level 2 by photon absorption, then escape in the continuum and be accelerated by the electric field. In Fig.1.6 (b) are sketched all the processes that contribute to the measured current. The absorption of the photon was treated in the previous section. Once the electron is excited in the state 2, its probability to escape the well p_{em} is again expressed as the competition between two phenomena: the relaxation to the ground state, and the escape toward the continuum [32]:

$$p_{em} = \frac{\tau_{relax}}{\tau_{relax}+\tau_{esc}} \tag{1.21}$$

The current generated by the photoexcited electron from one well $i_{photo}^{(1)}$ ((1) refers to a single well quantity) is proportional to the light flux ϕ and the absorption efficiency $\eta_{abs} = N_{qw}\eta^{(1)}$:

$$i_{photo}^{(1)} = e\phi\eta^{(1)}\frac{\tau_{relax}}{\tau_{relax}+\tau_{esc}} = e\phi\eta_{abs}\frac{p_{em}}{N_{qw}} \tag{1.22}$$

The photoemission will need to be balanced by an extra injection δi from the contact to maintain electrical neutrality in the well. In steady state, the conservation of the number of electrons before and after a quantum well leads to:

$$\delta i = i_{photo}^{(1)}/p_c = e\phi\eta_{abs}\frac{p_{em}}{N_{qw}p_c} \tag{1.23}$$

This extra injection is indeed the photocurrent I_{photo} read in the circuit. If the absorption efficiency η_{abs} is proportional to the number of wells, then the photocurrent is independent on the number of periods.

Photoconductive gain

Equation 1.23 defines the photoconductive gain of the detector g_photo, quantifying the number of extra electrons circulating in the circuit after a photon absorption:

$$g_{photo} = \frac{p_{em}}{N_{qw}p_c} \tag{1.24}$$

The evaluation of this quantity leads to the optimization of the design of the QWIP, notably the position of the second level with respect to the well: when the second level is almost in the continuum, at the top of the well, $p_{em} \simeq 1$. If the localized level is too far above the well, the oscillator strength will decrease though. This optimum is known in the literature as "Bound to quasi-continuum" QWIPs. It is the case depicted in Fig.1.6 and the photoconductive gain reads

$$g_{photo} \simeq \frac{1}{N_{qw} p_c} \simeq \frac{\tau_{capt}}{N_{qw} \tau_{trans}} = \frac{\tau_{capt} v_d}{N_{qw} L_p} \tag{1.25}$$

The first device with such design was realized in 1988 by Levine *et al.* on GaAs/AlGaAs [33]. This design also limits the bias necessary to extract electrons with respect to the devices with the second level within the well, limiting the dark current generated.

The width of the barrier, L_{barr}, can be chosen independently of the well. The expression of the photoconductive gain suggests having it as low as possible. The limit to this rule is the interwell tunneling, which was overlooked in the description of the transport in the device. A study on GaAs/AlGaAs QWIPs showed that with too thin barriers (10 nm) [34], the dark current was dominated at nitrogen temperature by interwell tunneling under reasonable electric fields (<20 kV/cm), also decreasing the measured photocurrent drastically. For other samples, no significant difference was observed for barriers between 20 and 46 nm. Moreover, at high temperature the gain converges to $1/N_{QW}$, meaning p_{capt} tends to 1: when the drift velocity becomes small, τ_{trans} increases and p_c becomes 1 [35]. Therefore, in the literature, barriers are never smaller than 20 nm.

a).2 Quantum Cascade Detectors

Fig.1.7 presents the band structures of two quantum cascade detectors (QCD). In order to operate without external bias, for photovoltaic operation, an artificial asymmetric potential is created by a careful bandstructure engineering. This type of photovoltaic detector does not suffer from the large dark current observed in a QWIP, at the expense of a reduced responsivity.

The QCDs are composed of an absorbing well with two levels akin to the QWIP (except that the second level is not close to the barrier edge), and an extractor region formed of a succession of wells with levels engineered to ensure the extraction of the photoexcited electrons toward the next period of the structure, also known as the cascade.
The transport within the cascade is controlled by various scattering processes:

- LO phonon spontaneous emission and absorption
- interface roughness, caused by growth imperfection at the junctions between materials
- alloy disorder in ternary materials

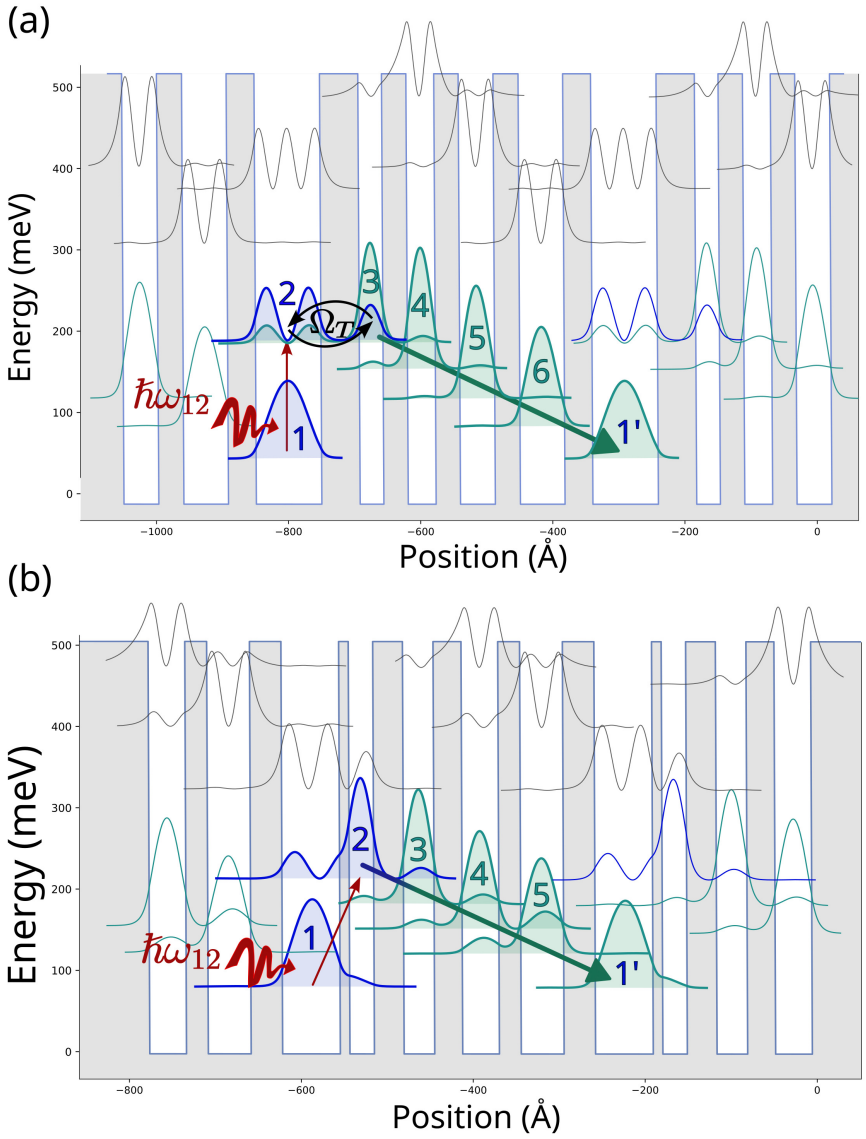

Fig. 1.7 *(a) Schematic representation of a vertical QCD. One period is highlighted with color fillings. Levels 1 and 2, in blue, are involved in the photon absorption. Levels 2 to 6 form the cascade, responsible for the extraction of the photoexcited electron to the next period. The transport between 2 and 3 is best modelled by resonant tunneling at angular frequency Ω_T. (b) Schematic representation of a diagonal QCD. As in (a), levels 1 and 2 in blue are responsible for photon absorption and green 3 to 5 are responsible for the extraction. The delocalization of 2 across two wells makes for an efficient transport to the extractor without resonant tunneling.*

The efficiency of each process is estimated in [36] for InGaAs/InAlAs heterostructures and are evaluated using the Fermi golden rule in the program that calculates the wavefunctions in heterostructures.

Vertical and diagonal QCDs

The first QCDs reported [37, 38] are the so-called vertical QCDs, where the absorption of the photons and the extraction of the excited electrons take place in two separated quantum

wells (Fig.1.7 (a)). The absorbing well and the extracting cascade are coupled through resonant tunneling between the excited state of the optical transition and the first level of the cascade. This leads to a good oscillator strength of the intersubband transition 1-2, but the extraction relies on a resonant phenomenon and is therefore very sensitive to the quantum well thickness and/or applied electric field.

In 2014, a second concept emerged with diagonal QCDs [39] (Fig.1.7 (b)). Now the active 1-2 transition occurs between two energy levels, localized in different but adjacent wells. The idea is to have more efficient extraction towards the cascade with respect to the vertical design, at the expense of a reduced oscillator strength. Note that a small difference in the epitaxy from the design would lead to a slightly different energy absorption, but the detector would still be functional.

The extraction through the cascade is characterized by p_{esc}, the escape probability, i.e. the probability of a photoexcited electron to reach the next period of the device. For a device with N_{qw} periods, the efficiency of the extraction of a photoexcited electron into the external circuit is $\eta_{int} = p_{esc}/N_{qw}$ [40]. Just like the photoconductive gain in the QWIP, η_{int} is a measure of the number of electrons circulating in the external circuit after a photon absorption.

Optimizing the active region of a QCD actually means choosing an absorption energy like in a QWIP, and optimizing the product $p_{esc} \cdot \eta_{abs}$, where η_{abs} is the absorption efficiency, expressed as $\eta_{abs} = 1 - \exp(-\alpha_{2D})$.

Escape probability

The complete calculation of the escape probability i.e. the transport from 2 to 1', is complicated since we must consider all possible transitions, up and down the cascade. Markovian approaches were developed [41],[42], calculating iteratively the probability density of a particle starting in the level 2 (excited state) after n-timesteps in a structure with N levels, by applying a N×N stochastic matrix T constructed from all the transition rates, to the power n. The elements of the matrix read $T_{ij} = p_{i,j} = \frac{\frac{1}{\tau_{ij}}}{\sum_k \frac{1}{\tau_{ik}}}$. The complete matrix T reads:

$$T = \begin{bmatrix} 1 & 0 & 0 & \cdots & 0 & 0 \\ p_{2,1} & 0 & p_{2,3} & \cdots & p_{2,N-1} & p_{2,N} \\ \vdots & \vdots & \ddots & \vdots & \vdots & \vdots \\ p_{N-1,1} & p_{N-1,2} & p_{N-1,3} & \cdots & 0 & P_{N-1,N} \\ 0 & 0 & 0 & \cdots & 0 & 1 \end{bmatrix}$$

In the limit of very large n, the escape probability can be calculated after defining $p_i[M]$, the probability of the electron to be in the level M after i timesteps:

$$\begin{aligned} p_0 &= [\,0 \quad 1 \quad \cdots \quad 0\,]^T \\ p_n &= T^n p_0 \\ p_{esc} &= \lim_{n\to\infty} p_n[N = 1'] \end{aligned} \tag{1.26}$$

An underlying hypothesis is that all scattered electrons are at the bottom of the subband, i.e. the intrasubband relaxation is faster than any intersubband process. This hypothesis is called the thermalized subband [43, 44] and justifies that the probability to go from i to j at time t does not depend on the probability density at time $t-1$.

Authors of [41] also consider the period on the left of the absorbing well for even more completeness. From this study, it appears that the extraction probability inside the cascade ($p_{k,k+1}$ for $k \in [3, N-1]$) is close to unity if the electronic states in the cascade are indeed separated by the energy of a LO-phonon (33 meV for InGaAs). We operate close to room temperature and the width of the transitions are few meV, therefore the energy separation is quite free.
Because of the number of parameters involved in the design of the full QCD, we will work under the simplifying approximation that an electron reaching the second level of the extractor can only relax towards lower energies. The probability to advance from one well is therefore simply expressed as the competition between the extraction into the cascade and the relaxation back to the initial state 1. For $i > 1$, we can write:

$$p_{i\to i+1} = \frac{\dfrac{1}{\tau_{esc}}}{\dfrac{1}{\tau_{esc}} + \dfrac{1}{\tau_{relax}}} = \frac{\tau_{relax}}{\tau_{esc} + \tau_{relax}} = \frac{\tau_{i\to 1}}{\tau_{i\to i+1} + \tau_{i\to 1}} \tag{1.27}$$

The calculation of $p_{2,3}$, crucial for the final performances of the device, will depend on the type of QCD (vertical or diagonal).

Vertical QCD and resonant tunneling

As shown in Fig.1.7 (a) vertical QCD, levels 2 and 3 are designed to be resonant. Because of tunnel coupling, the two levels actually split and are separated by an energy $2\hbar\Omega_T$. Furthermore, the corresponding wavefunctions are delocalized over the wells involved. If Ω_T is not negligible (with respect to the dephasing rate τ_{deph}^{-1}), the position of the electron oscillates between the two quantum wells at angular frequency Ω_T. The escape probability under this assumption can be evaluated as in [45]:

$$\frac{1}{\tau_{esc}} \simeq \frac{1}{\tau_{24}} = \frac{2\Omega_T^2 \tau_{deph}}{1 + 4\Omega_T^2 \tau_{deph}\tau_3} \tag{1.28}$$

where τ_{deph} is empirically estimated as $\tau_{deph} = 0.1$ ps [46]. If $4\Omega_T^2\tau_{deph}\tau_3 \gg 1$ (strong coupling), the expression simplifies: $\dfrac{1}{\tau_{esc}} = \dfrac{1}{2\tau_3}$ and is driven by the extraction rate from 3 to

4. If $4\Omega_T^2\tau_{deph}\tau_3 \ll 1$, on the other hand, the transport is governed by the dephasing time. This situation, unfavorable, would happen if the first barrier is very large or if the scattering rate τ_3^{-1} is weak, i.e. a poor design of the extractor.

Diagonal QCD

For diagonal QCD, we can easily calculate the complete escape probability in the absence of tunneling as the product of the single escape probability in 1.27 knowing the relaxation rates:

$$p_{esc} = \prod_{i=2}^{N} \frac{\tau_{i\to 1}}{\tau_{i\to i+1} + \tau_{i\to 1}} \tag{1.29}$$

Intuitively, most of the optimization occurs in the first couple of wells and the first barrier: by delocalizing the second level toward the extractor, we will limit the absorption efficiency but increase the extraction probability.

b) Figures of merit for unipolar detectors and state of the art

Different figures of merit help qualifying the performances of a detector.

- The absorption efficiency η_{abs} describes the probability for an impinging photon on the detector to be absorbed. It is related to the oscillator strength of the transition involved and the geometry of the light coupling in the detector and the number of quantum wells.
- The internal extraction efficiency η_{int} (also known as the photoconductive gain for QWIPs) describes the probability for a photoexcited electron to be transferred to the electrical circuit. It quantifies the transport in the structure.
- The quantum efficiency η describes the efficiency of conversion of an impinging photon into electron in the circuit, $\eta = \eta_{abs} \cdot \eta_{int}$;
- The responsivity $R = \frac{e\eta\lambda}{hc}$ expresses in A/W the quantum efficiency. Because of its definition, one must be careful when comparing performances of detectors at different wavelengths as it is proportional to λ. ISB devices aiming for the highest responsivity reached a record responsivity of 3.3 A/W at 7.3 µm with a single-well QWIP [47] at low temperature. Several works on QWIPs reach also the A/W level with several wells to improves noise figures [35] (at 9 µm) or bandwidth [48] (at 10 µm). The room-temperature responsivity is nevertheless significantly smaller, with 85 and 150 mA/W reported for the same devices. Regarding QCDs, a recent work showed responsivity at 10.3 µm of 120 mA/W at low temperature and 85 mA/W at room temperature [49].
- The current noise spectral density σ, in $A/\sqrt{Hz}$, is the noise current per unit of bandwidth. Different noise contributions can be explicited and $\sigma = \sqrt{\sum_i \sigma_i^2}$:
  - The thermal noise also known as Johnson noise : $\sigma_{Th} = \frac{4k_BT}{r}$, r being the resistance of the device [50].

  - shot noise, $\sigma_{shot} = 2e(I_{photo} + I_{dark})$.
  - $1/f$ noise, common to all electrical circuit.

  When measuring the detector performances, the noise current corresponds to the noise spectral density evaluated within the detector bandwidth. For continuous signals, the bandwidth can be reduced by increasing the integration time $t_{int} = 1/\Delta f$: $i_N = \sigma\sqrt{\Delta f}$.

- The Noise-equivalent Power (NEP) in W is the minimal optical power necessary to obtain a Signal-to-Noise Ratio (SNR) of 1 with a 1 Hz bandwidth.

- The detectivity $D = \dfrac{1}{NEP}$. The larger the detectivity of a photodetector, the more it is suitable for detecting weak signals which compete with the detector noise.

- The specific detectivity (D^*) in obtained by renormalizing the detectivity with respect to the surface of the detector A and the bandwidth : $D^* = \dfrac{\sqrt{A\Delta f}}{NEP}$. It is expressed in $cm\sqrt{Hz}/W$ or Jones, and is used rather than the NEP when comparing detectors based on different technologies, with different sizes. High specific detectivities can also be achieved: [35] presented a QWIP with $D^*(78K) = 2.10^{10}$ Jones and $D^*(300K) = 3.10^7$ Jones, and in [46], authors reached a $D^*(78K) = 2.10^{10}$ Jones, background limited specific detectivity both working at 9 µm.

- The electrical bandwidth Δf_{-3dB} is the modulation frequency of the impinging optical power at which the detector's output power is divided by 2. Until reaching the ultimate physical limit of the ISB dynamics, it is set by the electromagnetic environment of the detector. In ISB devices, the intrinsic lifetime of carriers is typically 1 ps in the case of LO phonon relaxation, so this upper limit of the electrical bandwidth would be hundreds of GHz [51]. Recent works indeed showed very large bandwidth of 30 GHz and 70 GHz at room temperature for InGaAs/AlInAs QCDs [49] and GaAs/AlGaAs QWIPs [48] respectively.

Mid-IR ISB detectors are often compared to most prevalent type of detector for that spectral region: the HgCdTe (also known as MCT) detector. This interband detector, with a bandwidth covering most of the IR spectrum, from 1 to more than 20 µm, exhibits high detectivities ($\geqslant 5.10^{10}$ Jones at 78 K with nitrogen cooling, and 2.10^8 Jones with thermo-electric cooling) and high quantum efficiency (up to 70% [52]), which equates a responsivity of approximatively 5 A/W at 9 µm. Their main limitation is the low speed response. With adapted electronics though, commercially available detectors are reaching 1 GHz bandwidth. A last negative feature characterizing these detectors is their low saturation threshold, making them inadequate for applications necessitating intense laser power.
The limited spectral bandwidth of ISB detectors can also be a competitive advantage in certain cases. In astronomy for instance, where the signal is faint and diluted in ambient blackbody from the optics, limited spectral bandwidth limits the current noise generated. For optical data transmission, as long as the laser is tuned with the detector, a large spectral bandwidth is also detrimental for the same reason.

c) Geometries for light coupling

The device architecture must comply with electrical and optical constraints. On top of the necessary electrical connections, the ISB polarization selection rule dictates specific geometries where the electric field has a significant component along the growth axis in order to obtain a sizeable light-matter coupling. Different strategies have been proposed and are sketched in Fig.1.8.

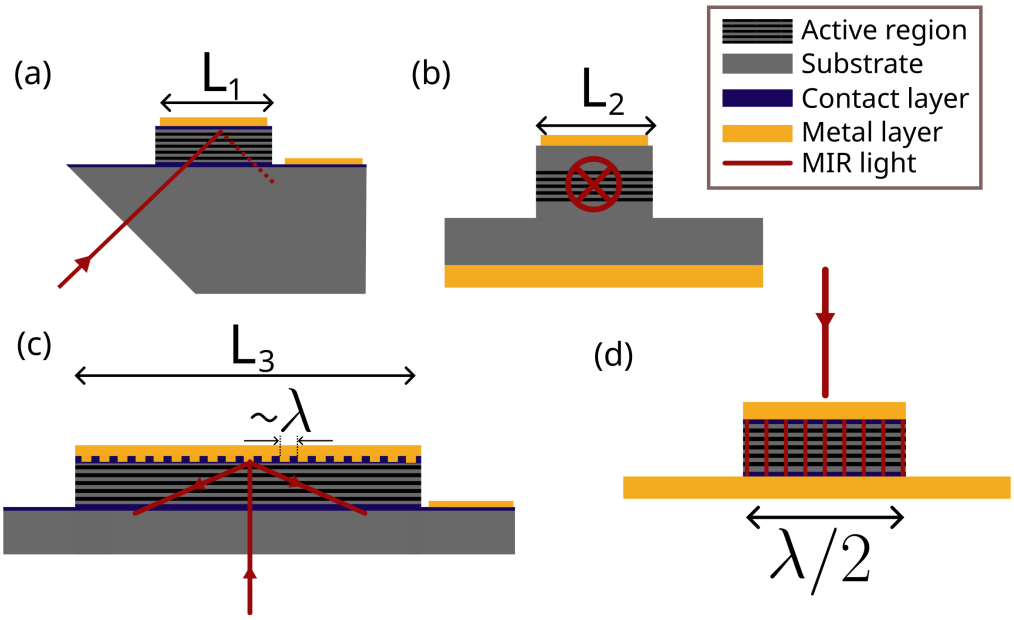

Fig. 1.8 *Different geometries respecting the ISB polarization selection rule. λ is the wavelength in the semiconductor and L_i are is a characteristic size of the device. (a) Mesa illuminated through a 45° facet polished in the substrate. (b) Waveguide geometry for facet illumination. (c) Reflective diffraction array on top of mesa allowing for normal incidence through the substrate. (d) Double metal cavity with its fundamental mode along the growth axis, allowing normal incidence.*

- The simplest device is the mesa (a). The active region is etched in a pillar then is illuminated through the substrate and a polished facet, usually at 45°. Metallic contact can easily be placed. The coupling factor appearing in the expression of the absorption in section 1.2.3 will then be $C = 2 \times \frac{\sin^2(45°)}{\cos(45°)}$ if the absorbed fraction of the light remains small. The $\sin^2$ comes from the ISB selection rules and the $2/\cos$ from the increased interaction length with respect the active region size. The transmission through the facet ($\simeq 70\%$) should also be taken into account. In the end, the absorption efficiency reads $\eta_{abs} = T_{facet}\left(1 - \exp\left(-2\alpha_{2D}N_{qw} \cdot \frac{\sin^2(45°)}{\cos(45°)}\right)\right)$.
- In order to fully benefit from a vertically polarized light (using a laser), it is possible to design a waveguide, encapsulated in a low refractive index material and inject the light through the side facet (b). Though this geometry gives a perfect coupling of the injected light with the ISB polarization, the quantity of light that can be injected is

limited by the thickness of the active region (hence smaller than a diffraction limited spot size at 10 μm) [53]. For monolithical integration purposes, this geometry is very important.

- A more complex geometry (in terms of processing) have been proposed, in particular for Focal Plane Arrays (FPA) requiring normal incidence: adding reflective diffraction gratings at the back of the active region (c). Normal light would go through the active region without being coupled, then be reflected and diffracted on the grating, at large angles, making a strong interaction possible [54]. This geometry can make pixel-like detectors compatible with Si readout integrated circuit (ROIC), which enabled the development of IR QWIP cameras [55, 41]. Different types of gratings were proposed: periodic, random, and even 3D [56].

- Another method, that will be used in this work, is the patch antenna resonator [57] (d). The active region is embedded between two metallic layers forming a resonator and verifying the polarization selection rule. Thanks to the quality factor ($\simeq 10$) of the resonator, the light-matter interaction length is significantly increased.[35].

1.3.2 Quantum Cascade Laser (QCL)

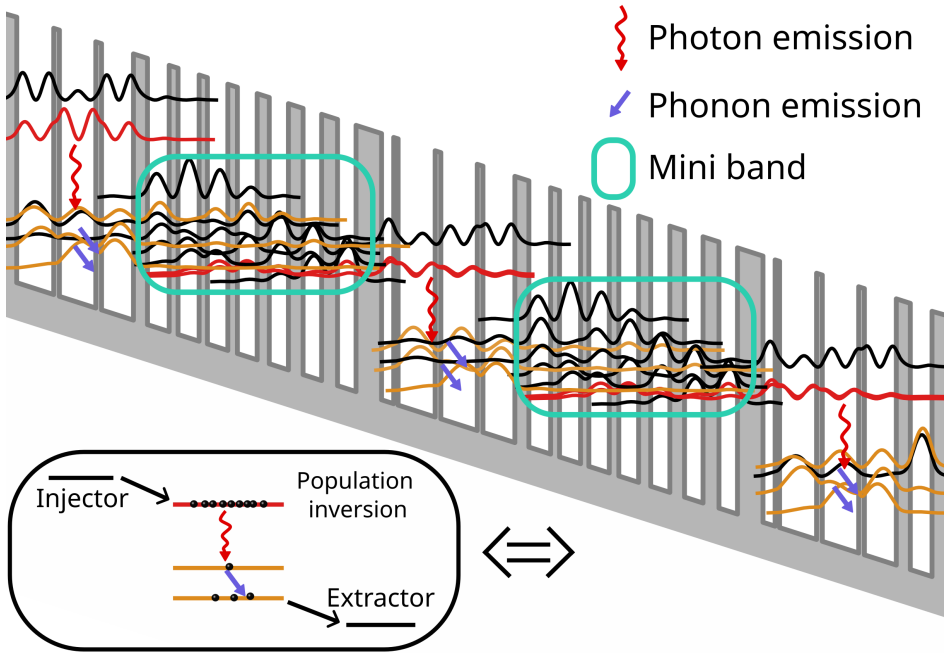

Fig. 1.9 *Quantum Cascade laser (QCL) active region. Heterostructure form [58].*

Quantum cascade lasers [2] (QCLs) are also unipolar semiconductor devices, based on intersubband transitions in the conduction band. Their active region is composed by the repetition of several ($\simeq 20 - 50$) identical periods, based on an injection region (a multi-quantum well), a system of few coupled quantum wells in which the radiative transition takes place, and an extraction region, which is also the injector of the following period of the cascade. The gain is achieved in the structure thanks to an accurate engineering of the

electronic lifetimes in the quantum wells. Fig.1.9 shows the band structure of two periods of a QCL and breaks down the different regions identified before (The upper state of the laser transition is in red). The equivalent typical 3-level laser picture for population inversion is reminded in the black inset. Most QCLs are processed into ridges (like in Fig.1.8 (b)), embedded into a lower index material and cleaved on both sides, in order to guide a mode between the two facets.

Invented in 1994 but working at cryogenic temperature, CW room temperature operation was shown in 2002 for the first time, at 9.1 µm [59]. The output power for MIR InP QCLs have since then tremendously enhanced and reach 3 W at 8.3 µm [60] and more than 10 W at 4.5 µm in cw operation and 100 W in pulsed mode, at room temperature [61].
Besides those records values from research laboratories, some industrial groups started commercializing fully packaged QCLs in the MIR. We used in this work two types of QCL operating at room temperature with thermoelectric cooling: a Distributed Feedback (DFB) laser, emitting up to 100 mW at 9 µm (from Thorlabs). A diffraction grating patterned on the cavity of the laser ensures a single mode operation (DFB, distributed feedback [62]). A second laser (from Daylight Solutions) tunable QCL was used. Instead of a reflective back facet, a diffraction grating is used. The grating can rotate and change the lasing wavelength. For a single active region, this laser is able to lase at room temperature between 9 µm and 11.3 µm, with a CM peak output power of 350 mW at 10 µm.

1.4 Conclusion and objectives

After almost 40 years of investigation, III-V semiconductor quantum well heterostructures proved a worthwhile platform for the development of optoelectronic devices for MIR applications. From the proof of concept of intersubband absorption or electroluminescence to today, huge progress has been made. Carried by a significant enthusiasm and research effort, the QCL is now a commercially available product working at room temperature. Regarding the detectors, if the QWIP design was thoroughly investigated over the years (particularly on GaAs substrate), the QCD is still being investigated as an improvable concept. The coupling of the ISB transition with free space propagating light is still a source of potential improvements, bringing new concepts from the photonic realm. State of the art detectors also work at room temperature.
Now that both the light sources and the photodetectors are mature enough for room temperature operations, the possibilities of applications for this technological platform broaden significantly. But in order to realize many complex functions, there is a need for a supplementary tool: the modulator. Coherent detection, AM spectroscopy and sensing, laser phase-locking [63] and most evidently optical communications would benefit from high speed, room temperature modulators. The realization of such devices was one of the objectives of my PhD.

Chapter 2

High frequency quantum devices for free space communication

In this chapter, we explore the possibility to establishing a free space optical link based entirely on unipolar quantum optoelectronic devices. We begin by establishing the basics of data transmission and identify the requirements necessary to realize such a system. Taking advantage of already commercially available QCLs, we focus on developing external modulators and detectors. We introduce the Stark effect for asymmetric coupled quantum wells and demonstrate how it can be exploited to realize electro-optic modulators for mid-infrared signals. A first sample, grown by our collaborators at C2N after a careful optimization of the MOVPE parameters, was fabricated. In the second part of the chapter, we discuss the optical properties of the sample and describe the fabrication of devices capable of high frequency operation, a necessary requirement to realize high bitrate data transmission. Finally, results obtained at 9 µm using the Stark effect modulator and a GaAs/AlGaAs QCD, both operating at room temperature, are presented.

2.1 Introduction: data transmission basics

The goal of wireless data transmission is to send a signal encoding bits to a receiver through the air. The most direct way is to use an electronically generated radiofrequency (RF) wave with the information encoded on its amplitude and/or phase. For radio frequencies (below $\simeq$ 1 GHz), the signal can be generated with a metallic antenna and an AC frequency generator and received on a second antenna before demodulation to recover the information. RF technology was historically developed for technologies now everywhere (radio, television, phones, GPS...), but the development of RF wireless transceivers of higher bandwidth (and low energy consumption, and small footprint) becomes challenging as they reach their upper physical limit: the frequency of the carrier. At higher frequency, in the tens of GHz, the millimeter waves suffer mainly from the higher absorption of the atmosphere.

In this context, the next frequency bands of the electromagnetic spectrum for potential carriers are the terahertz and mid-infrared. Regarding the terahertz, the lack of powerful sources and detectors, as well as the fact that it is heavily absorbed in our atmosphere, make

this frequency region unattractive for this kind of application, though short range high capacity links have been demonstrated in the low frequency part (f ∈[100 GHz;1 THz]) [64]. On the other hand, the atmosphere is particularly transparent over some regions of the infrared spectrum known as atmospheric transparency windows. They encompass the wavelengths from 8 to 12 µm (LWIR) and from 3 to 5 µm (MWIR). The existence of relatively powerful lasers for these wavelengths makes them very suitable candidates for the development of free space optical communication platforms. In this work, we will exclusively exploit the second window, specifically at 9 and 10 µm.

The carrier used for MIR optical transmission is generated by a Quantum Cascade Laser emitting around 10 µm (= 30 THz). Either via direct or external modulation, the binary zeros or ones constituting the message to be transmitted must be imprinted on this carrier. Various classical modulation schemes have been imagined for radiofrequency and are applicable to optical telecommunications. They rely on amplitude (AM) or phase modulation (PM). Fig.2.1 illustrates these modulation schemes in the simple case of a sinusoidal signal (purple, first line) sent on top of a carrier (blue) either using amplitude modulation (green, second line) or phase modulation (yellow, third line). The modulated signal writes

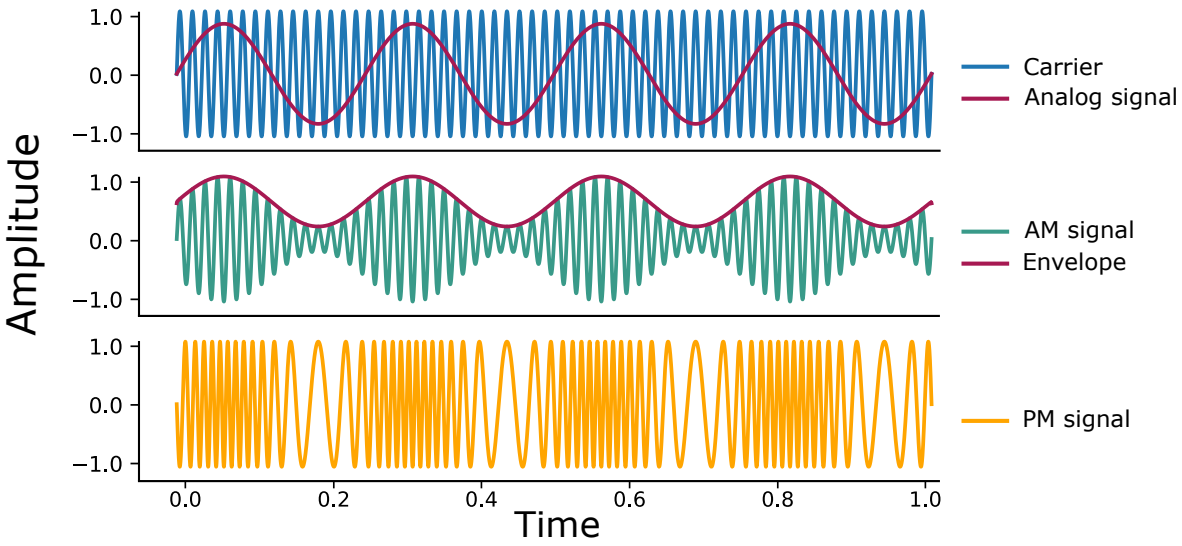

Fig. 2.1 *Examples of modulations to encode an analog signal on a carrier, either by amplitude modulation (AM, second row) or phase modulation (PM, third row).*

$I(t) = A_m.\sin(\omega_c t + \Phi)$ with ω_c the carrier frequency. In the case of amplitude modulation, the amplitude A_m is replaced by a function of time, proportional to the message signal. A MIR detector such as a QCD only sees the average value of the carrier, i.e. $A_m(t)$. In the case of phase modulation, Φ is the time-dependent function encoding the signal. Demodulation is possible by mixing the received signal with an oscillator at the frequency of the carrier.

Fig.2.2 shows the three devices we wish to implement in a MIR optical link: the QCL on the bottom right emits the MIR carrier at 33 THz; the light passes through a modulator which imprints an RF amplitude modulation on it thanks to external electrical bias; and

finally, the signal is detected on the QCD.

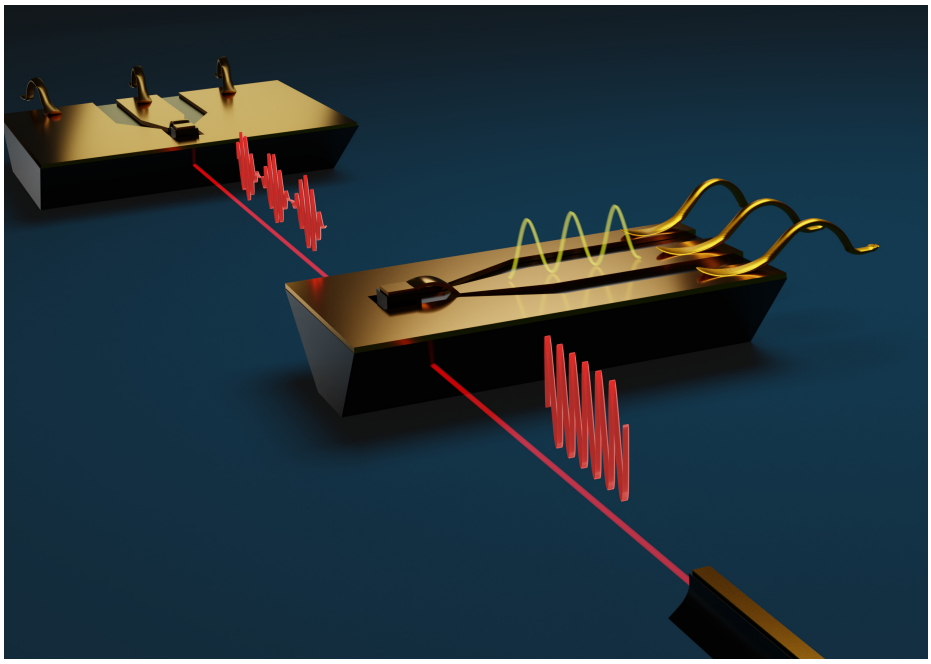

Fig. 2.2 *Schematic drawing of the free space optical data transmission setup. The DFB laser emits a 33 THz MIR radiation, the modulator writes databits on the laser amplitude and the QCD detects the modulated radiation.*

In this work we consider only amplitude modulation. In this scheme, the information is imprinted on the amplitude of the MIR carrier in the form of binary zeros and ones, in a sequence best represented by Pseudo Random Bit Sequences (PRBS), characterized by the number of symbols per unit time (unit: Baud=symbol/s). Different kind of sequences can be implemented. The simplest, called On/Off Keying (OOK), consists of a sequence of zeros and ones. One symbol contains one bit of information. More elaborate, the sequence named PAM-4 (standing for Pulse Amplitude Modulation 4-level) encodes the information on four amplitude levels. In this case, two bits are encoded with each symbol (4 levels = [00;01;10;11]), meaning that the bitrate is twice as large for the same baudrate, resulting in a higher system spectral efficiency. Nevertheless, the level spacing in PAM-N (with N>2) is reduced by a factor of N-1. This imposes the necessity for a higher signal-to-noise ratio (SNR).

In real systems, errors in the communication come from both noise and bandwidth limitations. For the latter, every component along the transmission line (generator, modulator, detector) can be modelled by a low-pass filter with a cutoff frequency $f_{c,i}$, where i denotes the component. Additionally, each element adds noise to the signal to be transmitted. Fig.2.3 summarizes the evolution (and deterioration) of the signal along a fictitious transmission line and how the signal is recovered. Starting from a PAM-4 sequence (the signal can be either 0, 0.33, 0.66 or 1) characterized by its symbol frequency f_s (a), the signal is rendered analogic by an Arbitrary Waveform Generator (AWG) characterized by a certain bandwidth (here $5f_s$) (b). The signal is transferred to the carrier via the modulator, which is characterized by its own cutoff (here $f_c = 2f_s$), and which adds its own noise (c). The envelope is captured

by the detector (d) and can be compared with the original signal. At each time $t = n/f_s$, $n \in \mathbb{N}^*$, the received signal is evaluated: it is correct, for instance, if the original value is 0.33 and the received value is in $[0.25, 0.5]$. The thresholds for evaluation are depicted in grey in (c). Here, the bandwidths of the modulator and detector are sufficiently large such that when comparing the received and the original signals, we find zero error (each comparison is marked by a dot, green means correct, red incorrect). In (e),an example of the same transmission is shown but for a modulator with a cutoff frequency of $f_c = 0.5f_s$. The comparison with the initial signal (green and red dots) shows that 30% of the symbols are actually transmitted wrong, which is obviously not satisfactory. Examining the errors more closely, we can see that some errors are caused entirely by insufficient bandwidth: going from 0 to 1 in $1/f_s$ is impossible due to the behavior of the low-pass filter. Some other errors are caused by the noise (here modeled as white gaussian noise with variance of 0.1): the average signal is in the correct quadrant for this symbol but the noise added at the instant of the sampling leads to an error.

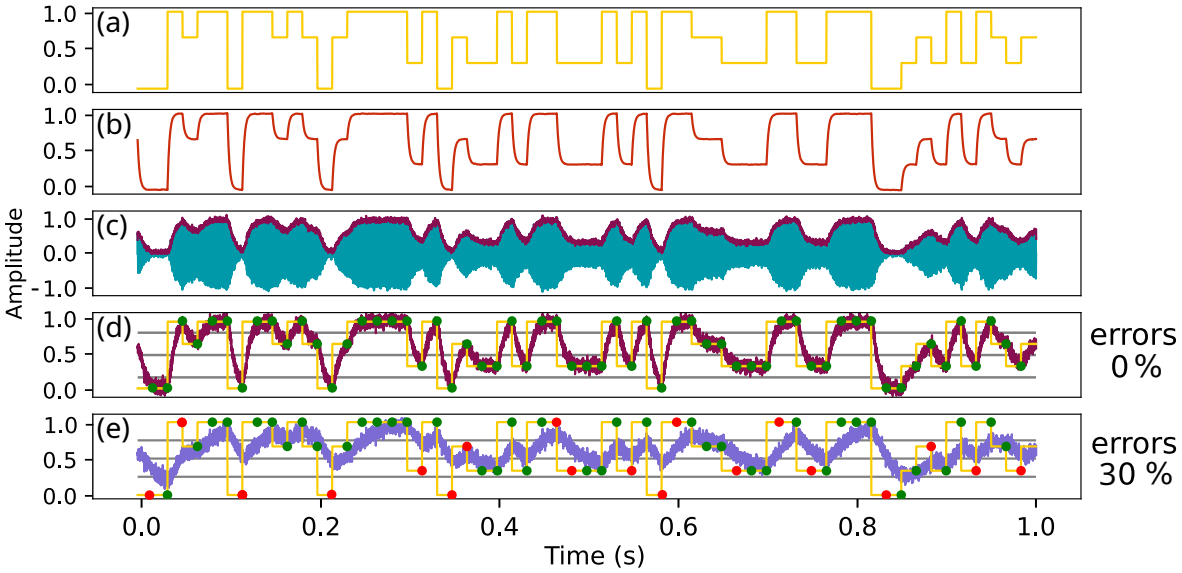

Fig. 2.3 *Typical evolution of the signal along the transmission line. (a) PAM-4 PRBS logical signal a user wants to send, characterized by its frequency f_s. (b) Analog signal sent to the modulator by the Signal Generator, with a bandwidth of $5f_s$. (c) In blue, amplitude of the carrier modulated. In purple its envelope. The modulator has a bandwidth of $2f_s$ and adds a white Gaussian noise. (d) The previous envelope is compared to the original signal. In grey are the thresholds to discriminate between the levels. Errors are evaluated for every symbol just before the next symbol to minimize the error count. Green dots mark a correct evaluation. No errors are found. (e) Retrieved signal with a modulator with a bandwidth of $0.5f_s$. Red dots mark an incorrect evaluation. 30% of the symbols are wrong.*

A commonly used representation of data transmission quality is the eye-diagram. The received signal is replotted by superposing time traces a few periods long, allowing one to see all the successions of possible bits at once. An example is shown in Fig.2.4, which results from the superposition of hundreds of thousands of traces. The name of this type of plot

comes from its shape. A good, error-free transmission is characterized by an "open" eye. When the Signal-to-Noise Ratio diminishes, the eye closes and the Bit Error-Rate (BER) eventually increases.

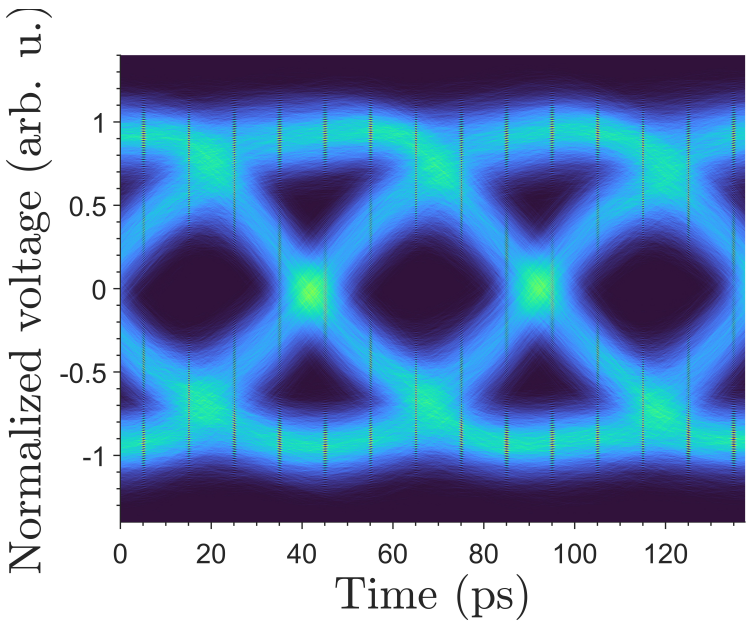

Fig. 2.4 *Example of an eye diagram of an error-free transmission. The colors' saturation represents the superposition of multiple traces (Courtesy of Pierre Didier, Telecom Paris).*

Numerically, the BER for OOK modulation can be expressed as a function of the characteristics of the devices involved in the link [65]:

$$BER = \frac{1}{2}\left[erfc\left(\frac{1}{\sqrt{2}}\frac{I_1 - I_0}{\sigma_1 + \sigma_0}\right)\right] \tag{2.1}$$

where $I_{0,1}$ are the photocurrents of the bits (0, 1), and $\sigma_{0,1}$ are their respective noise. These simple considerations inform the design of the elements of the optical link and the electronics: the detector and the modulator should have the largest possible electronic bandwidth. The modulation depth of the modulator, i.e. the ratio of the modulation excursions of the RF signal to the level of the unmodulated carrier, should be as close to one as possible in order to separate the levels efficiently. The responsivity of the detector should also be maximized. Simultaneously, noise sources in the system need to be minimized. This noise primarily takes the form of Johnson noise for QCDs and dark current noise for QWIPs operating at room temperature).

2.2 Stark modulator based on quantum wells

As mentioned in the first section, the main missing piece to build an optical link for data transmission is an optoelectronic modulator, a device capable of changing the amplitude of the laser light as a function of an applied electric field. Various strategies to realize an external modulator relying on bias-dependent ISB absorption have been reported in the literature. In

several works, optical modulation was achieved by modifying the absorption amplitude of a transition through external field induced charge depletion. In one work, a resonant tunneling effect was engineered between the ground level of an active well and a neighboring well [66, 67] as a means to deplete the active well and thus limit its absorption in a reversible manner. Pirotta et al. [68]used a more indirect approach, in which they deplete highly doped wells by applying a strong gate electric field thanks to Schottky contacts. Instead of relying only on the change of absorbance due to a modulation of electron density in the well, the goal was to embed the active region in a cavity to be able to switch from strong to weak light-matter coupling regime. At resonance, the absorption is shifted by the Rabi energy $\hbar\Omega_r$ with respect to the bare ISB energy, and if the linewidths involved are small enough, it becomes possible to modulate the light.
In my work, amplitude modulation is achieved through Quantum confined Stark effect within the conduction band.

2.2.1 Quantum confined Stark effect

We describe the electric field dependency of the resonance in quantum wells as a Stark effect in analogy to the effect discovered in 1913 by Johannes Stark [69] concerning the shifting and splitting of spectral lines of atoms and molecules under external electric field.

In a single quantum well, the influence of the electric field on electronic transitions between confined states in the conduction band is unfortunately very weak. Let us consider an infinite quantum well described by a Hamiltonian H_0 with eigenstates $|\phi_i^0\rangle$, $H_0|\phi_i^0\rangle = E_i^0|\phi_i^0\rangle$. Upon introducing an external electric field and may write the new system Hamiltonian as $H = H_0+V = H_0+eFz$ where F is the electric field applied along the growth direction z. We search for new solutions $H|\phi_i\rangle$ for which it holds that $H|\phi_i\rangle = E_i|\phi_i\rangle$. Second order perturbation theory gives us the new perturbed E_i as a function of the unperturbed eigenstates and energies:

$$E_i(V) = E_i^0 + \langle\phi_i^0|V|\phi_i^0\rangle + \sum_{j\neq i} \frac{\left|\left\langle\phi_j^0|V|\phi_i^0\right\rangle\right|^2}{E_i^{(0)} - E_j^{(0)}} \tag{2.2}$$

The first order correction, $\langle\phi_i^0|eFz|\phi_i^0\rangle$ is null because of symmetry since the $|\phi_i^0\rangle$ are sine or cosine functions of z. For the second order, however, the terms for i and j of different parities do not vanish, resulting in a change in the energies. We can write, neglecting the influence of non-neighboring levels:

$$\begin{aligned}
E_1(V) &\simeq E_1^0 + \frac{\left|\langle\phi_2^0|eFz|\phi_1^0\rangle\right|^2}{E_1^0 - E_2^0} = E_1^0 - \frac{512}{243}\cdot\frac{L^4e^2F^2m^*}{\pi^6\hbar^2} \\
E_2(V) &\simeq E_2^0 + \frac{\left|\langle\phi_1^0|eFz|\phi_2^0\rangle\right|^2}{E_2^0 - E_1^0} + \frac{\left|\langle\phi_3^0|eFz|\phi_2^0\rangle\right|^2}{E_2^0 - E_3^0} \\
&\simeq E_2^0 + \left(\frac{512}{243} - \frac{4608}{3125}\right)\cdot\frac{L^4e^2F^2m^*}{\pi^6\hbar^2} \simeq E_2^0 + 0.63\cdot\frac{L^4e^2F^2m^*}{\pi^6\hbar^2}
\end{aligned} \tag{2.3}$$

Looking at the energy of the 1-2 transition, one finds that

$$E_{12}(V) = E_2(V) - E_1(V) \simeq E_2^0 - E_1^0 + 2.74 \cdot \frac{L^4 e^2 m^*}{\pi^6 \hbar^2} \cdot F^2 \tag{2.4}$$

E_{12} only depends on the electric field as a second order correction because of the symmetry. Fig.2.5 this is numerically verified for finite quantum wells: the shift generated by the electric field is indeed quadratic and negligible. Over ±50 kV/cm, the transition energy changes by approximately only 1 meV. This simulation (and the ones following in the chapter), rely on the resolution of the Schrödinger equation for a given potential using the 3-band Kane model, taking into account the non-parabolicity. The plotted potentials are actually simulated within a box 30 nm larger than the region of interest.

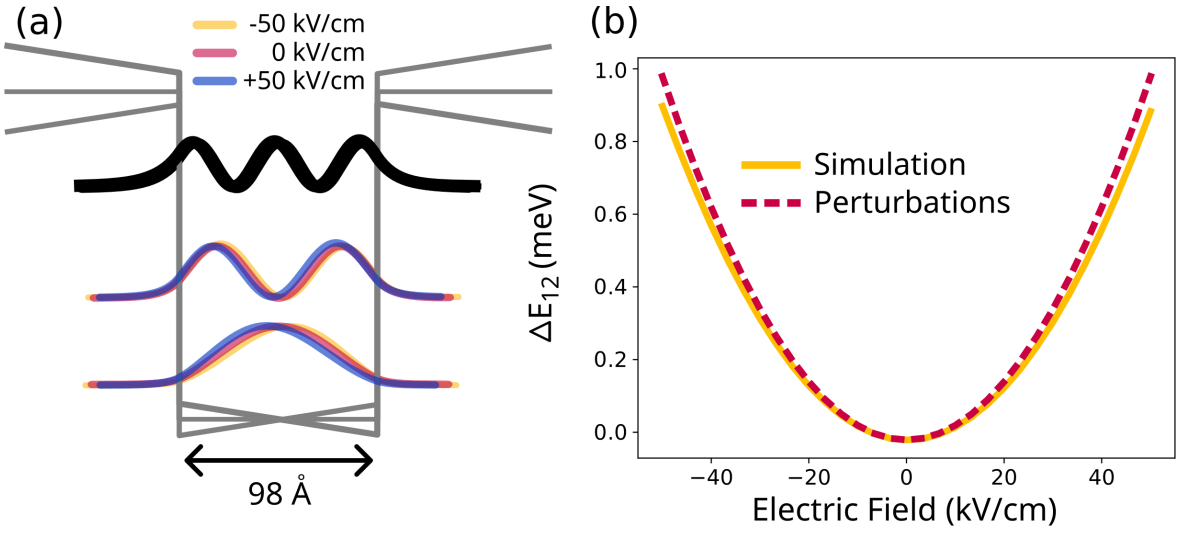

Fig. 2.5 *(a). Simulation of an InAlAs/InGaAs/InAlAs quantum well and square moduli of the wavefunctions plotted at the corresponding energies. (b) Energy difference between states 1 and 2 as a function of the electric field in the simulation and according to Eq. 2.4.*

The key for efficiently exploit of the Stark effect for electromodulation is to break the symmetry of the wavefunctions involved. Various strategies can be pursued to reach this goal, two of which are displayed in Fig.2.6. In every case, the goal is to spatially separate the centroids of the wavefunctions of levels 1 and 2 to create the asymmetry necessary to maximize the Stark shift.

- In 1986 the first Stark shift was observed in a single quantum well [70]. To observe this, the authors made a very wide quantum well, with the ground level sitting close to the bottom of the conduction band. Under an electrical field, the bending of the band creates a triangular potential for the first level whereas the other levels are weakly perturbed [71], leading to a change in E_{12} with the bias. The effect was not linear and small ($\simeq$ 1 meV shift) (Fig.2.6 (a)). Telecom technologies take advantage of this effect ("Quantum confined Stark Effect") [72, 73] in triangular wells for instance with III/V or Ge/SiGe quantum wells to realize modulators using interband transitions (at higher energies, around 1 eV $\simeq$ 1.3 µm). Indeed the holes states in the valence band

undergo the same modification as the electrons but in the opposite direction energy-wise, emphasizing the influence of the electric field since the effect on the levels involved in the interband transition add up instead of canceling out.

- Taking advantage of the progress in epitaxy in the early nineties, several authors fabricated step quantum wells by having more than two different materials (here GaAs and AlGaAs with different aluminum content) [74, 75] (Fig.2.6 (b)). The asymmetry between the first two levels here is present natively and the modulation can occur around zero bias. Much stronger Stark effect (8 meV for 18 kV/cm) is reported in this configuration with respect to the square well case [76]. This is enough with respect to the broadening of the absorption line to realize the first Stark modulator, designed for CO_2 laser.

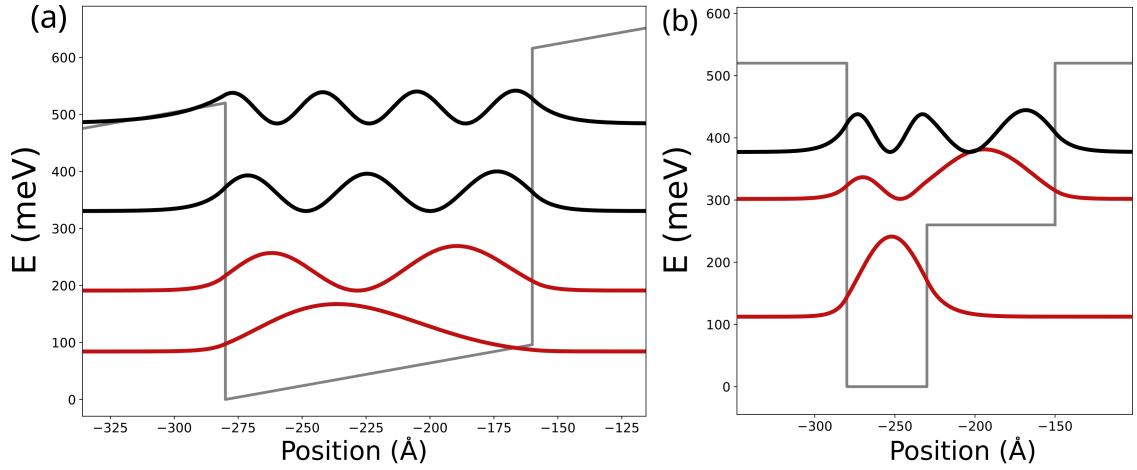

Fig. 2.6 *Potential and simulated square moduli of the wavefunctions for the different structures showing Stark shifts in the literature: biased large well (a) and step well (b). In both cases, the probability distributions of two first levels display different centroids.*

A third option, that we decided to implement, is to use two asymmetric coupled wells, also investigated in the literature. In [77], this active region was embedded in a region coupled to a QCL waveguide to tune the cavity losses and therefore electrically modulate the laser's emission. In [78] and [79], the authors describe a similar heterostructure, this time coupled with resonators to create metasurfaces with an electrically controlled absorption.

2.2.2 Principle of operation of the Stark modulator

Our Stark modulator relies on two asymmetric coupled wells, as shown in Fig.2.7. The InGaAs wells are 5.6 and 2.6 nm wide and separated by a 1.4 nm InAlAs barrier. The conduction band offset is 520 meV. Fig.2.7 shows the square moduli of the wavefunctions plotted at the corresponding energies, numbered 1, 2, 3 from low to high energy. All our focus will be on the two lower levels, spaced by 137 meV $\simeq$ 9 µm which is the targeted energy. The barrier separating the two wells is thin enough for the wells to be coupled, meaning the wavefunctions are delocalized across both of them. Moreover, the difference in size between the two wells

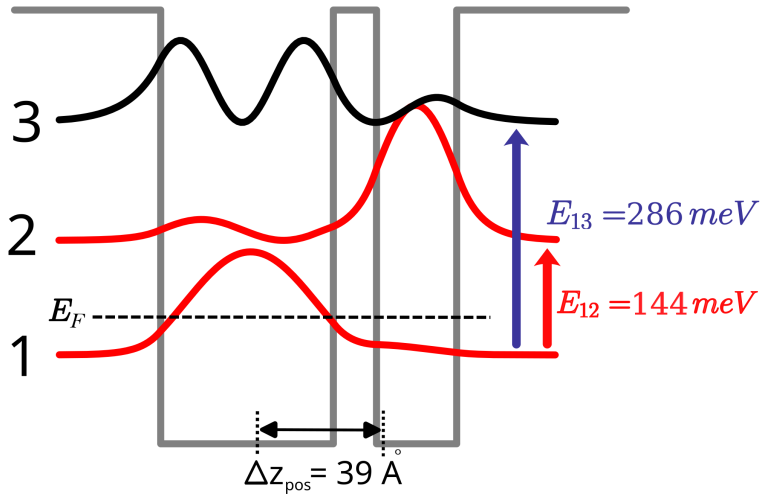

Fig. 2.7 *Potential and simulated square moduli of the wavefunctions for the Stark modulator. The levels of interest are in red separated by approximately 9 μm. the Fermi energy is indicated in dashed line, just above the ground level. The dashed lines at the bottom of the wells indicates the position of the centroid of the wavefunctions 1 and 2, separated by Δz_{pos}.*

gives rise to asymmetric wavefunctions. The average positions of the electrons in the first two states are close to the centers of the two wells. This difference makes the absorption energy E_{12} sensitive to an external electric field. Coincidentally, it breaks the parity selection rule found in Chapter 1 for the infinite quantum well: the 1-3 transition is not forbidden anymore since they do not have the same symmetry. This means that the oscillator strength for the 1-2 transition will be smaller. Fig.2.8 (a) shows the evolution of the wavefunctions with ±60 kV/cm electric field applied on the structure. It clearly appears that the 1-2 transition energy is strongly modified as a function of the bias applied, whereas the 1-3 transition is not since the two wavefunctions involved have approximately the same barycenter. The simulated values of E_{12} and E_{13} for this structure, as well as the oscillator strength of the transition, are plotted in Fig.2.8 (b). The linearity of the 1-2 transition energy variation with the bias, even for very strong electric fields, is remarkable (a linear fit over 200 kV/cm and 75 meV yields a coefficient of determination $R^2 = 0.9997$). The slope, i.e. the sensitivity of E_{12} to an external field, will be called the Stark shift S. The fit gives us here $S = 0.38$ meV/(kV/cm). The oscillator strength plotted in blue with the right Y-axis, though almost quadratic close to 0 V, changes of only 8 % over the investigated range.

The small variation in f_{12} and the linear variation of the energy means that at least as a first approximation we can consider that the wavefunctions are just shifted in energy under an external electric field F and the variation in E_{12} is simply proportional to the distance between the centers of mass of the two first wavefunctions at zero bias Δz_{pos}:

$$\Delta E_{12} \equiv S.F = \Delta z_{pos}.e.F \Rightarrow S = \Delta z_{pos}.e \simeq 0.39\,\text{meV/(kV/cm)} \tag{2.5}$$

This value is indeed very close to the simulated one. Under very high bias, above 100 kV/cm,

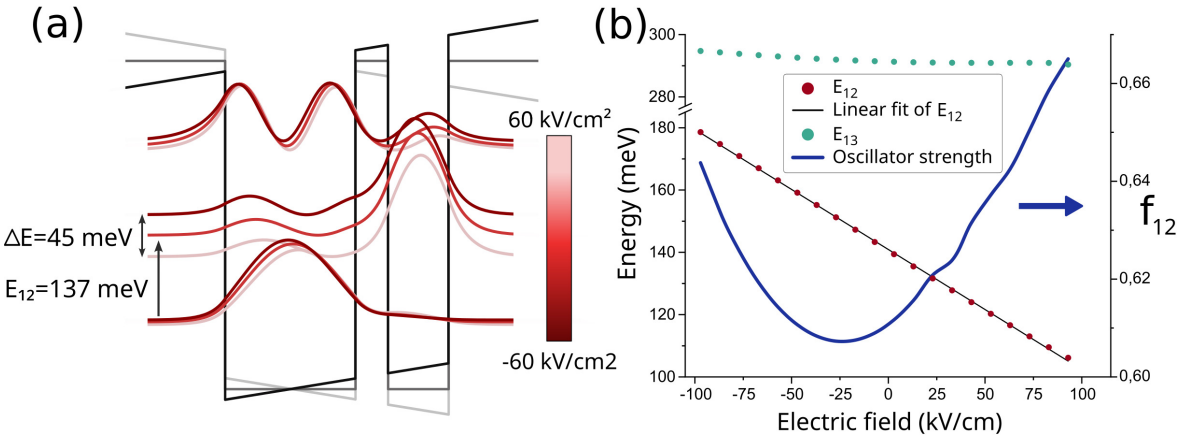

Fig. 2.8 *(a) Simulation of the potential and the bandstructure of our Stark modulator under -60 kV/cm, 0 kV/cm and 60 kV/cm. We see that the second level is by far the most impacted by the electric field, and level 1 and 3 are barely changed. (b) Evolution of the energies E_{12} and E_{13}, and the oscillator strength f_{12} associated to the 1-2 transition as a function of the bias applied on the structure. A strong linearity of the Stark shift over a range of 200 kV/cm and 75 meV is observed.*

levels 2 and 3 would be coupled and this approximation would not be valid anymore.

Thanks to the Stark effect, the ISB transition 1-2 can either be resonant with an incoming MIR radiation E_{12}, or completely detuned. The coupled quantum well system thus either absorbs or is transparent under laser illumination. This means that we must be able to shift the transition by an energy equivalent to half its linewidth. Diagonal transitions yield quite large, Gaussian peaks. For an absorption centered at 140 meV we can conservatively expect a FWHM of 30 meV (20%), so the $1/e^2$ intensity, closer to the base of the Gaussian would be 26 meV from the center, requiring a field of 68 kV/cm to be applied, which is within the range of linearity of the Stark effect determined earlier. The expected operation of the modulator is sketched in Fig.2.9.

2.3 MOVPE growth of the modulator

The first modulator structure used that I used in my PhD was grown using metal-organic vapor-phase epitaxy (MOVPE), by Konstantinos Pantzas, Grégoire Beaudoin, and Isabelle Sagnes of the Centre de Nanosciences et de Nanostructures (C2N – UMR 9001, CNRS Université Paris-Saclay). Metal-organic vapor-phase epitaxy is an epitaxial growth technique developed for semiconductors that, along with molecular-beam epitaxy (MBE), provides precise control of semiconductor alloys in layers as thin as the single atomic monolayer. Molecular-beam epitaxy still is the main technique employed for quantum cascade devices as it was thought to produce sharper interfaces, a higher degree of control over layer thickness and a lower residual doping – albeit mostly in GaAs/AlGaAs structures. Metal-organic chemical vapor deposition, however, offers several significant advantages in terms of fabrication of devices at the industrial scale – chiefly owing to lower downtimes for maintenance, the

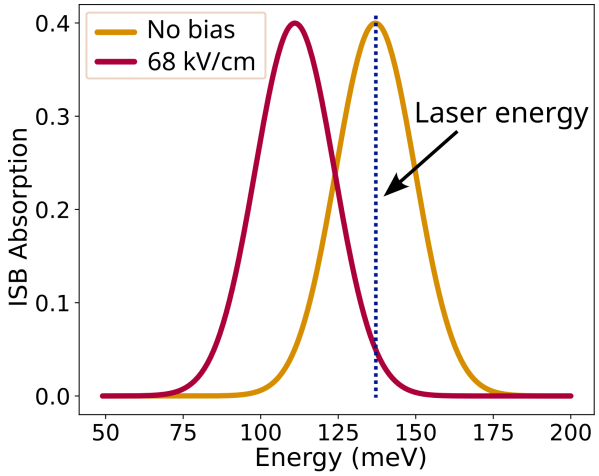

Fig. 2.9 *Expected behavior for the simulated Stark modulator. Under an external electric field of 68 kV/cm, the Gaussian absorption peak (purple), should shift by almost its full width and not absorb anymore at the unbiased (blue) peak absorption wavelength. This would allow an efficient optical modulation.*

fact that it does not require ultra-high vacuum, and the scalability of reactor chamber to simultaneously grow structures on up to 69x2" wafers (see Aixtron data for LED industry). Furthermore, it is the main technique used for the growth of (In,Al,Ga,As)-based materials on InP for datacom applications. There has, therefore, been a drive in the recent years to develop quantum cascade devices using MOVPE.

The main challenge when developing the MOVPE growth process of a quantum cascade device lies in gaining precise, layer by layer information on the composition and thickness of wells and barriers in the structure. Indeed, contrary to MBE, MOVPE does not operate under high vacuum, precluding one from using in situ monitor techniques that provide this information, such as RHEED. Furthermore, post-growth characterization techniques, such as X-ray diffraction, probe the structure as a whole and not on a per-layer basis. In 2016, our partners at C2N used transmission electron microscopy, specifically high-angle angular annular dark-field scanning transmission electron microscopy (HAADF-STEM), and an in-house algorithm [80], to obtain atomically-resolved chemical mappings of the elemental distributions in quantum cascade lasers. Using these mappings, they were able to identify that the aluminum content in InAlAs barriers was thickness dependent, i.e. that the thinner barriers ($\simeq$ 1 nm) are in fact InAlGaAs quaternary alloys. The reduced barrier height accounted for a shift in the target emission wavelength of the final device. The team at C2N was able to adjust the growth process to specifically counteract this effect by modulating the aluminum-precursor flow, thus correcting the shift in wavelength. Furthermore, the team showed that the compositions and layer thicknesses obtained from these mappings provided a more accurate model for band and transport simulations in the quantum-cascade laser [81]. These results provided the basis for the development of the Stark-effect modulator.

The procedure we used during my PhD was the following. I would design a modulator using numerical tools of the QUAD team and provide the MOVPE team with a target design. The team would then grow the design the structure, check it the structure using the method

(a)

#	Type	Targetted Thickness (nm)	TEM measure (nm)	In (%)	Al (%)	Ga (%)	Simu (%)
4	InAlAs	20	20	52	48	0	100
3	InGaAs	2.6	2.6	39.8	15.9	44.3	20
2	InAlAs	1.4	1.5	43.6	19.7	36.7	75
1	InGaAs	5.6	5.7	53	0	47	5

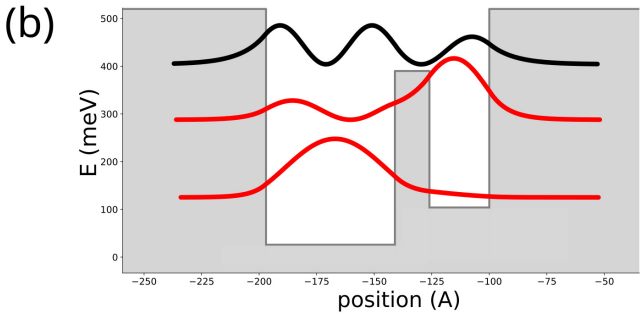

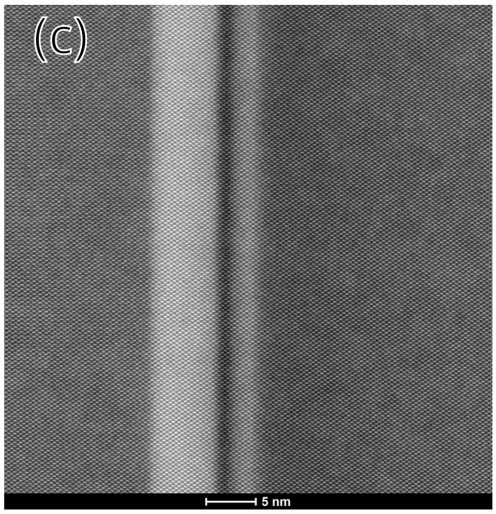

Fig. 2.10 *(a) Summary table of the thicknesses and alloy concentrations of the final modulator growth. (b) Corrected band structure of the sample V0351 after analysis of the spectrum and TEM measurement. (c) HAADF-STEM image of the final asymmetric quantum well structure grown by MOVPE, taken by Konstantinos Pantzas.*

described above and provide me with information on the actual crystal structure grown. I would process the device, test it and compare the experimental results against simulations that took into account the actual structure. We would then determine any adjustment necessary to the device and iterate the process until the target performance was met. Over a few iterations we were thus able to reach the finalized designed illustrated in Fig.2.10: in (a) is the summary of the measured values (both thickness and alloy composition), and in (b) the equivalent structure. A quick justification for the Conduction band offset linear interpolation for quaternary alloys is given in Appendix. Finally, a TEM image of one period of the modulator is shown in (c), where the two asymmetric wells are visible.

Further analysis: interface sharpness and modelling

The heuristic approach we took to converge on the target device, though reasonably fast, is still not optimal as it still requires several iterations of growth, TEM observation, device fabrication and testing. Establishing a model of the actually grown crystal, mined from the TEM data gathered over several iterations of design and growth would be much preferable, as we have shown that numerical simulations that take into account TEM data give the best fit to experimental data on the fabricated device. During my PhD, and within the framework of ANR project LIGNEDEMIR that funded it, our collaborators worked on establishing one such model. The model combines simple assumptions on the crystal alloys and the introduction of an interface grading to build a sample distribution of species for a given design. The main parameters for the model are the target composition for each layer. Among existing models for interface grading, the one that was chosen was that of a sigmoid

function, given in the equation below.

$$\theta_n(z) = 1 - \frac{1}{1 + e^{(z-z_n)/L_n}}. \tag{2.6}$$

Here, z_n is the position of the interface, and L_n the characteristic length of the transition between two layers of different compositions on either side of the interface.

An example of a simulated composition profile across an InGaAs/InAlAs interface is given in Fig.2.11.

Such shape for the interface was fit to experimental composition profiles data for a variety of

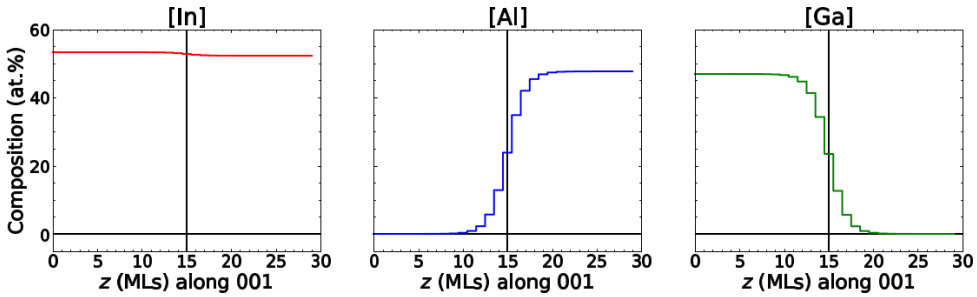

Fig. 2.11 *Simulated sigmoid composition profile across an InGaAs/InAlAs interface, courtesy of Konstantinos Pantzas.*

structures grown by MOVPE and observed in TEM to extract the best fit for the model's parameters. Interface grading, expressed as characteristic length L_n in the model, was found to be $\simeq$1.4MLs (monolayers), similar to values reported for both MBE and MOVPE by various other groups [82, 83, 84]. The fitted profile was used as a model of the crystal that is input in the METIS code of V. Trinité at III-V labs. This supplementary information were used to perform precise simulations, taking into account the sigmoid interfaces, strain, as well as the Poisson potential created by the doping in the large well (METIS software is best described in [42]). The graphical output of their simulation for this structure is shown in Fig.2.12 (a) and quantitative comparison between simulation and various thicknesses is made in [42].

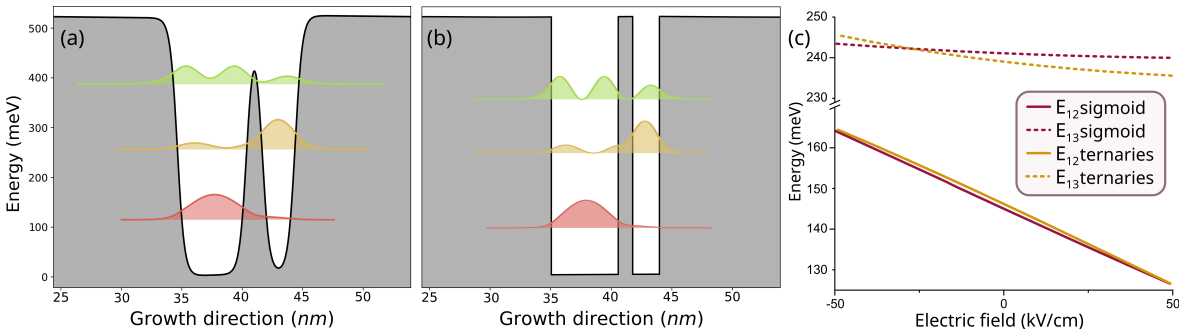

Fig. 2.12 *(a) Graphical output of the software METIS from III-V lab with quaternary interfaces. Courtesy of Thomas Poletti and Virginie Trinité. (b) Matching ternary simulation. (c) Comparison of the transition energies between the two simulations.*

We compared this simulated structure under bias and an equivalent ternary structure (the thicknesses of the wells and barriers are 6.8/**1.6**/2.4/**20** nm (InAlAs barriers are in bold)) giving the same transition energies. Under bias , in (c), we see that the influence of the shape of the barriers on the stark shift for the 1-2 transition is very small. For the 1-3 transition, we see that the quaternary interfaces will decrease the sensitivity to the electric field. Regardless of the qualities of such approach, and since we are only interested in the two first subbands, we chose except for the growth optimization phase to simulate our heterostructures in terms of ternary alloys, with effective length for the various wells and barriers determined by fitting the characterizations of the samples. In the following, well will mean ternary InGaAs and barrier ternary InAlAs.

2.4 Characterization of the modulators

2.4.1 Characterization of the MOVPE modulator

The MOVPE-grown device resulting from the optimization campaign is called V0351. The active region is a repetition of 30 periods of the asymmetric coupled QWs. The thicknesses of the wells and barriers are 6.8/**1.6**/2.4/**20** nm (InAlAs barriers are in bold). The first 6.8 nm well is Si-doped nominally to $1.5{\cdot}10^{18}$ cm^{-3}. The epitaxial growth was done on an InP:Fe insulating substrate. The nominal growth sheet is available in Appendix. This section will present the results of the V0351 growth, characterizing the optical and electrical properties of the device necessary to qualify its potential as an electrooptical modulator.

a) **Transmission spectrum**

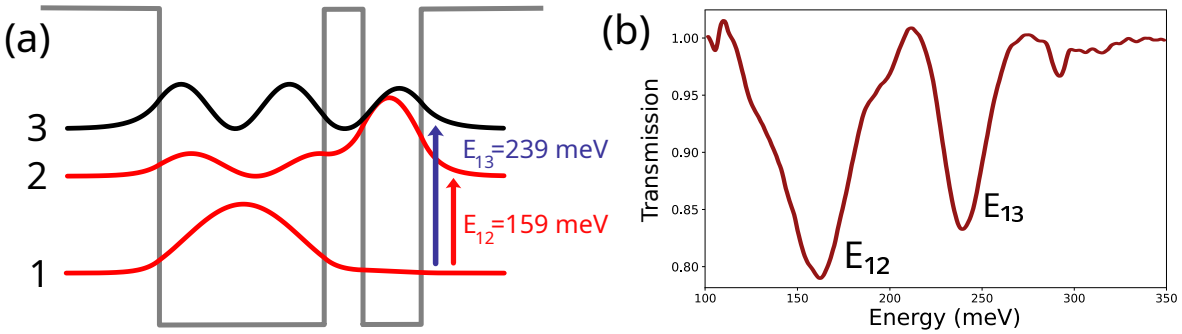

Fig. 2.13 *(a) Corrected bandstructure for modulator V0351. (b) Transmission spectrum of V0351 at 78K.*

The bandstructure adjusted to reproduce experimental data as well as the transmission spectrum of the sample is shown in Fig.2.13 (a and b). Two peaks are visible, one at 160 meV and the other at 239 meV. The FWHM of the first peak (E_{12}) measures 39 meV, which is very broad for this type of structure, compared to the 19 meV found for very similar structure in the literature [78].

Altogether, the broadening of the transition and the expected Stark shift for our 924 nm-thick active region mean that we will have to apply approximately 9 V on the structure

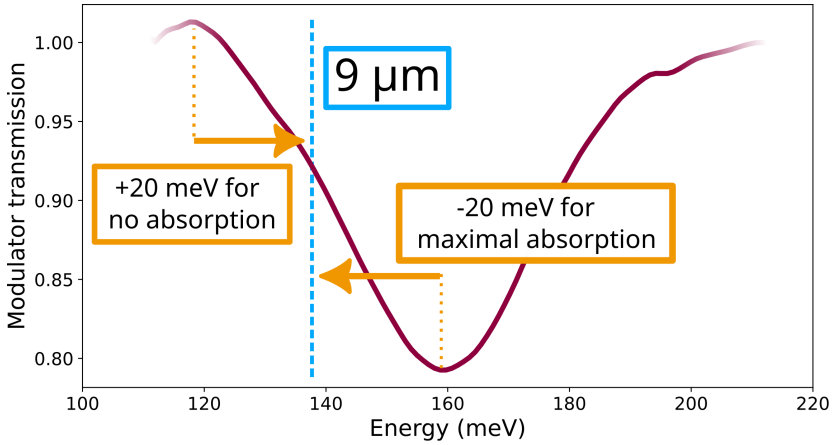

Fig. 2.14 *Zoom on the room temperature absorption spectra of the device around 9 µm. Shifting the absorption energy in one direction or the other will either increase or decrease the absorption of a 9 µm laser, in a close to symmetrical fashion.*

to go from maximal absorption to 10 % of that absorption. Fig.2.14 shows a zoom on the absorption peak of V0351 around the 1-2 transition. The fact that the absorption peaks at 159 meV is ideal: the targeted energy, 138 meV, lies close to the middle of the slope of the peak. Applying an AC bias will allow us to go from the absorbing state to the transmitting one without a DC offset.

b) Stark shift

We measured the Stark shift using a FTIR and an MCT detector. Between the interferometer and the detector, the light emitted by a blackbody (globar) is focused with parabolic mirrors and goes through the sample (see Fig. 2.15 (a)). In that regard, we processed a mutipass sample with a 0.75 mm-large ridge along the full length on the sample, with gold contacts on top of the ridge and on the side, on the bottom contact. Bias can be applied between the contacts with the help of gold wirebonds. (Fig.2.15 (b)). Making such large "mesa" assures us that we can couple most of the light from the large spot of the globar into the modulator, otherwise most of the light would not be absorbed and the contrast would be poor. The current flowing through such a large surface forces us to make the measurements in a cryostat at nitrogen temperature to be able to measure large biases.

Fig.2.15 (c) shows the transmission spectra of the device at 78K between 100 and 300 meV. To obtain such spectra and remove the baseline, we use a polarizer to measure both the TM and the TE spectra. Because of the polarization selection rule of ISB transitions, dividing the TM spectrum by the TE allows removing the contribution of the substrate and gases in the air. We repeat these measurements away from the ridge, only in the substrate to remove the contribution of the polarizer. Eventually, we plot the transmission spectrum T as:

$$T = \left(\frac{T(TM)}{T(TE)}\right)_{sample} / \left(\frac{T(TM)}{T(TE)}\right)_{substrate} \tag{2.7}$$

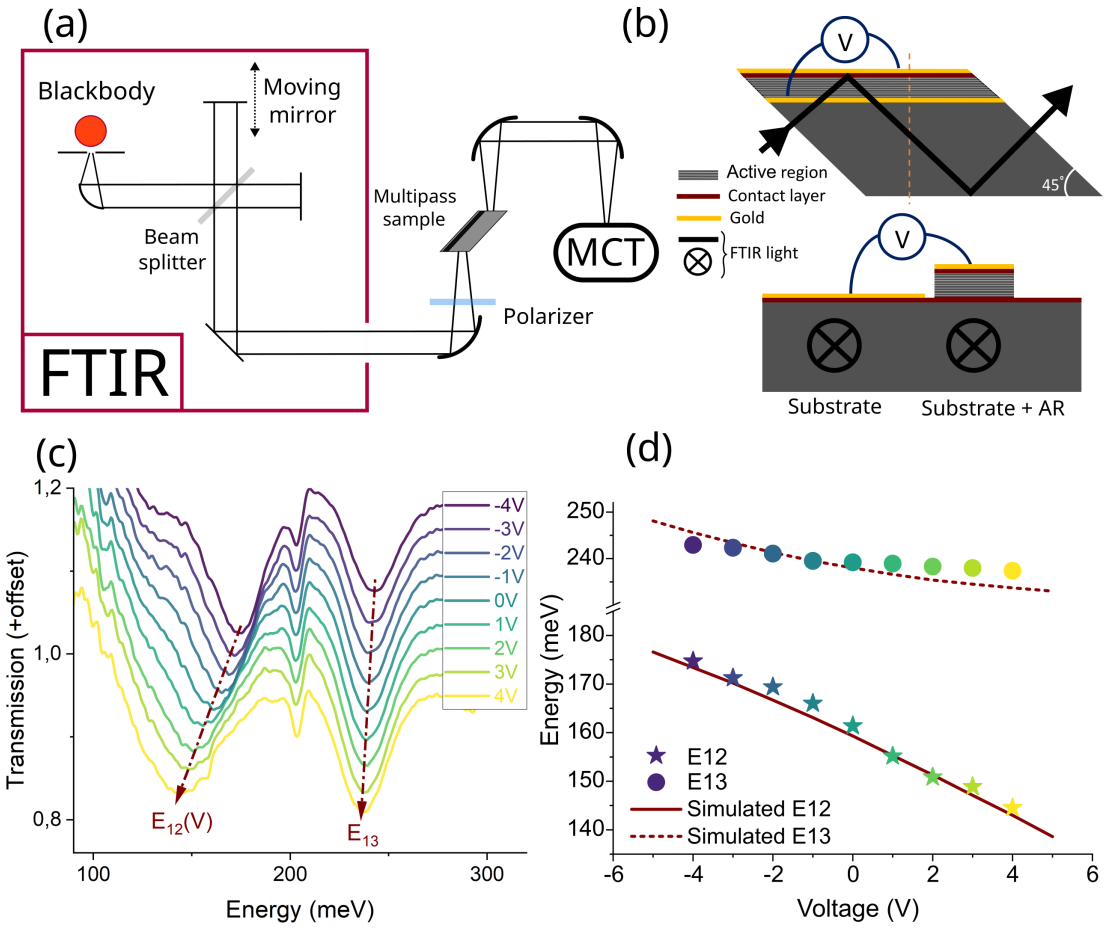

Fig. 2.15 *(a) Experimental setup for the measure of transmission spectra of an active region using a FTIR and an MCT detector. (b) Sketch of the modulator prepared for measurement of transmission spectra under bias. Two orthogonal cuts are shown to emphasize the 45° facets and the ridge. (c) Transmission spectra of the Stark modulator V0351 under various bias. E_{12} is changed with the bias whereas E_{13} stays practically constant. (d) Position of the absorption for E_{12} and E_{13} as a function of the bias (stars and dots) and corresponding simulation for the corrected structure (line).*

The peak associated to the energy E_{12} clearly shifts with the bias, while the second peak stays almost constant. The small peak around 200 meV is an artefact and only appears due to the normalization, likely caused by some gas absorption that changed between the measurement of the substrate and the active region transmissions. The absorption energy as a function of the bias extracted from this figure is reported for each transition in Fig.2.15 (d) with matching color code, along with the simulated values. The measured Stark shift from a linear fit of the experimental points for the 1-2 transition gives $S = 3.8$ meV/V $= 0.35$ meV.cm/kV given the thickness of the active region minus the contacts (we neglect the drop of bias in the doped contacts). This value is marginally smaller than that obtained from the nominal structure presented in Section 2.2, even though the wells are thicker. The discrepancy comes from the fact that the second level is less localized in the thin well here (visible in Fig.2.13 (a)), making the barycenters of the levels 1 and 2 closer. We recover indeed the correct behavior in the simulation.

A broadening of the transition is also observed. It was already reported in [4] for step potentials, though not explained. In this article the broadening seems to appear for any bias, whereas in our case positive bias seems to lead to thinner transition whereas negative bias tends to make the transition broader. The broadening is therefore larger when the two wavefunctions involved in the transition are more spread apart across the two wells. The transition linewidth might be more sensitive to the interface roughness in that case.

c) Modulation Depth

Another paramount quantity for data transmission is the modulation depth m, i.e. the normalized difference between the maximum and the minimum transmitted power P_{max} and P_{min}. Assuming a linear detector (with respect to the incoming power):

$$m = \frac{P_{max} - P_{min}}{P_{max}} = \frac{I_{max} - I_{min}}{I_{max}} \tag{2.8}$$

With I_{max} and I_{min} the maximum and minimum measured photocurrent.

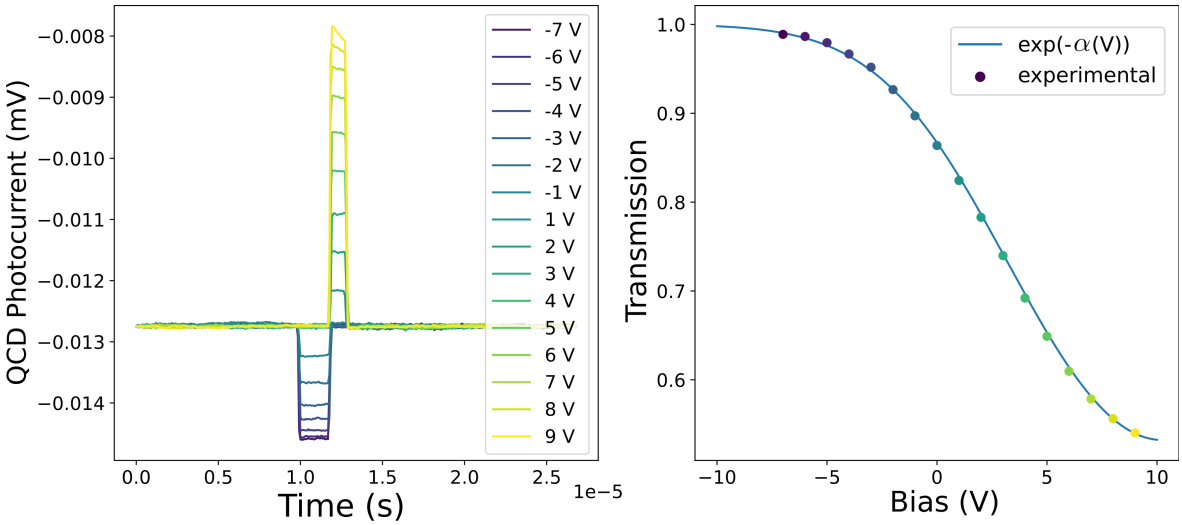

Fig. 2.16 *(a) Temporal traces of the photocurrent of a QCD after a modulator illuminated with a 9 µm laser. Short square pulses of different biases are applied on the modulator to evaluate its transmission as a function of the bias. (b) For each bias a colored dot represents the transmission of the modulator (colors match panel (a)). In blue is plotted the fit of the transmission using Beer-Lambert law with the modulator's Stark shifting Gaussian absorption.*

To measure this quantity, we shine a 9 µm laser on the modulator processed in 100 µm-diameter mesas, apply short square pulses on it of various amplitude and measure the photocurrent on a QCD. Average temporal traces are plotted in Fig.2.16 (a), with a color corresponding to the maximum bias applied. In (b) we assume that the large negative biases shift the transition energy enough so that the structure does not absorb any light, i.e. the transmission is equal to 1. After verifying that the dark current of the QCD is negligible, we calculate the transmission associated with each bias on the modulator. For the biases measured we reach a modulation depth of 47 %. We model this transmission using the Beer-

Lambert law, and assuming that the linear absorption coefficient α, is a Gaussian function moving linearly with the bias:

$$T = \exp(-\alpha(V)L) = \exp\left(-\alpha_0 \exp\left(\frac{(E_{laser} - E_{12}(V))^2}{2\Gamma^2}\right) L\right) \tag{2.9}$$

The shape of the experimental transmission as a function of the bias could be very well reproduced with $\alpha_0 \cdot L = 1.74$ taken here as a fit parameter and $\Gamma = 22$ meV, close to the FWHM of the spectra in Fig. 2.14. L is the light-matter interaction length and can be computed as $L = 2L_{qw}N_{qw}\frac{\sin^2(\theta)}{\cos(\theta)}$ knowing the number of quantum wells N_{qw} and their size L_{qw}. From the deduced value of α_0, we can verify the doping, which can typically vary from the nominal value, writing:

$$\alpha_0 = \frac{n_{3D}e^2\hbar f_{12}}{2\epsilon_0 c n_0 m^* \sqrt{2\pi}\Gamma} \tag{2.10}$$

From this equation, adapted from Chapter 1 with Gaussian linewidth, with $n_0 = 3.4$ the refractive index, $m^* = 0.041\ m_e$ the effective mass of the electron, c the speed of light and e the electron charge, we find a dopant density $n_{3D} = 2.1 \cdot 10^{18}$ cm^{-3}, close to the nominal value of $1.5 \cdot 10^{18}$ cm^{-3}.

2.4.2 Characterization of an MBE modulator using a tunable laser

I have also studied a second modulator, grown in an MBE reactor at III-V Lab by Axel Evirgen. This sample was grown in an attempt to have a thinner linewidth for the 1-2 transition. The nominal structure is the same as the previous sample, but only repeated 20 times: 5.6/**1.4**/2.6/**20** in nm (AlInAs barriers are in bold). The first 5.6 nm well is Si-doped nominally to 2·10^{18} cm^{-3}. [1]

We performed a second set of measurements using this new sample. The transmission spectrum for this structure, is showed in Fig.2.17 (a).

We then characterized this sample with a new method, taking advantage of a tunable laser (MIRcat-QT Mid-IR Laser, DRS Daylight Solutions) able to generate coherent light between 7.4 and 11.5 µm i.e. 107 and 167 meV, and an MCT detector, connected to an oscilloscope (Fig.2.18 (a)). Because of the reduced spot size and increased power (with respect to the globar) we could make small 150 µm-diameter mesas able to withstand ±10 V at room temperature without breaking. We processed them into thin transmission samples with two parallel 45° facets (Fig.2.18 (b)). The MCT detector (VIGO) has an optical bandwidth larger than the laser range of operation.

For each wavelength available with the laser (every 0.1 µm), we recorded with an oscilloscope the photocurrent as a function of the bias applied, and in particular the bias necessary to reach the maximal absorption. Fig.2.17 (b) shows the photocurrent recorded on the detector after the modulator for a laser line at 8.7 µm. With a bias of -2.2 V, the photocurrent

[1] This structure was grown on a conductive substrate which will make it unusable for the high speed processing presented in the next section. We nevertheless take advantage of it to characterize the second sample grown with a different method.

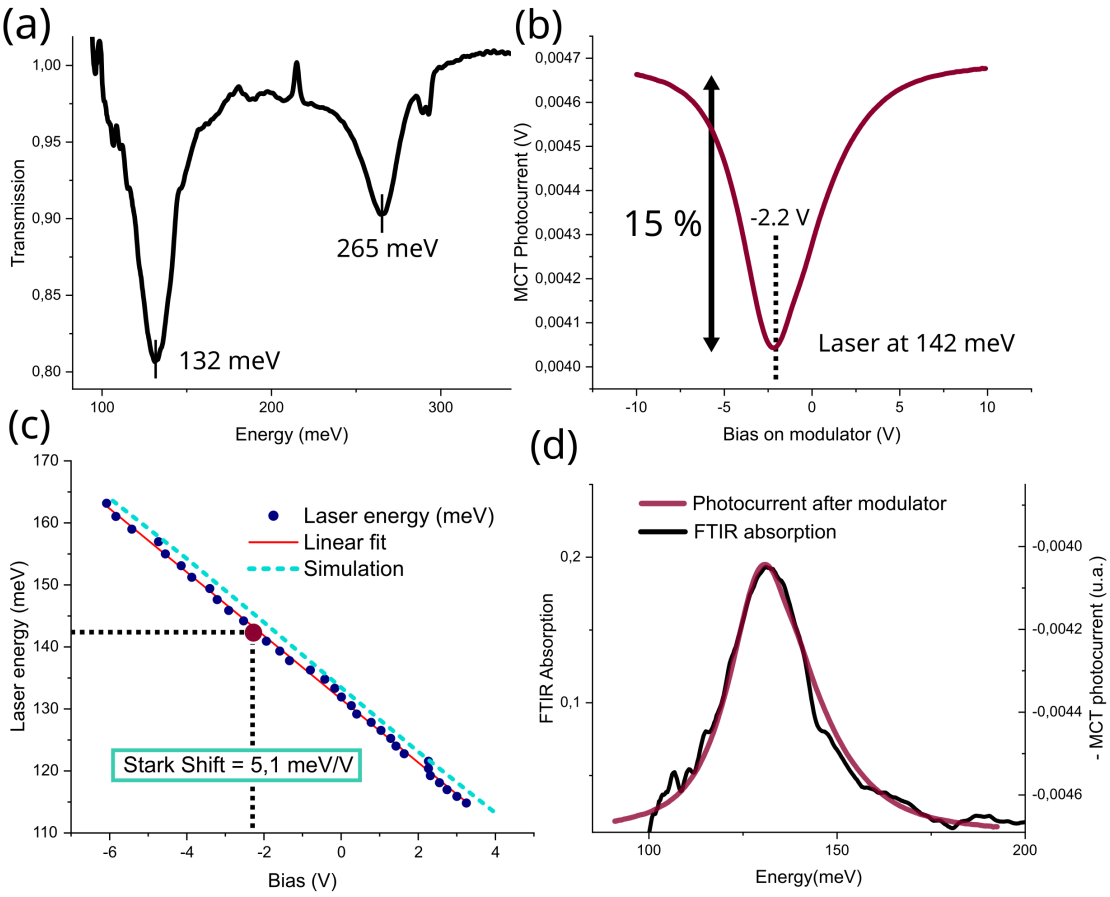

Fig. 2.17 *(a) FTIR Transmission spectrum of the modulator AC19 (multipass). (b) Photocurrent of an MCT detector after the modulator under illumination by a laser at 142 meV, as a function of the bias applied on the modulator. The bias to reach the minimal photocurrent at this wavelength is -2.2 V. (c) For each wavelength of the laser, we measured the bias necessary to reach the maximal absorption to deduce the Stark shift. The case of the laser at 142 meV of (b) is highlighted with dashed lines and a red dot. (d) We superposed on the same energy horizontal axis the absorption spectrum in black deduced from (a) and the transmission spectrum in red deduced from the photocurrent in (b) and rescaled thanks to the Stark shift measured in (c).*

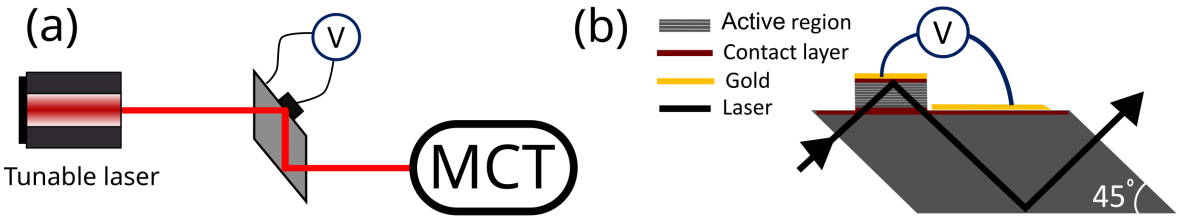

Fig. 2.18 *(a) Setup with the tunable laser allowing to use a mesa for spectral investigation. (b) Sketch of the thin transmission sample with an electrically connected mesa.*

is minimal, meaning that the ISB absorption of the modulator has been shifted to 8.7 µm. We are also able to deduce the modulation depth of this active region: we measure a depth of only 15 %, much lower than with the previous sample. Though the number of periods

has been decreased from 30 to 20, this means that the doping is approximately half of the expected value, i.e $\simeq 1 \cdot 10^{18}$ cm^{-3}. In Fig.2.17 (c), we reported the values of bias necessary to reach the minimum photocurrent for each wavelength, from which we could infer the Stark shift $S = 5.1$ meV/V$= 0.32$ meV.cm/kV and verify the linearity of the effect of the electric field over the range from 115 meV to 167 meV. The Stark shift is here slightly lower than for the first sample. In dark red is highlighted the data point extracted from (b).

In Fig.2.17 (d), knowing the Stark shift from (c), we can replot (b) as a function of the energy and superpose the absorption spectrum measured by FTIR spectroscopy. We observe that the shape is very well reproduced: the center energy, the broadening as well as the skewness are similar. This comparison confirms the value of the Stark shift and hints that we can infer the Stark shift from a measurement of photocurrent under bias at a single wavelength by fitting the transmission spectrum. Moreover, it confirms the small variation of the oscillator strength with the bias.

The information about the absorption energies from the transitions and the Stark shift allow us to deduce, as for the previous modulator, the equivalent ternary heterostructure that best fits all the data. We found that the ternary structure 56, **14**, 27, **20** nm works: the peaks at zero bias for the 1-2 transitions are 135 and the bias dependency of E_{12}, plotted in Fig.2.17 (c) in dashed light blue, corresponds to the experimental measurements. The values of the thickness for the equivalent ternary layers of this sample are very close to the nominal values.

In the end this second structure presents indeed a thinner linewidth for the transition of interest, but this advantage is heavily counterbalanced by a far lesser absorption as well. The Stark shifts for both structure are almost identical.

2.5 High frequency modulator

The advantage of the Stark modulator with respect to other modulators for data transmission is that there is no transport of the charges involved and therefore no upper speed limit to the device operation set by a drift velocity in the system. If we are only limited by the characteristic lifetime of the ISB photoexcited electrons, that would mean that these devices could work up to hundreds of GHz. But at frequencies above the GHz, the electronic environment of the active region becomes problematic: metal planes of contacts will create capacitances, wire inductances, and the characteristic size of the device so far will prohibit any high speed operation. The mesa used until now (circular, 100 µm radius) can be considered as a capacitor of surface $S_0 = 100^2\pi$ µm^2, thickness $e = 1$ µm and dielectric constant $\epsilon \simeq \epsilon_{InP}\epsilon_0 = 11.6\,\epsilon_0$. The associated capacitance is $C = \epsilon\frac{S}{e}$ and the resistance of the device is $R = 1k\Omega$. The high frequency cutoff associated is $f_{-3dB} = 1/(RC) = 310$ MHz. Furthermore, mesas are connected to the electrical circuit via long (multi-millimetric) wirebondings, which

act at high frequencies as antennas which will pick up the RF frequencies of the generator, and as inductances which will limit the bandpass frequency even further.

To circumvent this issue and reach higher frequencies, we processed smaller mesas, connected to coplanar waveguides through air-bridge connections (Fig.2.23) after [85]. There are several advantages. First, we can process mesa down to 10 µm since we do not require a minimal size to bond on them. Then, thanks to the air bridge, we limit the size of the bonding and the capacitance and antenna associated. Finally, the coplanar waveguide can be designed to adapt the impedance of the generator to the device.

2.5.1 Coplanar waveguide design

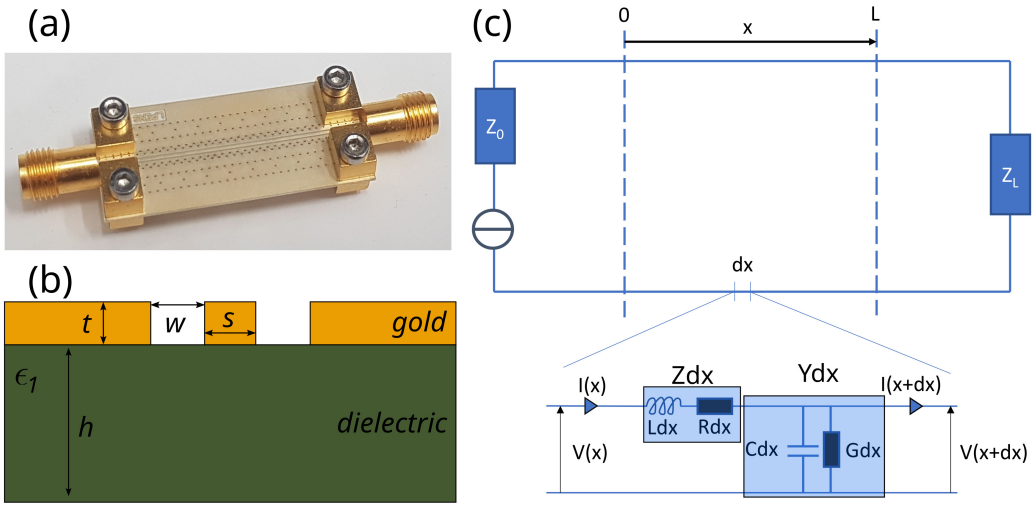

Fig. 2.19 *(a) Picture of Printed Circuit Board with gold deposited on a ceramic. (b) Sketch of a cut of a coplanar waveguide with all the relevant dimensions. (c) Equivalent electrical circuit to the experimental setup. The generator is represented by a perfect voltage generator with a $Z_0 = 50\Omega$ impedance, and the modulator is modelled by an impedance Z_L. The waveguide of length L is modelled as a succession of mesoscopic sections of length dx where the bias and the current are considered uniform.*

Used extensively in microelectronics, the coplanar waveguide (CPW) is a type of transmission line used for microwave signals. As shown in the photo in Fig. 2.19 (a) and sketched in Fig.2.19 (b), this guide is composed of a single conducting track of width t together with return conductors on both sides, spaced by w, deposited on a dielectric. Thicknesses are respectively t and h for the conductor (gold for us) and the dielectric. Fig.2.19 (b) shows the general electrical modelling of a waveguide connecting a generator of impedance Z_0 and a load (our modulator) Z_L. A transmission line is characterized in the most general case by a linear capacitance, inductance, resistance and conductance. In the sinusoidal regime, they can be gathered in a linear impedance Z and a linear admittance Y and we can write using

Kirchhoff's law:

$$\begin{aligned} V(x) = I(x)Zdx + V(x+dx) \Rightarrow \frac{\partial V}{\partial x}(x) = -ZI(x) \\ I(x) = V(x)Ydx + I(x+dx) \Rightarrow \frac{\partial I}{\partial x}(x) = -YI(x) \end{aligned} \tag{2.11}$$

Together, these equations yield:

$$\begin{aligned} \frac{\partial^2 V}{\partial x^2}(x) = ZYV(x) \equiv \gamma^2 V(x) \\ \frac{\partial^2 I}{\partial x^2}(x) = ZYI(x) \equiv \gamma^2 I(x) \end{aligned} \tag{2.12}$$

The complex amplitudes of the voltage and current then read:

$$\begin{aligned} V(x) = V_1 \exp(-\gamma x) + V_2 \exp(\gamma x) \\ I(x) = I_1 \exp(-\gamma x) + I_2 \exp(\gamma x) \end{aligned} \tag{2.13}$$

V_1, V_2, I_1 and I_1 are constants, related via Eq. 2.11. Indeed, we can show that $I_1 = V_1/Z_T$ with the characteristic impedance of the transmission line $Z_T = \sqrt{\frac{Z}{Y}}$, supposed constant. The impedance along the line is defined as:

$$Z(x) = \frac{V(x)}{I(x)} = Z_T \frac{V_1 e^{-\gamma x} + V_2 e^{\gamma x}}{V_1 e^{-\gamma x} - V_2 e^{\gamma x}} \tag{2.14}$$

The expressions in Eq.2.13 describe counter-propagating waves. We are interested in limiting the back-propagating wave, describing the reflection. We can write the reflection coefficient Γ as a function of x as:

$$\begin{aligned} \Gamma(x) = \frac{V_{backwards}}{V_{forward}} &= \frac{V_2}{V_1} \exp(2\gamma x) \\ &= \frac{Z(x) - Z_T}{Z(x) + Z_T} \end{aligned} \tag{2.15}$$

In particular, at an interface we need to adapt the impedance of our devices in order to reduce the reflection coefficient. Since the generator is always 50Ω, we will adapt our coplanar waveguide to 50Ω. The calculation of the geometric parameters leading to such impedance is done using formulas in [86]. The thickness and the permittivity of the dielectric layer are imposed by the substrate, and the track width is set by the mesa width on one end, and chosen to easily accommodate wirebondings on the other. The gap w is adapted to reach 50Ω. Fig.2.20 shows the design of the CPW that will be used for the following fabrication of devices.

The complete device including the connections to the CPW can therefore be modelled by a RC circuit, neglecting any inductance from the air-bridge, and we have at the end of the line in $x = L$, $Z_L = \frac{R}{1+j\omega RC}$. From there we can compute $\Gamma(L)$ and finally the transmitted power $P = 1 - |\Gamma|^2$. In Fig.2.21, knowing the approximate surface resistance of mesas, we estimate the available bandwidth using this model. As we can see in the inset, where the frequency cutoff is plotted as a function of $1/S_0$, the smallest mesas should reach several tens

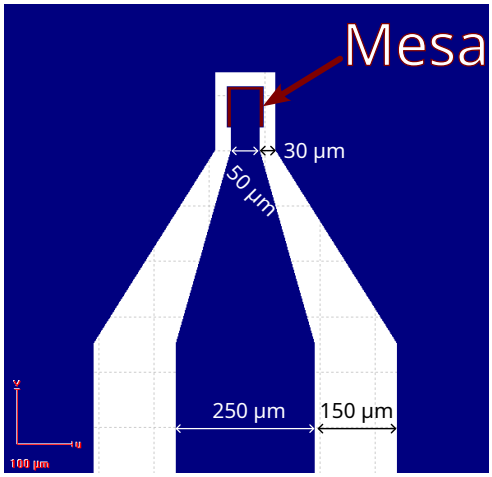

Fig. 2.20 *Lithography mask used for patterning the 50Ω CPW. On the bottom of the signal track, the width is sufficient to place a wirebonding. On the top, it is adapted to the mesa (here 55 µm).*

of GHz before the -3dB cutoff.

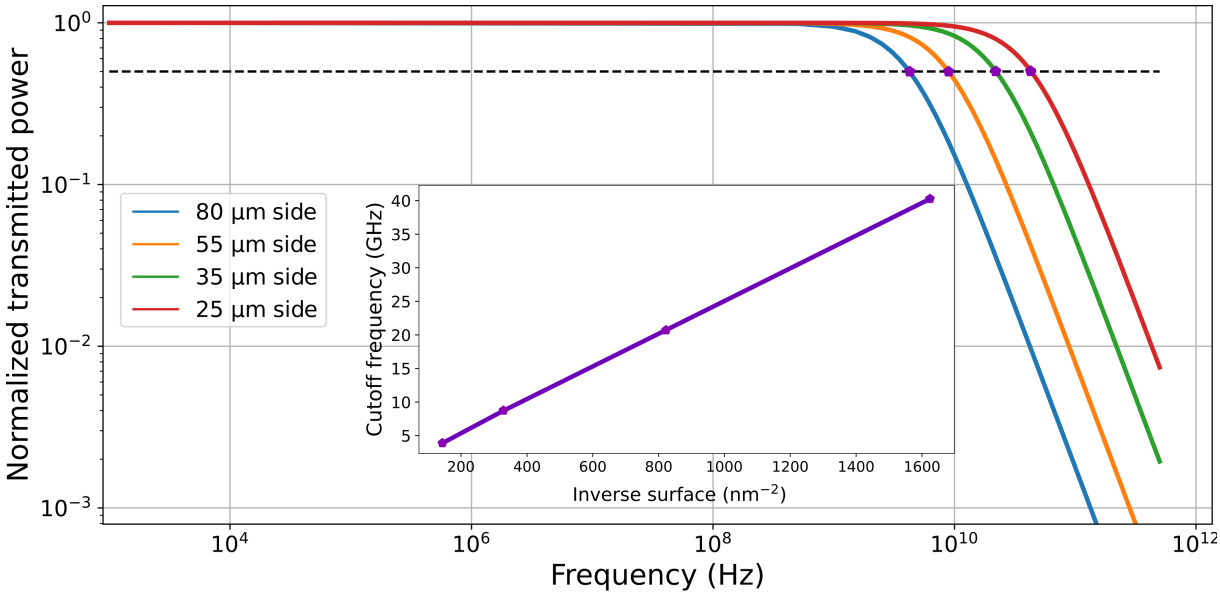

Fig. 2.21 *Simulated transmitted power from the generator to the modulator assuming a perfectly adapted coplanar waveguide for different mesa sizes. In the inset we reported the -3dB cutoff values for every mesa size, plotted as a function of the inverse surface.*

To make sure that the inductance was indeed negligible, we computed the expected value of L using the approximate formula for a rectangular conductor in [87], which gives values in the order of the pH. This would indeed have no influence in the plot of Fig.2.21 since at 10 GHz, $\omega L \simeq 0.1\Omega \ll R \simeq 5k\Omega$.

2.5.2 Clean-room fabrication

The different steps of the fabrication process are depicted in Fig.2.22.

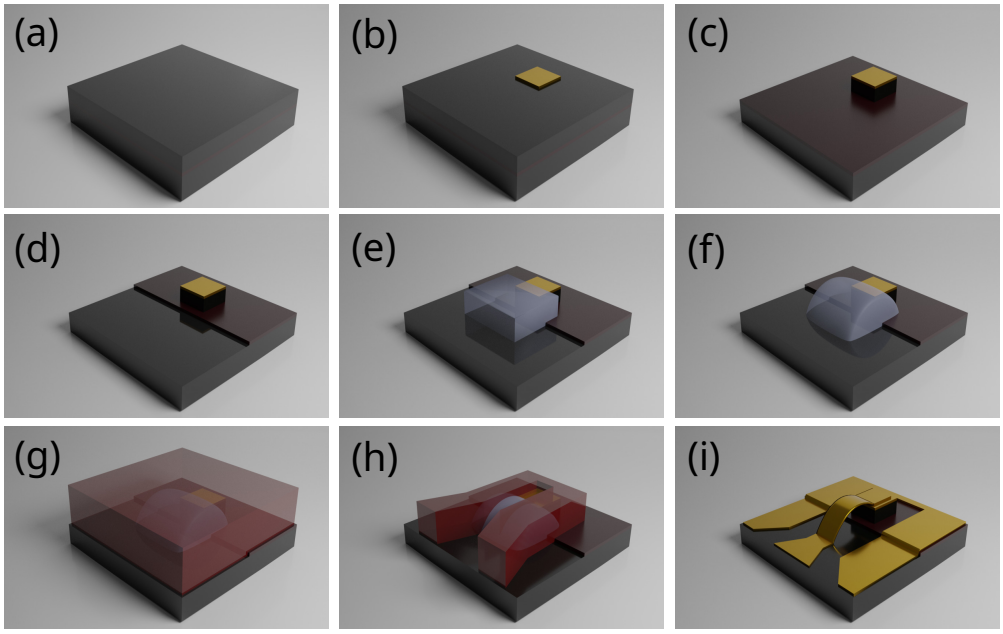

Fig. 2.22 *Fabrication steps of the high speed mesa with air-bridge connections.*

Starting from the epitaxial wafer (a), we define the mesas by depositing squares of gold of size 25, 35, 55 and 80 µm (b). The mesas are then chemically etched using a $H_3PO_4 : H_2O_2 : H_2O$, $1 : 1 : 38$ solution down to the middle of the bottom contact (etch rate approx. 120 nm/min), checking the depth regularly with a mechanical profilometer (Dektak, Bruker) (c). Once the second contact is revealed, we protect a large region at the edge of the mesa with resist, and proceed to selectively etch the remaining contact of the unprotected area with the previous acid solution (d). In MOVPE samples, a buffer between the substrate and the active region is present and must also be removed because it is not resistive enough to deposit the CPW on it. We use a 4:1 solution of $HCl : HCOOH$ to remove (not selectively) the buffer down to the InP:Fe insulating wafer. We now need to connect the top of the mesa to a waveguide, deposited on the insulating InP, through an air-bridge. We proceed in two steps. We deposit a first layer of positive resist, thicker than the active region plus the step in InP, and pattern large rectangles on the edge of the mesas, that will act as a support layer (e). To make their shape smoother, we reflow the positive resist at 150°C above the glass transition temperature for 3 min then cool it down to 110°C with steps of 3 min every 10°C (f). The contact line of the resist on the semiconductor does not move. The Ti/Au 50Ω coplanar waveguide is evaporated in one step using negative resist AZ5214 E for patterning (g). Lift off is done using a resist stripper SVC-14 at 80°C in order to remove both resists at once (i). A SEM image of the resulting device is shown in Fig.2.23. The bridge, as well as the step of the contact layer partially removed, are visible.

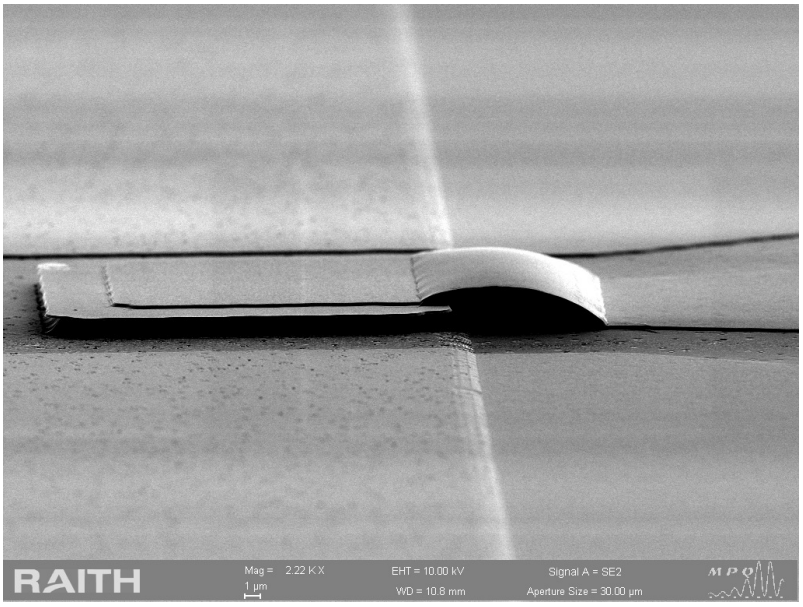

Fig. 2.23 *Tilted SEM image (x2220) of a 25 µm large mesa connected to the 50Ω coplanar waveguide.*

2.5.3 Electrical characterization

Once processed, the devices are electrically characterized using a RF-probe ("Ground-Signal-Ground") adapted to our geometry. The bandwidth is probed using a rectification method which relies on the non-linear I-V characteristic of our devices [88]. The idea is to measure the DC current generated by the application of a RF sinusoidal signal on the device. Indeed, in the small regime, we can write the following Taylor expansion:

$$I(V_0 + \delta V) = I(V_0) + \frac{\partial I}{\partial V}(V_0)\delta V + \frac{1}{2}\frac{\partial^2 I}{\partial V^2}(V_0)\delta V^2 + o(\delta V^2) \tag{2.16}$$

Now taking $\delta V = \delta V_m \sin(\omega t)$, and looking at the time average of the current:

$$\langle I \rangle = I(V_0) + \frac{1}{4}\frac{\partial^2 I}{\partial V^2}(V_0)\delta V_m^2 \tag{2.17}$$

The first term is just the DC current expected without small modulation, but the second, called the rectified current, is proportional to the squared amplitude of the voltage (i.e. proportional to the power) applied on the device. The rectified current (normalized by its low frequency value) depending on the modulation frequency of the bias, thus gives us the electrical response of our device.

The setup used for rectification measurements is shown in Fig.2.24 (a). We used a synthesizer (Anritsu MG3693B) going up to 30 GHz, and a sourcemeter (Keithley 2450) for measuring the DC current. The bias-Tee had a bandpass frequency going from 10 kHz to 45 GHz (SHF-BT45). The results are plotted in Fig.2.24 (b), along with the previous estimations accounting for the geometrical capacitances. We recover for each size the low-pass filter behavior expected from the simulations presented in Fig.2.21. In the inset, the -3db cutoff frequency is plotted as a function of the inverse mesa surface (experimental results are the

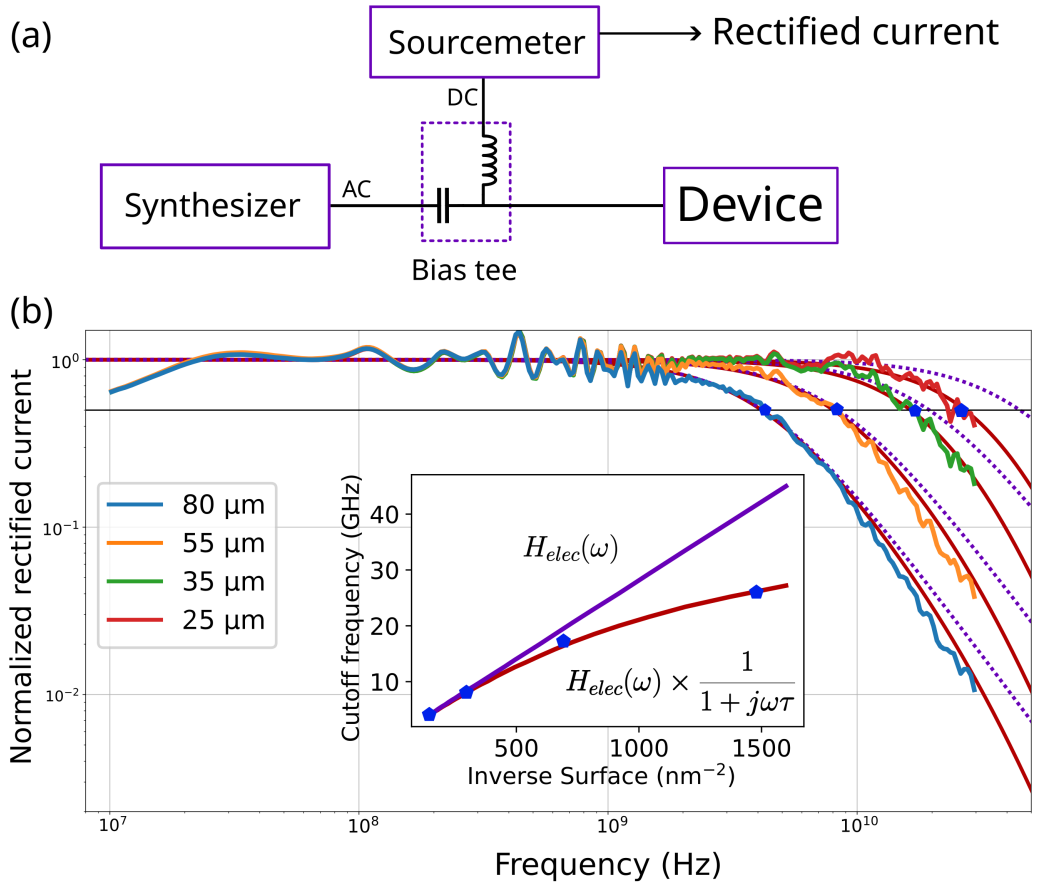

Fig. 2.24 *Normalized rectification measurements for each mesa side size taken with an RF probe. In dashed purple is the low pass behavior expected with the geometrical capacitance. In red, the transfer function product of the electrical lowpass and a second lowpass from the quantum structure, with $\tau = 4$ ps. In the inset, the -3dB cutoffs are plotted in blue versus the inverse surface of each mesa. The purple and red line show cutoffs of the fits with the two models.*

blue points and the previous electronic simulations are in purple). The measured values of the cutoffs are lower than simulated and nonlinear with respect to the inverse surface, especially at high frequency. The gap between the experimental values and the electronic predictions could indicate that a second timescale in the device is at play: if we expect some lowpass filter behavior caused by relaxation mechanisms in the heterostructure, we can construct a new transfer function reading $H(\omega) = H_{elec}(\omega) \times \frac{1}{1+j\omega\tau}$. The fit of our data with such filter yields $\tau = 4$ ps. The new transfer function is plotted in red in the Fig.2.24 and in the inset.

This time sets a lower limit for the maximal speed accessible with the Stark modulator ($\simeq 40$ GHz). Part of the discrepancy observed could also be due to a parasitic capacitance adding to the geometric one. In that case, the fitted τ would be smaller and the accessible bandwidth larger. A similar study was realized in [89] for vertical InGaAs/AlInAs QCD structure at 4.2 µm with similar geometry, and the authors concluded on a time of 1 ps (and a maximal frequency of 160 GHz) to fit their data. This time is more in line with the fastest ISB device

shown in the literature (a 9 µm GaAs/AlGaAs QWIP [48], that showed a flat response up to 70 GHz), though in those cases vertical intrasubband transitions are employed for the device operation.

2.6 Data transmission with the Stark modulator

2.6.1 Packaging of the modulator

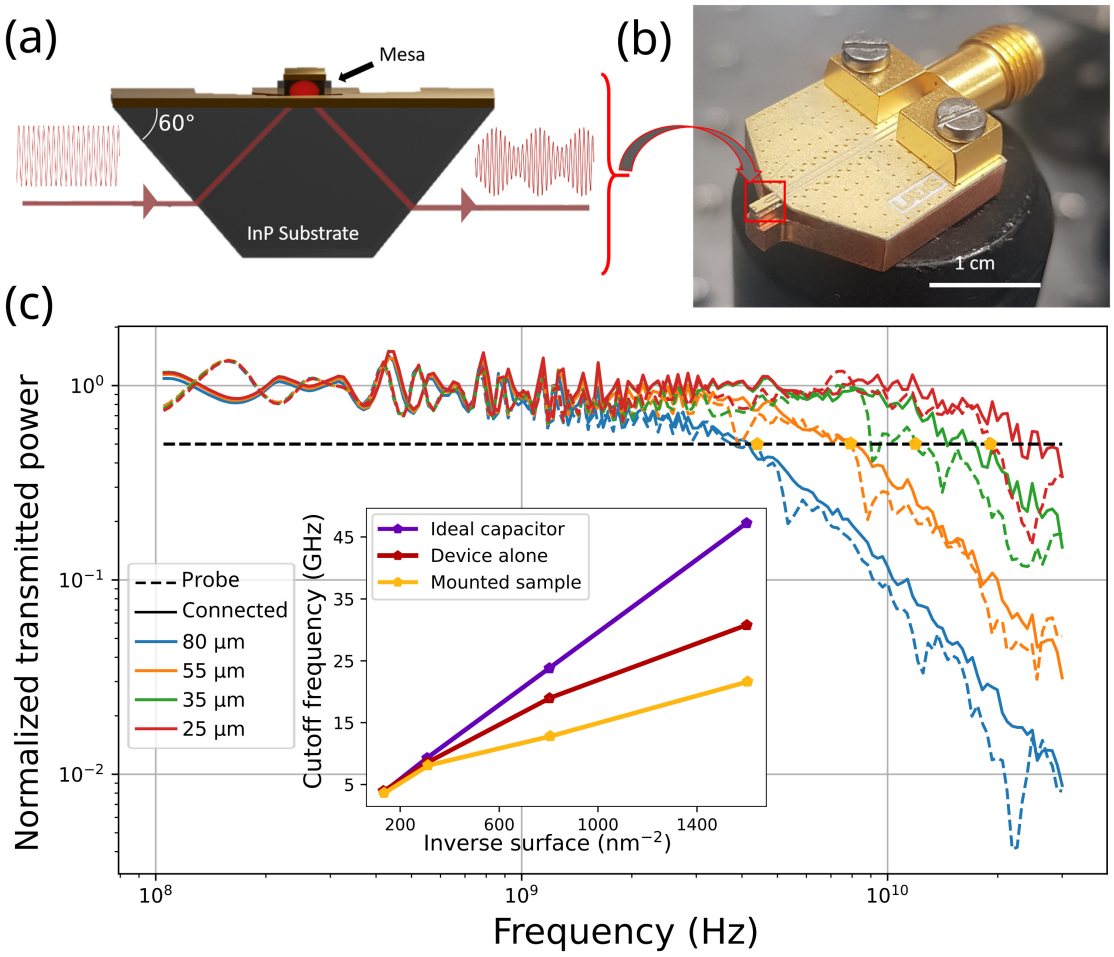

Fig. 2.25 *(a) Sketch of the operation principle of the mounted mesa modulator: the incoming laser is refracted to the mesa to be absorbed. By symmetry, the laser is reflected to the initial optical axis. (b) A custom holder for the transmission Stark modulator allows operations in transmission from the side and connection of the modulator to a PCB with an adapted coplanar waveguide and to an RF K-connector. (c) Normalized rectification measurements for each mesa side size taken with an RF probe on the wafer (full line) and once fully connected with K-cables (dashed lines). In the inset, the -3dB cutoffs are plotted versus the inverse surface of each mesa. The purple line shows the expected behavior if the cutoff was only due to the geometrical capacitance of the devices, the red the cutoff with the probe and in yellow the mounted samples.*

The results presented in the previous section have been obtained using an electrical probe. In order to be used in data transmission experiments, devices need to be packaged. Single

mesas are cleaved, and two facets are then polished at 60° as shown in Fig.2.25 (a) to make a 'double-pass' device: the light arrives parallel to the substrate, is refracted in the transparent InP:Fe substrate and is absorbed and reflected in the mesa. We chose a 60° instead of 45° wedge as it both increases the absorption ($\propto \frac{\sin^2\theta}{\cos\theta}$), and the bottom surface of the sample used to glue it on the custom holder (Fig.2.25 (b)). Finally, the CPW deposited on the InP substrate is connected to a PCB and a K-connector with wirebondings. However, those wirebondings are now only 300 μm long, limiting greatly the impact they will have on the mounted device. Indeed, Fig.2.25 (c) shows in dashed lines the new rectification measurements made on the mounted sample using K-cables on the connector, on top of the measurements made with the probe directly on the samples (full lines) as in Fig.2.24. In the inset of the figure, we compare the cutoff frequencies of the ideal capacitor with a 50Ω waveguide, the samples on the wafer with a probe, and the final mounted devices. Adding the complete connections seems to deteriorate the performances, but looking closely at the rectification curves, it appears that this apparent drop is mainly due to resonances, probably determined by the length of the PCB, and not to an additional capacitance or inductance in the circuit.

It is clear that smaller mesas have a higher cutoff and seem better for high speed modulation. Nevertheless, we need to focus all the light in the mesa otherwise a part of the light will not be modulated and will reduce the contrast. In order to choose the best suited device for our experiment, we measured the waist diameter of our laser (a commercial room temperature DFB QCL lasing at 9.0 μm (Thorlabs QD9000HHL-B)) at the focal point of 1" F1 lens (smaller focal length were prohibited by the size of the sample holder) using a knife edge method: by moving a razor perpendicularly to the optical axis and measuring the power passing as a function of the position of the razor, one obtains a sigmoid function as shown in Fig.2.26. Its cumulative integral is a Gaussian function that can be fitted to determine the size of the beam. The smallest value of the beam size along the optical axis is the waist. The beam waist at the position of the modulator was reduced by using a pair of lenses with focal length of 1" and 2" in an afocal telescope configuration to increase the collimated beam size at the entrance of the focusing lens. We eventually found a $1/e^2$ diameter of 52 μm, meaning that 95 % of the power is within this diameter. This is in free space however, and entering the substrate of the modulator the beam will be refracted, increasing the spot size by a factor $\tan(30°) \simeq 1.7$. For the following, given this value, we only used the larger mesa of 80 μm size.

2.6.2 Characterization of the detector

In order to realize the optical link, we used a 9.0 μm room temperature DFB QCL able to emit up to 100 mW at 20°C, and a GaAs/AlGaAs QCD designed to absorb at the same frequency. Fig.2.27 summarizes the main characteristics of this QCD, processed by Etienne Rodriguez in the same fashion as the modulators, with a mesa of 55x55 μm^2.

Fig.2.27 (a) displays the conduction band diagram of the QCD, highlighting the absorbing wells (in deep blue) and the cascade for the excited electron's extraction in green. The

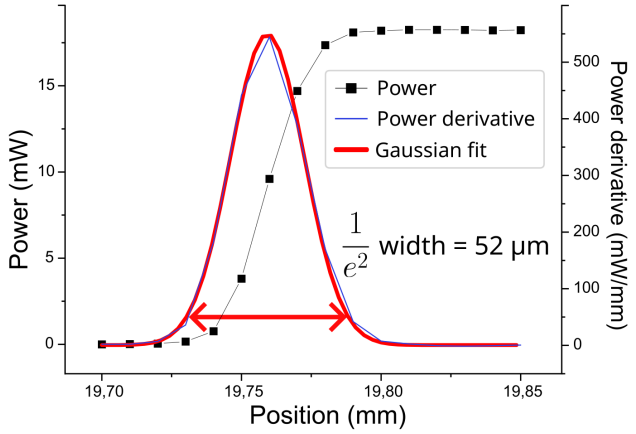

Fig. 2.26 *Knife-edge measurement of the beam size at the waist behind the F1 1-inch lens. From the derivative of the power as a function of the position of the blade we deduce a beam diameter of 52 µm.*

detector is based on a diagonal transition. The difference between the two levels in blue, defining the energy of operation for the detector, is 147 meV. Indeed, the measured photocurrent spectrum in Fig.2.27 (b) has a peak at the expected energy. Fig.2.27 (c) presents the photocurrent as a function of the incident power, showing the linearity of the detector response. This is important for databit transmission since a nonlinearity would translate in a deformation of the incoming signal. We actually see a slight saturation: between 0 and 100 mW, as the responsivity of the detector decreases from 4.9 mA/W to 3.7 mA/W. To limit the distortion induced by the saturation, we need to use less than 70 mW optical powers. Below 50 mW impinging on the detector, for instance, the responsivity varies by less than 15 %.

Finally, in Fig.2.27 (d) we present the bandwidth of our detector measured with two methods. First, in blue, we plot result of the rectification measurement, same as in Fig.2.24. In black we see the Fourier transform of the photocurrent of the QCD taken with a signal analyzer when illuminating it with a mid-infrared frequency comb (Menlo System FC1500-ULN), see Fig.2.28. The beating between the optical teeth of the comb appears as beatnotes separated by 100 MHz, which makes possible to see directly the full optical bandwidth of the detector. Both methods give the same frequency cutoff for the detector, 6 GHz.

2.6.3 Data transmission experiment

Fig.2.29 shows the energies of the laser emission (dashed red line), the QCD photocurrent spectrum (blue), and the absorption spectra of the modulator measured at two different biases, representing the '1' and the '0' states: the laser emits light almost perfectly at the QCD absorption peak. Under positive bias (red), the modulator will absorb up to 47 % of the laser power (after Fig.2.16). Under negative bias, on the other hand (green), there will be no absorption.

With this these three devices we can measure the frequency bandwidth of the full setup

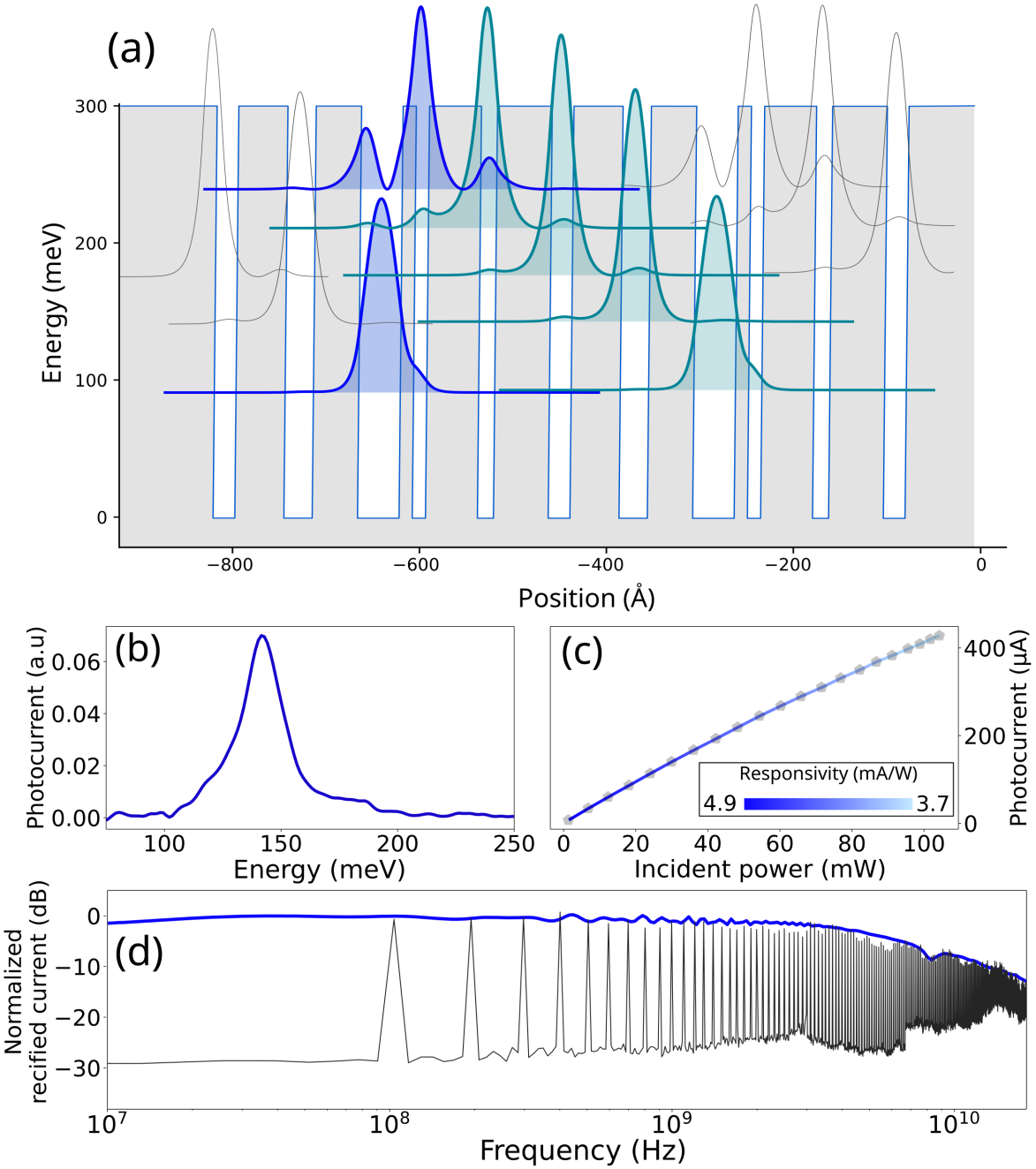

Fig. 2.27 *(a) Conduction band diagram of the QCD. The wavefunctions of one period are filled. The two levels involved in the absorption around 9 μm are in deep blue and the ones of the cascade for the extraction of the photoexcited electrons are in green. (b) Photocurrent spectrum of the QCD. (c) The photocurrent is plotted as a function of the incident power to see the saturation. A mild saturation is observed, equivalent to a drop in responsivity from 4.9 mA/W at low power to 3.7 mA/W at 100 mW. Experimental points are in grey while the line is interpolated to show the drop in responsivity with the color gradient. (d) The bandwidth of the QCD is investigated both electrically with a rectification measurement (blue) and optically using the frequency comb (black). Both methods yield a -3dB cutoff around 6 GHz.*

as shown in Fig.2.30. We use a sine wave synthesizer and a sourcemeter, connected to the modulator through a bias-tee. The detector's signal is collected with a high-speed oscilloscope

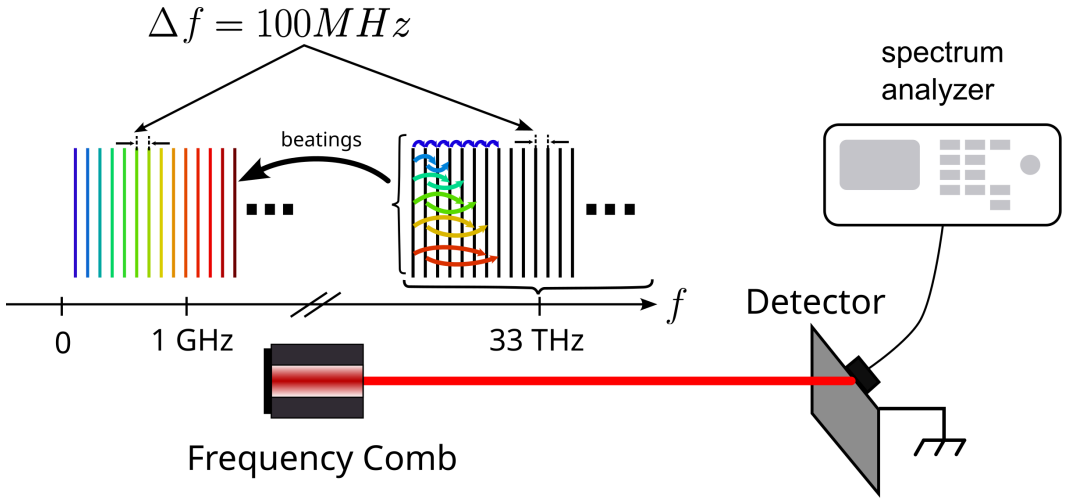

Fig. 2.28 *Bandwidth measurement using a MIR comb laser.*

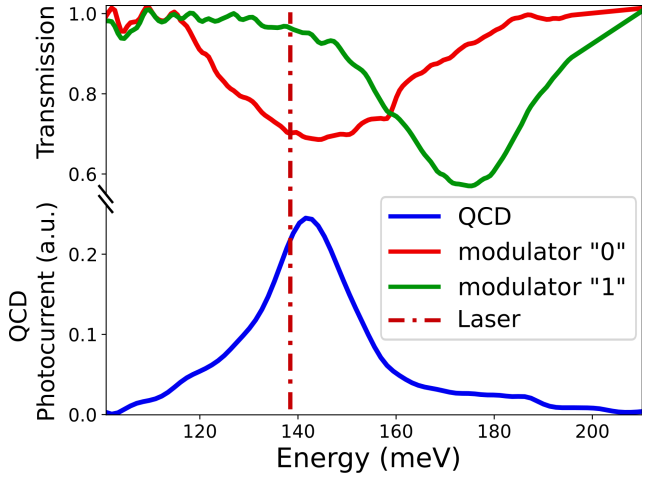

Fig. 2.29 *Laser emission (dashed red), QCD photocurrent (blue) and modulator absorption range (red and green for different biases leading to absorptive and transmitive states).*

(Teledyne LeCroy SDA16 Zi-B). We acquire a temporal trace (for 100 µs with 40 GS.s^{-1}) of the AC signal generated by the detector for each frequency on the oscilloscope and send it to the computer. Finally, a Fourier transform is performed to extract the relevant frequency component. We see that the cutoff of the full system is at 2 GHz, lower than that of each individual device since the roll-off behaviors of each device add up.

This bandwidth is not sufficient to know the data bitrate that can be transmitted using this setup. Indeed, errorless transmission can be performed at higher frequencies than the bandwidth as long as the signal-to-noise ratio is good enough. On the other hand, sending real bit sequences is harder than sine wave, because the spectral distribution is much richer. More relevant than the bandwidth, the quality of the transmission is therefore evaluated in terms of bit-error-rate for a pre-established sequence of symbols mimicking a transmission, as it was done in the example in section 2.1.

For the data transmission experiments, the modulator is connected to a pulse pattern generator that delivers a peak-to-peak voltage of 0.2 V on 50 Ω, which is then amplified with

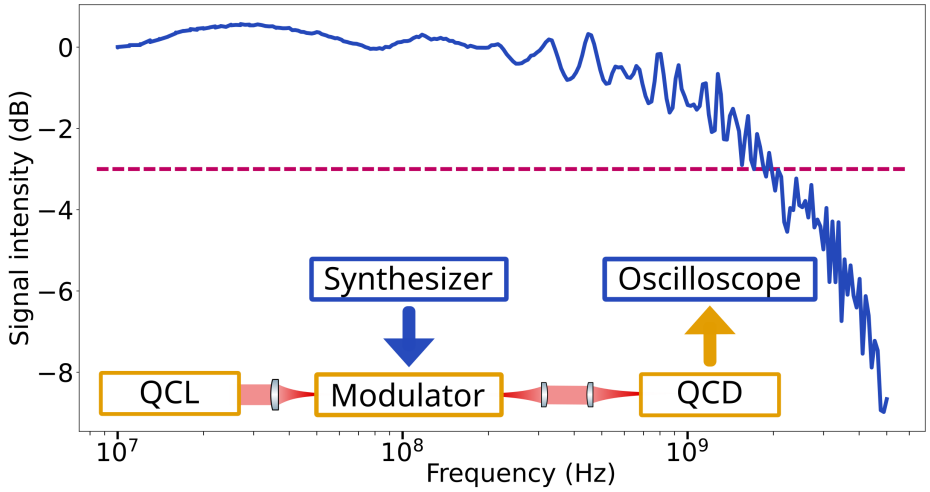

Fig. 2.30 *The full system cutoff is measured on the QCD photocurrent while modulating the external Stark modulator.*

a +25 dB amplifier. The peak-to-peak voltage on the modulator (which has an impedance of 3.5 kΩ) is then 15 V. A DC offset of 1.1 V is added to minimize the distortion: we operate in the regime were the modulator is the most linear and symmetric. The signal sent on the modulator is a 127 bit-long pseudorandom bit sequence (PRBS $2^7 - 1$) using a simple on-off keying (OOK) scheme (only in "zeros" and "ones") so we have one bit per symbol. The bitrate ranges from 1 to 12 Gbit·s^{-1}, limited by the pulse pattern generator. The modulated input signal from a random bit sequence at 7 Gbit·s^{-1} and the output of the QCD on the oscilloscope are shown in Fig.2.31 (a) (blue and red respectively). The laser power incident on the modulator is about 84 mW, kept constant for all data bitrates. The received optical power (after the modulator) is about 33 mW.

The transmission characteristics are analyzed using eye diagrams and BER. Fig.2.31 (c,d) displays eye diagrams taken at 7 and 11 Gbit·s^{-1} received on the QC detector. Eyes at 7 Gbit·s^{-1} are well-opened, i.e. the ones and zeros are well resolved, which is typical of a high-quality transmission, while at 11 Gbit·s^{-1} the eyes look closed, i.e. some traces go in the middle of the eye and it will be impossible to accurately determine if it is a "0" or a "1". In the temporal trace for 7 Gbit·s^{-1}, we see that during the fast successive switchings between 0 and 1 (at 6 ns for instance), the amplitude of the output signal diminishes because the system doesn't have the time to reach the maximum value before having to go down. Nevertheless, we can unambiguously determine if it is a 0 or a 1 in every case. At higher bitrates, the degradation can be seen in the BER (Fig.2.31 (b)): the BER presented is obtained by acquiring 100 µs temporal traces for different bitrates and analyzing them numerically[2]. Below 9 Gbit·s^{-1} the signal is strictly error-free. Given that a BER $< 4.10^{-3}$ can be corrected using error correction codes without excessive overhead (7 % HD-FEC, Hard

[2]The program to do so was done in-house by Hamza Dely: given the time traces from the oscilloscope, this program resamples the data at a constant sample-per-bit ratio and performs a time-correlation calculation on the input and received signals to calculate the delay between them and realign them accordingly. The sequences of bits associated with each signal were determined and finally compared to each other to get the bit error rate after selecting the most appropriate amplitude threshold.

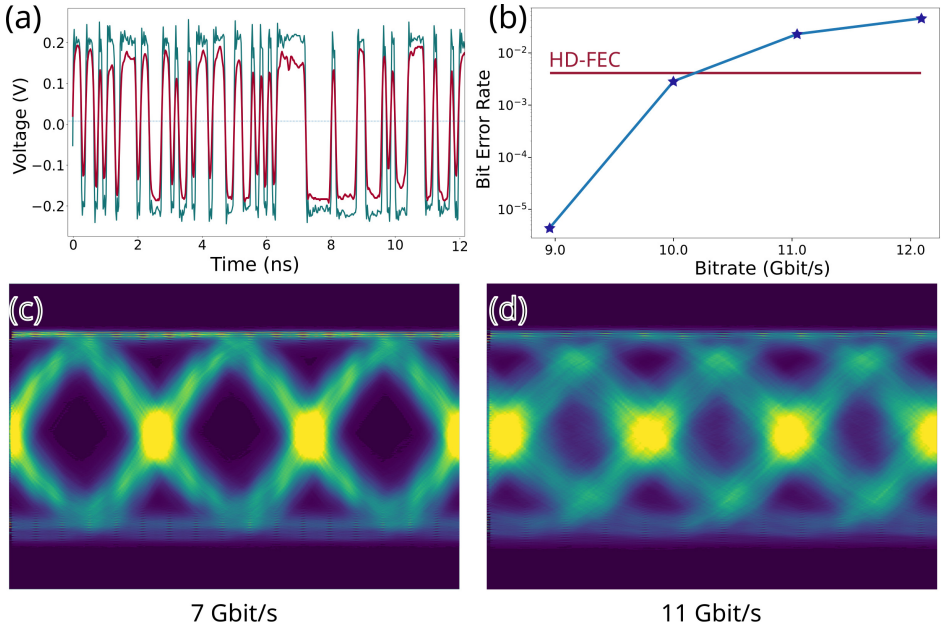

Fig. 2.31 *Data transmission results. (a) Modulated input signal (green line) from a random bit sequence at 7 Gbit·s^{-1} and output of the QCD on the oscilloscope (purple line) (b) Bit error rate obtained for transmissions above 9 Gbit·s^{-1}. The threshold for an error-free transmission assuming 7 % HD-FEC is showed in red dashes. 10 Gbit·s^{-1} would be considered error free. (c), (d) Eye diagrams of the transmission link for the corresponding bit-rates for 7 and 11 Gbit·s^{-1} respectively. 7 Gbit·s^{-1} is clearly well opened whereas one can see traces crossing the eye at 11 Gbit·s^{-1}.*

decision Forward Error Correction [22]), we achieved an acceptable transmission link up to 10 Gbit·s^{-1} [90].

This result, the fastest data transmission for a MIR optical link at the time of the experiment, was further improved by collaborators at Telecom Paris to 24 Gbit·s^{-1} using the exact same setup but with additional work regarding pre- and post-processing of the temporal traces, known as equalization of the signal [91]. Some details about the methods involved will be given in Chapter 4. The eye diagram is shown in Fig.2.32. In (a) is shown the eye diagram prior to any numerical treatment, and in (b) after the equalization, that corrects systematic channel defects and intersymbol interference.

The transmission over a longer distance in free space was also investigated using a multi-pass Herriott cell of 31 m, inducing an attenuation of the power and the divergence of the laser beam. The maximum bitrate was logically decreased but the possibility of data transmission with a bitrate of 14 Gbit·s^{-1} while keeping the BER below the 0.4 % limit was still proven. Though 31 m is not enough for practical applications yet, this work is a key step toward the realization of a real-field MIR free space optical system as it is, to the best of our knowledge, the first high throughput transmission setup on such a distance in this wavelength domain.

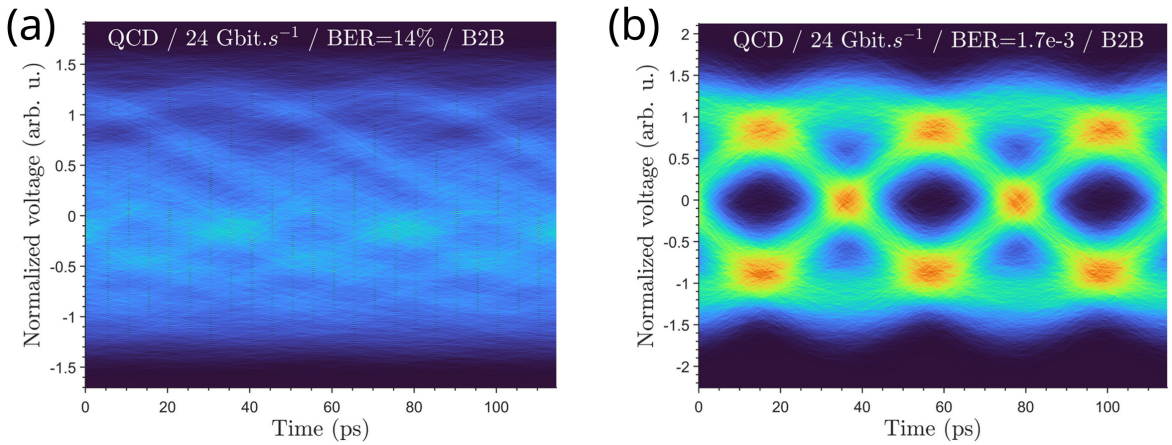

Fig. 2.32 *Comparison of two eye diagrams in back-to-back configuration at 24 Gbit·s^{-1}: (a) without equalization (b) after equalization of the temporal traces.*

2.7 Conclusion

In this chapter we demonstrated a free space optical link for data transmission at room temperature relying only on unipolar quantum optoelectronic devices. For the modulator, we demonstrated the efficiency of asymmetric coupled quantum wells displaying a strong Stark shift, sufficient with respect to the linewidth to operate efficiently. The active region was grown in a MOVPE chamber after careful optimization of the growth conditions by our collaborators at C2N, France, especially regarding the very thin barrier, crucial for the performances of the device. After the characterization of the optical properties of the heterostructure, the fabrication of an adapted electromagnetic packaging was done to achieve a functional device. We showed that the heterostructure could operate at least up to 40 GHz, and a prior cutoff is due to the geometric capacitor created by the device. The quantum confined Stark effect in quantum wells was here used to finally create, to the best of our knowledge, the fastest optoelectronic external modulator to date working in this atmospheric window, at room temperature furthermore, allowing for a 10 Gbit·s^{-1} transmission using OOK keying, without any equalization of the signal.
Measurement of the capacity of the optical link with equalization was eventually performed with the same devices outside of the lab at Telecom Paris and showed even higher throughputs and the possibility to realize optical links over longer distance (here >30 m).

During the time of the Ph.D., this Stark modulator was also used by collaborators outside of the lab for successful works: at KTH in Stockholm [92], and at Telecom Paris [91].

Chapter 3

Design and fabrication of metamaterial devices

3.1 Introduction

A natural step to improve the performances of optoelectronic devices is to engineer an *ad hoc* electromagnetic environment in order to enhance the interaction of the active region with the electromagnetic field, increasing the light-matter interaction effective length [93]. For intraband devices, depending on the wavelength of interest, various structures have been put forward to enhance the properties of devices ([94], [95]), the goal being always to be able to confine the electric field in a small region of space, overlapping with the quantum wells.

The structure investigated in this work is an array of double metal cavities, as sketched in Fig.3.1 (a): the active region is embedded in 1D- or 2D-arrays of double metal resonators with a characteristic size s commensurable with the wavelength. They act both as antenna and cavity for the MIR radiation for reasons that we will develop. They will be henceforth designated as Patches or Stripes for the 2D and 1D resonators respectively.

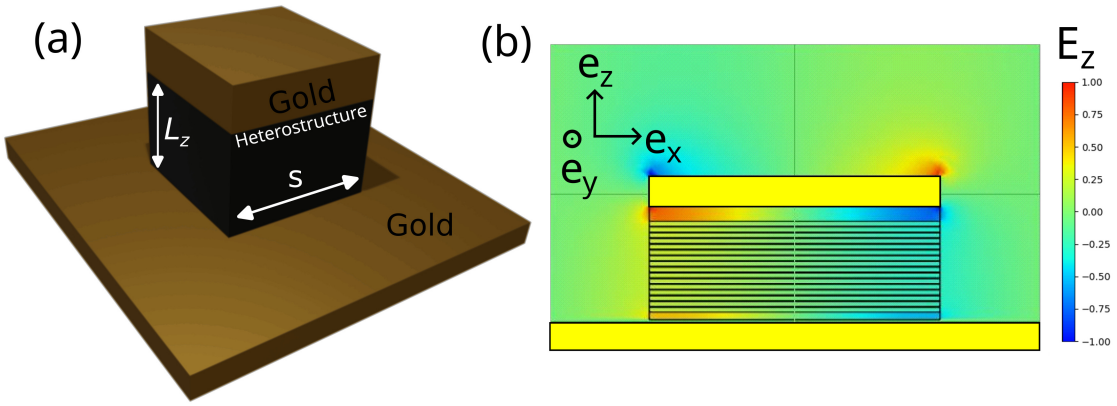

Fig. 3.1 *(a) Sketch of a patch resonator: a 2D resonator of thickness L_z and lateral size $L_y = L_x = s$, with the heterostructure sandwiched between two gold layers. The growth direction of the epitaxy is along z. (b) Numerical simulation of the electric field along the z-axis in the cavity for the $TM_{0,1,0}$ mode.*

The patch resonator can be seen a 3-dimensional cavity, supporting modes with the electric field $\mathbf{E}$ verifying the homogeneous wave equation:

$$(\nabla^2 + k^2)\mathbf{E} = 0 \tag{3.1}$$

Assuming that the gold is a perfect conductor (no tangential electric field on the boundaries) and that the sidewalls of the resonators are perfect magnetic conductor (only tangential electric field on the boundaries), one can express the electric field in the structure:

$$\begin{aligned} E_x(x,y,z) &= E_x^0 \sin(k_x x)\cos(k_y y)\sin(k_z z) \\ E_y(x,y,z) &= E_y^0 \cos(k_x x)\sin(k_y y)\sin(k_z z) \\ E_z(x,y,z) &= E_z^0 \cos(k_x x)\cos(k_y y)\cos(k_z z) \end{aligned} \tag{3.2}$$

The wavevectors are quantized by the confinement induced by the gold and the air. Much alike the confined wavevectors in quantum wells, they can be expressed [96] using integers l,m,n, as:

$$k_x = \frac{l\pi}{L_x} \qquad k_y = \frac{m\pi}{L_y} \qquad k_z = \frac{n\pi}{L_z} \tag{3.3}$$

With the angular frequency of the modes:

$$\omega_{lmn} = \frac{c}{n_{eff}}\sqrt{\left(\frac{l\pi}{L_x}\right)^2 + \left(\frac{m\pi}{L_y}\right)^2 + \left(\frac{n\pi}{L_z}\right)^2} \tag{3.4}$$

n_{eff} is the effective index of the metamaterial.

It can be shown that by using a cavity thinner than the effective wavelength in the semiconductor, only one mode (n=0) can be supported in the cavity. The cutoff condition for the n-*th* mode, expressing the possibility to have a non-zero wavevector along z, writes:

$$\omega_{cutoff,n=1} = \frac{\pi c}{n_{eff} L_z} \Rightarrow L_{z,lim} = \frac{\lambda}{2n_{eff}} \tag{3.5}$$

If the cavity is thinner than $L_{z,lim}$, $k_z = 0$ which in turn sets $E_x = E_y = 0$ after eq.3.2. The electric field along z is then $E_z(x,y,z) = E_z^0 \cos(k_x x)\cos(k_y y)$. This distribution of the field along x results in an electric dipole in the metallic top gold (and its mirror counterpart in the bottom gold) excited by the incoming electric field [96],[57]. For a maximal coupling, the electric field must be in the plane of the gold hence a normal incidence of light on the patch.

In conclusion, the patch or the stripe, if thin enough, accommodates modes where the electric field is only along z. These resonators fulfill the polarization selection rule required by intraband transitions and they are excited by a normal incoming light at the wavelength $\lambda = 2n_{eff}s$, with $s = L_x (= L_y$ for patches). In the following, we will exclusively be using the 1st, low energy mode of the cavities, (1,0,0) or (0,1,0), often known as $TM_{0,1}$. Fig.3.1(b) shows the simulation of the vertical electric field in a patch resonator at the energy of the $TM_{0,1}$ mode. We see that the field is maximal (in absolute value) along the horizontal direction at the edges of the patch, with a zero in the center; and is constant along the vertical direction.

In this simple model we have considered perfect interfaces both with the gold and the air. In reality, at the interface with air there is a fraction of the field "leaking out" of the resonator (visible in Fig.3.1 (b)), leading to an effective length of the mode and the use of the effective

refractive index of the mode in the cavity n_{eff}. This index is close to the bulk semiconductor refractive index but slightly higher to account for the non ideal interfaces. A study [97] showed that unetched patches, without a strong impedance mismatch at the edge of the mode, had higher n_{eff}, synonym of a larger leakage of the electric field outside of the electrical area.

At the interfaces with the metal, the non-zero skin depth will allow an evanescent field into the metal and induce non negligible dissipation by free carrier absorption. Other sources of losses can be identified, namely the scattering at the rough semiconductor/air interface, free carrier absorption by the doped layers, optical phonon resonances, and of course the desired ISB absorption in the quantum wells.

In fine, the mode in the cavity can be described as a damped oscillator, losing its energy at a decay rate γ_{tot}. The quantity $Q = \omega_{0,1}/\gamma_{tot}$, known as the quality factor, is proportional to the number of roundtrips of the mode in the cavity, i.e. the increase of the effective interaction length of the mode with the electrons. In the literature, this type of cavity exhibited quality factors of approximately 10 [48, 35].

Finally, an array of patches acts as an antenna [98] and absorbs photons from an area larger than the sum of surfaces of the resonators [35]. We can define a *photon collection* area, larger than the *electrical* area, from which photons can be collected. The periodicity p of the array will be for us a supplementary degree of freedom to tailor the coupling of the metamaterial with the light.

To summarize, the appeal of such structures stems from several reasons:

- The quality factor expected from the cavity increases the effective interaction length between the radiation and the active region,
- The antenna effect allows for an electrical footprint smaller than the device photon absorption area, leading to smaller dark current and higher bandwidth,
- The intersubband absorption selection rules are perfectly verified by the fundamental mode of the cavity, allowing for a strengthened interaction and for an easier manipulation since normal incidence is now possible.

The aim of the first part of this chapter is to put forward the key features of metamaterials for increased light matter interaction and show how the metamaterials can be efficiently modeled in the Coupled Mode Theory (CMT) framework in order to optimize the performances of optoelectronic devices.

Going forward, and starting from a fully classical equivalent model, the coupled harmonic oscillators, we will highlight important properties of coupled oscillators in general. From there on, we will introduce the very convenient framework of Coupled Mode Theory and clarify how to apply it to our system. We then introduce quantities peculiar to our devices with a parametric study of a set of cavities embedding a bulk GaAs layer. Once the order of magnitude of these parameters established, we will present the strategies of design of our

optoelectronic devices in cavity. Finally, in the last part, we will address the fabrication of such devices in a clean room facility and the particularity of the processing of InP-based devices designed for high speed operation.

3.2 Coupled mode theory for metamaterial design

Interacting systems and their most simple modelling, coupled harmonic oscillators, are involved in many fields: they are at the very foundation of cavity-electrodynamics, but are also present in electronics (RLC circuits) or even biochemistry [99]. The aim of this section is describing how two coupled oscillators can exchange energy. The intensity of the coupling between the two systems can lead to two limit cases (and everything in-between): the so called weak and strong coupling regimes. In the following we will see how they arise through a fully classical toy model: two springs coupled through a third one (Fig.3.2).

3.2.1 A toy model: coupled oscillators

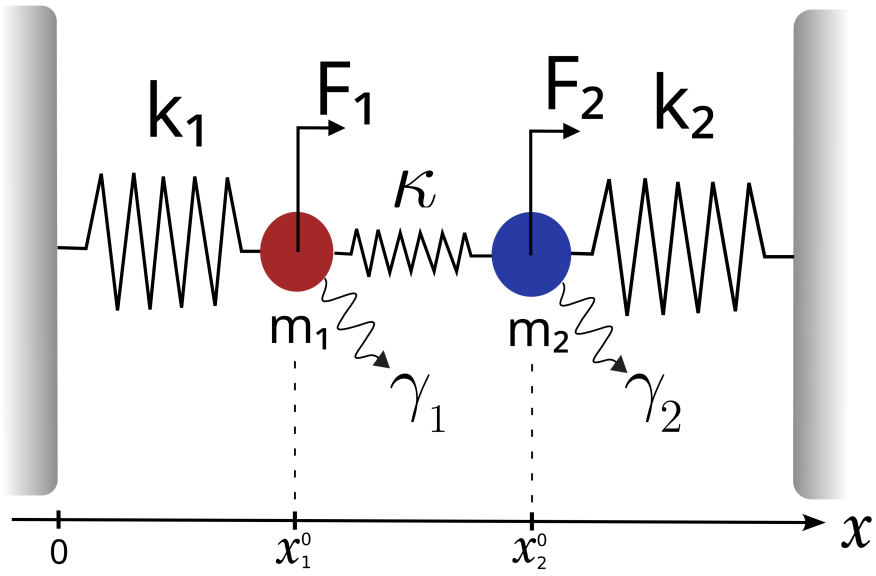

Fig. 3.2 *Two springs coupled through a third one, undergoing some damping in the air and submitted to external driving forces.* x_1^0 *and* x_2^0 *are the equilibrium positions.*

We consider a mechanical model system composed of two masses, m_1 and m_2, attached to opposite walls through two springs of constants k_1 and k_2 and coupled through a third spring of constant κ. The distance of the masses from their respective equilibrium position, x_1 and x_2, can easily be derived through Newton's equation of motion. This fully classical toy model is already enough to observe different concepts that will drive our work : how the energy is distributed in the system and the possible emergence of anti-crossing in the frequencies of the oscillators in the strong coupling regime.
The differential equations governing the movement of the masses (as long as the coupling spring is always pulling because stretched) write:

$$m_1\frac{d^2x_1}{dt^2}+\gamma_1\frac{dx_1}{dt}+k_1x_1-\kappa\,(x_2-x_1)=0$$
$$m_2\frac{d^2x_2}{dt^2}+\gamma_2\frac{dx_2}{dt}+k_2x_2-\kappa\,(x_1-x_2)=0 \tag{3.6}$$

We look for harmonic solutions in the form $x_i(t)=x_ie^{-i\omega t}$. For simplicity, let's neglect the damping for now ($\gamma_1=\gamma_2$=0) and set $\omega_1^2=\dfrac{k_1}{m_1}$ and $\omega_2^2=\dfrac{k_2}{m_2}$. This system has solutions if and only if

$$\begin{vmatrix}-\omega^2+\omega_1^2+\kappa/m_1 & -\kappa/m_1\\ -\kappa/m_2 & -\omega^2+\omega_2^2+\kappa/m_2\end{vmatrix}=0 \tag{3.7}$$

which eventually yields two new (positive) frequencies :

$$\omega_\pm^2=\frac{1}{2}\left(\omega_A^2+\omega_B^2\pm\sqrt{(\omega_A^2-\omega_B^2)^2+4\Gamma^4}\right) \tag{3.8}$$

where we have redefined

$$\omega_A^2=\frac{\kappa+k_1}{m_1}=\omega_1^2+\frac{\kappa}{m_1}\qquad \omega_B^2=\frac{\kappa+k_2}{m_2}=\omega_2^2+\frac{\kappa}{m_2}\qquad\text{and}\qquad \Gamma^4=\frac{\kappa^2}{m_1m_2} \tag{3.9}$$

If we remove the coupling ($\kappa=0$), we recover the oscillations of the uncoupled springs with $\omega_+=\omega_A=\omega_1$ and $\omega_-=\omega_B=\omega_2$. The solutions $\omega_\pm$ are plotted in Fig.3.3 as a function of $\Delta\omega=\omega_2-\omega_1$. We can see that, with a non-zero coupling constant, the eigenfrequencies of the

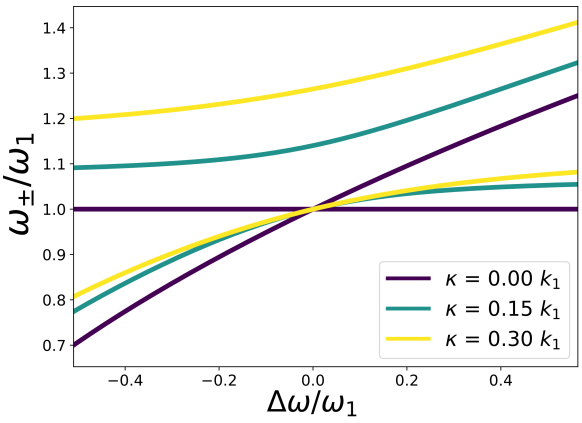

Fig. 3.3 *Renormalized eigenfrequencies $\omega_\pm$ of two springs as a function of $\frac{\Delta\omega}{\omega_1}=\frac{\omega_2-\omega_1}{\omega_1}$. In purple the uncoupled case and green and yellow an increasing coupling is added: an anticrossing appears.*

system present a different behavior: an anticrossing is visible when the oscillation frequencies of the two springs are close enough and the difference in eigenfrequencies increases with κ. Far from resonance, both oscillators recover their isolated behavior except for a shift induced by the coupling of the third spring.

3.2.2 Role of the damping

Adding losses ($\gamma_i\neq0$) in the system can be readily done and the main consequence will be that the new eigenfrequencies will have an imaginary part, resulting in the damping of the

movement of the coupled system.
The system 3.6 becomes:

$$\begin{bmatrix} -\omega^2 - i\frac{\gamma_1}{m_1}\omega + \omega_A^2 & -\frac{\kappa}{m_1} \\ -\frac{\kappa}{m_2} & -\omega^2 - i\frac{\gamma_2}{m_2}\omega + \omega_B^2 \end{bmatrix} \begin{bmatrix} x_1 \\ x_2 \end{bmatrix} = \begin{bmatrix} 0 \\ 0 \end{bmatrix} \tag{3.10}$$

Close to the resonance, $\omega + \omega_{A,B} \approx 2\omega$ and $\tilde{\omega} \approx (\omega_A + \omega_B)/2$. We thus obtain:

$$\begin{bmatrix} \omega_A - \omega - \frac{i\gamma_1\omega}{m_1(\omega_A+\omega)} & \frac{-\kappa}{m_1(\omega_1+\omega)} \\ \frac{-\kappa}{m_2(\omega_2+\omega)} & \omega_B - \omega - \frac{i\gamma_2\omega}{m_2(\omega_2+\omega)} \end{bmatrix} \begin{bmatrix} x_1 \\ x_2 \end{bmatrix} = \begin{bmatrix} 0 \\ 0 \end{bmatrix}$$

$$\Rightarrow \begin{bmatrix} \omega_A - \frac{i\gamma_1}{2m_1} - \omega & \frac{-\kappa}{2m_1\tilde{\omega}} \\ \frac{-\kappa}{2m_2\tilde{\omega}} & \omega_B - \frac{i\gamma_2}{2m_2} - \omega \end{bmatrix} \begin{bmatrix} x_1 \\ x_2 \end{bmatrix} = \begin{bmatrix} 0 \\ 0 \end{bmatrix} \tag{3.11}$$

The last equation will have non trivial solution if the determinant of the last matrix is equal to 0. We recognize here that solving $|H - \omega I| = 0$ is the same as diagonalizing:

$$H = \begin{bmatrix} \omega_A - \frac{i\gamma_1}{2m_1} & \frac{-\kappa}{2m_1\tilde{\omega}} \\ \frac{-\kappa}{2m_2\tilde{\omega}} & \omega_B - \frac{i\gamma_2}{2m_2} \end{bmatrix} \tag{3.12}$$

The solutions are:

$$\omega_\pm = \frac{1}{2}\left(\omega_A + \omega_B - \frac{i}{2}\left(\frac{\gamma_1}{m_1} + \frac{\gamma_2}{m_2}\right) \pm \sqrt{\left(\omega_A - \omega_B + \frac{i}{2}\left(\frac{\gamma_1}{m_1} - \frac{\gamma_2}{m_2}\right)\right)^2 + \left(\frac{\Gamma^2}{\tilde{\omega}}\right)^2}\right) \tag{3.13}$$

We see again the splitting appearing without the damping for $\omega_A = \omega_B = \tilde{\omega}$:

$$\omega_\pm = \tilde{\omega} - \frac{i}{4}\left(\frac{\gamma_1}{m_1} + \frac{\gamma_2}{m_2}\right) \pm \frac{1}{2}\sqrt{\left(\frac{\Gamma^2}{\tilde{\omega}}\right)^2 - \frac{1}{4}\left(\frac{\gamma_1}{m_1} - \frac{\gamma_2}{m_2}\right)^2} \tag{3.14}$$

The eigenfrequencies are now complex. In the Fourier space, this will result in a broadening of the modes, proportional to the sum of the damping terms. To visualize this properly, we numerically solve for the steady state of the dissipative system driven by a harmonic force at the frequency ω:

$$\begin{bmatrix} -\omega^2 - i\frac{\gamma_1}{m_1}\omega + \omega_A^2 & -\frac{\kappa}{m_1} \\ -\frac{\kappa}{m_2} & -\omega^2 - i\frac{\gamma_2}{m_2}\omega + \omega_B^2 \end{bmatrix} \begin{bmatrix} x_1 \\ x_2 \end{bmatrix} = \begin{bmatrix} F1 \\ F2 \end{bmatrix} \tag{3.15}$$

We are now interested in the power dissipated by each oscillator $P_i = \omega^2\gamma_i|x_j(\omega)|^2$ for F_2=0, i.e. when only the mass 1 is driven. In Fig.3.4 we plot in colorscale the total power dissipated in the system $P_1 + P_2$ (upper row) and P_2 (lower row) for various values of parameters κ and

$\gamma_1 = \gamma_2$.

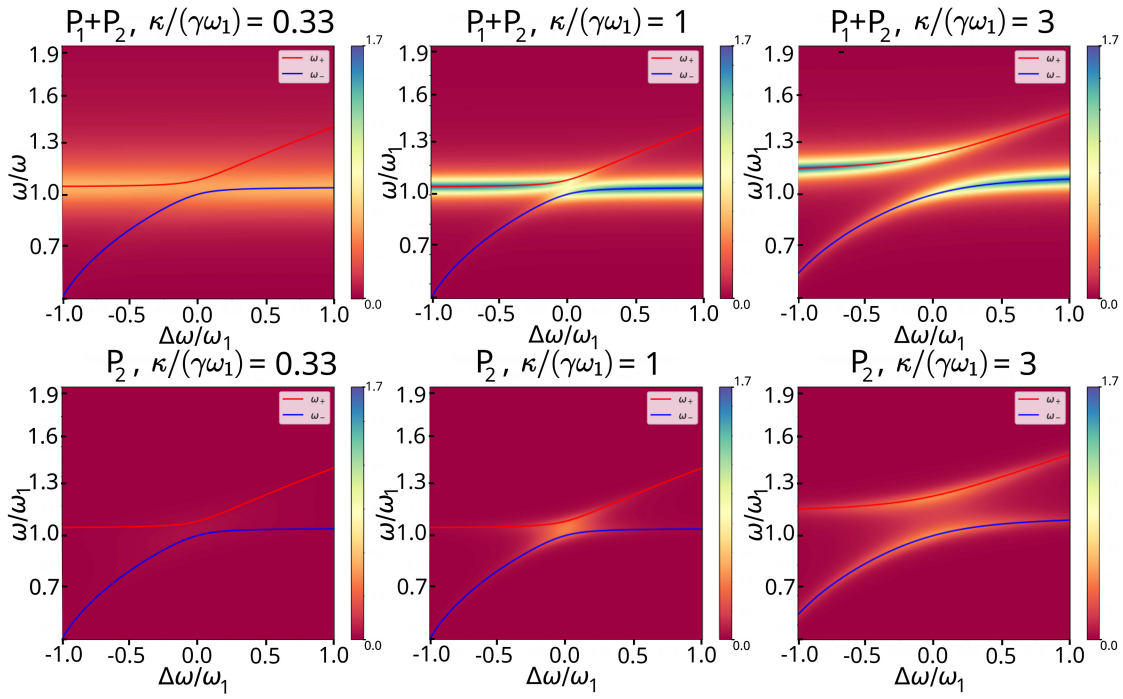

Fig. 3.4 *Power dissipated by the system $P_1 + P_2$ in the first row, and by the second non-driven resonator P_2 in the second row. From left to right: $\kappa/(\omega_1\gamma)$ with $\gamma = \gamma_1 = \gamma_2$ increases and the splitting becomes more and more visible.*

In Fig.3.4 the left column illustrates the case where the system is too damped with respect to the coupling strength for the power to be transferred from oscillator 1 to 2, which thus dissipates no power. For any ω_2, the energy is dissipated at ω_1 by the first oscillator. Going to the second column, the damping has been reduced and we have $\kappa/(\omega_1\gamma) = 1$. The linewidth diminishes, the splitting begins to be visible and the second oscillator starts to dissipate power when $\omega_2 = \omega_1$. Finally, in column 3, the coupling strength is multiplied by 3. Now the splitting is clearly visible and we now see modes appearing at the frequencies ω_+ and ω_- and the oscillator 2 dissipates energy in a wider frequency range.

For $\kappa \gg \gamma_i\omega_1$ we see that the resonators can exchange energy and dissipate it at new eigenfrequencies, whereas in the opposite case $\kappa \ll \gamma_i\omega_1$, no energy exchange occurs. The limit between both cases is set by the broadening due to the damping and the coupling strength.

Looking at the solutions at resonance ($\omega_A = \omega_B$), Eq.3.13 yields more precise insights :

- If $4\left(\frac{\Gamma^2}{\tilde{\omega}}\right)^2 - \left(\frac{\gamma_1}{m_1} - \frac{\gamma_2}{m_2}\right)^2 \geqslant 0 \Leftrightarrow 4\frac{\kappa^2}{m_1 m_2} \geqslant \tilde{\omega}^2\left(\frac{\gamma_1}{m_1} - \frac{\gamma_2}{m_2}\right)^2$ the square root is real and the eigenfrequencies are distinct and separated by a quantity $\sqrt{\frac{\kappa^2}{\tilde{\omega}^2 m_1 m_2} - \left(\frac{\gamma_1}{m_1} - \frac{\gamma_2}{m_2}\right)^2} < \frac{\Gamma^2}{\tilde{\omega}}$: it is the strong coupling regime.
- $4\frac{\kappa^2}{m_1 m_2} < \tilde{\omega}^2\left(\frac{\gamma_1}{m_1} - \frac{\gamma_2}{m_2}\right)^2$ yields a degenerate unique solution. The dampings have

an effect on the broadening of the mode but no splitting occurs: it is the weak coupling regime.

3.2.3 Coupled Mode Theory formalism

Though exact, these methods for tackling coupled resonators are system dependent. We will here introduce a more general approach to the coupled oscillator problem, that yields very close results and that, once established, is more physically meaningful.
Starting from a canonical harmonic oscillator of frequency ω_0 and setting $X(t) = x(t) - l_0$ with l_0 the equilibrium length, we introduce the complex quantity $a_\pm = \sqrt{\frac{m}{2}}\left(\frac{dX}{dt} \pm i\omega_0 X\right)$ (formally similar to the ladder operators in the solution of the quantum harmonic oscillator). We can recognize

$$\frac{d^2X}{dt^2} + \omega_0^2 X = 0 \iff \begin{array}{l} \frac{da_+}{dt} = i\omega_0 a_+ \\ \frac{da_-}{dt} = -i\omega_0 a_- \end{array} \tag{3.16}$$

Fixing $X(0) = X_1$ and $X'(0) = 0$ gives solution for X: $X(t) = X_1 \cos(\omega_0 t)$ We can therefore write:

$$\begin{aligned} a_+ &= \sqrt{\frac{m}{2}}\left(\frac{dX}{dt} + i\omega_0 X\right) \\ &= \sqrt{\frac{m}{2}}\left(-\omega_0 X_1 \sin(\omega_0 t) + i\omega_0 X_1 \cos(\omega_0 t)\right) \\ &= \sqrt{\frac{m}{2}}\omega_0 X_1 e^{i\omega_0 t + \pi/2} \end{aligned} \tag{3.17}$$

Finally it is possible to recognize the potential energy E_p:

$$|a_+|^2 = \frac{1}{2}k_1 X_1^2 = E_p(0) = E_m \tag{3.18}$$

Indeed the mechanical energy E_m is constant in time without damping and the kinetic energy is null at $t = 0$. This gives us insights on the meaning of a_+: it is the mode amplitude. As a_+ and a_- are complex conjugates, only one of them is enough to describe our mode.
We now introduce the damping γ:

$$\frac{da}{dt} = i\omega_0 a - \gamma a \tag{3.19}$$

Note that this is only equivalent to the introduction of the damping with a first time-derivative in the differential equation (Eq 3.6) as long as the damping is small. Indeed, solving the damped-equivalent second order differential equation in X, leads to a characteristic equation resulting in the complex solution $r = -\frac{\gamma}{2} + i\omega_0\sqrt{1 - \left(\frac{\gamma}{2\omega_0}\right)^2}$. We effectively neglect the correction to ω_0 induced by the damping.

To complete the formalism, we finally need to be able to couple two resonators. Let a_1

and a_2 describe two resonators. The system of coupled equations of motion writes:

$$\begin{aligned}\frac{da_1}{dt} &= i\omega_1 a_1 - \gamma_1 a_1 + i\kappa a_2 \\ \frac{da_2}{dt} &= i\omega_2 a_2 - \gamma_2 a_2 + i\kappa a_1\end{aligned} \tag{3.20}$$

It is possible to verify that, without damping, we recover the same solutions as in the previous section. We look for harmonic solutions depending on $e^{i\omega t}$. We obtain the following system:

$$\begin{cases} i\omega a_1 = i\omega_1 a_1 - \gamma_1 a_1 + i\kappa a_2 \\ i\omega a_2 = i\omega_2 a_2 - \gamma_2 a_2 + i\kappa a_1 \end{cases} \iff \begin{bmatrix} i\omega - i\omega_1 + \gamma_1 & -i\kappa \\ -i\kappa & i\omega - i\omega_2 + \gamma_2 \end{bmatrix} \begin{bmatrix} a_1 \\ a_2 \end{bmatrix} = 0 \tag{3.21}$$

In order to have non trivial solutions, the determinant should be zero, writing:

$$\begin{vmatrix} i\omega - i\omega_1 + \gamma_1 & -i\kappa \\ -i\kappa & -\omega - i\omega_2 + \gamma_2 \end{vmatrix} = 0 \tag{3.22}$$

We obtain the same solutions as in 3.13:

$$\omega_\pm = \frac{1}{2}\left(\omega_1 + \omega_2 - i\left(\gamma_1 + \gamma_2\right) \pm \sqrt{\left(\omega_1 - \omega_2 + i\left(\gamma_1 - \gamma_2\right)\right)^2 + \kappa^2}\right) \tag{3.23}$$

Where $\omega_{A,B}$ were replaced by $\omega_{1,2}$, because the coupling links now a_1 to a_2 and not to $a_2 - a_1$. This change, actually matching to our physical system as we will see in the next paragraph, only removes the κ shift between $\omega_{A,B}^2$ and $\omega_{1,2}^2$ but the other conclusions hold.

3.2.4 The patch antenna resonator in the Coupled Mode Theory

The Patch Antenna Resonator introduced before can be modelled as a system of two coupled oscillators. The first oscillator is the cavity TM_{01}-mode and the second the plasma-shifted intersubband transition $\tilde{\omega}_{12}$ of the quantum well embedded in it.

The bare cavity mode is coupled with an impinging harmonic excitation from a wave $S_{in}e^{i\omega t}$, like a driven harmonic oscillator. $|S_{in}|^2$ is the power of the incoming wave. Its influence is two-fold: it can excite the mode of the resonator, and it also creates a channel for power dissipation, at a rate Γ_a. The non-radiative dissipation channel is introduced through a non-radiative damping term γ_a. The evolution of a, the amplitude of the mode in the cavity under excitation, reads in the CMT formalism:

$$\frac{da}{dt} = i\omega_a a - (\gamma_a + \Gamma_a)a + \kappa S_{in} e^{i\omega t} \tag{3.24}$$

κ defines the quality of the coupling between the drive and the resonator. It can be shown, relying only on energy conservation [100], that the factor κ depends on the radiative losses of the mode through $\kappa = \sqrt{2\Gamma_a}$. Indeed, these radiative losses are also what allows a mode that travels in free-space to couple into the cavity.

Now let's consider the second oscillator in our problem, the polarization field P associated with the ISB transition in the active well. We will assume that the free-space radiation only couples with the cavity mode and not with the ISB transition directly. The ISB absorption thus can only occur *through* the coupling of the ISB transition with the cavity mode *via* a coupling constant Ω_r. This is equivalent to set $\Gamma_P = 0$. The only losses associated with P are the non-radiative losses γ_P.

The full system of equations is therefore the following:

$$\begin{aligned}
\frac{da}{dt} &= i\omega_a a - (\gamma_a + \Gamma_a)a + \sqrt{2\Gamma_a}S_{in} + i\Omega_r P \\
\frac{dP}{dt} &= i\omega_P P - \gamma_P P + i\Omega_r a \\
S_{out} &= -S_{in} + \sqrt{2\Gamma_a}a
\end{aligned} \tag{3.25}$$

The quantities involved in this system of equations are specified below.

- Ω_r is the Rabi frequency $2\Omega_r = \sqrt{\frac{f_{12}e^2 N_{QW}(n_1 - n_2)}{\varepsilon_r \varepsilon_0 m^* d}} = \sqrt{f_w}\omega_p$, coupling the cavity photons and the ISB transition. f_w is the spatial overlap of the resonator's mode with the doped quantum wells and ω_p is the plasma frequency. d is the thickness of the quantum well. The $n_i's$ are the surface densities of electrons on the subbands 1 and 2 involved in the transition.

- The uncoupled modes' energies ω_P and ω_a are respectively $\tilde{\omega}_{12}$ for the plasma-shifted ISB transition and the cavity TM_{01}-mode $\omega_a = \frac{\pi c}{n_{eff}s}$ with s the lateral dimension.

- The non-radiative losses of the ISB transition γ_P describe the losses through non radiative processes (phonons, alloy disorder, interface roughness). The typical timescale involved, less than 0.5 ps, compared to the typical spontaneous emission time of 100 ns, explains why we do not consider any radiative reemission through a term Γ_P.

- The non-radiative losses of the cavity γ_a describe the photons lost by various non-radiative channels: mainly by free carrier absorption in the metal, but also in the active region, and any scattering that can occur on interfaces.

  Finally, one could add a term to describe the losses through diffraction. The radiative coupling between the cavity mode and the k-th diffraction order is quantified by the diffraction radiative losses Γ_d^k. This term will be neglected for the moment.

In this model, we will consider that the optical mode overlaps perfectly with the resonators. f_w can therefore be identified with the filling fraction of doped quantum wells in the heterostructure.

Fig.3.5 summarizes the different quantities involved in the modelling of a patch antenna resonator with the CMT.

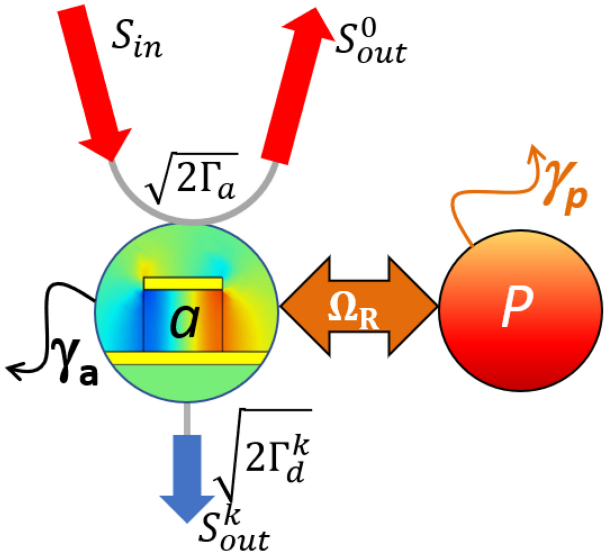

Fig. 3.5 *a) Coupled modes theory representation of the system. The cavity is coupled directly to the incoming field S_{in} but the dipole of the ISB transition can only be excited through its coupling to the cavity. Non radiative losses occur in both the cavity and the quantum wells. Reflected S^0_{out} or diffracted S^k_{out} outgoing fields escape the cavity.*

Solving the set of equation 3.25, we calculate the amplitude of the modes of each oscillator (a for the cavity mode and P for the ISB polarization). At resonance, for $\omega = \omega_a = \omega_P$, the absorbance, i.e. the dissipation of the system through non-radiative channels, is :

$$A = A_{cav} + A_{isb} = 2\gamma_a \frac{|\mathbf{a}|^2}{|S_{in}|^2} + 2\gamma_P \frac{|\mathbf{P}|^2}{|S_{in}|^2} \tag{3.26}$$

while the reflectivity is:

$$R = \frac{|S_{out}|^2}{|S_{in}|^2} = \frac{|\sqrt{2\Gamma_a \frac{|\mathbf{a}|^2}{|S_{in}|^2}} - S_{in}|^2}{|S_{in}|^2} \tag{3.27}$$

The ISB absorption can be calculated for arbitrary values of ω, ω_a and ω_P:

$$A_{isb} = \frac{4\gamma_P \Gamma_a \Omega_r^2}{\left[\gamma_P(\omega-\omega_a) + (\gamma_a+\Gamma_a)(\omega-\omega_P)\right]^2 + \left[\gamma_P(\gamma_a+\Gamma_a) + \Omega_r^2 - (\omega-\omega_a)(\omega-\omega_P)\right]^2} \tag{3.28}$$

For a resonant cavity ($\omega_a = \omega_P$), searching for maxima of the absorptivity, we find that two maxima are present for $\Delta = 4\Omega_R^2 - 2(\gamma_P^2 + (\gamma_a^2 + \Gamma_a^2)) > 0$, at frequencies $\omega = \omega_a \pm \frac{1}{2}\sqrt{\Delta}$. The two modes resulting from the interaction of the cavity photons and the ISB transition are called (ISB) polaritons.

The value defining the onset of the strong coupling regime between the resonator mode and the ISB oscillator reads therefore:

$$\Omega^2_{r,lim} = \frac{1}{2}\left(\gamma_P^2 + (\gamma_a + \Gamma_a)^2\right) \tag{3.29}$$

For $\Omega_r > \Omega_{r,lim}$, two modes are solutions of the system. It is not strictly the condition found

for the springs by the evaluation of Eq. 3.14, but actually a more demanding requirement: when this new criterium is verified, there necessarily are two non degenerate solutions to the CMT system. Contrarily, depending on the value of the losses, the two peaks will not always be resolved because of the losses.

3.3 Parametric study of empty cavities

Before delving into the optimization and fabrication of devices, we need to evaluate the quantities at play. In order to understand the role of the different parameters on the electromagnetical properties, we will begin with a resonator filled with a bulk undoped semiconductor. This approach will allow us to evaluate the intrinsic losses of the cavities. We performed an extensive parametric study, tackling periodicity, width and thickness of the resonators without active region. The goal of this study is to link radiative and non radiative losses with the resonator geometrical parameters, in order to be able to design more efficient structures for cavity optoelectronic devices.

3.3.1 CMT for an empty cavity

In Eq. 3.25, we remove the oscillator P. Because we will consider arrays of resonators with a periodicity sometimes larger than the wavelength, diffraction can occur and it needs to be taken into consideration in the equations. We associate radiative losses Γ_d^k to each *k-th* diffracted order S_{out}^k. The CMT (Eq.3.25) writes:

$$\begin{aligned}
\frac{da}{dt} &= i\omega_a a - (\gamma_a + \Gamma_a + \sum_k \Gamma_d^k)a + \sqrt{2\Gamma_a}S_{in} \\
S_{out} &= -S_{in} + \sqrt{2\Gamma_a}a \\
S_{out}^k &= \sqrt{2\Gamma_d^k}a
\end{aligned} \tag{3.30}$$

By solving this system of equations, we retrieve the reflectivity R in the specular direction:

$$R(\omega) = \frac{|S_{out}|^2}{|S_{in}|^2} = \frac{(\Gamma_a - \gamma_a - \sum_k \Gamma_d^k)^2 + (\omega - \omega_a)^2}{(\Gamma_a + \gamma_a + \sum_k \Gamma_d^k)^2 + (\omega - \omega_a)^2} \tag{3.31}$$

A typical reflectivity spectrum is plotted in Fig.3.6 with its Lorentzian fit. The full width at half the maximum (FWHM) 2Γ and the contrast $C = 1 - R(\omega_a)$ are also shown. These two easily accessible quantities will help us determine the losses. Indeed, from the expression of the reflectivity Eq. 3.31 we derive:

$$\begin{aligned}
\Gamma &= \Gamma_a + \gamma_a + \sum_k \Gamma_d^k \\
C = 1 - R(\omega_a) &= 4\frac{\Gamma_a \gamma_a \sum_k \Gamma_d^k}{(\Gamma_a + \gamma_a + \sum_k \Gamma_d^k)^2} = 4\frac{\gamma_a \Gamma_a \sum_k \Gamma_d^k}{\Gamma^2}
\end{aligned} \tag{3.32}$$

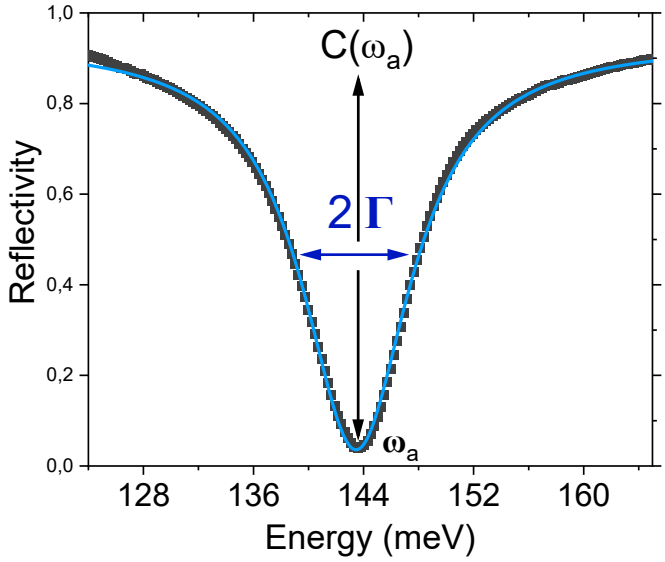

Fig. 3.6 *Reflectivity spectrum of a GaAs patch resonator (black points) and Lorentzian fit (in blue). Full width at half the maximum* 2Γ *and contrast* C *are indicated. From [101].*

From these two equations we are able to find γ_a and Γ_a as long as there is no diffraction. In this case, this imposes a limit on the periodicities accessible as we will see in the following. In particular, it appears that the contrast is maximal and equal to 1 when the radiative losses equate the non radiative ones. This condition is called critical coupling and is met for a perfect absorber: all the light is coupled into the cavity, and it is completely dissipated inside of it.

3.3.2 Experimental setup and samples

For processing reasons we chose to perform this study using a GaAs substrate. Indeed, the physical etching necessary to realize the cavities was considered routine in the clean room facility for this material, whereas the etching of Indium-containing semiconductors was much more challenging, especially for thick structures. To fabricate the different arrays of cavities, we used a sampled composed of 300 nm of Al-rich AlGaAs (etch stop) and different thicknesses H bulk GaAs: 570 nm, 1020 nm and 1710 nm. To make the thinner structures, we started by etching the GaAs layer before the substrate transfer. After having reported the GaAs structure covered by a thick Ti/Au layer on a new GaAs host wafer using epoxy glue (Epotek 353ND), we removed mechanically and then chemically the former substrate using citric acid down to the AlGaAs layer. Then using HF, we selectively removed the etch-stop. Ti/Au patches were patterned on GaAs using e-beam lithography, and then etched using a Cl-based Inductively Coupled Plasma (ICP) etching method, down to the ground gold layer. Eventually, we end up with a GaAs layer embedded in two metallic layers forming a microcavity.

The metamaterial and the setup used for our study are presented in Fig.3.7. Panel (a) presents a sketch of our experiment. The infrared radiation from the globar of the FTIR is

sent into a reflection unit which, coupled to an external Mercury Cadmium Telluride (MCT) detector, allows specular reflection measurements at an incidence angle $\theta = 15°$. Reflectivity spectra are performed for incident p- (the electric field is parallel to the incidence plane) or o- (the electric field is orthogonal to the incidence plane) polarized light.

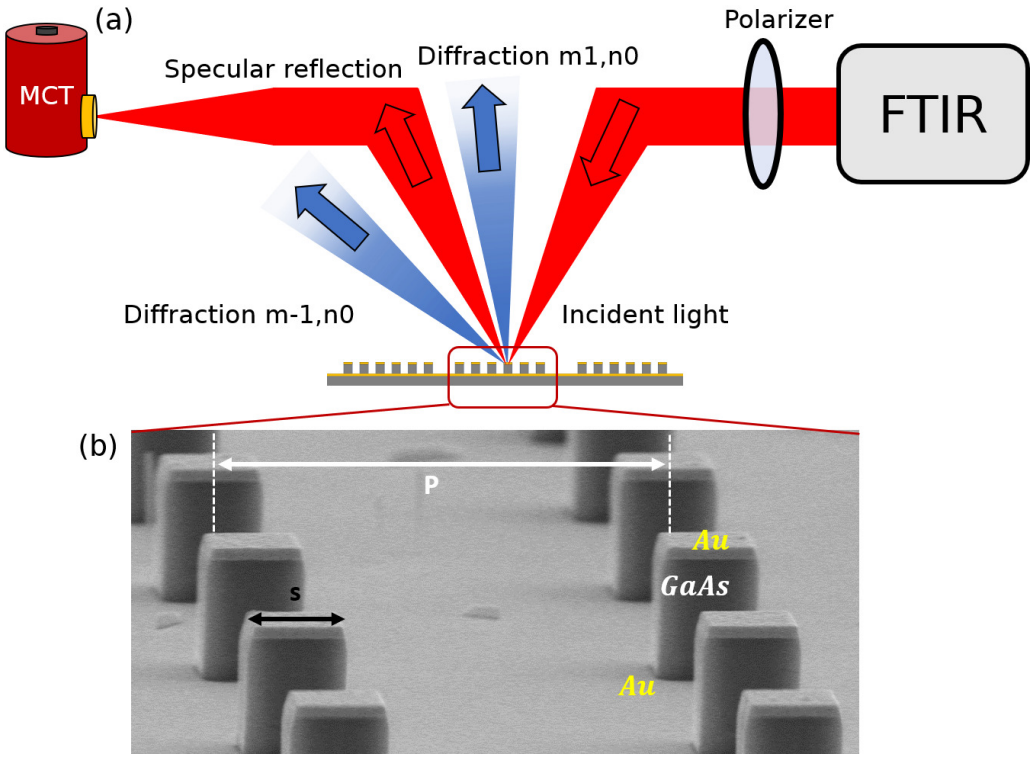

Fig. 3.7 *(a) Schematic representation of reflectivity measurements, the polarized incident light is focused on an array of patch antennas and the specular reflection is collected by an external MCT detector. (b) SEM picture of one array of patch antennas. The main geometrical parameters of the cavities and arrays are represented in the picture. From [101].*

A scanning electron microscope (SEM) image of one of the samples is shown in Fig.3.7 (b). It consists of a GaAs layer with thickness H, sandwiched between a metallic ground plane and a square metallic patch of width $s = 1.35$ µm. We made millimeter-large two-dimensional arrays of patches with period p to make sure that we would be able to focus all the incoming light from the FTIR. For periods greater than the wavelength, in addition to the specular reflection, diffracted orders represented by the blue arrows in Fig.3.7 (a) can propagate as well. The width s of the patches was set to sustain the fundamental mode of the cavity $TM_{0,1,0}$ around the energy $E_{010} = \dfrac{hc}{2n_{eff}s} = 140$ meV.

Spectra from 90 meV to 250 meV obtained for $H = 570$ nm and various periodicities ($p = 3$, 4.5, 5.5, 6.5 µm) are shown in Fig.3.8. The lower energy mode observed in these spectra close to 140 meV for every periodicity is the fundamental mode $TM_{0,1}$ of the cavity. It does not change with polarization. The energy of the absorption resonance, knowing the size $s = 1.35$ µm of the cavity, allows us to retrieve the effective mode index $n_{eff} = \lambda/(2s) = 3.21$. This value is actually slightly lower than that of the refractive index of bulk GaAs, $n = 3.28$

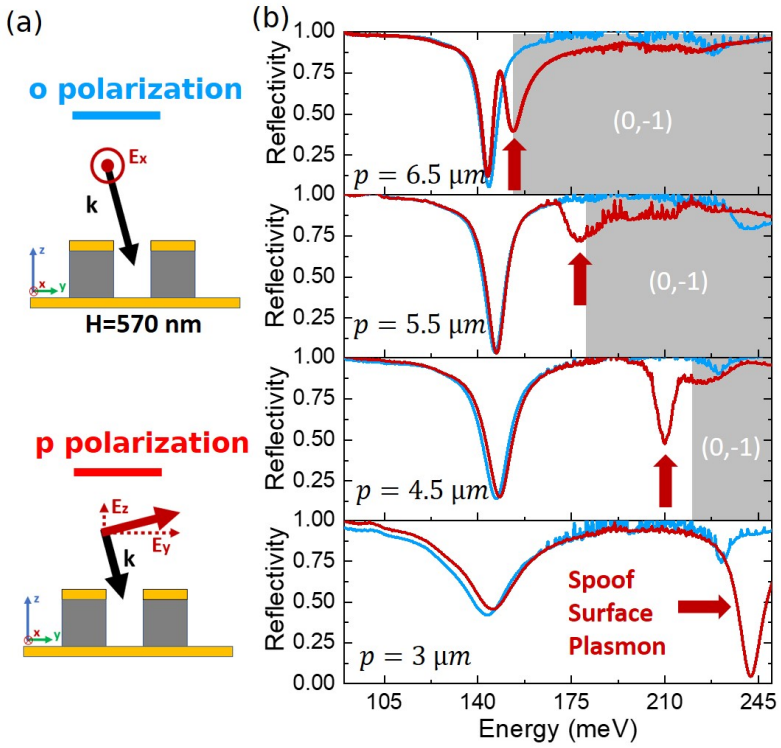

Fig. 3.8 *(a) Schematics of the incident electric field components for experiments in o-polarization (E-field perpendicular to the plane of incidence) and p-polarization (E-field contained in the plane of incidence). (b) Comparison of experimental reflectivity spectra for o- (solid blue line) and p- (solid red line) polarized incident light for different periodicities for a patch height $H = 570$ nm. The red thick arrow indicates the energy position of the spoof surface plasmon. The grey area indicates the onset of the $(0, -1)$ diffraction order according to Eq. 3.33. From [101].*

at this wavelength [102]. The fact that these values are so close indicates that the geometrical overlap of the mode with the patch is close to 1. The width of the absorption on the other hand strongly decreases with the periodicity p, while the contrast increases with p form $p = 3$ to $p = 5.5$ μm.

On the spectra another striking feature can be noted: a second peak is visible, only in the p-polarization, and dispersive with p. This mode is a spoof surface plasmon. A surface plasmon is a mode confined at the interface between a metal and a dielectric by coherent oscillations of free electrons. At a simple interface, this mode should not couple with free space radiation because its dispersion relation reads $E = \hbar c k_{\|} \sqrt{\frac{1}{\varepsilon_m} + \frac{1}{\varepsilon_1}}$ (with $k_{\|}$ the wavevector of the light along the surface, ε_m the dielectric constant of the metal and ε_1 that of the dielectric), and is always strictly below the light line $E_0 = \hbar c k_y \sqrt{\frac{1}{\epsilon_0}}$. However, as described in [103], in the presence of diffraction, newly accessible wavevectors allow such coupling. According to the diffraction grating formula, diffraction occurs at the angle θ_r for light impinging at angle θ_i at a wavelength λ on a grating of period p following:

$$\sin(\theta_i) - \sin(\theta_r) = n\frac{\lambda}{p} \tag{3.33}$$

with $n \in \mathbb{Z}$.

In order to avoid diffraction effects, we work at wavelengths smaller than $\lambda_{threshold} = p(1 + \sin(\theta_i))$. On Fig.3.8, this diffraction threshold is indicated in grey on the right part of the spectra. The surface plasmon is not excited by a o-polarized incident radiation. For the rest of this study, we will only consider o-polarized light to disregard spoof surface plasmon contributions, and be able to study the fundamental mode of the cavity.

3.3.3 Experimental spectra and numerical simulations

Reflectivity spectra for three periodicities (p=3, 5.5 and 8 µm) and the three values of H are shown on Fig.3.9 in blue. Our experimental setup allows only for the collection of the specular light. The experimental results were compared to those of numerical simulations (in red in Fig.3.9), performed by E. Rodriguez with a commercial finite-element simulation software (COMSOL Multiphysics). In order to simulate the reflectivity spectra in the same geometry

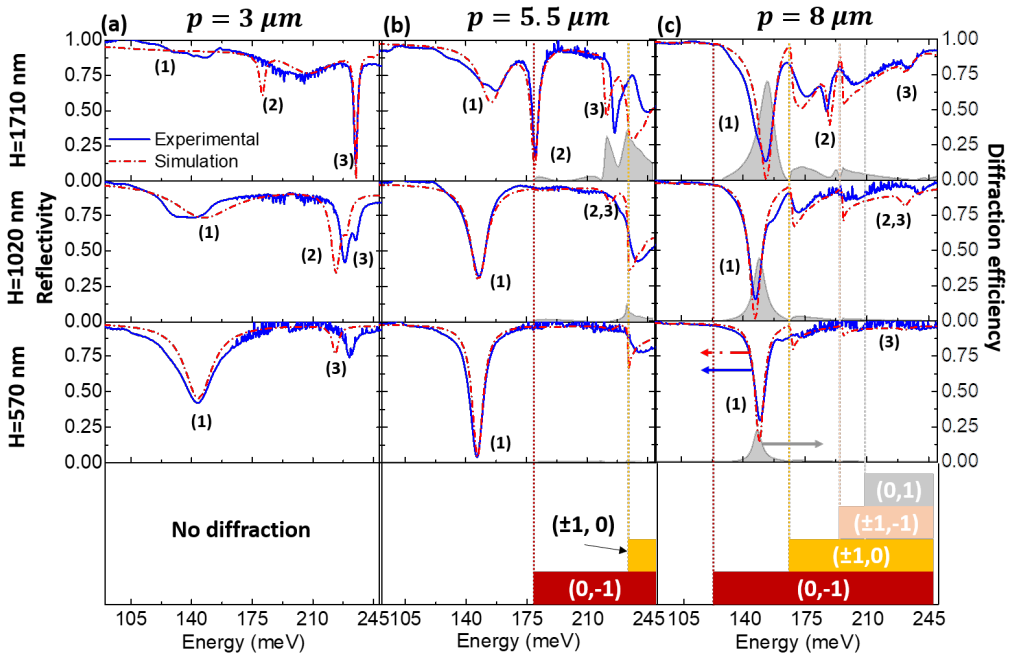

Fig. 3.9 *Experimental and simulated specular reflectivity spectra plotted respectively in solid blue and dashed red lines with a periodicity of 3 µm (a), 5.5 µm (b) and 8 µm (c) for incident o-polarized light. The grey filled area is the diffraction efficiency. The resonant cavity modes are indicated on the reflectivity spectra by (1), (2) and (3). The bottom panel indicates the energy range of existence of the different diffraction orders for the considered periods. From [101].*

as our experiments, we use an incident beam in the (x, z)-plane, with an angle $\theta = 15°$ with respect to the z-axis, and only the specular light is plotted in red. These simulations make possible for us to unambiguously identify the modes of the cavity: (1) is the TM_{010}, (2) is the TM_{011}, and (3) is the TM_{110}. For high periodicities, the diffraction efficiency in the various directions is also plotted in grey. This corresponds to the sum of the power in every direction but the specular one, divided by the incident power. The threshold for the appearance of

each diffraction order is displayed in the fourth row of the figure.

Spectra are very well reproduced by our simulations, as shown in Fig.3.9. This helps us discriminating the power absorbed by the cavity, from that diffracted in a different direction in space and not collected by the MCT detector. To match the experimental data, the values of the non-radiative losses in the top and bottom metallic layers have been increased by a factor of four with respect to those given in Ordal [104]. Indeed, ohmic losses are the only source of non radiative losses in the simulation, whereas experimentally we also have scattering at the (rough) vertical sidewalls, higher losses in the Ti adhesion layer which absorbs more the gold [105], and non radiative losses in the semiconductor.

Fig.3.10 shows the values of Γ and C extracted from the resonance associated with the $TM_{0,1,0}$ mode in all the measured spectra (in blue). We observe that the absorption line strongly narrows with the periodicity p. Moreover, the critical coupling (characterized a contrast of 1) is reached at higher values of p for thicker samples. The simulated spectra measured and the extracted values of Γ and C are plotted in red on the same graph for comparison and yield very close result.

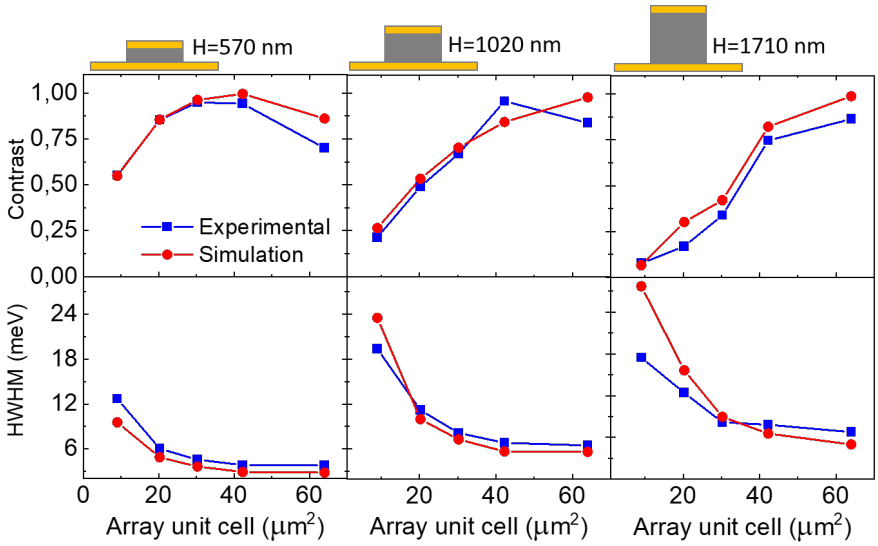

Fig. 3.10 *a) Study of the contrast (top) and HWHM (bottom) as a function of the array unit cell for a height of (a) 570 nm, (b) 1020 nm and (c) 1710 nm. The blue lines - squares present the parameters extracted from the measured spectra, while the red lines - circles show the values extracted from the simulated spectra.*

3.3.4 Analysis and conclusions

From now on, all the losses will be expressed in meV.

In Fig.3.11 (a), (b) and (c), we plot for each periodicity and thicknesses the radiative losses, the non radiative losses, and the diffraction losses (in blue the experimental data, in red the simulated ones). In (d), an experimental spectrum ($p = 6.5\mu$m, $H = 1020$ nm) in black is compared with the corresponding simulated one in dashed yellow. The blue dashed line is a simulated spectrum which includes specular reflection plus the three diffraction orders

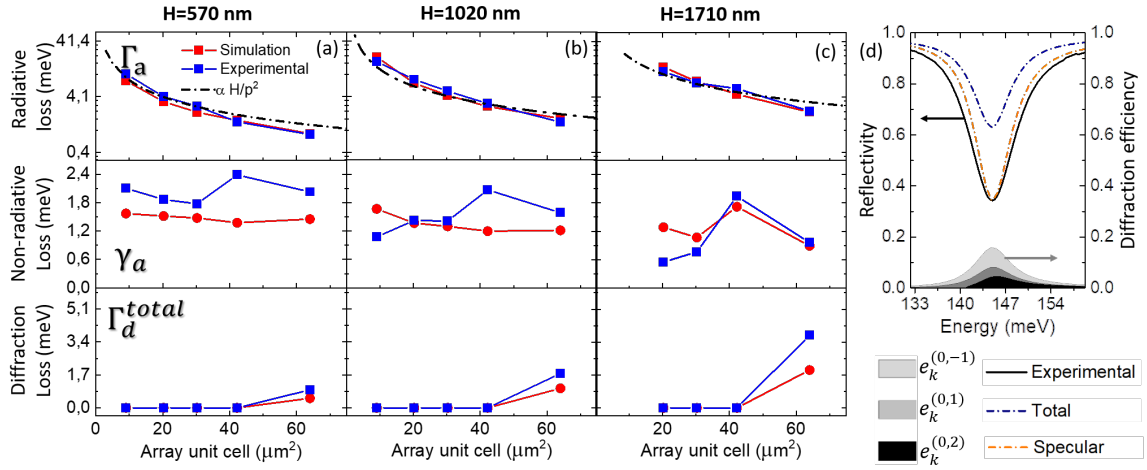

Fig. 3.11 *Radiative, non radiative and diffraction loss extracted from experimental spectra (in blue) and corresponding simulations (in red) for heights 570 nm(a), 1020 nm (b) and 1710 nm (c). The black dashed line is obtained by fitting the data with the function $\alpha.H/p^2$, α a fitting parameter. In (d) the contribution of the different refractive orders are separated and highlighted.*

present at this periodicity. The grey filled spectra represent the normalized power that goes in the different diffraction orders. The excellent agreement between the data and the simulated specular reflectivity proves that in our experiment only the 0th order is collected.

In the expressions of C and Γ (Eq 3.32), Γ_a and γ_a play a perfectly symmetric role. In order to be able to distinguish their contributions from the spectra, we consider a continuous evolution and study the extreme cases. The array of patches has been described in the literature [106, 42] as an array of radiating slots, whose individual radiated power in the far field is calculated in [96]. The calculation yields a dependence of the radiative losses Γ_a of the system scaling as $\frac{1}{p^2}$. Assuming such dependency helped us discriminating between radiative and non-radiative losses.

In Fig.3.11, the radiative losses are fitted in black with the function $\alpha.H/p^2$, with α a fitting parameter. For each thickness, $\alpha = (35 \pm 2)$ meV.µm, showing the proportionality between the radiative losses and H/p^2.

On the other hand, the non-radiative losses appear to be constant with the periodicity but decrease slightly with the height. Finally, the diffraction losses are null until the diffraction threshold (Eq 3.33).

The analysis of the spectra for different geometries allowed us to measure the quantities of the CMT related to the cavity only and to draw conclusions as to the strategies for designing a metamaterial:

- the non-radiative losses are constant with the periodicity,
- the non-radiative losses decrease slowly as the height increases, likely due to the fact that the penetration of the electric field into the lossy metallic layers is decreased [107],
- the radiative losses decrease quickly as $1/p^2$. Approximate analytical description of the

far field emitted power of arrays of radiating slots can be found in [42, 106] and confirms this trend,

- radiative losses vary linearly with H. That is the manifestation of the fact that the patch antennas are aperture antennas, where the radiation apertures are the two openings with an area $\propto s \cdot H$,
- Below the diffraction threshold, no diffraction occurs but, above threshold, diffraction losses can very quickly become larger than the non radiative losses and should be avoided.

In conclusion, we have identified the leverages available for the design of cavity metamaterials. Remembering that a critical coupling is the situation where the different losses equate, the most convenient way of proceeding for a given active region is to play with the periodicity to tune the radiative losses to the fixed non radiative losses, keeping in mind that the upper limit is set by the diffraction. For the design of a new active region, the height of the cavity can be a new degree of freedom to optimize the absorption into the cavity.
When introducing an active region in the cavity, it must be taken into account that a new source of non-radiative losses is added in the system with the intersubband absorption, γ_P, that will modify this balance. Depending on the device we want to design, different strategies must be considered and will be detailed in the next section.

3.4 Design strategies for optoelectronic devices: detectors and modulators

Thanks to the parametric study of the empty cavities, we have extracted the relevant parameters related to our cavities. The other parameters necessary for numerical optimization and estimations of the possible performances of the future devices are related to the active regions involved: we need ω_P, γ_P and Ω_r. As previously, these quantities will be expressed as energies, implying the prefactor $\hbar$ to simplify notations.
ω_P and γ_P can be deduced from an absorption spectrum, with the energy of the absorption peak ($E_{abs} = \hbar\omega_P$) and its broadening (γ_P =FWHM). $2\Omega_r = \sqrt{\frac{f_w f_{12} e^2 n_{2D}}{\varepsilon_r \varepsilon_0 m^* L_{eff}}}$ can be calculated knowing the doping, the dimension of the quantum well, the oscillator strength of the transition involved and the total thickness of the structure.

3.4.1 Detectors

a) QCD

Internal quantum efficiency

The main quantity we will want to optimize for a detector, that limited us in Chapter 2 for data transmission, is the responsivity. The responsivity reads $R = \eta_{abs} p_{esc} \frac{e\lambda}{N_{qw} hc}$. Here

we actually focus on the absorption quantum efficiency η_{abs}, the number of photoexcited electrons per photon impinging on the structure. This is exactly A_{isb} in the CMT in Eq. 3.28. We are only considering the coupling with the light, with a fixed design of the active region, that defines p_e. Assuming a cavity resonant with the ISB absorption ($\omega_a = \omega_P$), we can simplify Eq. 3.28:

$$A_{isb}(\omega = \omega_a = \omega_P) = \frac{4\gamma_P \Gamma_a \Omega_r^2}{\left[\gamma_P\left(\gamma_a + \Gamma_a\right) + \Omega_r^2\right]^2} = \frac{4\gamma_{isb}\Gamma_a}{\left[\gamma_a + \Gamma_a + \gamma_{isb}\right]^2} \tag{3.34}$$

Where $\gamma_{isb} = \dfrac{\Omega_r^2}{\gamma_P}$. We have shown in the previous section that the non radiative losses of the cavity γ_a are the less sensitive parameter with respect to a variation of the periodicity, and $\gamma_P \simeq 2$ meV. Nevertheless, A_{isb} is strictly decreasing with γ_a and non radiative losses should be as low as possible. Fig.3.12 (a) shows the evolution of A_{isb} as a function of Γ_a and γ_{isb} for a fixed $\gamma_a = 2$ meV.

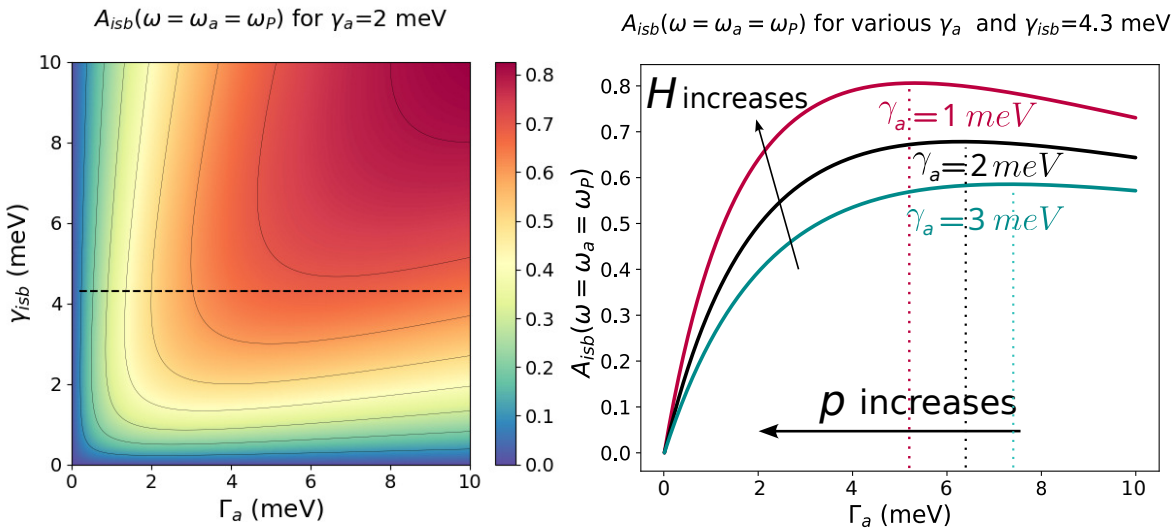

Fig. 3.12 *(a) Colorplot of A_{isb} plotted at resonance as a function of Γ_a and γ_{isb} for a fixed $\gamma_a = 2$ meV. (b) Cut of A_{isb} along $\gamma_{isb} = 4.3$ meV for various γ_a. The case $\gamma_a = 2$ meV corresponds to the dashed black line in (a). A maximum is reached for $\Gamma_a = \gamma_{isb} + \gamma_a$.*

For a given quantum well, γ_{isb} is fixed. Γ_a, through a change of periodicity p should be chosen to maximize A_{isb} following:

$$\frac{\partial A_{isb}}{\partial \Gamma_a} = 0 \Leftrightarrow \Gamma_a = \gamma_{isb} + \gamma_a \tag{3.35}$$

Fig.3.12 (b) displays the case $\gamma_{isb} = 4.3$ meV and $\gamma_a = [1, 2, 3]$ meV, and we can indeed see that the maximum absorption quantum efficiency is reached for $\Gamma_a = [5.3, 6.3, 7.3]$ meV respectively. Eq. 3.35 formally looks like the critical coupling condition of an empty cavity, with the introduction of a new non-radiative losses source. Nevertheless, A_{isb} will always be strictly inferior to unity for non-zero γ_a. But looking at the complete absorption of the

system:

$$A_{tot}(\omega = \omega_a = \omega_P) = A_{isb} + A_{cav} = \frac{4\gamma_a\Gamma_a}{[\gamma_a + \Gamma_a + \gamma_{isb}]^2} + \frac{4\gamma_{isb}\Gamma_a}{[\gamma_a + \Gamma_a + \gamma_{isb}]^2}$$
$$\Rightarrow A_{tot}(\omega = \omega_a = \omega_P) = \frac{4(\gamma_{isb} + \gamma_a)\Gamma_a}{[\gamma_a + \Gamma_a + \gamma_{isb}]^2} \tag{3.36}$$

We find that the conditions for A_{isb} and A_{tot} to be maximum are the same: $\Gamma_a = \gamma_{isb} + \gamma_a$. For these values, $A_{tot,crit} = 1$ but $A_{isb,crit} = \frac{\gamma_{isb}}{\gamma_{isb} + \gamma_a}$.

Fig.3.13 summarizes up the repartition of the power dissipated in the system: (a) and (b) show the dissipation in the cavity and in the ISB transition, respectively, around the resonance energy, with $\omega_a = \omega_P$. (c) displays the total absorption of the system, the sum of (a) and (b), while (d) presents the dissipation in the same cavity but without the ISB transition (doping has been set to zero). A_{isb} and A_{tot} share the same maximum position in

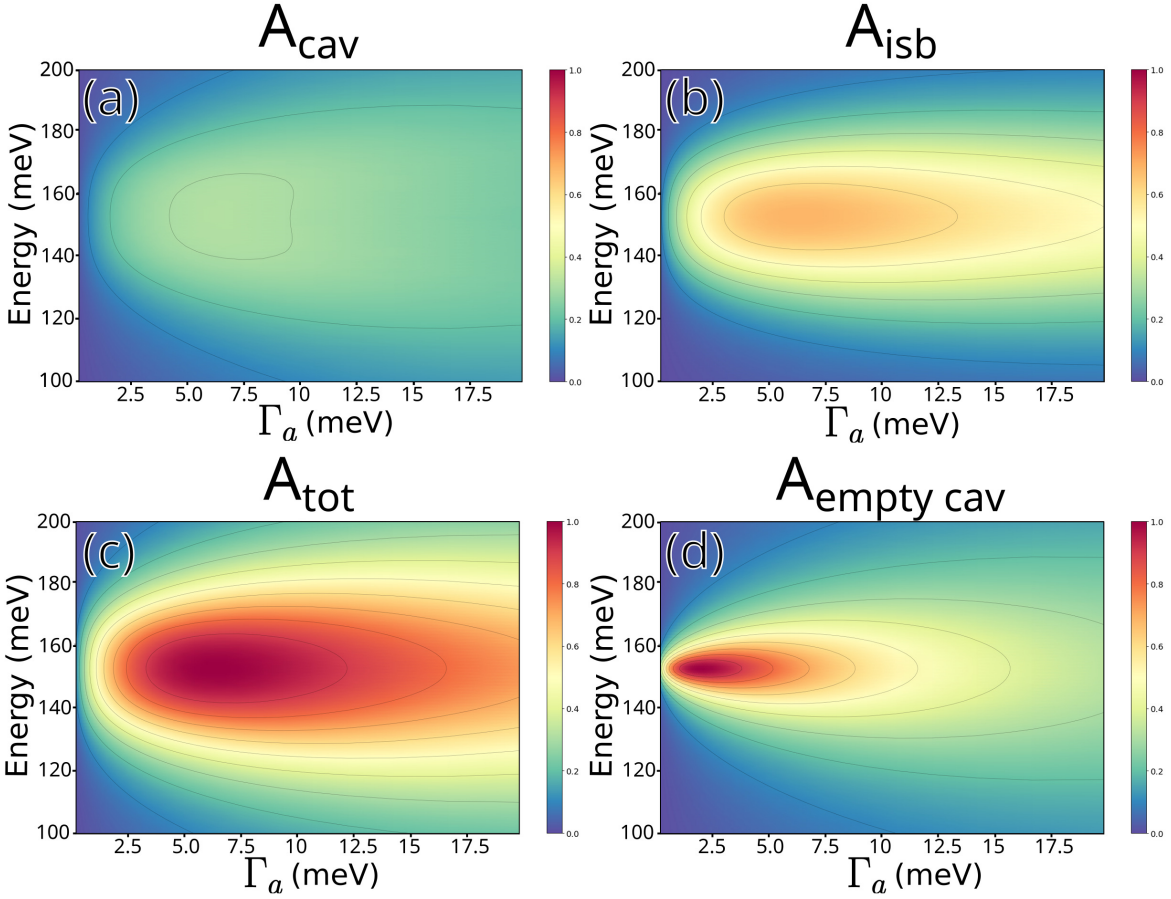

Fig. 3.13 *Partition of the power dissipation in a typical cavity with a QCD embedded ($\gamma_a = 2$ meV, $\gamma_{isb} = 4.3$ meV). (a) Non radiative absorption by the cavity. (b) Non radiative absorption by the ISB transition. (c) Total absorption of the system. (d) Absorption by the same cavity without quantum wells.*

the (Energy/Γ_a)-space, which can be mapped to the (s,p)-space, but not $A_{empty\ cav}$. This means, in term of workflow of the optimization of a metamaterial for a given heterostructure, that it is correct to optimize the reflection of an array of cavities by testing different sizes

and periodicities in order to optimize the ISB absorption for a weak coupling detector.

The value of γ_{isb} was estimated from the values expected for the diagonal QCD presented at the end of Chapter 2, with a doping of 10^{18} cm^{-3} for the absorbing wells. Diagonal QCDs have rather large values γ_P in the order of 15 meV, and oscillator strength lower than their vertical counterpart, around $f_{12} = 0.65$. Nominal doping is $1e18$ cm^{-3}, filling fraction of the active region $f_w = 0.15$. Altogether, this yields $\Omega_r \simeq 8$ meV and $\gamma_{isb} \simeq 4.3$ meV. These losses cannot allow strong coupling according to Eq. 3.29 since we have:

$$\Omega_r^2 < \frac{1}{2}\gamma_P^2 < \frac{1}{2}\left(\gamma_P^2 + (\gamma_a + \Gamma_a)^2\right) = \Omega_{r,lim}^2 \tag{3.37}$$

In other words, for diagonal QCD, no matter the parameters chosen for the cavity, strong coupling is unreachable. This assures us that we can safely maximize the interaction without having the emergence of the strong coupling, that would shift the position of the maximum absorption.

In conclusion, optimizing the cavity for a high quantum efficiency absorption for a diagonal QCD means having as low non radiative cavity losses γ_a as possible, and matching the radiative losses to the total non radiative losses $\gamma_{isb} + \gamma_a = \frac{\Omega_r^2}{\gamma_P} + \gamma_a$, while having high Γ_a and γ_{isb}. This advocates for rather dense resonators ($p \leq 4\,\mu$m), highly doped and thick structures.

Responsivity, bandwidth and thickness

For QCDs, increasing the height means increasing the number of periods, which will be detrimental for the internal extraction efficiency $\eta_{int} \propto \frac{1}{N_{qw}}$, limiting the overall responsivity. The positive impact of increasing H on γ_a and subsequently A_{isb} will not balance this effect. On the contrary, the bandwidth of the detector linearly increases with the thickness of the active region [89], making the number of period pivotal in a trade-off between bandwidth and responsivity, both essential for data transmission with free space optical links.

Vertical QCDs

Not considered in this work, it appears though that vertical QCDs, with higher oscillator strength and lower γ_P, would benefit more from the cavity than diagonal QCDs. They could even, as shown in [108], display strong coupling. The same behavior is expected for QWIPs, also with vertical transitions.

b) QWIPs

In the idea of increasing the responsivity of our devices, we also decided to investigate QWIPs, which have shown much higher responsivities [47] than QCDs, at the expense of an increased dark current.

Everything mentioned for the optimization of QCDs in the weak coupling regime stands for QWIPs, but it now becomes possible to also explore the strong coupling regime. Assuming

realistic values of $\Omega_r = 8$ meV, $\gamma_P = 8$ meV, $\gamma_a = 2$ meV, Fig.3.14 shows the calculated ISB absorption spectra according to the CMT as a function of Γ_a. Below $\Gamma_a = 6.5$ meV, the spectra split into two peaks, which is the signature of the strong coupling regime as defined in section 3.2.4.

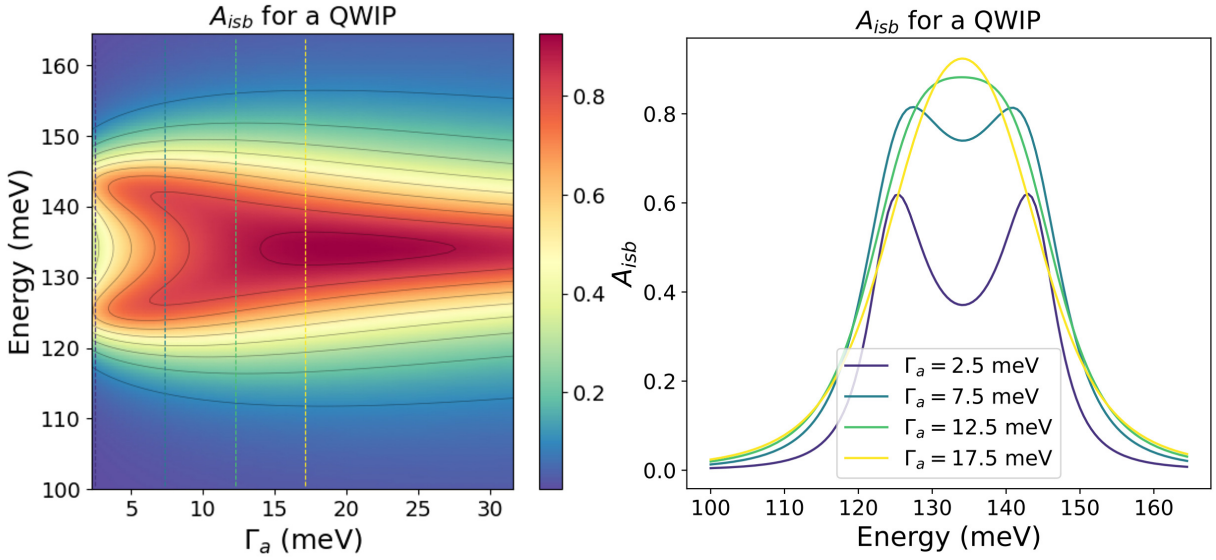

Fig. 3.14 *(left) Colorplot of A_{isb} plotted at resonance for a QWIP as a function of the energy. Decreasing the radiative losses eventually lead to the strong coupling regime where we see the intersubband spectrum split into two peaks. (right) Corresponding absorption spectra for selected Γ_a.*

The maximum value of A_{isb} beyond the threshold of strong coupling can be calculated for $\omega_P = \omega_a$ as:

$$A_{isb,SC,max}(\omega_P = \omega_a) = \frac{4\gamma_P \Gamma_a \Omega_r^2}{(\gamma_a + \gamma_P + \Gamma_a)^2 \left[\Omega_r^2 - \frac{1}{4}(\gamma_P - \gamma_a - \Gamma_a)^2\right]} \tag{3.38}$$

$A_{isb,SC,max}(\omega_P = \omega_a)$ is a monotonously increasing function of Γ_a and Ω_r. Going further into the strong coupling regime (by increasing p) will only lead to a poorer absorption quantum efficiency, so strong-coupling is not a desired feature for a detector with high absorption quantum efficiency. Increasing Ω_r via the doping will increase the absorption but the radiative losses should be matched to stay in the weak coupling regime.
Nevertheless, it appears that our platform easily allows an excursion in the strong coupling regime through a simple change of periodicity of the metamaterial.

Finally, it becomes also possible in QWIPs to change the thickness H of the patch without changing the number of wells by changing the thickness of the barriers between the wells: the filling fraction of the quantum wells in the total thickness is then modified. In the model, the filling fraction is identified with f_w since we consider that the geometrical overlap of the cavity mode with the resonator volume is equal to 1. Fig.3.15 illustrates the impact of this new degree of freedom: in the left column the number of wells is kept constant while the thickness varies (a,c), and in the right column the filling fraction is fixed (b,d). The

first line illustrates the evolution of the absorption quantum efficiency while the second line shows the responsivity associated, assuming a transport of the photoexcited electrons where $p_e = p_c = 1$ i.e. photoconductive gain considered equal to $1/N_{QW}$ as it is often considered at room temperature [35]. For very dense active regions (fixed number of QWs(a,c), low thickness) the system enters again the strong coupling regime because Ω_r increases while Γ_a decreases. On the contrary, a change in the radiative losses only, with Ω_r constant is not sufficient to reach the strong coupling regime, as seen on the right (b,d). It appears that the best responsivities are as expected to be reached for a low number of quantum wells because of the $1/N_{QW}$ dependence of the photoconductive gain. The important takeaway is that, contrarily to the mesa case, the responsivity is no longer independent on the number of periods, since the absorption is not proportional to the number of wells. N_{qw} should therefore be considered when optimizing metamaterial detectors. In [47], the authors fabricated a metamaterial QWIP with a single quantum well and showed the record responsivity of 3.3 mA/W at 78 K and 6.8 µm.

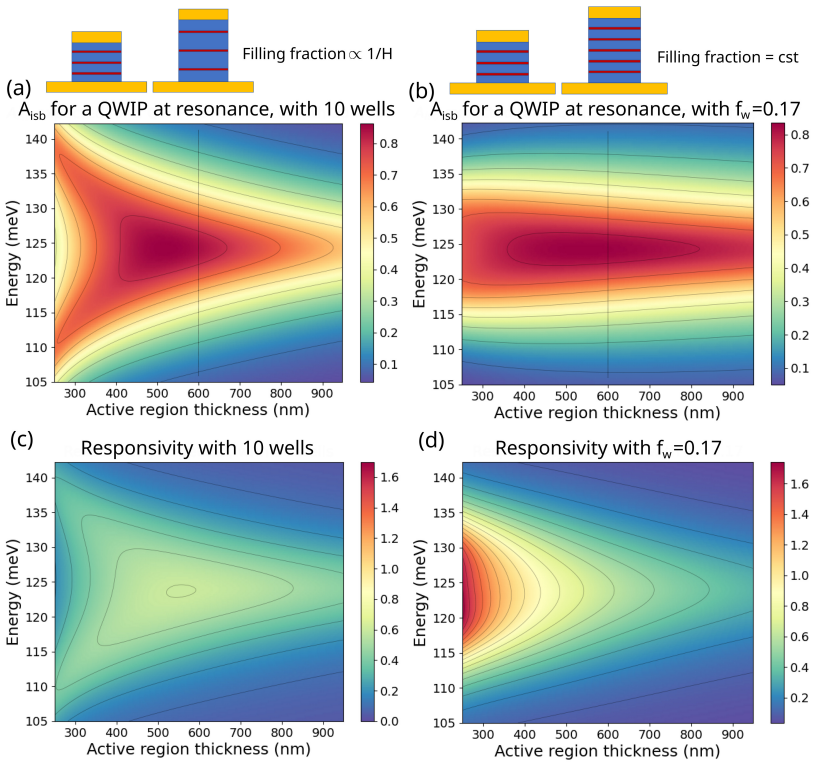

Fig. 3.15 *(a) Colorplot of A_{isb} plotted at resonance for a QWIP as a function of the height while considering the number of active wells constant, effectively lowering the filling fraction. (b) Colorplot of A_{isb} plotted at resonance for a QWIP as a function of the height while considering the filling fraction constant. The plots are continuous for simplicity though in reality they could only be discrete with an integer number of wells. In both cases, Γ_a and γ_a are affected by the thickness according to the conclusions of section 3. Along the black dashed line, both colorplot have the same values of A_{isb} since they have the same filling fraction.(c) and (d) Responsivities calculated assuming a photoconductive gain equal to $1/N_{QW}$.*

Nevertheless, reducing drastically the number of wells comes at a cost since it will re-

duce the resistivity of the device, increasing the dark current and the Johnson noise. The bandwidth will also be limited by the decreased thickness.

c) Conclusions on the design of metamaterials for photodetection

From the previous considerations, we can identify the main optimization rules for metamaterial photodetectors.

- The lateral size s of the resonators should be used to set the resonant energy of the cavity considering effective index.
- The increase of the thickness H will positively impact the bandwidth, at the expanse of the responsivity. This drawback can be partially mitigated by decreasing the filling fraction, by increasing the width of barriers for QWIPs, or in a smaller extent by increasing the size of the extractor for QCDs. It should be noted that we did not take into account in this discussion the possible decrease of the geometrical overlap of the cavity mode with the resonator as H gets thicker.
- The periodicity p is the main and last fabrication parameter to be considered. It should be chosen as to optimize the radiative losses with respect to the other losses in the system, defined by the doping, filling fraction and thickness.

3.4.2 Modulators

Optimizing the Stark modulator consists in making the total absorption of the device as sensitive to the bias as possible. Without cavity, we can model the modulator as a bias-sensitive absorber, where the center of the Gaussian absorption spectrum linearly shifts with the bias. Modelling the Stark modulator embedded in a resonator will require the CMT. We will now be looking at:

$$A = A_{cav} + A_{isb} = 2\gamma_a \frac{|\mathbf{a}|^2}{|S_{in}|^2} + 2\gamma_P \frac{|\mathbf{P}|^2}{|S_{in}|^2} \tag{3.39}$$

The effect of the Stark shift will now be to tune or detune the energy of the ISB absorption with respect of the resonator $TM_{0,1}$-mode's energy. Two limit situations can be considered, depending on the light-matter coupling regime in which the device operates. Fig.3.16 illustrates these two situations: first row for the weak coupling and second for the strong coupling. In the first row is presented reflectivity spectra of a cavity with large radiative losses and with a modulator active region displaying large γ_P, leading to the weak coupling regime. Panel (a) shows the reflectivity spectra in color intensity for each bias applied on a 700 nm-thick structure, while panel (b) summarizes limit cases. At zero bias, the cavity mode is resonant with the ISB absorption (plotted in red in (b)). At large negative or positive bias, the ISB transition is shifted far away and the reflectivity spectrum of the empty cavity is recovered (plotted in black in (b)). In that case, the laser should be at the same energy as the cavity

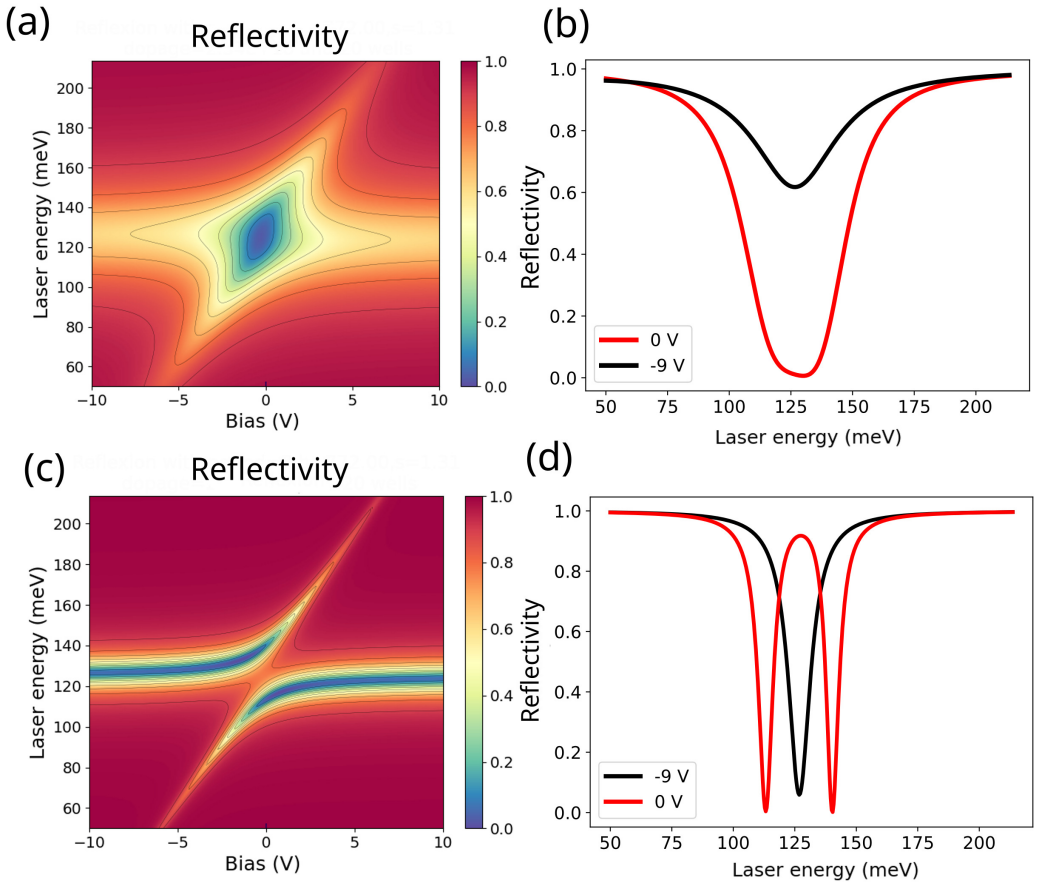

Fig. 3.16 *(a) Colorplot of the reflectivity as a function of the energy and the bias for a stark modulator in cavity, in the weak coupling regime. Losses were chosen arbitrarily. (b) Reflectivity spectra for 0 V and 9 V to illustrate the reflecting and absorbing states of the modulator. (c) and (d) Same as (a) and (b) but the radiative loss Γ_a and the ISB non radiative losses γ_P were decreased to reach the strong coupling regime. The value of γ_P, unrealistically low, was chosen for graphical clarity.*

mode. The contrast will be bound by the difference between these two values:

$$\Delta A_{tot,max} = A_{tot}(\omega = \omega_a = \omega_P) - A_{cav}(\omega = \omega_a) = \frac{4(\gamma_{isb} + \gamma_a)\Gamma_a}{[\gamma_a + \Gamma_a + \gamma_{isb}]^2} - \frac{4\gamma_a\Gamma_a}{[\gamma_a + \Gamma_a]^2} \tag{3.40}$$

The idea is therefore to start from a "bad" cavity, and reaching critical coupling when the ISB losses are added. It would be possible to also consider the opposite case, with an empty cavity at critical coupling, becoming overcoupled in presence the of the ISB losses. But this scenario, while staying in weak coupling, implies very low doping and therefore poor performances.

In the second row of Fig.3.16, a second cavity with lower radiative losses, and an active region with a smaller value of γ_P is considered. As we can see in (c) with the colors representing the reflectivity, the strong coupling regime is reached and the situation changes. When the energy of the ISB matches the cavity mode, the absorption splits into the polariton

branches. In (d) is compiled a choice of two spectra for different biases representing the ideal modulation in the strong coupling regime.

Unfortunately, for realistic values of the losses and linewidths, contrarily to the previous case, the splitting is not very pronounced and the maximal contrast is not necessarily reached when the resonator energy matches the laser's one. The key will be to have a large energy separation $\sqrt{\Delta}$ (from Eq. 3.28's resolution), with $\Delta = 4\Omega_r^2 - 2(\gamma_P^2 + (\Gamma_a + \gamma_a)^2)$, larger than the broadening corresponding to the empty cavity case. This calls for a highly doped active region with a thin ISB absorption line.
Regarding the cavity, the non radiative losses have a trivially negative impact, but the radiative losses have antagonistic effects. When reduced (by increasing the periodicity p), the detuned cavity will have a narrower absorption, but A_{isb} will be reduced (as in Fig.3.15). The maximum contrast then must be looked for by optimizing ω_a and Γ_a, i.e. the resonator size s and the periodicity p once the active region and the energy of interest are fixed. Fig.3.17 (a) summarizes the full picture of the search for the best metamaterial parameters for a Stark modulator based on the AC19 active region, for operations at 9 µm. For every relevant (p,s) couple, the figure shows the maximum contrast achievable within a range of accessible bias of ±5 V.

Three points (couples (s,p)) are chosen to give more details about the operation of the modulators. In panel (b), the reflection spectra for the parameters chosen are plotted. With parameters '1' ($p = 3.5\,\mu m\, s = 1.39\,\mu m$), we are close to the weak coupling case explained before, and the maximum absorption is reached when the cavity and the ISB are tuned Parameters '3' ($p = 7\,\mu m\, s = 1.2\,\mu m$) shows the best contrast achievable, as the splitting starts appearing. Note that the cavity in that case is not exactly tuned to the laser's energy. Finally, with parameters '2' ($p = 5.4\,\mu m\, s = 1.26\,\mu m$) we observe a contrast almost null when the laser and the cavity are tuned and the system is over-coupled. In panel (c), the simulated operation of these three samples at 9 µ, which also lets us see the minimal bias necessary for the modulation, the linearity and if a DC bias is necessary for operations.

For these simulations performed with realistic values, the strong coupling allows for superior contrasts and lower bias necessary to achieve it. Some general guidelines can be drawn for the optimization of Stark modulators:

- The lateral size s of the resonators should be used to set the resonant energy of the cavity, slightly detuned from the laser emission energy.
- Periodicity p should be chosen as to optimize the contrast in conjunction with s. All other things equal, choosing a large p will dilute the array, and furthermore improve the bandwidth. The upper limit for the value of p is set by the diffraction threshold.
- The thickness H will positively impact the bandwidth when increased. Though no transport is to be considered anymore, increasing H will increase the radiative losses and broaden the width of the cavity spectra. The decrease of the non radiative losses will not mitigate this significantly. The contrast will therefore be deteriorated. Moreover,

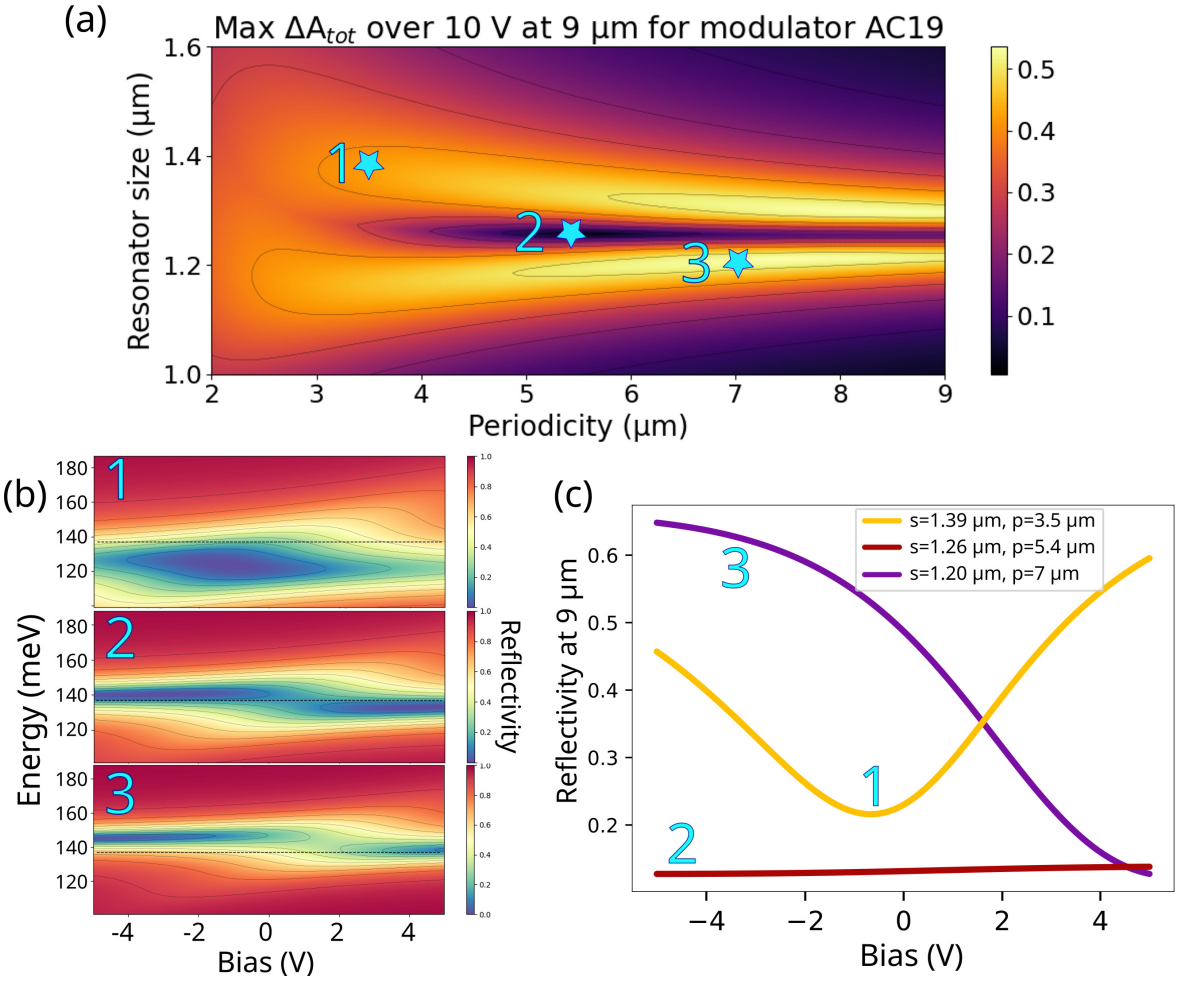

Fig. 3.17 *Optimization of a cavity for Stark modulators for the active region of AC19 modulator operating at 9 µm. (a) displays the maximum contrast accessible in a 10 V range. Three points are highlighted. (b) Reflection spectra of the devices corresponding to the three points for biases in ±5 V. (c) Operation of the three modulators at 9 µm as a function of the bias.*

a thick structure will require a higher operation bias, which means more amplification with high frequency signal generators typically able to deliver 1V on 50 Ω.

Regarding the active region, some conclusions can also be drawn:

- The doping should be as high as possible to increase the Rabi splitting Ω_r, as long as the losses are not deteriorated, and the Fermi level does not reach the second subband (even with bias).
- The barrier between two periods should not be too large as to keep a large filling fraction and a high Ω_r. Studies on QWIPs nevertheless showed that this barrier should be kept above 20 nm to limit interwell tunneling currents [34].

To conclude, the optimization of metamaterials for modulation is different from that of detectors though it plays on the same leverages to adjust the different losses. Here we will consider simply the "strongly-coupled" modulators, believed to be more promising. Quotation

marks are used because these devices do not verify the strong coupling criteria presented at the beginning of the chapter, but take advantage of the anticrossing of the resonances nevertheless.
With respect to the mesa structures, we should obtain devices with a smaller electrical area and therefore a larger bandwidth, and a large modulation accessible with less bias applied on the structure. Moreover, the normal incidence operation allows to significantly reduce the power loss due to reflection on the facets in the mesa case. This makes the metamaterial Stark modulator a very promising candidate for a MIR external modulator.

3.5 Fabrication of InGaAs/InAlAs high-speed metamaterial

3.5.1 Introduction

The objective of this work is to realize InP based optoelectronic devices. One of the challenges faced was to adapt the processes developed on GaAs as in Fig.3.18 [35] to this material system.

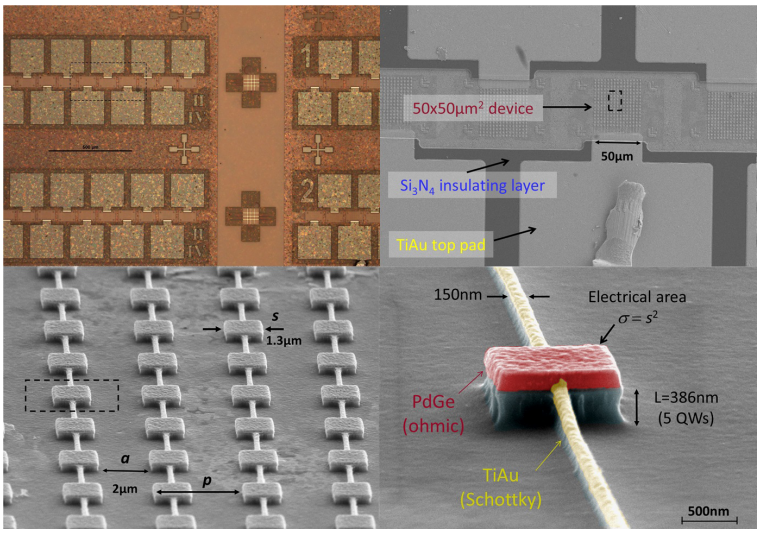

Fig. 3.18 *Different zooms of the GaAs patch cavities from Daniele Palaferri's Ph.D. thesis [35]. The etched patch cavity and the wires connecting them to the contact deposited on SiN insulator are visible.*

The second objective was to create devices compatible with high frequency signals. The strategy here is simply to manage to connect the metamaterial to a coplanar waveguide in the same fashion as described in Chapter 3 for mesa structures.

Regarding the change of material, a few main differences between GaAs and InP-based materials must lead to changes in the process:

- Acid etching sensitivities are different: some recipes change and in particular the selectivities change [109].

- Physical plasma etching conditions are more drastic and recipes are therefore completely different and must be (re)developed.

- Metallization for the contact has to be revisited: contrarily to GaAs, any metal contact on InGaAs is ohmic [110] and will not display Schottky behavior.

In the present section, I will describe the final process used for the realization of the devices, highlighting the choices made to adapt the clean room processing steps to the new material.

3.5.2 Processing of waferbonded devices

The process that I realized can be separated in three steps starting from the grown wafer to the final device: first the substrate reversal, including wafer bonding and substrate removal; then the patterning and etching of the resonators; and finally the creation of high-speed connections.
With the exception of the waferbonding step that was performed at C2N by Isabelle Sagnes, Abdelmounaim Harouri and Nathalie Isac, all the steps were performed in the clean room facilities of the Paris Centre consortium, both in the LPENS at ENS and MPQ at Université Paris Cité.
A summary of the steps is presented in Fig.3.19.

a) Waferbonding and substrate removal

Starting from a 2" or 3" wafer with the epitaxial layers on top, the first step is to manage to have gold beneath the epitaxial layers. No semiconductor crystal can be grown on gold so we need to transfer the sample on a new host wafer and do a wafer bonding. We start by cleaving the wafer into halves or quarters and preparing future host wafer pieces of the same dimension with an undoped GaAs wafer. Both samples are to be cleaned and recovered with a thick evaporated Ti/Au layer before being bonded together by thermocompression. Larger surfaces than the one mentioned are hard to efficiently waferbond because of insufficient planarity of the epitaxial layers. Contrarily to GaAs, using simply gold instead of a diffusive alloy here is sufficient because an ohmic contact will be formed. This will actually be a key characteristic later on and limits the application of this process to GaAs. We also asked to have the thinnest Au layers possible because we will need to eventually remove it and the minimum we could get for an efficient waferbonding was around $2\times$ 300 nm = 600 nm.
We then need to remove the epitaxial substrate to end up with a host substrate/TiAu/Active region stack. The double wafer is simply put into pure HCl to dissolve the InP. The GaAs host substrate is insensitive to this acid and the first layer of any InP optoelectronic device -the contact- in doped InGaAs will act as a very selective etch stop. The reaction of InP with HCl will cause a vigorous effervescence of phosphine PH_3 (very toxic). The end of the bubbling signals the end of the reaction. A mirror-like surface should be recovered.

Mechanical etching can be considered to remove most of the InP prior to chemical etching for a slightly faster process, but the room temperature HCl etch rate of the InP is already around 5 µm/min and can be increased by heating the solution to 50°C without apparent loss in selectivity.

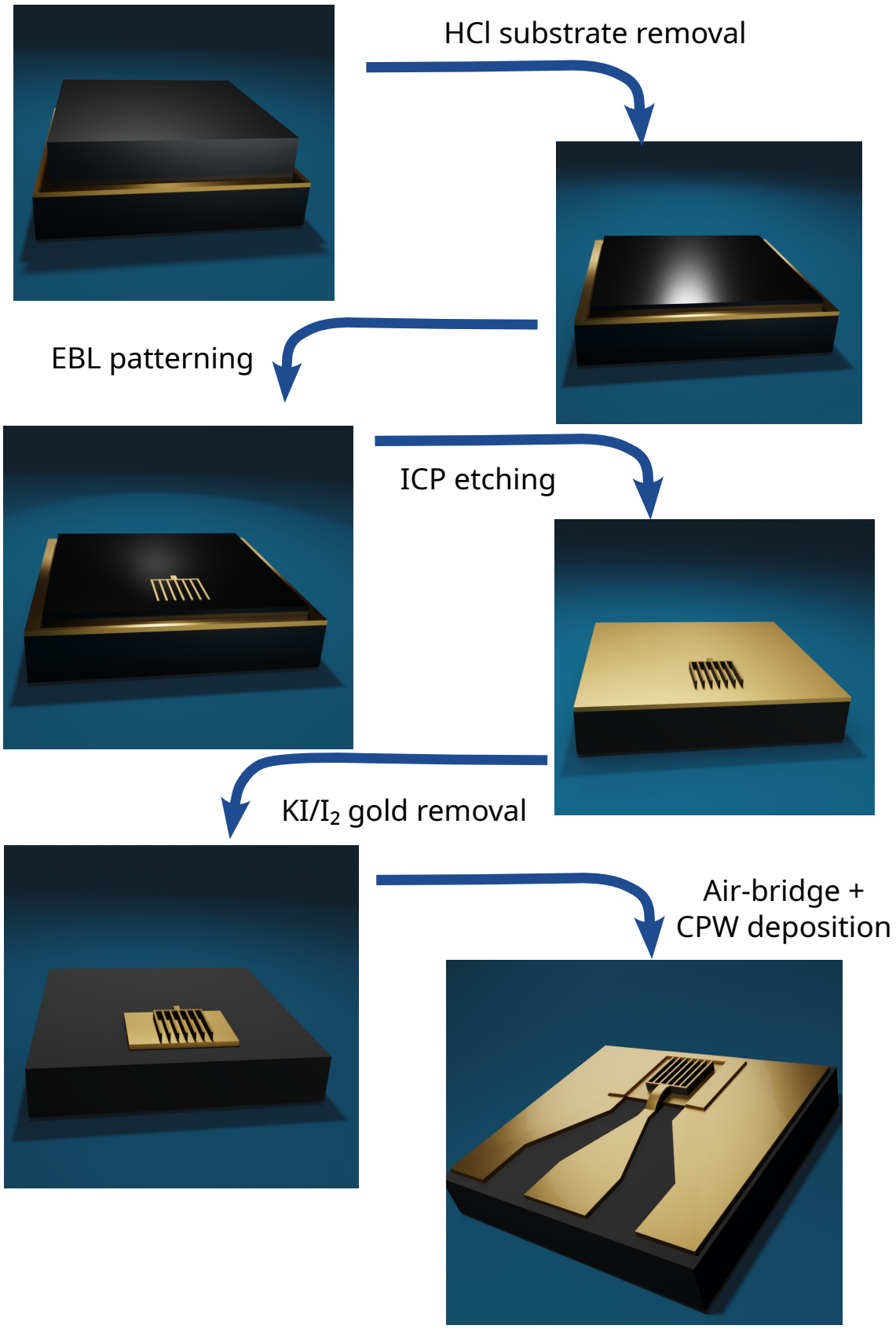

Fig. 3.19 *Sketched summary of the main steps of the process for making the high frequency metamaterial device.*

b) Resonator Patterning

The sample can now be cleaved into easy to handle centimetric pieces. The next step consists in patterning the resonators. This step requires electron beam lithography because of the micrometric dimensions of the devices and resolution needed to fabricate the cavities.
For the subsequent ICP-RIE etching (Inductively Coupled Plasma, Reactive Ion Etching), we will need to cap the Ti/Au deposition with a thin Nickel film. Unfortunately, lift-off of micrometric structures of Nickel tends to peel off. I therefore used a bilayer process to make sure to have a sufficient underetch under the patterned e-beam resist and make the lift-off smoother: PMGI-SF6 is spun at 4000 rpm (∼250 nm) and baked at 180°C for 5 min before spinning the electrosensitive PMMA (A6 950K: ∼300 nm when spun at 5000 rpm) and baking it 5 min at 180°C. After patterning with the e-beam, the PMMA is developed in MIBK:IPA 1:3 for 45 s and rinsed in water. The PMGI layer is almost not electrosensitive and not reactive to this organic solvent. It can be slowly dissolved, only under the accessible developed area, using alkaline solution (Fig.3.20). AZ400K:H2O 1:8 offers a good control over the etch with a lateral etch rate of approximately 2 µm/min. This rate is strongly dependent on the baking temperature and time. MF319 can otherwise be used off the shelf for similar results but is more toxic (TMAH). Metal deposition (Ti/Au/Ni 5/100/50) can be

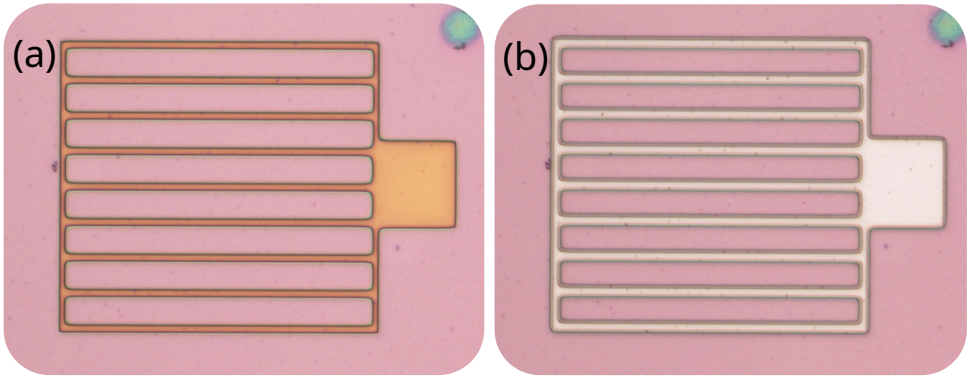

Fig. 3.20 *Microscope image (x100) of patterned bilayer before (a) and after (b) alkaline dissolution of the PMGI. Underetch is visible under the PMMA in (b). Resonant stripes are 1.4 µm large.*

performed and the lift-off in hot DMSO ensures a good patterning without peeling nor need for ultrasonic bath.

c) Physical etching

The etching of resonators requires physical etching because chemical etching cannot provide vertical walls nor high aspect ratio structures because it is an isotropic etching (or along specific crystal axis, but this is also a priori unusable here). The method of choice is the ICP etching and many examples of very successful InP etching exist in the literature [111, 112, 113]. The ICP etching method combines physical and chemical etching: reactive ionized species are directed to the surface by an electric field, but the goal is to create volatile compounds on the surface that can be easily evacuated. Passivation of the sidewalls created

by a carbon or silicon-based polymer (from the support wafer or gases) can help creating a highly vertical structure. Ionized inert gases (typically Argon) can also be added for supplementary anisotropic milling.

Three types of chemistry are used for InP etching, based on either Bromine [114], Chlorine [111] or Methane [115] chemistries. The Paris Cité facility only has access to $SiCl_4$ so it dictated this choice. Two main difficulties were identified: creating vertical and as smooth as possible sidewalls, and ending up with metal on top of the resonators. For GaAs processes this was made trivial by the fact that the ICP etching of GaAs leaves the gold pristine and gold can perfectly act as a selective mask.

For InP, the problem is different because of the Indium: no volatile compounds with Indium can be created with Chlorine under $\sim 200°C$ [115]. Much higher forward power is moreover necessary to achieve any etching. This makes gold no longer a good hard mask. It is worth mentioning here that the Methane-based recipes, working at low temperature, leave the gold untouched and would be a good solution [105] though verticality of the sidewalls seems less good.

Previous works in the group [116] lead to a recipe working relatively well, with $SiCl_4$ (3 sccm), H_2 (4 sccm) and Ar (1.8 sccm), with a chamber at 200°C and 6 Pa, and with an ICP power (for the plasma creation) of 350 W forward bias power of 1000 W, close to what can be found in the literature [117]. This recipe indeed yielded nice etchings but it required a SiN or SiO mask because the damage on a metal mask was overwhelming.
The possibility of using such mask is discussed in Appendix B but to limit the number of steps in the process and the general difficulty (and increase the yield), the solution chosen was using a Nickel cap on top of the gold during patterning. Indeed Nickel is more selective with respect to this chemistry and more resistant to ion milling. Chromium was also quickly investigated but seemed less resistant. This solution is imperfect though, since the purely physical etching still etches the mask slightly.

In parallel I tried to adapt the recipe to make it more compliant with the metal mask. The number of free parameters and their intrications, as well as the broad literature on a variety of ICP systems make such study complicated and time-consuming. Besides, being the only InP user in the clean room, access to the machine was complicated: any of my etching sessions had to be followed by an opening and a deep cleaning of the plasma chamber and negatively impacted the quality of the following GaAs etching by other users. So campaigns had to be dense and separated. The strategy was therefore to start from a few recipes from the literature [111, 116, 118], loosely adapted to our machine (distance between the electrodes when known and forward bias, stoichiometry when Cl_2 or BCl_3 was used instead of $SiCl_4$), and then changing parameters in a random walk fashion in a first step, then reiterating from the more interesting points. I settled eventually for the following parameters: $SiCl_4$ (4 sccm), H_2 (11 sccm) and Ar (1.8 sccm), 200°C chamber, 0.07 Pa pressure, 800 W ICP

power for plasma generation, -110 V RF forward bias. The sample was fixed on a Si carrier using a grease to help thermalization. Eventually, 1 µm-deep highly vertical etchings could be reached with a 50 nm nickel layer.
One major flaw of this recipe is the difficulty to etch between close patterns. Though it is a recurring problem in ICP etching in general, here I found it difficult to properly reach the bottom metal if the characteristic size between my patterns was less than 3 µm for 750 nm high structures. In this situation, grazing starts appearing (Fig.3.21 (b)), maybe caused by micromasking due to $InCl_x$ still insufficient volatility. For thinner structures this problem vanishes for the targeted densities of arrays.

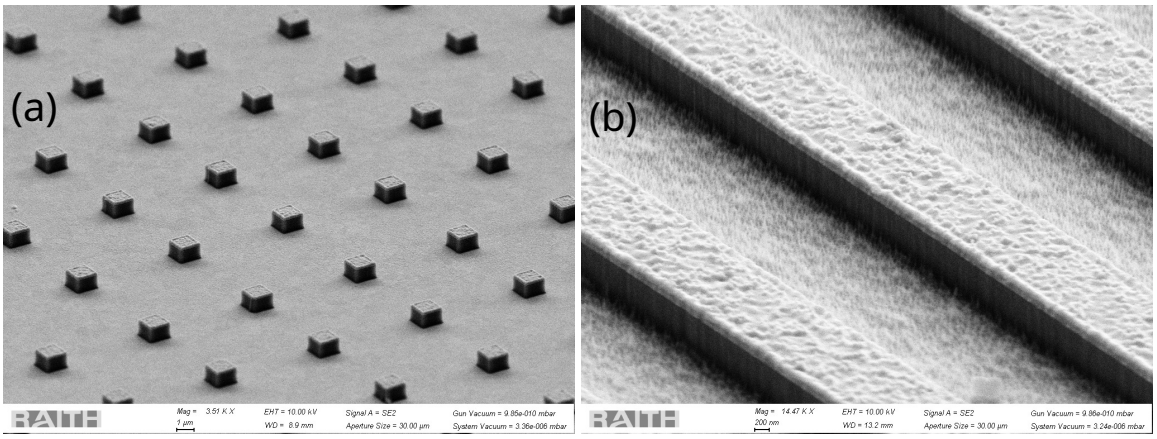

Fig. 3.21 *(a) SEM picture of a patch-resonator sparse array of a 770 nm-thick InGaAs/AlInAs heterostructure using the final recipe. (b) SEM picture of a stripe-resonator array of periodicity 3 µm and lateral size 1.4 µm. Grazing at the bottom is visible.*

d) High speed connection

The final step was to connect the resonator through a coplanar waveguide (CPW) much alike what was done for the mesas. For this purpose we added a small area next to the array (visible in Fig.3.20) so we could hang the air-bridge there.
However, the CPW needs to stand on an insulating surface. After the ICP etch, the gold of the waferbonding is reached (there technically could be a layer of Ti left but it was actually removed by the ICP every time) and needs to be removed to reach the insulating GaAs beneath.
After protection of the resonators with photoresist (S1805), the sample is dipped in a KI/I_2 solution (4 g KI + 1 g I_2 in 40 mL of water, can be reused). The etch rate is approximately 500 nm/min for the gold but it also etches the semiconductor very fast. Conveniently the Ti bottom layer from the waferbonding on the host substrate acts as a perfect etch stop. Lateral underetch beneath the structure is dangerous though and the protection should be ∼10 µm larger than the patterns. Note that this would not work on PdGeTiAu used for GaAs ohmic contact and purely physical etching with accelerated Ar^+ ion should be done instead, though more complicated because the ion-implanted resist becomes almost impossible

to remove (several short protection/etching/cleaning cycles might be needed). Leftover Ti layer is finally removed using SF6-based RIE etching. This step is selective (enough, not quantified) and does not damage the gold nor the semiconductor.
Finally, the coplanar waveguide can be deposited: first, a positive support resist is deposited and reflowed where the bridge is to be put. Then, a second negative optical lithography defines the contour of the CPW. Tilted Ti/Au deposition (+10°/0/-10°) ensures a good quality for the bridge. Lift-off is done using a resist stripper (SVC14) at 80°C to remove both the negative and the reflowed positive resist at the same time.

3.5.3 Conclusions on the fabrication process

A finished device is shown in Fig.3.22. This process for InP substrates is actually remarkably simple (only one e-beam step without any alignment, etchings are selective, no annealing necessary) and makes good use of the specificities of the material.

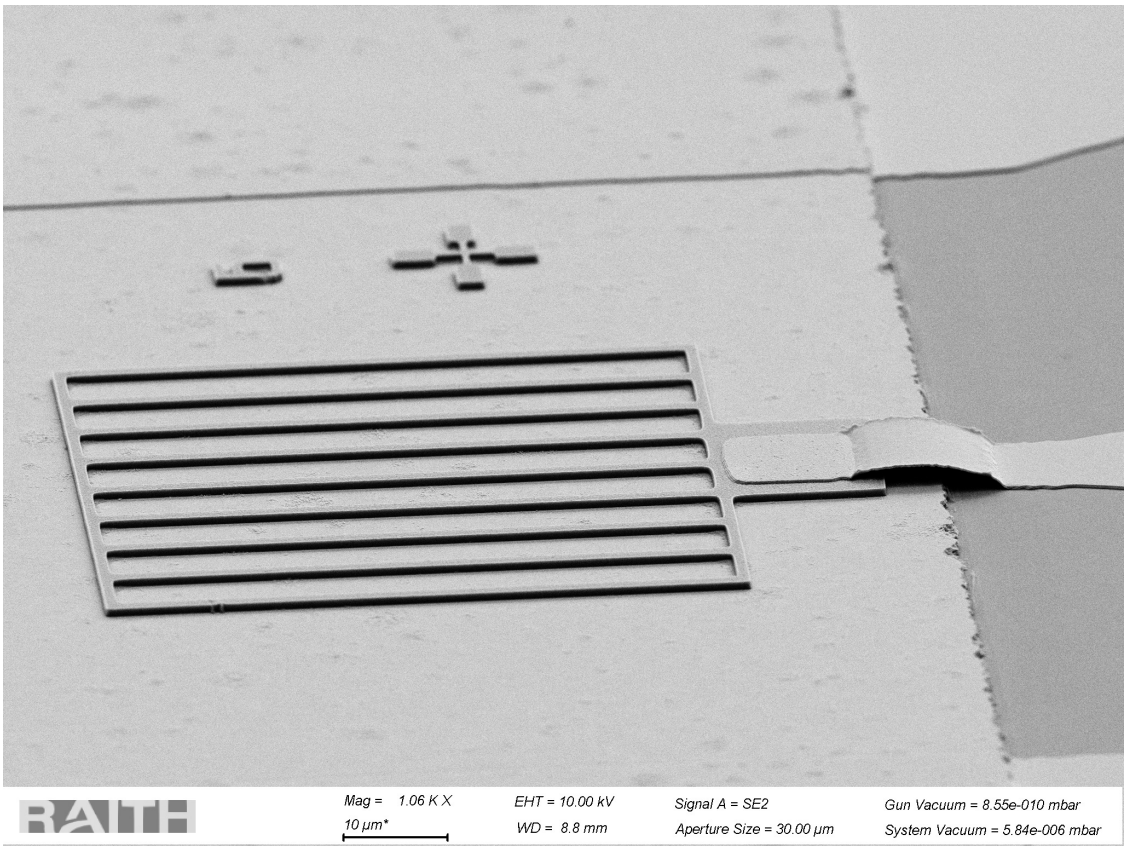

Fig. 3.22 *SEM image of a finished device.*

The choice to ”go back” to 1D resonators will be discussed in the next chapter but is also strongly motivated by the simplicity it generates by avoiding supplementary steps for the wires. Indeed wires cannot be made with Schottky contacts as in [35] and should be also self-standing. A process to do it was nevertheless developed (see Appendix B) but the complexity was not deemed worth it at this stage, though the advantages are well established especially in terms of dark current for QWIPs, and bandwidth. A nice corrollary to this is

that the finished sample can easily be manually cleaved every mm^2 to separate each device without damaging it even without prior encapsulation.
The most debatable choice is in my opinion the Ni ICP mask. This *ad hoc* solution is not entirely satisfactory: the nickel thickness has to be fine-tuned to handle the etching and to be mostly removed during etching because it oxidizes afterward otherwise. The canonical solution is to use a hard Silicon oxide mask and though it adds an aligned e-beam lithography step (and PECVD SiO deposition as well as RIE etching), I think this would be a worthy time investment if etching more than ~ 500 nm. On the contrary, for thin structures, since metal is sputtered in the chamber anyway, I would argue that using thicker sacrificial gold (with a selectivity of around 8 for 1 with InP in my experience) might be sufficient.

In Appendix B are described alternative process strategies that were envisioned and at least partially tried in order to bypass some problematic steps. Though aborted, I believe that at least some might be worth pursuing if the specifications of new devices were to change and become more demanding.

3.6 Conclusion

In this chapter, we have set the framework for the next generation of metamaterial-based optoelectronic devices. After explaining its origin, we showed that the Coupled Mode Theory is a convenient semiclassical framework to address the coupling of light with our resonators. Thanks to a parametric study of empty cavities, we could estimate the numerical values of the cavity parameters and their evolution with the geometry of the resonators. These relations between geometry and electromagnetic properties were used to imagine guidelines for the optimization of devices, were they detectors or modulators. Finally, we summarized the effort conceded to design a robust clean-room process suitable for fabrication of metamaterial based high-speed devices in InGaAs/InAlAs.

Chapter 4

Metamaterial detectors and modulators for data transmission

In the previous chapter I have presented a Coupled Mode Theory approach to model the light-matter interaction in cavity-embedded optoelectronic devices. We have used it to devise guidelines on how to design optimized cavities either for maximizing the ISB absorption for detectors or the contrast in reflectivity of Stark modulators as a function of the applied bias. In this chapter, we will apply these methods to design and fabricate metamaterial QCD, QWIP and modulator grown on InP. Each type of device, embedded in cavities, will be experimentally investigated. Finally, we will conclude on a data transmission experiment performed with these metamaterial devices to highlight the improvements made with respect to the first generation presented in Chapter 2.

4.1 Stark modulator

I have designed a Stark modulator, operating in the strong light matter coupling regime. Two samples (AC19 and AC715) were fabricated by MBE at III-V Lab. The corresponding growth sheets are given in Appendix.

4.1.1 Samples characterization and passive metamaterials

The sample AC19, was presented already in Section 2.4.2 (Fig.2.17). The absorption spectrum has 2 energy peaks very close in energy to the expected values at 132 and 265 meV. The FWHM of the 1-2 transition is 25.5 meV and the measured Stark shift 5.1 meV/V. The modulation depth was limited to 15%, less than half of what was expected in comparison with V0351. This was attributed to a lower doping level than the nominal one. Sample AC 715 was designed to have a nominal doping three times larger than that of AC19. Fig.4.1 shows the transmission spectra of both samples. The increased absorption between the samples (factor of 3, while multipass samples had the same length) is coherent with the increased electronic density. We also measure a 7 meV red-shift between the two spectra, and would have expected $\tilde{E}_{isb}$ to change by 10 meV from the depolarization shift induced by the increased doping.

Nevertheless, the FWHM of the 1-2 transition was largely increased, from 25.5 meV to 41.8 meV. This broadening is detrimental to our objective of making a strong-coupling Stark

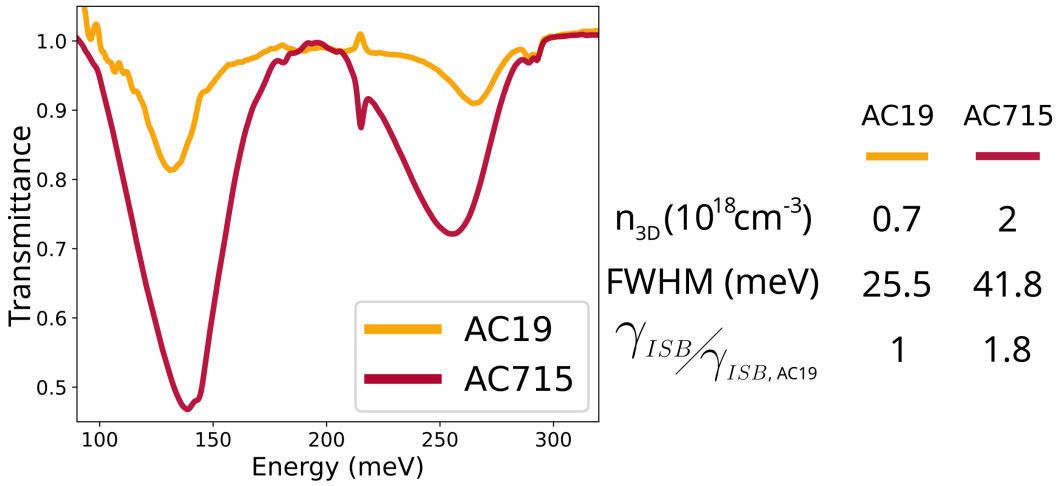

Fig. 4.1 *Multipass transmission spectra at 45° of MBE 20 period-modulators AC 19 and AC715 (doping x3).*

modulator as shown in Chapter 3. Altogether, and assuming that γ_P is proportional to the FWHM, the quantity γ_{isb}, related to the dissipation by the ISB transition in a cavity is 1.8 times larger in this second sample than in AC19, and the splitting between the maxima of $A_{isb,SC}$, $\sqrt{\Delta} = 4\Omega_r^2 - 2\gamma_P^2 - (\gamma_a + \Gamma_a)^2$ will also be greater. We therefore focused on sample AC715 for the rest of the work.

a) Passive devices reflectivity spectra

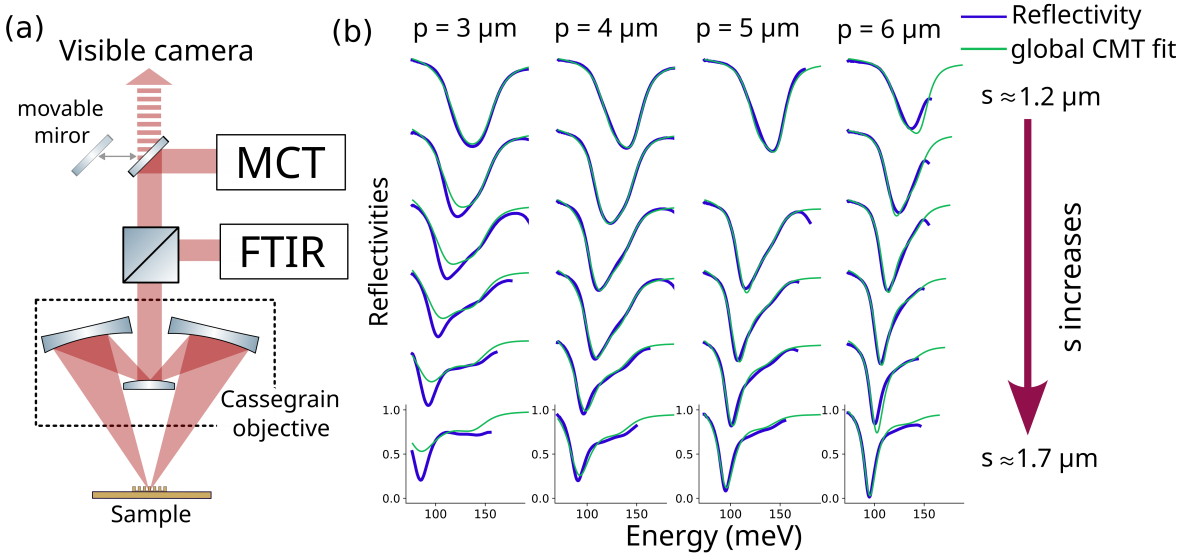

Fig. 4.2 *(a) Sketch of the Cassegrain objective coupled to the FTIR. A movable mirror allow to switch from a visible camera for alignment and the MCT IR-detector for the spectra measurement. (b) Reflectivity spectra in blue for passive stripes of modulator AC715 for p=3,4,5,6 µm and s between 1.2 and 1.7 µm. In green the CMT best fit of the whole set of spectra with a single geometrically independent set of parameters.*

In order to complete our knowledge of these samples before devising the final device, we processed arrays of resonators, patches and stripes, with different sizes (6 widths every 100 nm from 1.2 µm on) and periodicities (3, 4, 5, 6 µm) to create a set of data allowing us to retrieve the values of all the losses in our system. To efficiently measure reflectivity spectra, we used a Cassegrain microscope objective coupled to a FTIR and an MCT detector, sketched in Fig.4.2 (a), making possible to probe regions smaller than 100 µm x 100 µm with a much greater sensitivity than with the reflectivity unit used in Chapter 3, and with ease. This also reduced drastically the writing time with the e-beam lithography, allowing for a wider range of parameters to be probed. These measurements were done at ONERA with the help of Patrick Bouchon and Baptiste Fix. Fig.4.2 (b) shows the reflectivity spectra of the stripes for this set of samples in blue. The microscope objective sends lights from 12° to 24° and collects the reflected light between 0° and 12°. This limits the region of the spectrum that we can probe especially with large periodicities, since light will be diffracted at high energy and will not be collected.
For each spectrum, in the spectral region defined by the lower bound of the MCT detector and the diffraction threshold (as a function of p), we globally fitted the data with the CMT. In green is plotted the resulting fit of the whole set of spectra: all of them are fitted using a single set of parameters independent on the geometry. To do so, each s and p were measured with a SEM, and we assume the relations $\omega_a = \frac{\pi c}{n_{eff} s}$ and $\Gamma_a = \frac{\Gamma_{a,0}}{p^2}$.

The spectra with a low periodicity and large width (bottom left in Fig.4.2) are poorly fitted. This is explained by the difficulties of the processing of the devices with such sizes. Indeed, the physical etching of these samples, as mentioned in Chapter 3.5, was not able to uncover the bottom gold because the space between the patterns was too small.

Table 4.1 summarizes the values found for the losses, Rabi splitting and mode index of

Stripes					Patches				
$\Gamma_{a,0}$ meV·µm^2	γ_a meV	γ_P meV	Ω_r meV	n_{eff}	$\Gamma_{a,0}$ meV·µm^2	γ_a meV	γ_P meV	Ω_r meV	n_{eff}
151	2.3	20.1	13.6	3.6	112	2.7	20.1	12.4	3.05

Table 4.1: CMT parameters for AC715 modulator extracted from arrays of metamaterials.

both stripes and patches (spectra not shown here). The ISB transition losses γ_P, have the same value for patches and stripes since they are only linked to the quantum wells. The values of γ_a, the non-radiative losses of the cavity, are very close for stripes and patches. This means that this quantity is not proportional to the surface of gold in the array as one could have expected for a dissipation occurring mainly in the metal. This was already visible in the empty cavity study, since γ_a did not depend on p in that case (3.11, section 3.3.4). The radiative losses Γ_a, on the other hand, are significantly larger (+35%) for stripes than for patches. Nevertheless, this is mitigated by a smaller Rabi frequency for patches. As the doping is necessarily the same in both structures, this lower value can stem either from a lesser mode confinement in the patches than in the stripes (more field is leaking from the lateral openings), or by the fact that electrons close to a rough surface can be trapped by

defects and not be available, reducing effectively the density of electrons available for the optical transition. The Rabi energy observed for the stripes, assuming a perfect overlap of the mode cavity with the patch, corresponds to a volume doping of $2.34{\cdot}10^{18}$ cm^{-3}. Finally, the effective index for stripes for the $TM_{0,1}$ mode is 3.6[1], significantly larger than for patches (3.05). This also indicates a larger leakage of the field in the case of patches with respect to stripes.

b) Device fabrication : patches or stripes ?

Using the fully characterized CMT parameters for our device, we can now devise the geometry desired for the optimized Stark modulators. For both the patches and the stripes, we can proceed to the optimization, as described in Chapter 3. In Fig.4.3, using both sets of values of Table 4.1, we simulate the maximum contrast possible for each geometry, i.e. the variation of the total absorptivity ΔA_{tot} under the application of $\pm$10 V.

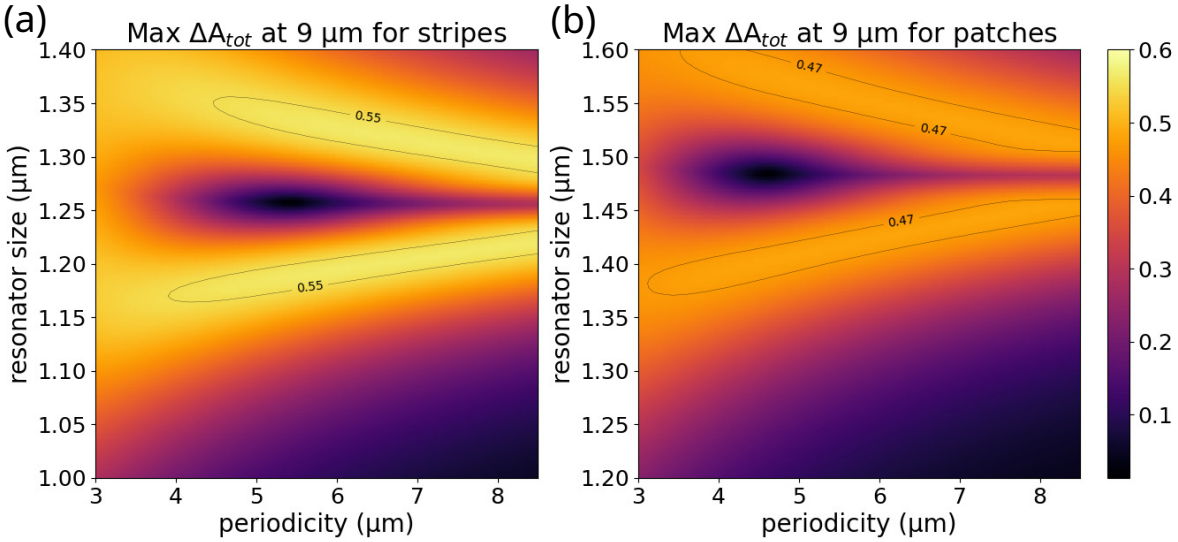

Fig. 4.3 *Maximum contrast deduced for the CMT for AC715 Stark modulator in cavity for patches (a) and stripes (b) as a function of their geometry.*

It appears that a slightly better maximal contrast is expected for the stripes (0.56) than the patches (0.48). Besides, this modulator is destined to work with polarized laser light. As a consequence, polarization insensitivity is not particularly useful. Finally, the fabrication of stripes is significantly easier. The only expected drawback is a slight limitation of the bandwidth due to the increased electrical area. To mitigate this, we will design the modulator with a periodicity of 7 µm, the highest value below the onset of diffraction. The best s should be 1.2 µm, allowing for a contrast > 0.5.

[1]The index is actually linearly decreasing with s, but the variation is small, $\frac{dn}{ds} \simeq 0.2\,\mu\ m^{-1}$

4.1.2 Characterization of the devices

The final stripes devices were eventually fabricated according to the fabrication steps described at the end of Chapter 3. Various values of s were used, in order to have various wavelengths at which the devices may work.

a) Reflectivity spectra under bias

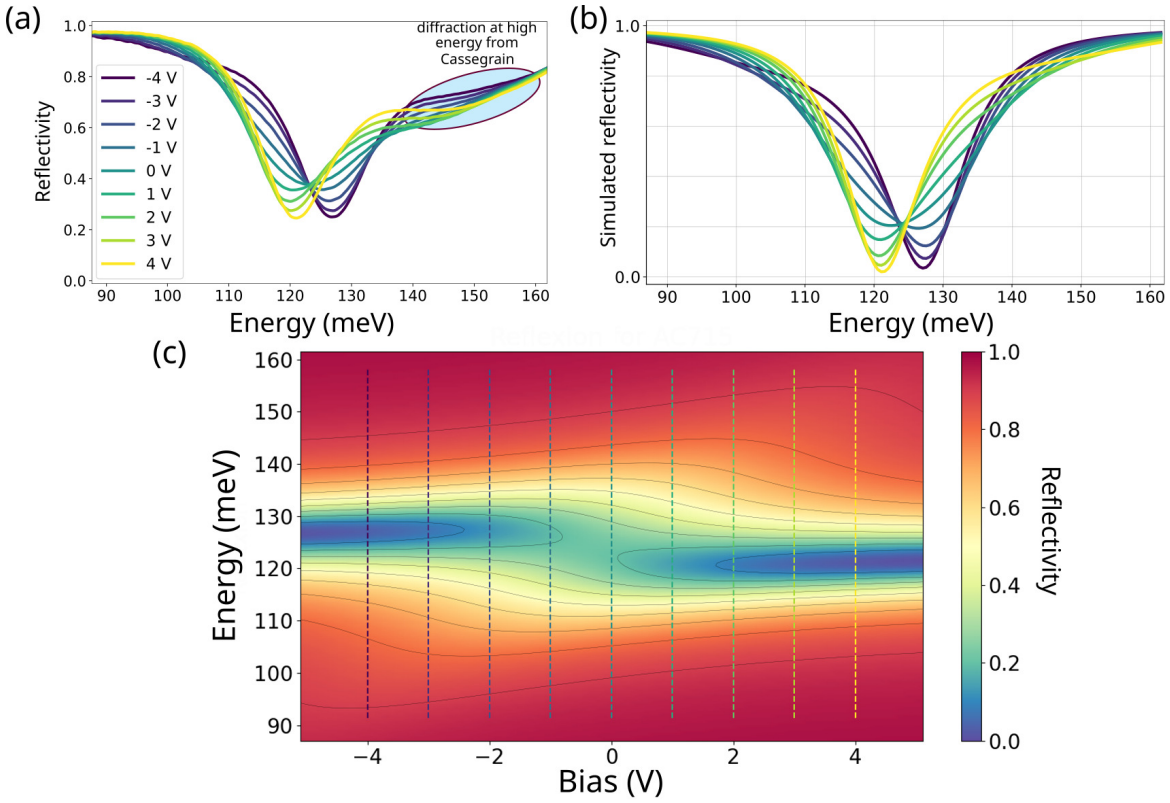

Fig. 4.4 *(a) Experimental reflectivity spectra under DC bias (-4 V to +4 V) for the final device ($s = 1.27\,\mu m$, $p = 7\,\mu m$). (b) Corresponding spectra simulated using the CMT. (c) Complete map describing the CMT reflectivity of the modulator as a function of the energy of the laser and the bias applied. Colored dashed lines indicate the position of the spectra shown in (b).*

We used the microscope+FTIR setup at ONERA and measured the reflectivity spectra while applying DC bias on the device. Spectra for $s = 1.27\,\mu m$ at different bias are gathered in Fig.4.4 (a) and compared with their corresponding CMT simulation (b). Fig.4.4 (c) shows the simulated reflectivity spectra of the sample as a function of the applied bias. Apart from the diffraction related feature observable above 140 meV, the two sets of spectra in (a) and (b) are very similar. However, in order to match the experimental spectra, the Rabi energy had to be decreased from 13.6 meV (found with the passive arrays) to 10.9 meV. This value cannot be used to fit the dataset of Fig.4.2, hinting at a genuine difference between the two samples. Assuming that the doping density is homogeneous accross the wafer, the overlap between the optical mode and the resonators must cause this discrepancy: there is a significant difference between infinite arrays (for the passive spectra) and the current devices.

In these devices, orthogonal wires for connections and lack of periodic boundary conditions for the edge stripes might be detrimental to the coupling of the resonators with the optical field. A second difference between Fig.4.4 (a) and (b) is the fact that in the simulations the reflectivity tends to zero for large positive or negative biases. Experimentally, the minimum reflectivity of the devices for any bias is around 0.3. From now on we will manually add a 0.7 numerical prefactor to the absorption of the CMT simulations to account for this discrepancy.

In any case, it is clear that we are not in the strong coupling regime as defined in Chapter 3 and we do not see the polaritonic splitting we counted on. Nevertheless, the anticrossing of the cavity energy and the bias-sensitive ISB energy yields a sizeable contrast with the bias.

b) Modulation depth

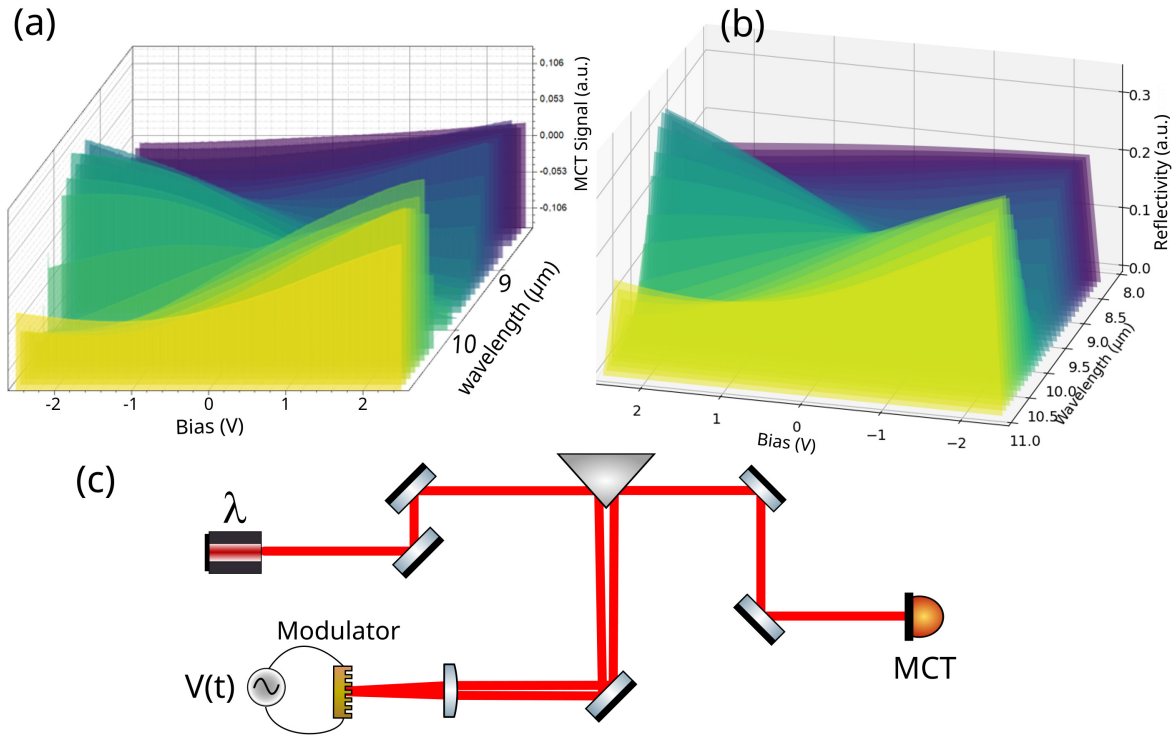

Fig. 4.5 *(a) AC signal from an MCT detector for every wavelength accessible with the MIRcat laser as a function of the bias. Colors match the wavelength and are only a guide for the eyes. (b) Simulated reflectivity with the CMT. The average value of the reflectivity for each wavelength was subtracted from the simulated spectra and a 0.2 offset was added to resemble (a). (c) Sketch of the optical setup used, with the tunable laser, the stripe modulator and the MCT. A silver 90° prism is used to send the laser toward the reflection modulator and collect the reflected signal.*

We used a tunable laser external cavity QCL to probe the same system in real operation conditions at different wavelengths between 8.3 µm and 11 µm with AC bias. Fig.4.5 (c) shows the optical setup used to perform the characterization. A single lens is used to focus the laser beam on the metamaterial and to collimate the reflected and modulated beam. A silver-coated 90° prism is use to separate the incoming and outcoming beams as sketched. On the receiver's end, the signal is read on an MCT detector, with an optical bandwidth larger

than the tunable laser's range of operation. Fig.4.5 (a) shows the AC photocurrent measured for each wavelength, renormalized by the laser output power, and as a function of the applied bias. The responsivity of the detector was considered flat over the investigated range. We compare the measured photocurrent with the simulated reflectivity, as they are proportional, in Fig.4.5 (b). This corresponds to horizontal cuts in Fig.4.4 (c). In order to have a better graphical comparison, we subtracted for each wavelength the average reflectivity over the bias range studied (-2.5V,2.5V) and added a constant offset. This purely qualitative comparison comforts us in our understanding of the system. Such plots also allow us to find the most appropriate wavelength for one modulator (in this example 9.7 and 10.7 µm).

Switching the MCT for a QCD in order to access the DC current, we measure the maximum modulation depth of the Stark modulator by applying 5.5 Vpp AC bias and plotting the photocurrent versus the bias applied on the modulator in Fig.4.6 (a). The deduced modulation depth for this bias is 28 %. The shape hints that a slightly larger maximal modulation depth should be reachable with a larger bias (supported by the simulation in orange) but we restricted the modulator operation to 5.5 Vpp bias to work in the linear regime, useful for data transmission. In (b) we plotted the updated maximum contrast map with the value of Ω_r experimentally found for the device and with the 0.7 numerical factor for the absorption, assuming that a 8 Vpp bias can be applied. 31% of the total incoming power still appears to be reachable and a larger bias would not improve this value significantely. Compared to Fig.4.3 (a), this plot shows the high sensitivity of the performances of the modulator to the Rabi energy.

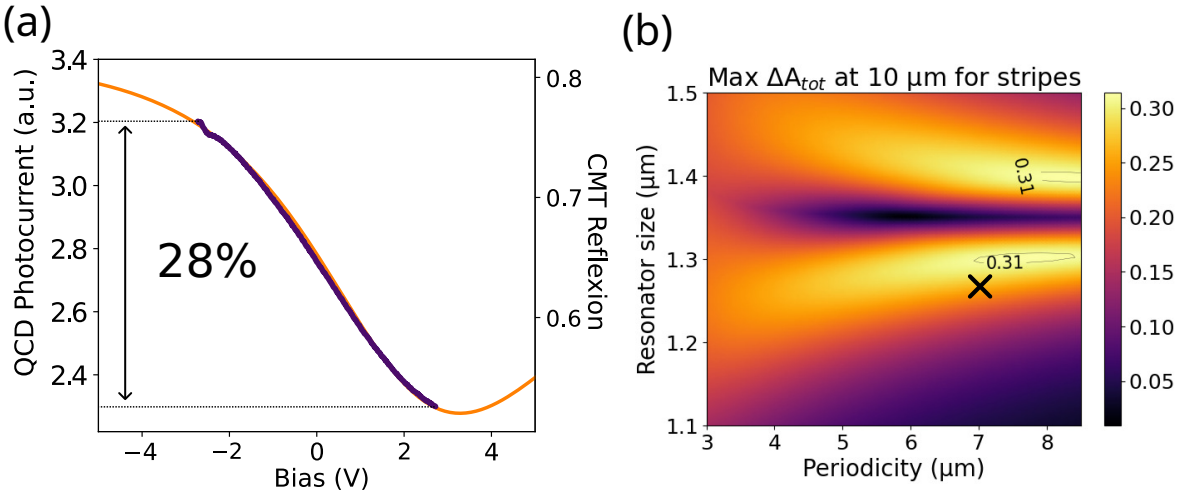

Fig. 4.6 *(a) Photocurrent on a QCD after the stripe modulator as a function of the bias, in purple. The reflectivity from the CMT for this devices is also plotted in orange. (b) Updated maximum contrast map with the reduced value of Ω_r for the device and a 0.7 prefactor to the absorption. The black cross shows the investigated device parameters.*

c) Electrical characterization

The electrical bandwidth of the device was measured through a rectification experiment. The result is plotted in Fig.4.7: a -3dB frequency cutoff just above 10 GHz was found. Going

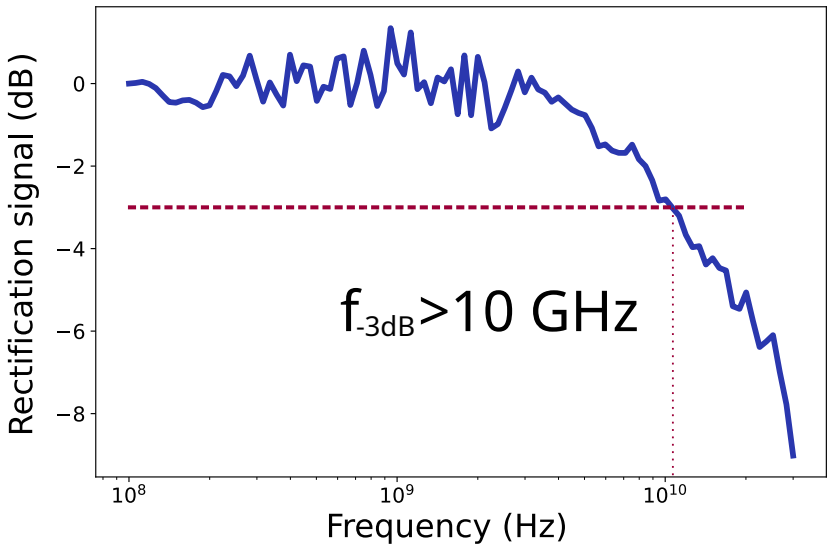

Fig. 4.7 *Electrical rectification of the final modulator device.*

back to the mesa equivalent cutoff from Chapter 2, we obtain such bandwidth for a mesa of side 50 µm. After renormalizing the geometric capacitance by the height, our device has the bandwidth of a mesa (of same height) of side 40 µm. The actual footprint of our device is 1215 $\mu m^2 \simeq 35^2$ μm^2. These two values are very close, meaning that considering the geometrical capacitance, paired with the lowpass filter from the heterostructure determined in Chapter 2 (with characteristic time of 4 ps) for the bandwidth is still a good approximation. This result could have been counterintuitive given that the wavelength at 10 GHz in InP is 1 cm and 3 cm in the air, both orders of magnitude larger than the patterning size of the resonators. The RF signal does therefore not "see" an equivalent surface equal to the optical area that the photons see.
This result makes in the end a case for patches: maintaining a 60x60 μm^2 optical area with a periodicity of 7 µm only makes an electrical area of 22^2 μm^2, leading with the same approximations to a bandwidth exceeding 26 GHz, more than the double of stripes.

4.1.3 Phase modulation

The Stark modulator has been used until now as an amplitude modulator as the ISB absorption is a bias-dependent function. This change in the absorptivity with the bias, hence in the imaginary part of the electric susceptibility, must have an influence on the real part of the electric susceptibility according to the Kramers Krönig relations. For a plane wave propagating in the x-direction $E(x,t) = E_0 \exp(-i(\omega t - \frac{n\omega x}{c}))$,the complex refractive index is $n = \sqrt{1+\chi_0+\chi} \simeq n_0 + \chi/2n_0$ with $n_0 = \sqrt{1+\chi_0}$ the bulk semiconductor refractive index. The influence of the ISB transition is contained in $\chi/2n_0 \equiv \bar{n}_{isb} = n_{isb} + i \cdot \kappa_{isb}$

The transmission T through a sample of length L at a frequency ω can be expressed as a

function of χ as:

$$T(\omega, L) = |\frac{E(L)}{E_0}|^2 \Rightarrow \ln(T) = \frac{-2\kappa_{isb}\omega L}{c} = \frac{-\omega L}{c}\frac{\Im(\chi)}{n_0} \tag{4.1}$$

By definition of the absorbance, we can also write: $\ln(T) = -\alpha(V)L$ with $\alpha(V)$ the absorbance of the Stark modulator. $\Im(\chi)$ therefore reads:

$$\Im(\chi) = \frac{n_0 c}{\omega}\alpha(V) \tag{4.2}$$

On the other hand, the phase added by the active region is related to the real part of χ:

$$\phi = \frac{n_{isb}\omega L}{c} = \frac{L\omega}{c}\frac{\Re(\chi)}{2n_0} \tag{4.3}$$

Finally, since $\Re(\chi) = \mathrm{H}(\Im(\chi))$ with H the Hilbert transform from the Kramers Krönig relation (which is linear), we find:

$$\phi(V) = \frac{1}{2}\mathrm{H}(\alpha(V)L) \tag{4.4}$$

In our devices, the transmission is zero because of presence of the bottom gold. We can thus consider the reflectivity R to be $R = 1 - A$,with $A = \alpha(V)L$ the absorptivity. The phase can then be simulated from the CMT as $\phi(V) = \frac{1}{2}\mathrm{H}(\ln(1 - A_{tot} \cdot \beta))$. β is a numerical factor, 0.7 here, added to match the experimental reflectivity of Fig.4.4. Fig.4.8 shows the resulting color map of both the reflectivity and the phase added by the system. The value of the phase calculated through the Hilbert transform is very sensitive to the value of the absorption, rendering predictions risky: without the numerical factor, we found an almost 180° added phase.

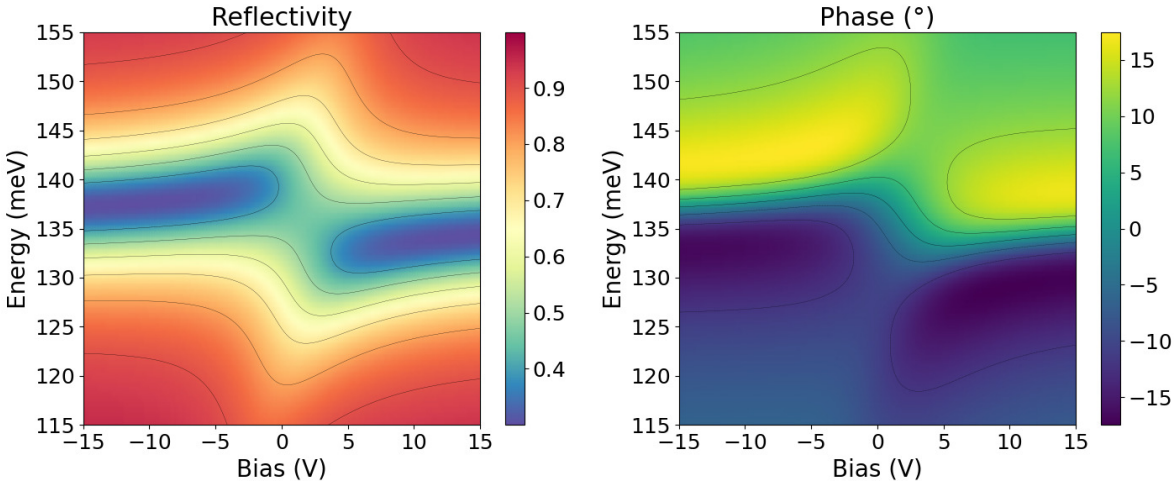

Fig. 4.8 *CMT simulated reflectivity and phase map for the stripes Stark modulator with $p = 7\,\mu m$ and $s = 1.22\,\mu m$.*

In order to measure the phase change induced by the modulator, we build a heterodyne setup depicted on Fig.4.9. We use two lasers at 9 µm. There are actually two heterodyne

detections: the first is used to lock the phases of the two lasers together, while the other one serves for measuring the modulator properties once the laser phases are set.

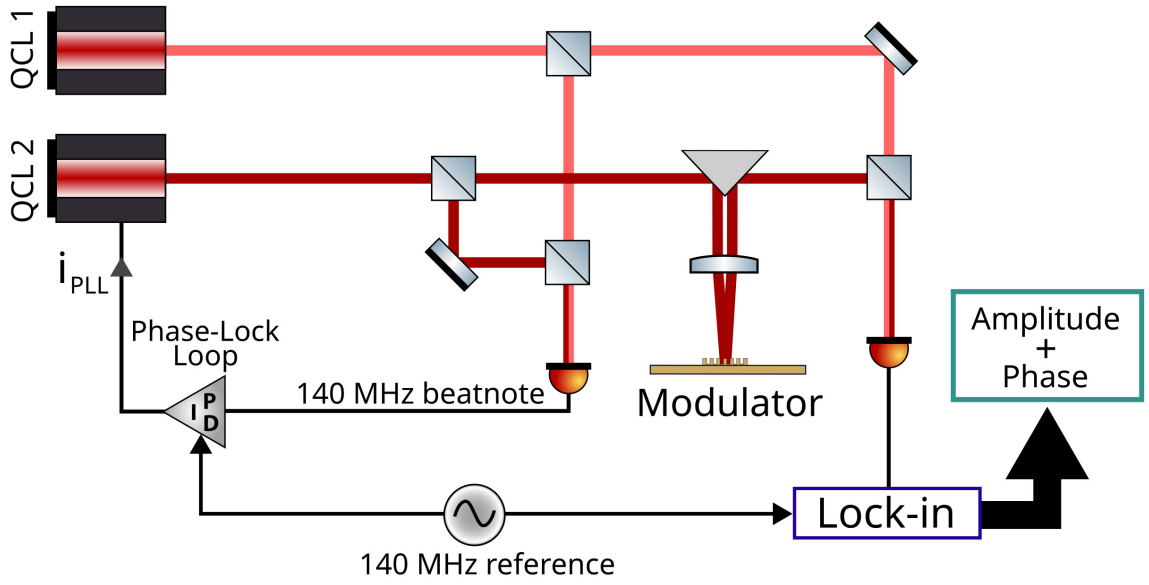

Fig. 4.9 *Heterodyne setup used to measure both amplitude and phase modulation. A first detector receives the beating between the two lasers to measure the frequency difference between them and implement a phase-lock loop with a reference signal at 140 MHz. Before the second detector, the modulator is added on one arm. The second detector sends the beatnote to the lock-in amplifier for demodulation using the same 140 MHz reference.*

Both laser beams are divided by beamsplitters into the two arms. In each arm, both lasers are recombined on an MCT detector. We assume perfect 50/50 beamsplitters. The first arm is used for phase locking of the two lasers. The electric field on the first detector can be written as:

$$E_{det1}(t) = E_{1,0}\exp(i(\omega_0 t + \phi_1(t))) + E_{2,0}\exp(i((\omega_0 + \Delta\omega)t + \phi_2(t))) \tag{4.5}$$

where ω_0 is the frequency of interest, 9 µm, $\Delta\omega$ the frequency difference between the two laser sources, ϕ_1 and ϕ_2 the phase of the first and second beam respectively, and $E_{i,0}$ the amplitude of the electromagnetic field emitted by the laser i after the two beam-splitters. The heterodyne signal generated by the first detector reads (without the high frequency signal):

$$I_{det1}(t) \propto |E_1(t) + E_2(t)|^2 = |E_{1,0}|^2 + |E_{2,0}|^2 + 2E_{1,0}E_{2,0}\cos(\Delta\omega t + \phi_1 - \phi_2) \tag{4.6}$$

The beating at $\Delta\omega$ is injected in a phase-lock loop to compare it with a pure sine reference at 140 MHz and correct the current of one of the lasers so as to keep them locked in phase, i.e. $\phi_1 = \phi_2$.
On the second arm, the modulator will modify the amplitude and the phase of the laser 2,

depending on the voltage applied on it. While the lasers are locked, we can write the electric fields arriving on the second detector:

$$\begin{aligned} E_{1,arm2}(t) &= E_{1,0}\exp(i\omega_0 t) \\ E_{2,arm2}(t) &= E_2(V)\exp\Big(i(\omega_0+\Delta\omega)t+\phi_{mod}(V)\Big) \end{aligned} \tag{4.7}$$

The amplitude in the second arm $E_2(V)$ is defined through the reflectivity of the modulator $R(V)$ as $|\frac{E_2(V)}{E_{2,0}}|^2 = R(V)$.

The second detector receives the square modulus of the sum of the two electric fields, generating a heterodyne current I_{det2}:

$$I_{det2}(t) \propto |E_{1,0}|^2 + |E_2(V)|^2 + 2E_{1,0}E_2(V)\cos\Big(\Delta\omega t+\phi_{mod}(V)\Big) \tag{4.8}$$

The beatnote generated at the frequency $\Delta\omega$ carries the phase $\phi_{mod}(V)$ introduced by the modulator, that can be retrieved using a lock-in detection at the reference frequency, 140 MHz. The frequency modulation imposed by the modulator has to be slow enough to be in the bandwidth of the lock-in. In our case, the modulation frequency was 30 kHz and the bandwidth 100 kHz. The phase output of the lock-in amplifier, as well as the amplitude, are sent on an oscilloscope where they are averaged 128 times to reduce the noise. The results are plotted in Fig.4.10. Multiple time traces of the phase (in pink) and the amplitude (in light blue) are superimposed and plotted as a function of the bias applied on the modulator. We chose the size of the resonator to maximize the phase sensitivity to the bias at the laser energy 137 meV (the reflectivity and phase maps of Fig.4.8 correspond to this sample: $s = 1.22$ µm). This leads to a poor amplitude modulation, which explains the larger noise observed for the amplitude.
The traces are averaged numerically (full lines) and compared to the simulated values (dashed lines). The effective mode index used in the simulation was 3.73 to fit the experimental results. This comparison for the phase works quantitatively but only because of the correction factor β applied on the absorption amplitude, heavily influencing the phase shift. However, these results are consistent with the spectra of Fig.4.4. The comparison for the amplitude is only qualitative here because we did not calibrate the power, but the trend is similar.

A maximum phase modulation of 12° between -2 V and +4 V is observed. According to the simulation, this device could go up to 16° between -2 V and +10 V. A 40 nm thinner device, better tuned to the laser wavelength would be able to modulate the phase over 26° between -10 V and +8 V.

In our setup, the phase modulation was very sensitive to feedback i.e. when a fraction of the laser power is reflected back by the modulator and injected in the QCL cavity. Using optical densities, absorbing 90 % or 99 % of the power in the arm just before the modulator reduced this effect (the reflected beam is absorbed twice). We observed in the "feedback" regime that the phase modulation was not constant with the frequency though we were within the electrical bandwidth, while the amplitude modulation stayed constant. Playing with the incidence angle of the modulator and the optical densities, we managed to find configurations

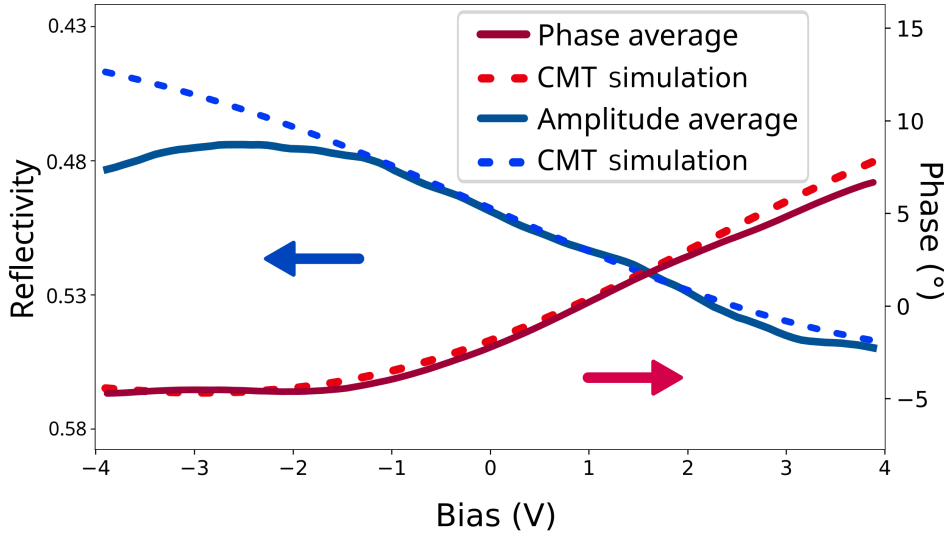

Fig. 4.10 *Phase and amplitude modulation with the stripe Stark modulator, measured simultaneously with the double heterodyne setup, as a function of the applied bias. The averaged experimental data (full lines) is compared to the CMT simulation (dashed). Experimental amplitude modulation is rescaled on the reflectivity scale of the CMT.*

where the phase response was flat as a function of the modulation frequency. In that configuration, we estimate that the observed modulation is indeed induced by the modulator. The data presented in Fig.4.10 were acquired in such configuration.

4.1.4 Conclusions

I investigated Stark modulators embedded in resonator metamaterials. Initially investigated for their reduced size and increased light-matter interaction, their operation and optimization proved more complex than those of their mesa counterparts. The benefits in terms of electrical bandwidth (with identical optical footprint) is significant and could even be increased if patches are used instead of stripes.

In terms of modulation depth, the results obtained were inferior than with the mesa (28% vs 47%). The comparison is nevertheless limited for practical data transmission. In the case of the mesa, $\simeq 60\%$ of the power is lost because of reflection at the facets, and the modulation depth concerns only the light that was coupled in the mesa: the difference between the level 1 and the level 0 in power on the detector is therefore $P_1 - P_0 \simeq 0.2 P_{laser}$ where P_{laser} is the initial laser power. On the other hand, with the metamaterials presented in Fig 4.4 (a), $P_1 - P_0 \simeq 0.25 P_{laser}$. In terms of modulated power at the output of the modulator, the new system is thus actually competitive, as long as the detector does not saturate.

I would also like to points out that the handling of the device used in reflection is significantely more user friendly in terms of optical alignment. It nevertheless brings a new

difficulty with the risk of feedback into the laser. If this issue is rather easy to bypass by playing with the alignment for amplitude modulation, this becomes much more challenging for phase modulation. The fabrication of efficient isolators at this wavelength might become critical for this kind of development to become possible.

4.2 Metamaterial quantum cascade detector

In this section I will present metamaterial quantum cascade detectors grown on InP.

4.2.1 Design of InP diagonal QCD

The working principle of Quantum cascade detectors was presented in Chapter 1, and an example is shown in Fig.4.11. Designing a new QCD active region consists in optimizing the product between the absorption efficiency in the active well (levels 1 and 2), and the extraction probability of the photoexcited electrons towards the next period (levels 2 to 5 of the cascade). We chose in this work to focus on the design of a diagonal QCD given the versatility of the Stark modulator: if the detector does not work exactly at the targeted energy because of a discrepancy between simulations and growth, we can adapt the design of the metamaterial for the modulator, while the design of the QCD is robust enough with respect to a variation in the size of the QWs [39].

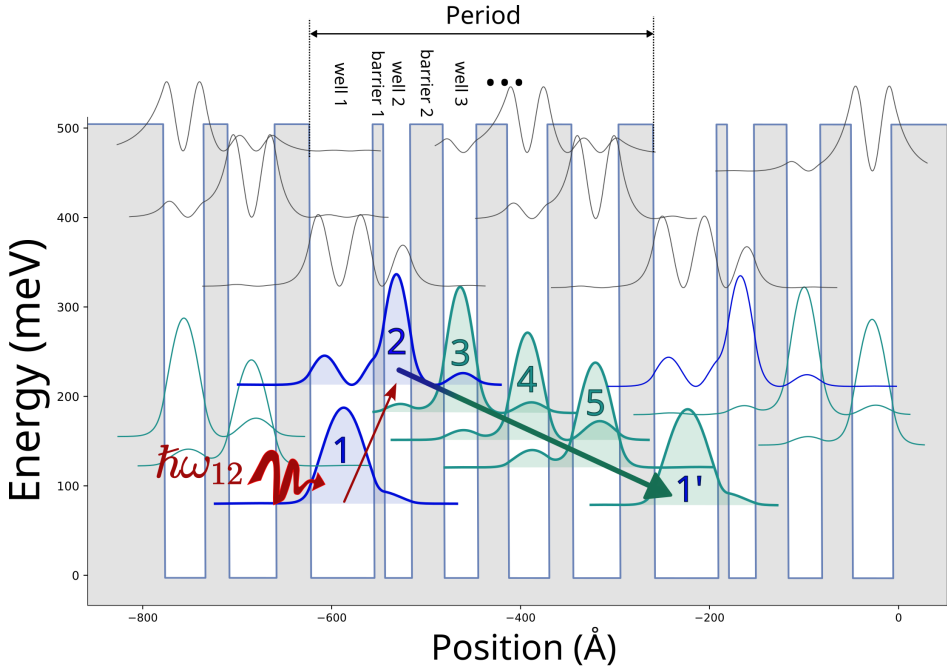

Fig. 4.11 *Conduction band profile and square moduli of the wavefunctions for the initial structure for a diagonal QCD. Relevant wavefunctions are highlighted with color fillings. Levels 1 and 2, in blue, are responsible for the photon absorption. Levels 2 to 1' in green form the cascade, responsible for the extraction of an excited electron in 2 to the next period.*

Intuitively, most of the optimization procedure occurs in the wells where the absorption

takes place and the thin barrier between them: by delocalizing the second level toward the extractor, we reduce limit the absorption efficiency but increase the extraction probability. In the next section, we will show how we tried to find a structure optimizing the product of these two quantities.

In order to design a diagonal QCD, we start from the following requirements:

- The first couple of wells should be designed in order to have an absorption energy E_{12} close to 137 meV.
- The wells in the extractor should be designed such that their states are separated by the energy of a LO-phonon to maximize the scattering rate.
- The first well is rather large in order to have the ground state of the transition close to the bottom of the conduction band.
- The width of the first thin barrier should not be less than 1 nm to avoid the formation of a quaternary alloy, as discussed in Section 2.3.

The previous requirements are satisfied by the InGaAs/AlInAs structure shown in Fig.4.11 and defined by the following thicknesses (in nm) of the layers (InGaAs wells are in bold): **6.2**,1.5,**2.8**,4.0,**3.5**,3.2,**4.2**,2.5,**4.9**,3.6. This structure will serve as a starting point for the optimization procedure.

We assume that an electron in the extractor can only relax towards lower energies. The escape probability in the diagonal QCD is then the product of the escape probabilities from each level of the extractor:

$$p_{esc} = \prod_{i=2}^{N} \frac{\tau_{i\to 1}}{\tau_{i\to i+1} + \tau_{i\to 1}} \tag{4.9}$$

The absorption efficiency of the electron gas confined in the state 1 for light polarized along the growth direction is calculated at resonance following Eq. 1.13 as:

$$\alpha_{2D} = \frac{e^2 k_B T}{2\varepsilon_0 c n \hbar} f_{12} \ln\left[\frac{1+\exp\left(\left(E_F - E_1\right)/k_B T\right)}{1+\exp\left(\left(E_F - E_2\right)/k_B T\right)}\right] \frac{1}{\pi\gamma} \tag{4.10}$$

The quantum design of the structure is then optimized using a Python code I developed. The results of the Schrödinger equation are plugged into this program, that identifies the relevant wells and wavefunctions in the structure for the absorption and the extraction, and gathers the corresponding energies, lifetimes, and oscillator strengths. The detector characteristics (p_{esc},α_{2D}, R) are finally computed.

For the initial structure, we obtain $p_{esc} = 0.62$ and $\alpha_{2D} = 2.6 \cdot 10^{-3}$, leading to a responsivity $R = \frac{e\lambda}{hc}\eta_{abs} p_{esc} = 16.9$ mA/W for a single period device illuminated at 45°.

The size of the wells and barriers are then modified to see their impact on the structure, with a resolution of 1 Angstrom. An example is given in Fig.4.12, which presents one step during the optimization of the QCD heterostructure. The responsivity is evaluated as a

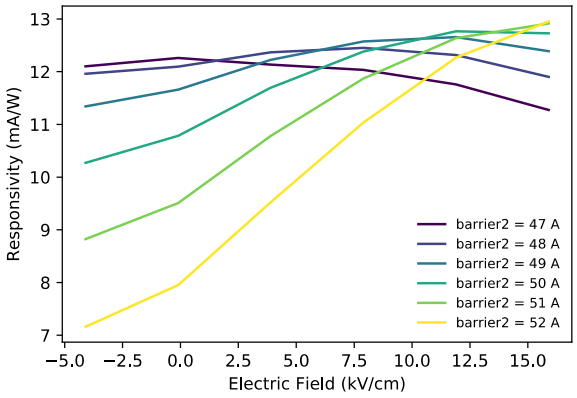

Fig. 4.12 *Calculated responsivity of the QCD presented in Fig.4.11 while varying the thickness of the second barrier in the structure.*

function of the bias, for thickness of the second barrier from 4.7 nm to 5.2 nm. 4.8 nm would be chosen before moving forward in this example.

We started with the first barrier and second well because it seemed they are the most critical parameters and looked for a local maximum of R at zero bias. As expected intuitively, increasing the size of the barrier increases p_{esc} but reduces η. The responsivity is maximal for a barrier size slightly smaller than 1 nm, but we chose 1.1 nm to satisfy the requirements of the epitaxial growth.

The thickness of the second barrier is also quite important: when it is too thin, the extraction is maximal, but the absorption is smaller because the wavefunction of state 2 becomes delocalized, reducing the oscillator strength. When considering the states further down in the extractor, the choices are simpler and less impactful: levels should be separated by the energy of a LO-phonon and barriers are kept large enough to forbid relaxation to 1, but thin enough not to have scattering times larger than a few *ps*. Fixing the best parameters every time, we adjusted each level of the cascade in the same manner and started over until converging to a structure. Adding a supplementary well in the beginning of the extractor to create a miniband and separate further the doped wells from one another proved also beneficial.

The final QCD structure used for the rest of this work is represented in Fig.4.13. The thicknesses (in nm) are the following: **6.7**,1.1,**2.8**,4.9,**3.2**,3.5,**3.5**,3.5,**3.7**,3.4,**4.9**,3.3 (InGaAs in bold). The escape probability is computed to be 84% at zero bias, and the 2D absorption $\alpha_{2D} = 3.3 \cdot 10^{-3}$, leading to a responsivity per period of 29 mA/W for a mesa illuminated through a facet at 45°.

To conclude, this method allowed us to design a diagonal QCD at the target energy with a low computational time and power, using a simplified model for the extraction. The risk of this optimization workflow is to get stuck in local extrema of the parameter space constituted of all the well and barrier sizes. A more rigorous approach would use optimization algorithm such as differential evolution algorithm [119],[120] for instance.

The last decisions to take in order to prepare the growth sheet are the number of periods

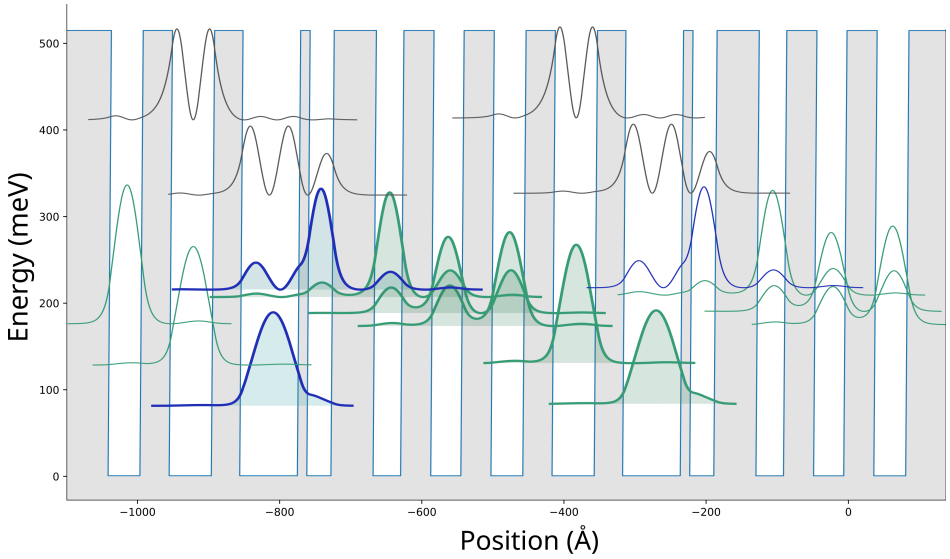

Fig. 4.13 *Conduction band profile and square moduli of the wavefunctions of two periods of the QCD structure designed and used in the following work. Absorption (in blue) and extraction (in green) states are highlighted in the central period.*

and the doping levels of the active wells.

Due to the diagonal design, even for a high electronic density, the metamaterial device will operate in the weak coupling regime. We chose a doping of $n_{3D} = 1 \cdot 10^{18}$ cm^{-3}. Concerning the number of wells, it will set the photoconductive gain and the total thickness of the structure. As seen in Section c), we have to find a compromise between the bandwidth and the responsivity. We decided to set $N = 9$, for a total height without contacts of 416 nm.

4.2.2 Presentation of the sample and metamaterial design

The QCD was grown by MBE at ETH Zürich by Mattias Beck in the group of J. Faist (EU2863). The growth sheet can be found in Appendix. Fig.4.14 shows the transmission spectrum of the QCD measured in a multipass configuration, as well as the photocurrent spectrum taken with a mesa at 78K. Though designed to work at 137 meV, the absorption is centered around 122 meV. The fact that the QCD works despite this discrepancy confirms the efficiency of the diagonal design of QCDs. The miniband at the beginning of the extractor of the QCD likely offers a supplementary safeguard. The fitted FWHM of the photocurrent spectrum is 17 meV and that of the transmission peak is 24 meV.

Before designing the most adapted metamaterial for this QCD, we first studied the reflectivity spectra of passive devices. Fig.4.15 (a) shows the reflectivity spectra (in blue), taken at ONERA, of large arrays of stripes containing the QCD active region. The spectra were then fitted (green) using the CMT with the set of parameters in Table 4.2.

The non radiative losses, as well as the mode index, have the same values as the modulator ones, as expected. The radiative losses are on the other hand much lower. The difference of thickness between the two samples explains most of it as $\Gamma_{a,0,QCD}/h_{QCD} = 1.16 \cdot \Gamma_{a,0,mod}/h_{mod}$. As anticipated for a diagonal QCD we have $\Omega_r^2 < \frac{1}{2}\gamma_P^2$, so the devices will operate in the weak coupling regime no matter the periodicity.

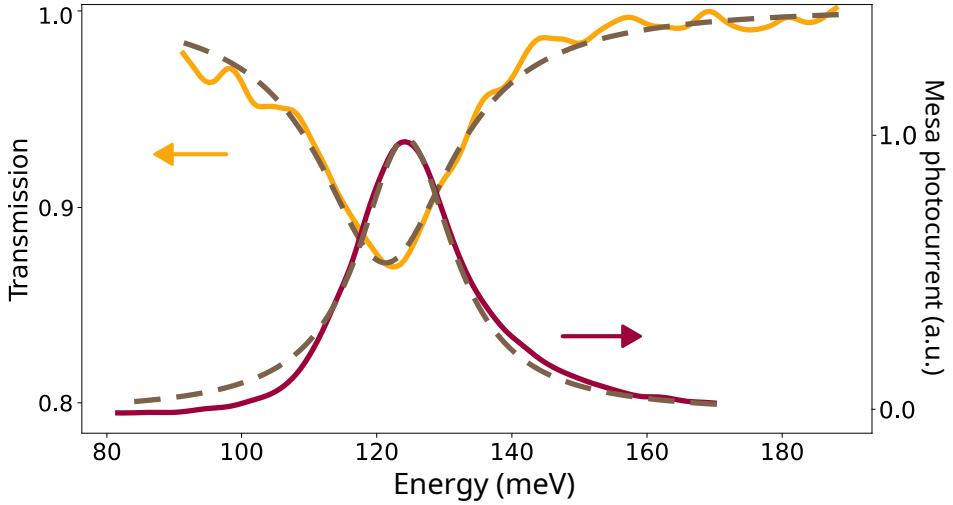

Fig. 4.14 *Transmission spectrum in multipass configuration and photocurrent from a mesa device at 78K and -200mV bias for EU2863 QCD.*

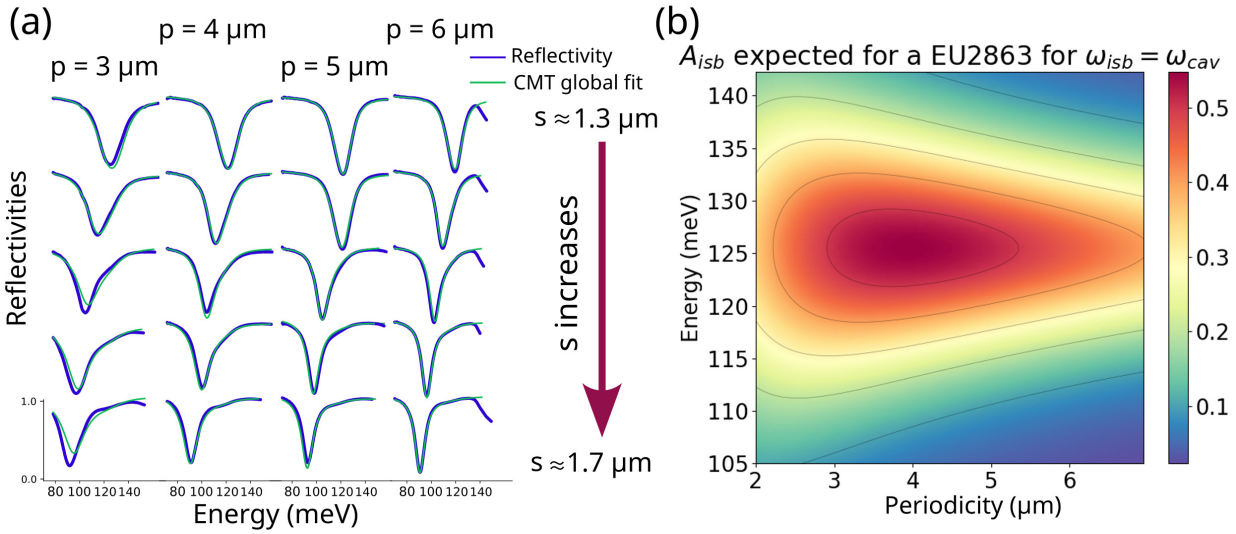

Fig. 4.15 *(a) Spectra of passive arrays of EU2863 QCD for different periodicities (3, 4, 5, 6 μm) and width (s ∈ [1.3 μm, 1.8 μm]). (b) ISB absorption spectrum simulated for the QCD as a function of the periodicity.*

QCD Stripes				
$\Gamma_{a,0}$ meV·μm^2	γ_a meV	γ_P meV	Ω_r meV	n_{eff}
87	2.5	16.9	6.9	3.6

Table 4.2: CMT parameters for EU2863 QCD extracted from passive arrays of metamaterials.

In Fig.4.15 (b) we plotted the A_{isb} spectra as a function of the periodicity in order to find the most adequate parameter for the design of the metamaterial. In this plot, the resonant energy of the cavity was chosen to be equal to the plasma-shifted ISB transition energy, assuming the electronic density extracted from the fits. Since the system is always

in the weak coupling regime, we can fix in advance the same cavity size (s=1.39 µm in the simulation) for all periodicities. From Fig.4.15 (b) we decided to fix $p = 4$ µm.

This choice of periodicity is linked also to the thickness fixed earlier. Had we chosen a smaller number of periods, the resulting optimal p would be smaller, which would lead to more complicated etchings. Fig.4.16 confirms that this choice of couple (H,p) is adequate and the simulations consistant: for $p = 4$µm, $H \simeq 400$ nm allows maximizing the ISB absorption in the cavity, which partially mitigates the drop in responsivity associated with the photoconductive gain.

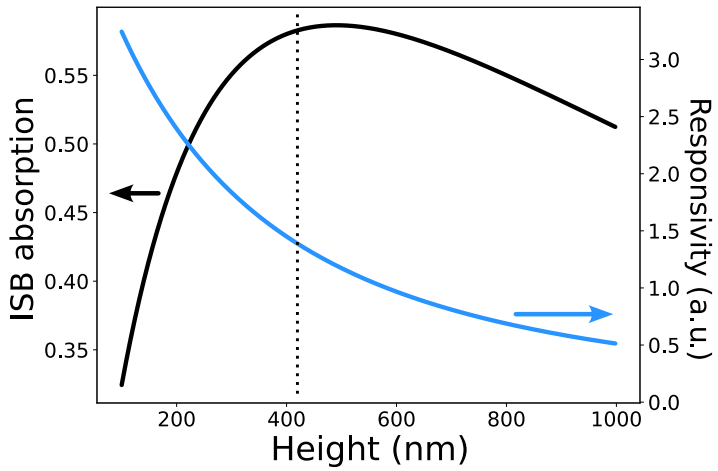

Fig. 4.16 *Simulated ISB absorption and responsivity of the QCD, with p=4 µm and width set to have the cavity mode resonant with the ISB transition, as a function of the thickness of the stripe.*

4.2.3 Responsivity of the metamaterial QCD

After fabrication using the same process as for the modulator, the devices were characterized in responsivity at room temperature. We fabricated 5 different sizes of resonator (s= [1.21, 1.27, 1.33, 1.40, 1.46] µm), around the simulated best value of s=1.39 µm. Fig.4.17 shows the responsivity spectra for all the resonator sizes, as well as the corresponding reflectivity spectra of the finished devices.

As expected, the reflectivity spectra display a unique resonance, indicating that the devices operate in the weak coupling regime. When increasing the size of resonator, the reflectivity peak shifts towards lower energy and the shape is only slightly deformed by the ISB transition.

Contrarily to the reflectivity, the shape of each photocurrent spectrum, as well as its magnitude, is heavily dependent on the size of the resonator. The responsivity spectra were calibrated from the measure of the responsivity of the device $s = 1.33$ µm under illumination by the tunable laser emitting 50 mW at 123 meV. This responsivity, reaching 26 mA/W at 124 meV for this device, was increased 10-fold with respect to the value obtained with a mesa processed on the same wafer, evaluated at 2.6 mA/W at room temperature and zero bias. This increase in the responsivity can be explained by the quality factor of the cavity at this

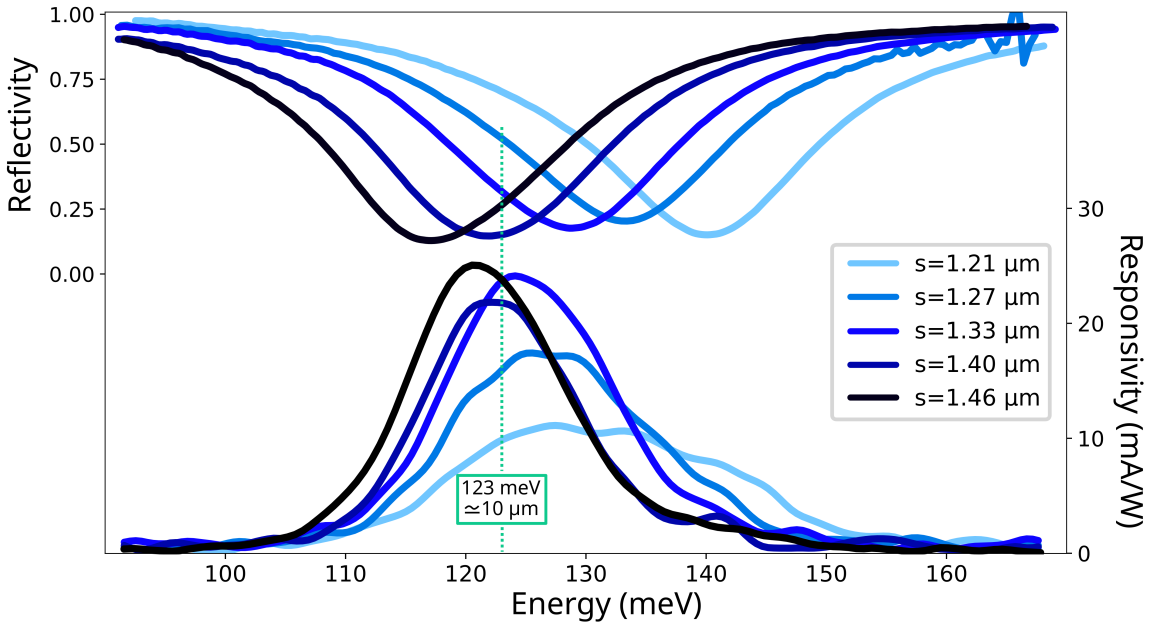

Fig. 4.17 *Reflectivity and responsivity spectra for different metamaterial width of the EU2863 QCD. The responsivity spectra were taken at room temperature and zero bias.*

energy $Q = \frac{\omega_{12}}{\Gamma_a + \gamma_a + \gamma_P} = 10.3$ and interpreted simply as an increase of the light-matter interaction length due to the cavity.

The measured absorptivity and the responsivity lead to an external efficiency (number of electrons detected per incoming photon) of 0.53% for the best device.

The shape of the photocurrent observable in Fig.4.17 does not correspond to that of the CMT simulation of the ISB absorption (plotted in Fig.4.18), though the total cavity absorption is correctly fitted. Indeed, the measured photocurrent and the ISB absorption in the cavity are mediated by the transport in the heterostructure. This observation indicates that the function describing the transport in the structures should be energy-dependent.

In order to experimentally access this quantity, we divide the responsivity spectra by the measured absorptivity. Fig.4.19 (a) shows the resulting transfer function for each device, corresponding to the ratio of electrons in the circuit created by the photons absorbed in the cavity. In other words, this function is the external extraction efficiency of the impinging photons. The transfer functions obtained for all the stripe sizes have the same shape and are actually almost identical, as it should be since this function is only dependent on transport in the heterostructure. Fig.4.19 (b) shows the transfer function for the device with s=1.33 µm, and its Lorentzian fit. All devices were fitted (not shown) and we obtain a resonance at 123.4±0.2 meV and a width of 20.7±1.7 meV. We will call the transfer function $TF_{QCD}(\omega)$. The variation of the amplitude of the function between devices is attributed to a variation of the alignment for the measurement of the photocurrent.

Fig.4.20 shows the reflectivity simulated by the CMT, as well as the product of the total

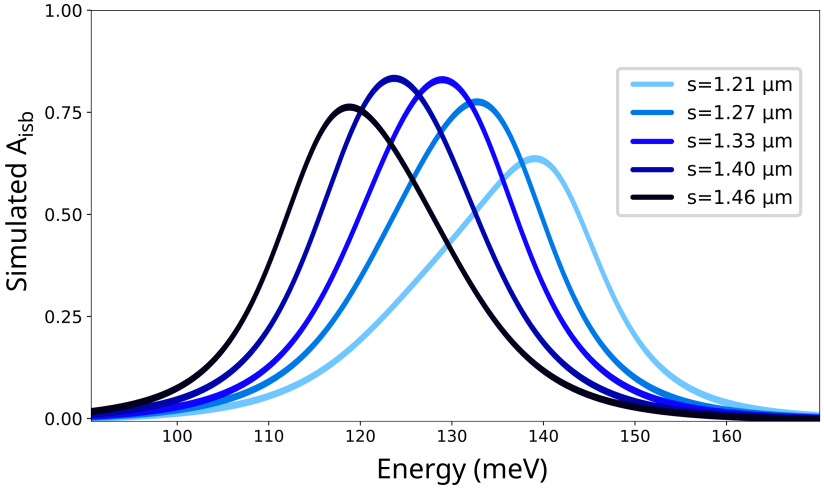

Fig. 4.18 *A_{isb} simulated by the CMT for the metamaterial QCD for different stripe widths. The parameters of the simulations are the losses of Table 4.2.*

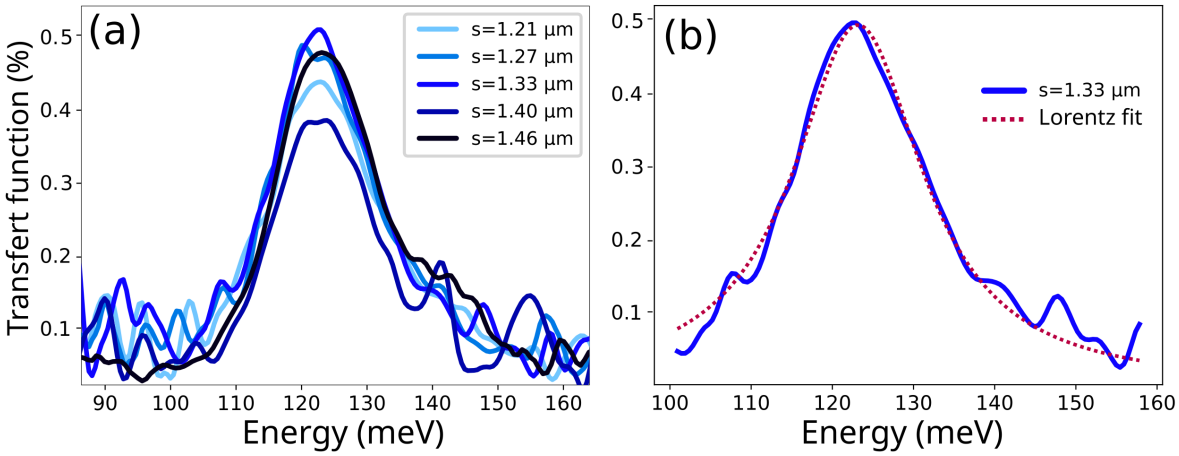

Fig. 4.19 *(a) External efficiency for different stripe widths. (b) Transfer function for the device with $s = 1.33$ µm and its Lorentzian fit.*

absorptivity (1-reflectivity) by the transfer function, for each resonator size. These spectra reproduce very well the shape and amplitude of the measured photocurrent.

The microscopic origin of the transfer function TF_{QCD} is not immediate. In the following, we try to obtain an alternative expression, starting from the ISB absorption A_{isb} instead of the cavity one A_{tot}.
Going back to the CMT equations discussed Chapter 3, we can express the ratio $\frac{A_{isb}}{A_{tot}}$ in the general case. The starting point is the time evolution of the polarization:

$$\frac{dP}{dt} = i\tilde{\omega}_{isb}P - \gamma_P P + i\Omega_r a \tag{4.11}$$

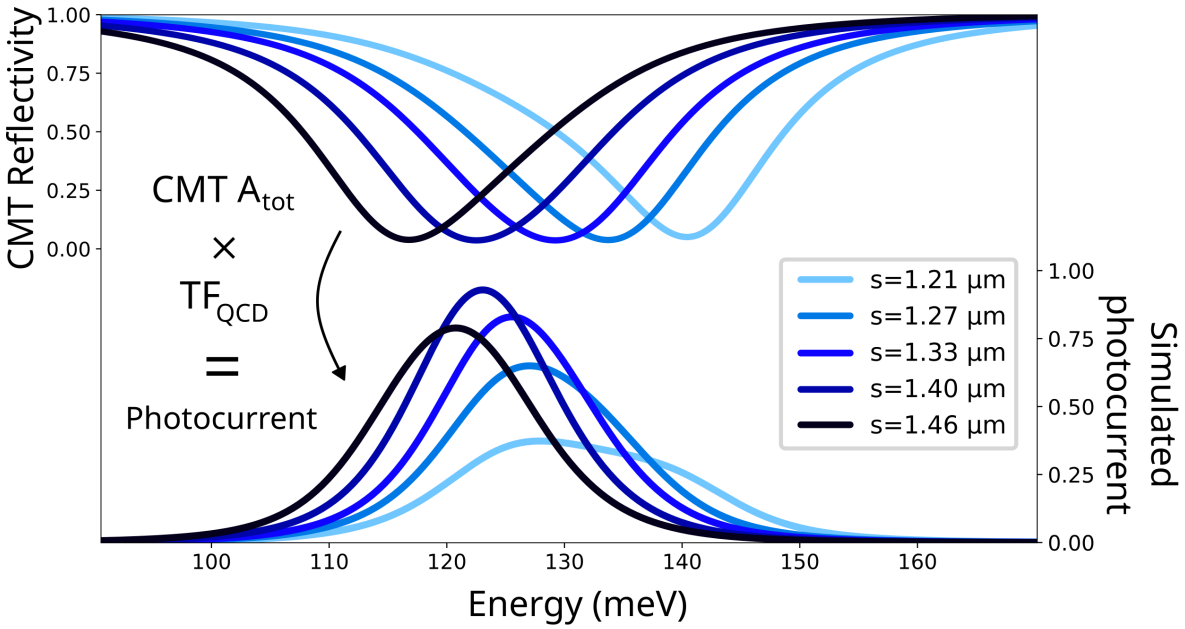

Fig. 4.20 *Reflectivity (on top) simulated with the CM. On the bottom, the absorptivity is multiplied by the Lorentzian transfer function (centered at 123.4 meV with a width of 20.7 meV) to simulated the photocurrent.*

In the forced oscillation regime, we find: $\frac{a}{P} = \frac{(\omega - \tilde{\omega}_{isb})^2 + \gamma_P^2}{\Omega_r^2}$ and subsequently $\frac{A_{isb}}{A_{tot}}$:

$$\begin{aligned}\frac{A_{isb}}{A_{tot}}(\omega) &= \frac{\gamma_P |P|^2}{\gamma_a |a|^2 + \gamma_P |P|^2} = \frac{1}{1 + \frac{\gamma_a |a|^2}{\gamma_P |P|^2}} \\ &= \frac{\Omega_r^2 \gamma_P / \gamma_a}{\Omega_r^2 \gamma_P / \gamma_a + \gamma_P^2 + (\omega - \tilde{\omega}_{isb})^2} \equiv \mathcal{L}_{tot \to isb}(\omega) \end{aligned} \tag{4.12}$$

We recognize another Lorentzian function, peaked at $\tilde{\omega}_{isb}$ with a FWHM of $2\sqrt{\Omega_r^2 \gamma_P / \gamma_a + \gamma_P^2}$. Numerically, the amplitude is 0.58 and the FWHM is 52 meV. Interestingly, this function depends on the cavity through the non radiative losses. This is because we initially supposed that the ISB transition did not couple directly with the free space. This also means that this function does not depend on the parameters chosen for the metamaterial fabrication (s, p). We can therefore now write the photocurrent as a function of the ISB absorption, TF_{QCD} and this new Lorentzian function $\mathcal{L}_{tot \to isb}$ for all the devices:

$$I_{photo} = A_{isb} \cdot \frac{TF_{QCD}}{\mathcal{L}_{tot \to isb}} \tag{4.13}$$

Though this last step is simply a reformulation, we have now separated the photocurrent into a term purely related to the photon absorption, known from the CMT, and a term only related to the transport in the heterostructure, independent on the device parameters. This second term is the internal extraction efficiency η_{int}. The escape probability can then be deduced: $\eta_{int} = \frac{TF_{QCD}}{\mathcal{L}_{tot \to isb}} = \frac{p_{esc}}{N}$. For this QCD, we plot in Fig.4.21 the internal efficiency (in orange) and the external extraction efficiency related to the total absorption of the cavity

(in red).

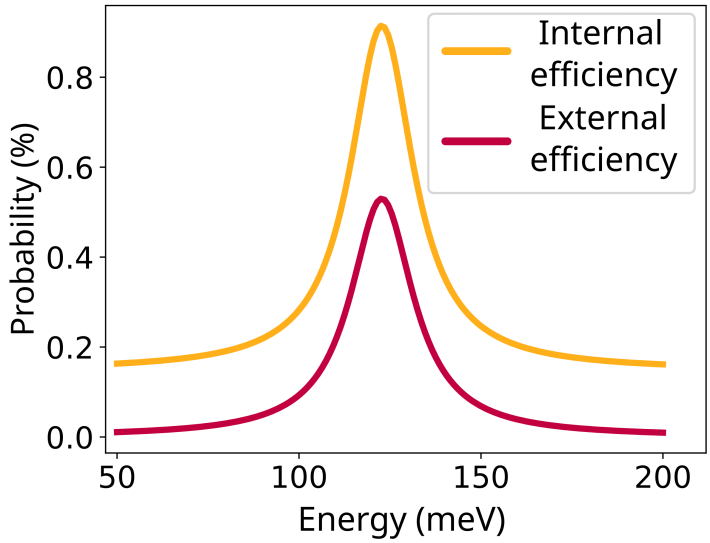

Fig. 4.21 *Internal/External efficiencies linking ISB/cavity absorption and photocurrent in the QCD.*

Taking advantage of the Lorentzian expression of the functions involved, after some calculation, we can write:

$$\begin{aligned} p_{esc} &= \frac{TF_{QCD} \cdot N}{\mathcal{L}_{tot \to isb}} \\ &= \frac{N}{A_{\mathcal{L}_{tot \to isb}}} \left(1 - \left(\frac{\Gamma_{TF_{QCD}}}{\Gamma_{\mathcal{L}_{tot \to isb}}}\right)^2\right) TF_{QCD} + \left(\frac{A_{TF_{QCD}}}{A_{\mathcal{L}_{tot \to isb}}}\right) \cdot \left(\frac{\Gamma_{TF_{QCD}}}{\Gamma_{\mathcal{L}_{tot \to isb}}}\right)^2 \end{aligned} \tag{4.14}$$

where the Γ_i's are the FWHM of the Lorentzian functions i and A_i's their amplitudes. For this calculation, we identified the peak of TF_{QCD} with $\tilde{\omega}_{ISB}$. This allows us to cast the transport function linking ISB absorption and photocurrent of the QCD into a Lorentzian function peaked at $\tilde{\omega}_{isb}$, sitting on a constant. The escape probability is thus not a scalar function but this new peaked function. The fact that the maximum of this transport function is at the same energy as the ISB absorption (strictly in the calculation and very close experimentally) means that the extractor is correctly aligned with the absorption level.

The value at resonance of p_{esc}, estimated here to be almost 8 %, is surprisingly low with respect to the simulations (84 % !) and the literature regarding the diagonal QCD. The previous remark regarding the peak energy of the transport function implies that the issue does not lie in a misalignment of the levels between simulations and epitaxy. The problem then would lie in the estimation of the escape probability, and the hypothesis that transport in the "wrong" direction is negligible. This is especially true at high temperature, where phonon absorption is more efficient.

In order to close the loop, we can go back to the mesa and consider this shape for the escape probability function and multiply it by the absorptivity deduced from Fig.4.14. The

expected photocurrent is therefore the product of the fitted absorptivity and p_{esc}.

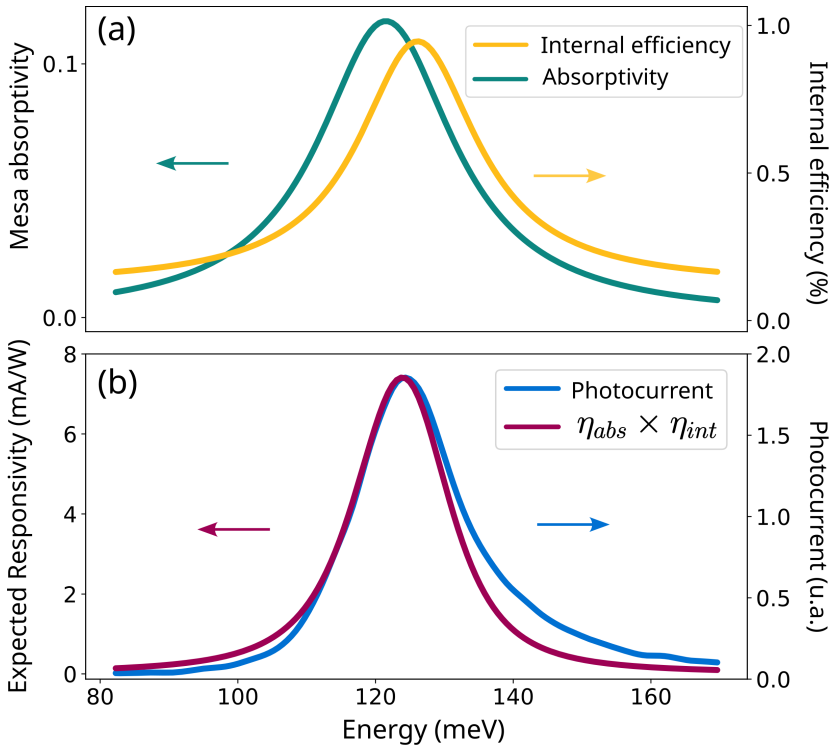

Fig. 4.22 *Renormalized simulation of the mesa photocurrent (purple) using the fitted absorptivity (green) of the heterostructure and the extraction efficiency (yellow). The experimental photocurrent is plotted in blue.*

This simulation works very well to reproduce the peak (slightly shifted from the absorption) and its lower energy tail. On the other end, the high energy skewness is missing. The complete behavior could be better captured by a more precise fitting of the transfer function in Fig.4.19. An asymmetry is distinguishable but the limited signal-to-noise ratio makes this exercise hazardous. Quantitatively, this absorptivity and internal efficiency lead to an expected peak responsivity of 7.3 mA/W, which is slightly less than 3 times the measured responsivity. The discrepancy with this estimation comes from the absorptivity measurement, in multipass. The sample is approximately 2 mm-long and 300 µm-thick. With an incoming light at 45°, these dimensions correspond indeed to three reflections on the gold in geometrical optics picture, and leads to a quantitative agreement between those measurements.

4.2.4 Performances of the metamaterial QCD detectors

As we have seen in Fig.4.17, the peak responsivity of the best device operating at 10 µm wavelength is 26 mA/W at room temperature and zero bias. In Fig.4.23 (a), we present the measured dark current as a function of the bias for the device with $s = 1.33$ µm , and the current under illumination using a laser at 10 µm, with bias between -1 V and +0.5 V. We deduced the photocurrent by subtrating the two. Knowing the impinging power (27 mW), we plotted in red the responsivity as a function of the bias. Black lines at 0 V and 0 mA show the photovoltaic operation point, without dark current.

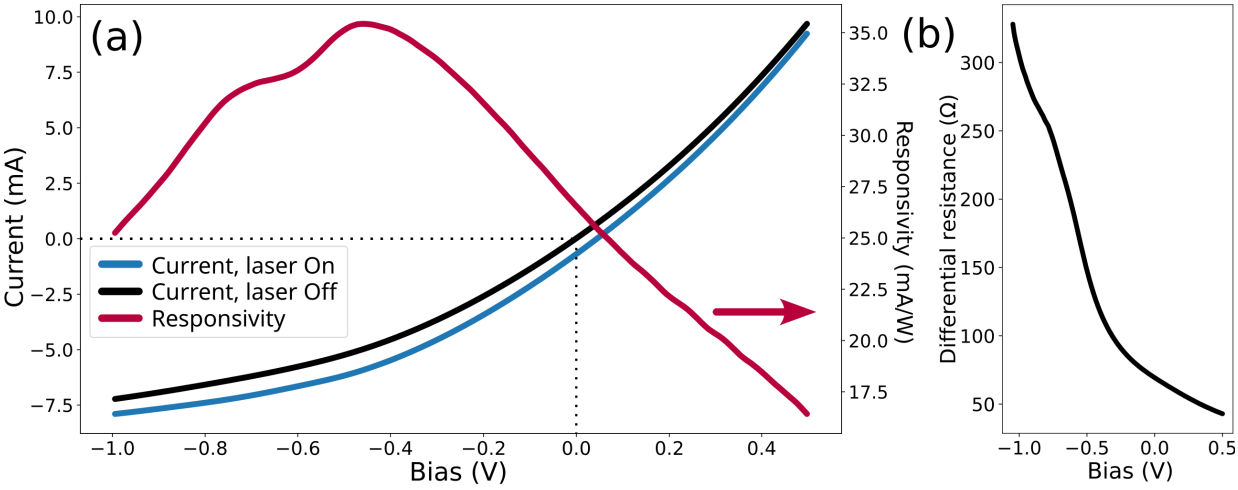

Fig. 4.23 *(a) Dark current (black) and current under illumination (10 µm, 27 mW) (blue) for the s = 1.33 µm metamaterial QCD, and deduced responsivity (red) as a function of the bias. black lines prolongate 0 V bias and 0 mA current. (b) Differential resistivity of the device over the same bias range.*

A maximum of the responsivity is observed at -0.45 V which corresponds to an electric field of 11 kV/cm. This is the field necessary to properly align the excited state of the ISB transition with the extractor.
In (b), we extracted from the dark current the differential resistance of the device, which is helpful to estimate the Johnson noise. At zero bias, this resistance is 68 Ω.

Finally, the electrical bandwidth of the device with the best peak responsivity (s=1.33 µm) was measured using the rectification method. Fig.4.24 shows the rectified signal as a function of the frequency. The -3dB cutoff is measured at 11 GHz. On top of the expected low pass filter behavior, a first small drop in the rectified current is observed at 4.5 GHz.

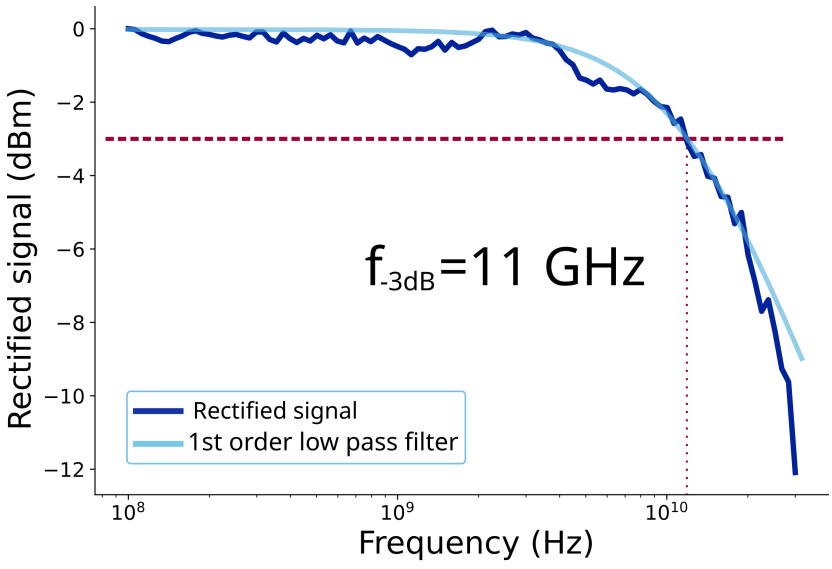

Fig. 4.24 *Electrical rectification of the final metamaterial QCD.*

4.2.5 Conclusions

In this section, I presented an InGaAs/InAlAs QCD design at 10 µm and its processing into an adapted metamaterial. Though the responsivity of the mesa was low with respect to that of state of the art, we showed that it greatly benefited from the metamaterial architecture: responsivity was multiplied by ten with respect to the mesa device, and it has a larger bandwidth thanks to the reduced size. Because the weak coupling regime is imposed by the active region, the optimization of the geometry (s and p parameters) is quite straightforward and does not require any compromise. Further gain in bandwidth can be achieved by using patches or using a thicker active region.

I nevertheless believe that significantly better performances could be obtained with a better optimization of the simulation/growth part of the work, done at the mesa level. They would automatically translate to the metamaterial device.

This platform was also used to show the existence in the photocurrent of an energy filter due to the transport of the electrons in the structure. It would be interesting in a future work to study the evolution of this function with the bias.

4.3 Quaternary QWIPs

The conduction band discontinuity in InGaAs/AlInAs heterostructures, 520 meV deep, makes the design of a 137 meV (9 µm) bound to quasicontinuum QWIP impossible. But having the possibility to engineer the gap of the barrier material using $(\mathrm{InGaAs})_x(\mathrm{InAlAs})_{1-x}$ quaternaries gives us the supplementary degree of freedom necessary to design bound-to-quasicontinuum QWIPs at the right energy. As with the modulators, I. Sagnes, K. Pantzas and G. Beaudoin at C2N developed the method with the MOVPE to have quaternary alloys in order to reduce the energy of the conduction band offset.

4.3.1 Presentation of the active region

The sample is constituted of 13 InGaAs wells, 8 nm thick, and separated by 36.7 nm large InAlGaAs barrier, grown on Si-doped InP. The size of the well ensures an absorption wavelength close to 9 µm, and thanks to the quaternary alloy the transition should be bound-to-quasicontinuum. The doping is $5 \cdot 10^{17}$ cm^{-3}. The choice of Si-doped InP for the substrate forbids any illumination through the wafer, for transmission spectra or mesa photocurrent. It was dictated by processing issues, because usual InP:Fe semi insulating wafer led to rough surfaces after substrate removal. For metamaterial working in reflectivity though, since the original substrate is chemically removed, it is not a problem.
The absorption spectrum, in Fig.4.25 (a), for this sample was therefore measured after the substrate removal, in a reflection setup as shown in Fig.4.25 (b), taking advantage of the gold layer beneath the active region. The angle of illumination is set as close to 90° as possible to maximize the component of the electric field in the growth direction for the polarization selection rule. The final spectrum is obtained by dividing the TM spectrum by the TE one.

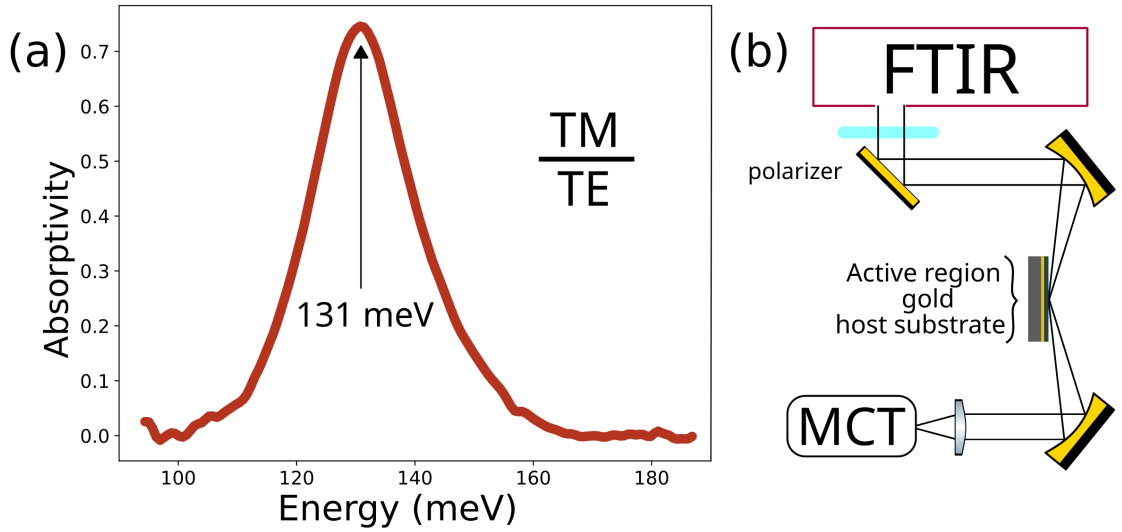

Fig. 4.25 *(a) Absorptivity of the quaternary QWIP V0786. (b) Measurement setup for absorption measurement after wafer bonding and substrate removal.*

The absorption is peaked at 131 meV, and the FWHM is 19 meV. We performed the measure of the activation energy of the QWIP by measuring the dark current flowing in a mesa as a function of the temperature and the bias. Assuming a dark current in the form $I_{dark} \propto e^{-\frac{Ea}{k_b T}}$, we fit $\ln(I_{dark})$ and deduce the activation energy E_a. Fig.4.26 (a) shows the IV dark characteristics and the deduced activation energy. The fit was performed in Fig.4.26 (b) for several biases for temperatures between 78K and 110 K. The calculated Fermi energy

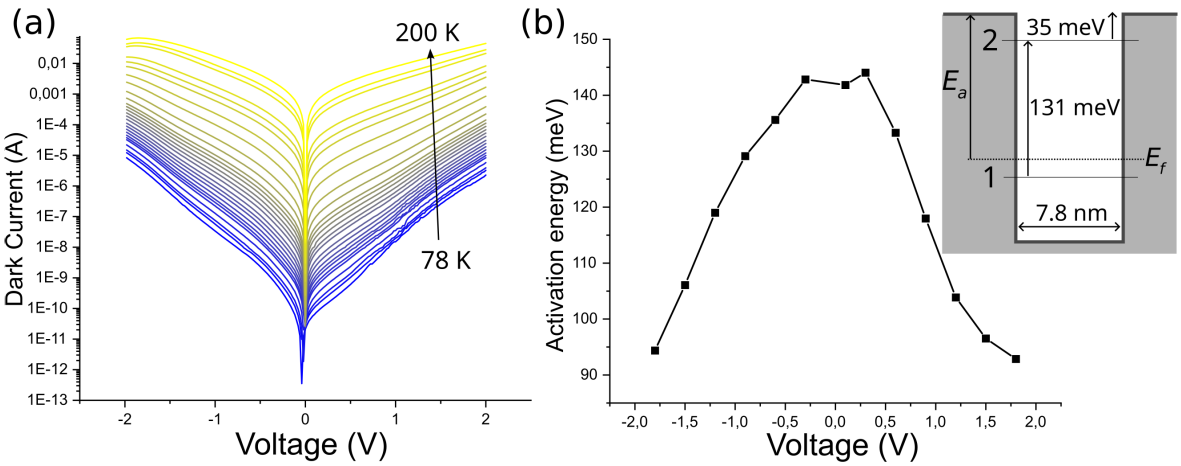

Fig. 4.26 *(a) Dark Current-Bias characteristic of the QWIP between 78 K and 200 K. (b) Activation Energy as a function of the bias. In inset is drawn the bandstructure at zero bias from the spectrum and the activation energy.*

is 24 meV. The activation energy E_a deduced in Fig.4.26 (b) can be expressed given the well parameters as $E_a = V_b - E_1 - E_f - eFL_{well}/2$, accounting for the lowering of the barrier with the field. At zero bias we deduce that $V_b - E_1 = E_a + E_f = 166\,\text{meV} = \tilde{E}_{12} + 35\,\text{meV}$, meaning that the second level is approximately 35 meV below the barrier and not perfectly bound-to-quasicontinuum.

4.3.2 Determination of the metamaterial parameters

Following the same procedure as for the Stark modulator and the QCD, this QWIP was processed into stripe arrays of multiple widths and periodicities of 4 and 7 μm. The reflectivity spectra of the devices were measured using the ONERA setup presented in Fig.4.2 (a). They are presented in Fig.4.27 and 4.31 in respective sections. In Table 4.3 are gathered the values found from the fitting procedure.

Stripes				
$\Gamma_{a,0}$ meV·μm^2	γ_a meV	γ_P meV	Ω_r meV	n_{eff}
119	2.6	5.5	8.6	3.65

Table 4.3: CMT parameters for V0786 QWIP extracted from a fit of the reflectivity spectra of a set of devices with p=4 μm, $s \in [1.25; 1.47]$ and p=7 μm, $s \in [1.02; 1.77]$.

Radiative and non radiative losses of the system are in line with those found in the previous samples. The γ_P value does not match at all the FWHM (Γ_{QWIP}) of the absorption spectrum of the active region. This discrepancy could be due to radiative broadening of the absorption spectrum due to the high angle used. The expression of this broadening $\Gamma_{QWIP} = \gamma_P + cst \cdot \frac{\sin^2(\theta)}{\cos(\theta)}$ [121], indeed shows that broadening can indeed become very large for close to $\pi/2$ angles.

Given the values of Table 4.3, the strong coupling regime is accessible for periodicities higher than 3.8 μm. We processed two types of devices: a set of devices with $p = 4$ μm, at the onset of the strong coupling regime, where we expect the best performances in terms of responsivity, and a set of $p = 7$ μm devices, where we should observe the most pronounced splitting, but still be free of diffraction effects at 9 μm.

4.3.3 $p = 4$ μm devices

a) Spectra

Fig.4.27 shows the measured reflectivity spectra, as well as photocurrent spectra taken at room temperature under a 1 V bias, for each size processed (between 1.25 and 1.47 μm). The reflectivity spectra do show two polaritonic peaks.

Before discussing the shape of the photocurrent spectra in the next section, we focus on the performances of the detector when the cavity mode is resonant with the ISB transition, at 131 meV.

b) Room temperature responsivity and bandwidth

Using the device with $s = 1.36$ μm and a laser at 131 meV, we measured the current with and without illumination for biases inferior to 1.4 V, threshold at which the dark current

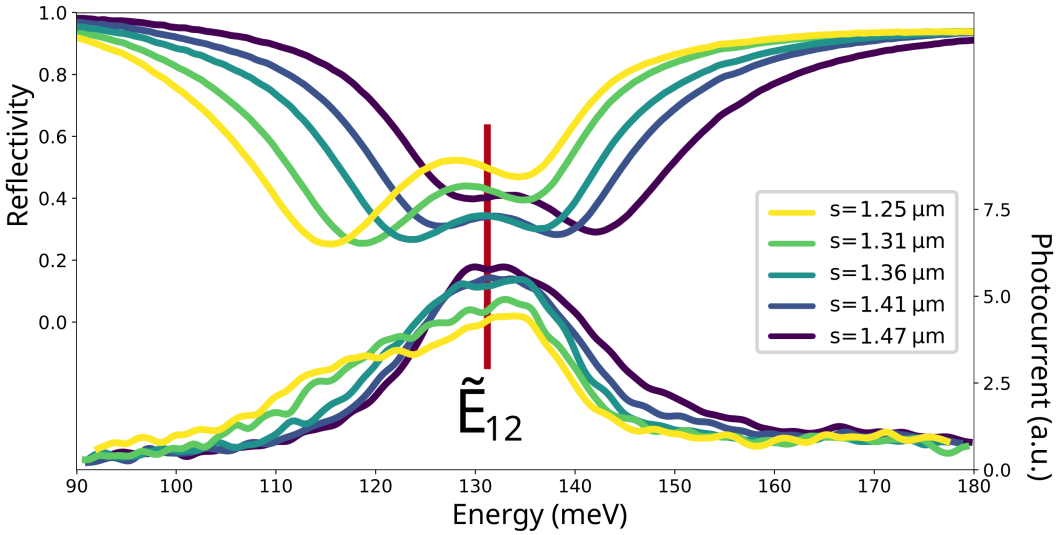

Fig. 4.27 *Reflectivity and responsivity spectra of the QWIP V0786 for different stripe widths for $p = 4\mu m$.*

becomes hazardous for the device (as a rule of thumb, when the total current exceeds 50 mA the device risks breaking). The laser shines directly on the QWIP, placed at the focal point of a 1", F1 lens.

Fig.4.28 shows the background current as well as the photocurrent for bias between 0 and 1.4 V for two different powers of the laser (1 V for higher power because the photocurrent in significant). From the photocurrent and the impinging power we deduce the responsivity at room temperature and 9.4 µm.

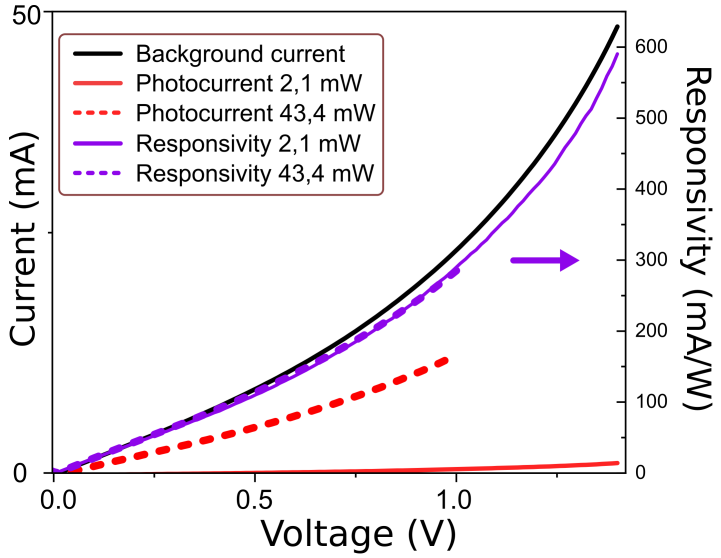

Fig. 4.28 *Background and photocurrent for the QWIP with $p = 4$ µm and $s = 1.36$ µm. The impinging power is 2.1 mW (full lines) and 43.4 mW (dashed lines). The deduced responsivities are plotted in purple.*

First it appears that the same responsivity is found for both powers, showing the absence of saturation, at least up to 43 mW. The value of the responsivity itself is much higher than for the QCD: for external biases superior to 1.3 V, the responsivity of the device becomes

larger than 500 mA/W, but the background current exceeds 40 mA. For the investigated bias, no roll-off behavior is observed in the responsivity but we could not increase the bias: because of the current in the device, the device ends up breaking when the total current becomes too large.

The differential resistance of the device is 55Ω close to zero bias but decreases almost linearly increasing with the bias, down to 24Ω at 1 V.

Since the device is responsive at 9 µm, we used the frequency comb to characterize the bandwidth of the device as in Chapter 2, Fig.2.28. Fig.4.29 shows the signal detected and sent to an analyzer. Surprisingly, the -3dB cutoff is reached between 5 and 7.5 GHz (if we do not consider the small dip around 6 GHz), even though the device is thicker than the QCD.

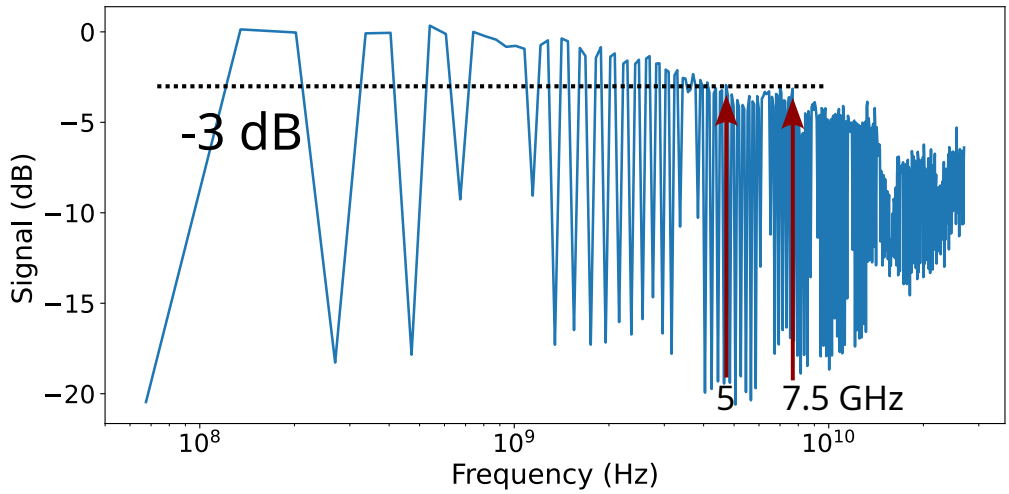

Fig. 4.29 *Electrical bandwidth of the QWIP in stripes. The measurement is done looking at the Fourier transform of the response of the detector to the frequency comb. Teeth from the beatings are separated by 100 MHz.*

This device exhibits the largest room temperature responsivity for ISB devices working at this wavelength found in the literature. Comparable metamaterial QWIPs are often fabricated on GaAs/AlGaAs for processing reasons: ICP etching of GaAs based material can be done using gold as a mask without damage. Devices in [48, 35] show room temperature responsivities of 150 and 200 mA/W with electric field of 100 and 21 kV/cm respectively, both with active regions made of 5 periods. The larger effective mass explains some of the difference observed since $m^*_{GaAs} = 0.067m_0$ and $m^*_{GaAs} = 0.041m_0$ and the responsivity is be inversely proportional to it.

c) Low temperature operation

When decreasing the temperature, QWIPs usually exhibit an exponentially increasing resistivity, leading to much lower dark current and improved performances. The mesa indeed showed such behavior as seen from the measurement of the activation energy in Fig.4.26.

The metamaterial QWIP with periodicity 4 µm unfortunately did not work at low temperature: the resistivity only linearly increased while decreasing the temperature and no

enhancement in the photocurrent was observed. The root of this issue is probably in the fabrication since the devices with $p = 7\,\mu m$ worked. After the ICP physical etching of the resonators, the sidewalls displayed a roughness that likely did not come from the etching itself, but either from a chemical reaction during the etching or from metal sputtering from the bottom gold at the end of the etching. Fig.4.30 (a) shows a SEM image of a patch obtained after the ICP with the recipe described in Chapter 3. Stripes have the same kind of patterns. Panels (b) and (c) show respectively the equivalent circuit of a shorted patch and the resisitivity in that scenario: the active region resistivity increases exponentially as the temperature lowers, but the surface resisitivity does not. At low enough temperature, the current would only flow at the surface.

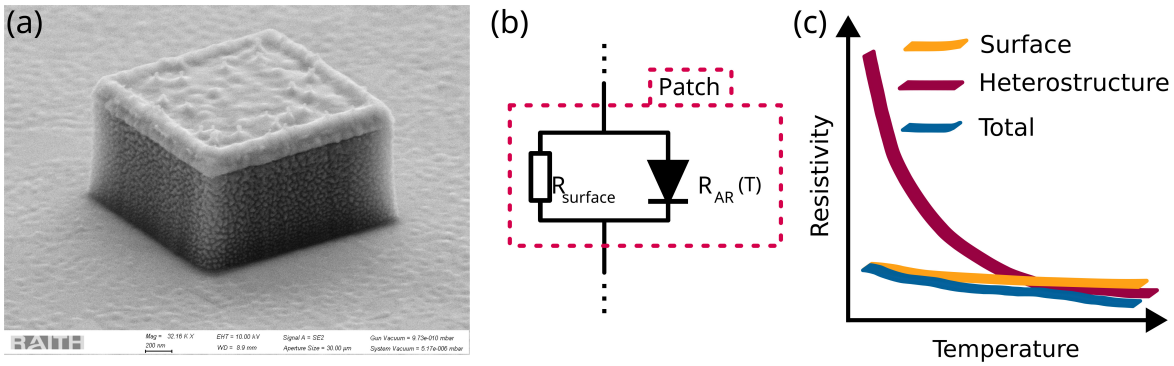

Fig. 4.30 *(a) SEM image of a typical patch after ICP etching. Sidewall roughness is visible. (b) Equivalent circuit of one shorted patch. (c) Sketched resisitivity of the shorted structure as a function of the temperature.*

The roughness of the layer seems to display a vertical gradient (smaller typical grain size on the bottom), that could be the sign of the first hypothesis, since the upper part spends more time revealed in the chamber. Except for the metal of the mask and the bottom layer, the other suspected species in the chamber is Silicon (from the $SiCl_4$ and the carrier wafer used to support the etched sample in the ICP chamber), that can form polymers on the surfaces. No chemical study was undertaken though. This layer is insensitive to everything we tried: O_2 plasma, organic solvents (Water, Acetone, Isopropanol, MIBK, DMSO, NMP), acids (HCl, HF), bases (TMAH), inorganic solvents (AZ400K).

Nevertheless, the devices with larger periodicities ($p = 7\,\mu m$) with the same active region, fabricated to observe strong coupling, display the expected behavior at low temperature with resistivities close to $100\,M\Omega$ at low bias. The ICP etching of devices with large periodicities is easier: the inter-stripe area is revealed at a rate close to the interdevice area so the devices stay less time in the plasma while part of the gold is revealed already. This second observations implies that the layer is caused by sputtered gold at the end of the etching. If so, more work should be done on the ICP recipe, maybe changing recipe close to the end (lowering forward bias and/or Ar concentration to reduce physical etching).

4.3.4 $p = 7$ µm devices: Strong coupling regime

By significantly reducing the radiative losses (increasing the periodicity of the metamaterial), we can reach the strong coupling regime for this QWIP.

a) Absorption spectra and photocurrent spectra

To observe the strong coupling over a large range of energy, we fabricated 7 devices with widths from 1 µm to 1.8 µm all with $p = 7\,\mu$m. In Fig.4.31, we plotted the reflectivity spectra and room temperature photocurrent spectra, under 1 V bias.

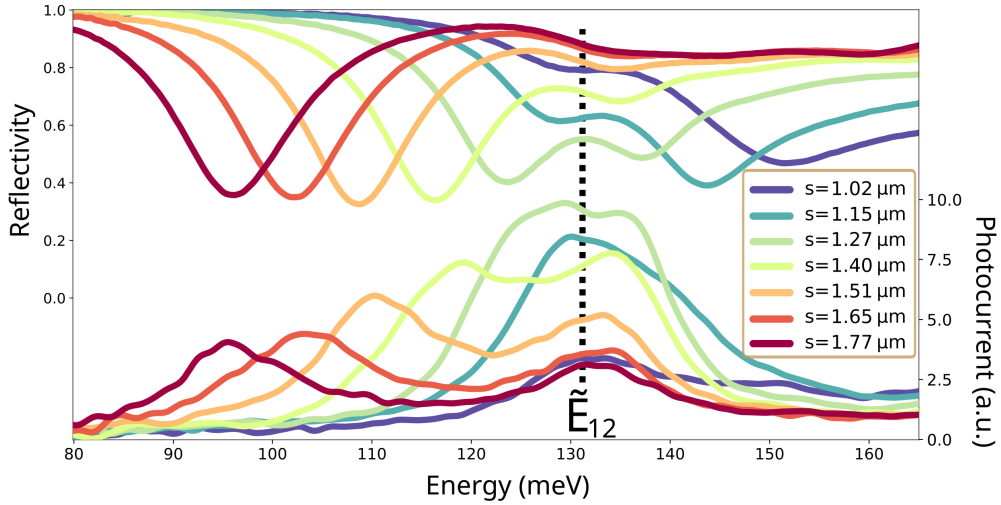

Fig. 4.31 *Reflectivity and responsivity spectra of the QWIP V0786 for different metamaterial width for $p = 7\,\mu$m.*

The reflectivity spectra display polaritonic modes over a very large energy range. In Fig.4.32, we plotted the resonance energy, for both periodicities, as a function of the inverse width of the resonators. On this plot, the calculated energy of the polariton modes is shown in dashed purple. The empty cavity energy as well as the absorption energy $\tilde{E}_{isb}$ are also plotted in black to highlight the anticrossing when the cavity energy matches the absorption. The data of the devices superpose with the two values of p since the energy of the peaks is only a function of parameters related to the active region and not radiative coupling, assuming that the cavity mode overlaps with the resonators perfectly in both cases. Looking closer, when the stripes are close to one another, the increased coupling between resonators might be detrimental to this hypothesis. The anticrossing in the data for p=4 appears indeed to be slightly smaller than for p=7. This could be empirically added in the CMT by including a p-dependency to Ω_r. We mainly have data with the cavity energy lower than the ISB because the diffraction prevents us from measuring on the higher energy side.

Regarding the photocurrent spectra, we strikingly have photocurrent matching the absorption peaks in a very wide energy range: the largest cavity (in dark red) absorbs around 95 meV (50 meV lower than the barrier height) and we are able to measure the photocurrent at this energy. As we did with the QCD, we can use the function $\mathcal{L}_{tot\rightarrow isb}$ (adapted with the losses of this system) to establish a link between photocurrent and the ISB absorption. In

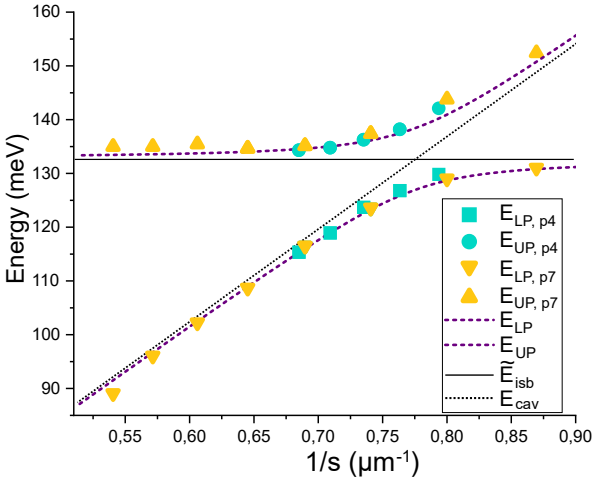

Fig. 4.32 *Dispersion of the polariton energies for the metamaterial QWIPs for $p = 7$ (in yellow) and $p = 4\,\mu m$ (in blue). The theoretical energy of the polariton is shown in dashed purple. The empty cavity energy as well as the absorption energy $\tilde{E}_{isb}$ are also plotted in black.*

Fig.4.33 (a) we superpose, for the case $s = 1.15\,\mu m$ and $s = 1.77\,\mu m$ the photocurrent (same as in Fig.4.31), and the product $(1 - R) \cdot \mathcal{L}_{tot \to isb} = A_{isb}$ where R stands for the reflectivity.

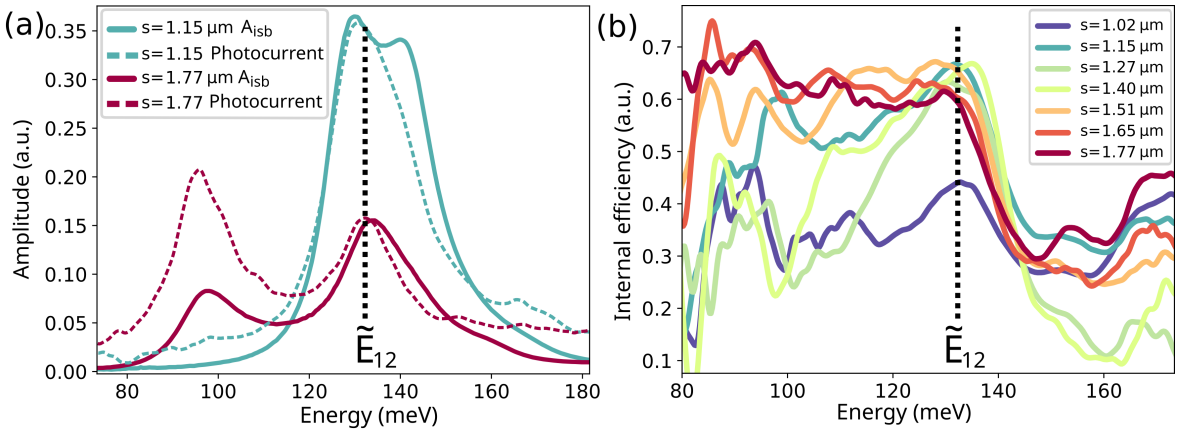

Fig. 4.33 *(a) ISB absorption extracted from the reflectivity spectra and photocurrent spectra for two resonators ($s = 1.15\,\mu m$ and $s = 1.77\,\mu m$). (b) Internal efficiency for all resonators.*

It is clear that again there is a transport phenomenon at play: proportionally, the low energy photons absorbed generate more photoelectrons in the circuit. On the contrary, absorption at higher energy than $\tilde{E}_{isb}$ seem to not participate in photocurrent. In Fig.4.33 (b), we divided the photocurrent by the ISB absorption for each width to deduce the internal efficiency.

When doing this operation, we suppose that all photocurrent is mediated by the 1-2 absorption coupled with the cavity mode, neglecting in that process electrons absorbed in or near the continuum in localized levels, that could participate in the photocurrent.

The behavior of the internal quantum efficiency at low energy in Fig.4.33 (b), especially

for thin cavities is hard to interpret here due to the fact that the photocurrent tends to zero and so does the ISB absorption. Nevertheless, a common feature to all these curves is a sharp cutoff for energies higher than $\tilde{E}_{12}$. The energy of the cutoff is close to that of the barrier at this bias. Surprisingly, the electrons excited at energies below the barrier participate to the photocurrent at room temperature, while the internal efficiency drops for energies above the activation energy.

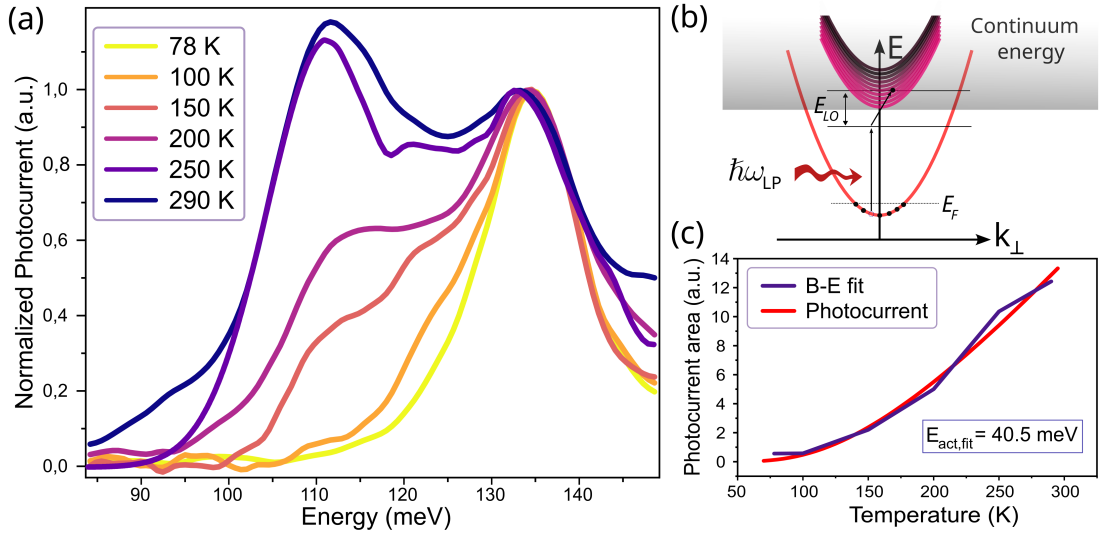

Fig. 4.34 *Photocurrent spectra of the QWIP with $p = 7\,\mu m$ and $s = 1.51\,\mu m$ for temperature in [78, 100 , 150 , 200, 250, 290] K.*

To understand the underlying phenomenon, we measured the photocurrent of the cavity $s = 1.51\,\mu$m for various temperatures[2]. Fig.4.34 shows photocurrent spectra for temperatures 78 K, 100 K, 150 K, 200 K, 250 K, 290 K. We clearly observe that the photocurrent at the energy of the lower polariton vanishes at low temperature.

Our hypothesis given this thermal activation is a phonon assisted transport to the continuum, sketched in Fig.4.34 (b). The LO phonon population in the crystal follows a Bose Einstein distribution:

$$n_{LO} = f_{BE}(T, E_{LO}) = \frac{1}{\exp(\frac{E_{LO}}{k_B T}) - 1} \tag{4.15}$$

Fig.4.34 (c) shows the evolution of the integral of the photocurrent between 90 and 135 meV as a function of the temperature and indeed the phenomenon seems thermally activated. We fitted the integral with the Bose Einstein function, in order to estimate the activation energy involved. The fit yields $E_{act} = 40.5$ meV, close to the average of LO phonon of ternary InP lattice-matched $In_{0.53}Ga_{0.47}As$ (33 meV) and $In_{0.52}Al_{0.48}As$ (45 meV [122, 123]).

b) Comparison with the p=4 device

We compare in Fig.4.35 the responsivities (panel (a)) and the dark currents (panel (b)) of $p = 7\,\mu$m and $p = 4\,\mu$m devices.

[2]Thanks to Jihye Baik for her help acquiring these data.

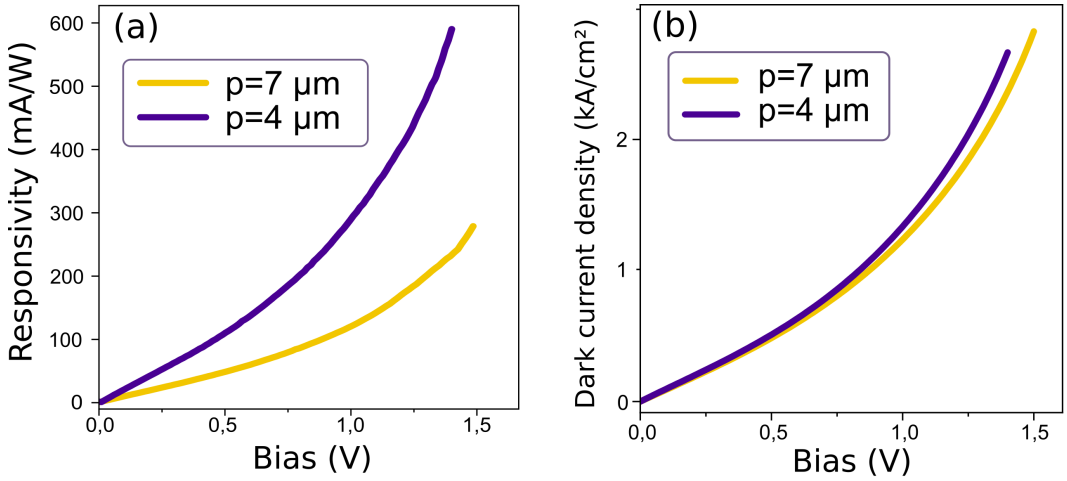

Fig. 4.35 *(a) Comparison of the room temperature responsivities at 9.4 µm as a function of the bias for QWIPs with $p = 4$ and $p = 7\,\mu m$.(b) Comparison of the dark currents densities as a function of the bias for QWIPs with $p = 4$ and $p = 7\,\mu m$.*

We confirm in (a) that the responsivity is lower for the larger periodicity, by a factor of 2.3 almost constant over the range of bias studied. We can compute with the losses from Table4.3 the ratio $\frac{A_{isb}(9.4\,\mu m,\, p=4\mu m,\, s_{opti})}{A_{isb}(9.4\,\mu m,\, p=7\mu m,\, s_{opti})} = 2.0$, very close to the observed value. The dark current is nevertheless smaller for the larger periodicity since the electrical surface is reduced. In (b), the dark current density is almost equal for both devices. Once again, in the case of QWIPs, this is a new incentive to use patch devices rather than stripes, since the reduction of surface is proportional to p^2 and not p with respect to a mesa with the same optical area.

4.4 Data Transmission at 10 µm with metamaterial devices

4.4.1 Choice of the detector

The QWIP and QCD do not have exactly the same energy, but we use the tunable laser and we have equivalent modulators for both energies, so the choice of the detector was guided by the expected performances using the BER formula in Eq.2.1, as well as the noise estimations for each detector. We can estimate the noise power densities σ_i at play, knowing the differential resistivity R_0, the responsivity R, the currents and the bandwidth Δf_{-3dB}.

For the QWIP, assuming an operation at 1.2 V at room temperature, we can estimate the noise in the detector:

$$\begin{aligned}
\sigma^2_{Th} &= \frac{4k_BT}{R_0}\Delta f_{-3dB} = 8.1\cdot 10^{-22}\Delta f_{-3dB} = 5.7\cdot 10^{-12}[A^2] \\
\sigma^2_{shot\,noise} &= 2eR\Delta f_{-3dB}\cdot P_{opt} = 1.3\cdot 10^{-19}\Delta f_{-3dB}\cdot P_{opt} = 9.0\cdot 10^{-10}[A^2/W]\cdot P_{opt} \\
\sigma^2_{dark\,shot\,noise} &= 2eI_{dark}f_{-3dB} = 9.6\cdot 10^{-21}\Delta f_{-3dB} = 6.7\cdot 10^{-11}[A^2]
\end{aligned} \tag{4.16}$$

For the QCD, in photovoltaic operation :

$$\sigma_{Th}^2 = \frac{4k_BT}{R_0}\Delta f_{-3dB} = 2.6 \cdot 10^{-12}[A^2]$$
$$\sigma_{shot\,noise}^2 = 2eR\Delta f_{-3dB} \cdot P_{opt} = 1.1 \cdot 10^{-11}[A^2/W] \cdot P_{opt}[W] \quad (4.17)$$

In the shot noise we only considered the photocurrent, assuming the QCD is operated in the photovoltaic regime and does not have dark current.

Two additional noise sources are to be considered for both devices:

- The noise generated on the detector by the Relative Intensity Noise of the laser (RIN), estimated at -140dB/Hz. We can write $\sigma_{RIN}^2 = R^2P^2 10^{RIN/10}\Delta f_{-3dB}$ where R is the responsivity of the detector and P the optical power impinging on the detector,

- An amplification noise coming from the electronic amplification, estimated to be $\simeq$3 dB over the whole bandwidth.

The QCD benefits from its larger bandwidth, higher resistivity and the absence of dark current. On the other hand, the QWIP has a more than 10 times higher responsivity.

In Fig.4.36 we plotted the value calculated with the Eq 2.1 for the BER for OOK transmission for each detector in equivalent conditions as a function of the frequency of the modulated signal.

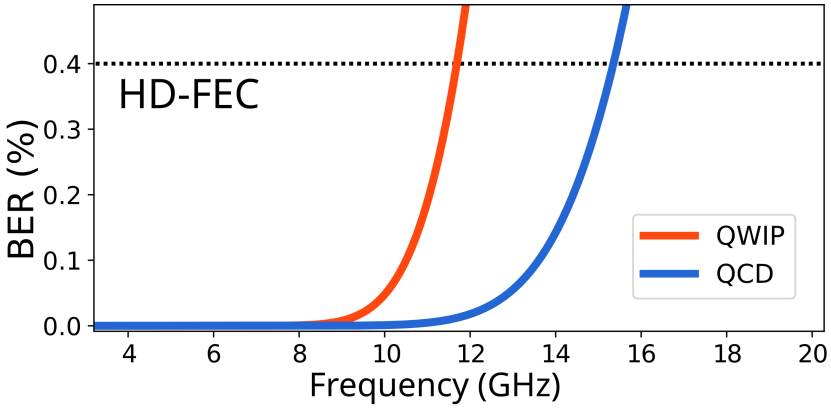

Fig. 4.36 *Estimated BER for OOK transmission for the QCD and the QWIP. The QWIP reached the 0.4% BER limit around 11.5 GHZ and the QCD around 15 GHz.*

It appears that the QCD should perform efficiently up to higher frequencies than the QWIP. The difference in the bandwidth is not balanced at all by the responsivity. In particular, the largest noise contribution (before amplification) is from the RIN of the laser. Also proportional to the responsivity, σ_{RIN} limits the benefit of the increased responsivity.

We neglected in this computation the noise from the modulation source (the AWG) and the modulator and their bandwidths, because identical for both detectors.

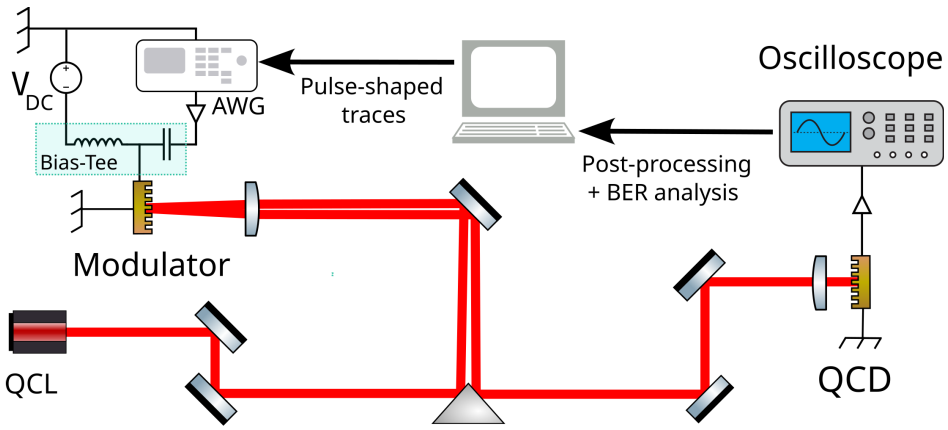

Fig. 4.37 *Experimental setup for data transmission.*

4.4.2 Data transmission results

For data transmission, we used the optical setup presented in Fig.4.37. The QCL operates at 10 µm thus matching the QCD energy with 100 mW output power.

An Arbitrary Waveform Generator (AWG) delivering an initial voltage of 400 mV is connected to the modulator through a 25 dB amplifier (SHF 826H) and a 10 dB attenuator reducing the power reflected back to the amplifier. A bias tee, after the amplifier and the attenuator, allows applying a small DC bias (180 mV) on the modulator, operating in the linear regime.

The signal received by the detector is amplified by a 35 dB amplifier before being analyzed by a 70 GHz bandwidth oscilloscope.

The full system bandwidth is probed first using the AWG to send sine at various frequencies and the oscilloscope as a spectrum analyzer. The results, shown in Fig.4.38, demonstrate a 6 GHz bandwidth before -3dB attenuation, with the attenuation remaining as low as 10 dB up to 16 GHz, where a steep cutoff occurs.

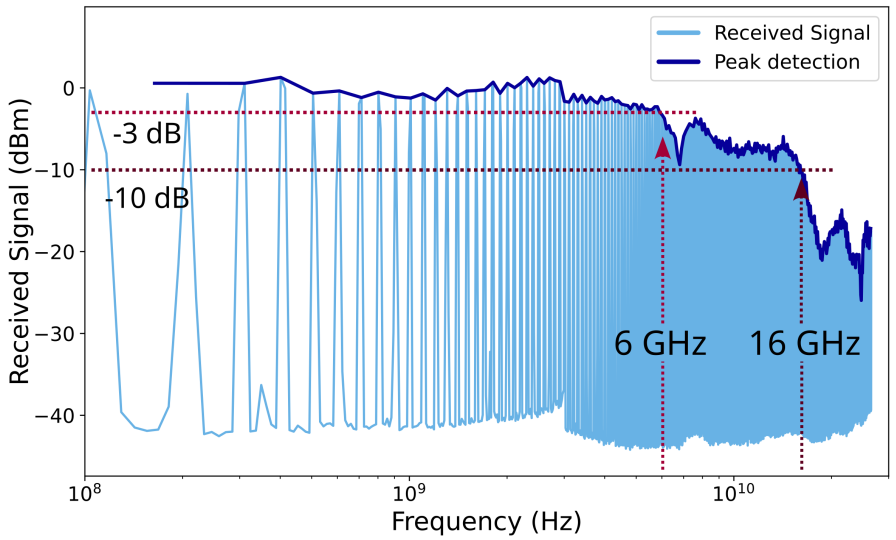

Fig. 4.38 *Optical bandwidth of the complete data transmission system.*

We tested increasingly important bitrates, measuring the BER until it reached the 0.4% limit, maximum acceptable error rate that HD FEC error correction code can handle (with 7% of overhead in the message).

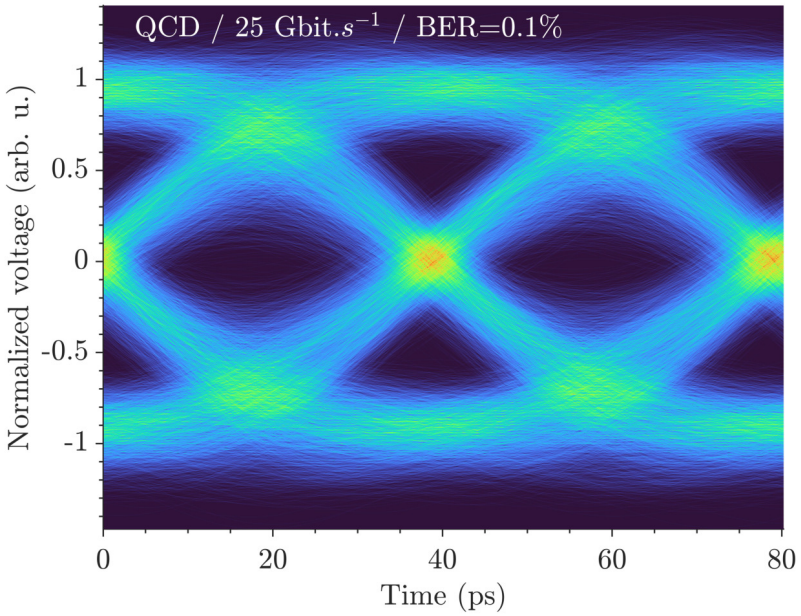

Fig. 4.39 *Record data transmission at 25 Gbit·s^{-1} OOK obtained with the QCD and the modulator processed into metamaterial devices.*

Fig.4.39 shows the eye diagram of the best transmission made possible with this new system: an "errorless" 25 Gbit·s^{-1} OOK optical transmission obtained with metamaterial devices operating at room temperature and 10 μm. This result improves by more than twice the previous record established by using the mesa devices.
Finally, in order to push the performances of this system, we implement digital data processing methods to improve the achievable bitrates.

4.4.3 Equalization of the transmission for enhanced performances

Many methods to increase the bitrate, developed for telecommunications with established technologies, are immediately applicable to our system. With the help of collaborators at Telecom Paris, we implemented some of them on our optical link, reaching new record values. This work, will not be entirely detailed here but we will present the philosophy of the strategies chosen, as well as the results it yielded. Extensive details about these methods can be found in [124].

a) Digital processing ideas

The operations made to improve the bit error-rate with a fixed transmitter and receiver can be separated into two categories: *the preparation of the traces* to be used for the transmission, that can be adapted to the system and its limitation, and *the post processing of the received signal*, called equalization.

Regarding the preprocessing, the first possibility is to reduce the spectral extension of the signal. Because of the limited bandwidth of the system, a pulse will have an extension in time domain that can lead to "intersymbol interference" (ISI), meaning one symbol will influence the next. The idea is to use a spectral (low pass) filter that creates a new signal that verifies good properties for the transmission while constricting its bandwidth within the system's bandwidth, limiting the deformation during the transmission. This method is also called pulse shaping. When a message is to be sent, it is first mapped on an OOK, PAM-4 or more complicated encoding, pulse-shaped, then sent to the transmitter.

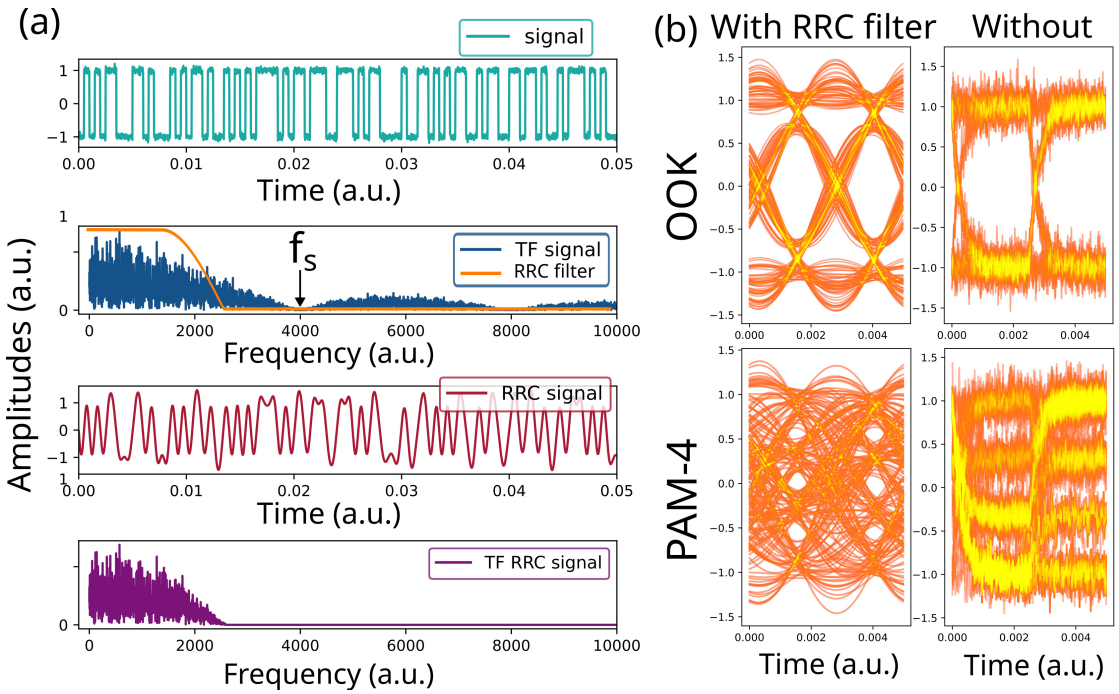

Fig. 4.40 *(a) Example of an OOK time traces (line 1) and its Fourier transform (line 2). The RRC frequency filter leads to a new signal to be send to the system (line 3). Its Fourier transform (line 4) shows a reduced extension. (b) Simulated eye diagrams for noisy transmissions with and without RRC pulse shaping (roll-off 0.3) for both OOK and PAM-4 schemes.*

The filter employed in our case is called root raised cosine filter (RRC). Its implementation is summarized in Fig.4.40 (a). The message (OOK) in the first line, is spectrally decomposed in the second line. The filter (in orange) is applied (multiplied in Fourier space). The resulting signal and its spectral decomposition are shown in line 3 and 4. The filter is characterized by a coefficient $\rho \in [0; 1]$ known as the roll-off factor, smoothly varying from a rectangular filter of extension $f_s/2$ ($\rho = 0$) to a cosine ($\rho = 1$). In Fig.4.40 (a), $\rho = 0.3$. The idea (for the simplest case $\rho = 0$), is that the impulse response is a sinc function, with a zero at $t = T_s$, when the next symbol is given. This helps in reducing the intersymbol interference. Though the impulse response slightly changes with ρ, this property is conserved.

The filter is in practice splitted in two: a "square-root raised cosine" before the transmission, and a second one on the receiver side, refiltering the signal. In Fig.4.40 (b), we simulate eye diagrams for a noisy transmission, with and without the filter, for both OOK and PAM-4.

The high frequency noise is filtered, and the smoother shapes reduce the lateral opening of the eyes but help maintaining some vertical separation when the SNR becomes limiting.

Regarding the postprocessing, the use of algorithms helps in deciding the value of a received bit. A known "pilot" sequence is sent before the message and compared to the received one. Digital equalization filters are deduced from the observed difference between the pilot sequence and the received one. The difference is caused by noise along the transmission and ISI. The equalization filters are temporal filters, compensating the broadening of the impulse response due to the limited bandwidth. This process generates a filter that will be applied to the complete transmission.
After this step, the digital signal is demodulated and mapped onto logical bits after deciding the best position of the threshold(s) between levels. The workflow and the different steps are summarized in Fig.4.41.

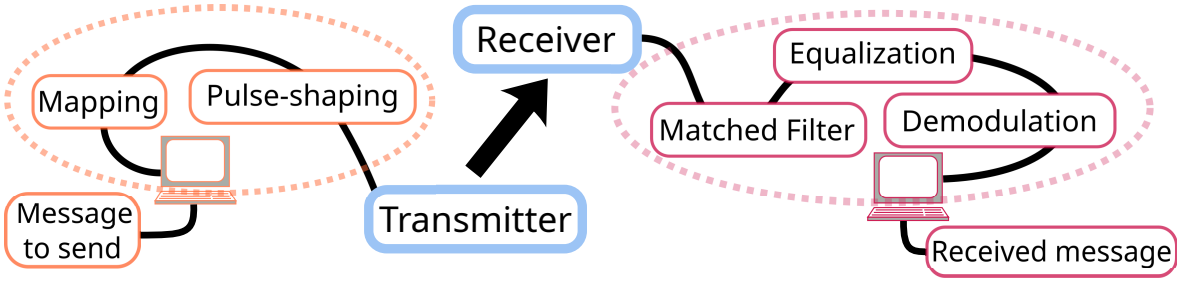

Fig. 4.41 *Digital pre- and post-processing of a message to be sent through a transmission link.*

The implementation of the equalization of the signal was done for this system by Pierre Didier. Another more detailed example of the optimization of the equalization was done with the previous generation of mesa devices at KTH Stockholm, and the results are published in [92].

b) Final results

PRBS 2^{15} bit-long data traces (significantly longer than those presented in Chapter 2, and therefore more difficult to transmit) with RRC are generated by a computer and sent to the AWG to test the newly established link with both OOK and PAM-4 codings.

With the new traces and post processing of the data, a new record 60 Gbit·s^{-1} transmission below the HD-FEC limit is achieved with PAM-4 (eye diagram in Fig.4.42 (a)). Using OOK traces, the best transmission was limited to 40 Gbit·s^{-1} (Fig.4.42 (b)). PAM-8 transmission was also attempted but did not improve the results further: the SNR is not large enough to separate 8 levels sufficiently.

Fig.4.42 (c) summarizes the BER after equalization for bitrates between 10 Gbit·s^{-1} and 80 Gbit·s^{-1}. We see that above 30 Gbit·s^{-1} for OOK and 40 Gbit·s^{-1} for PAM-4, the BER increases exponentially with the bitrate, before reaching the 0.4% at threshold. With a higher threshold, corresponding to different error correction code necessitating larger overhead in

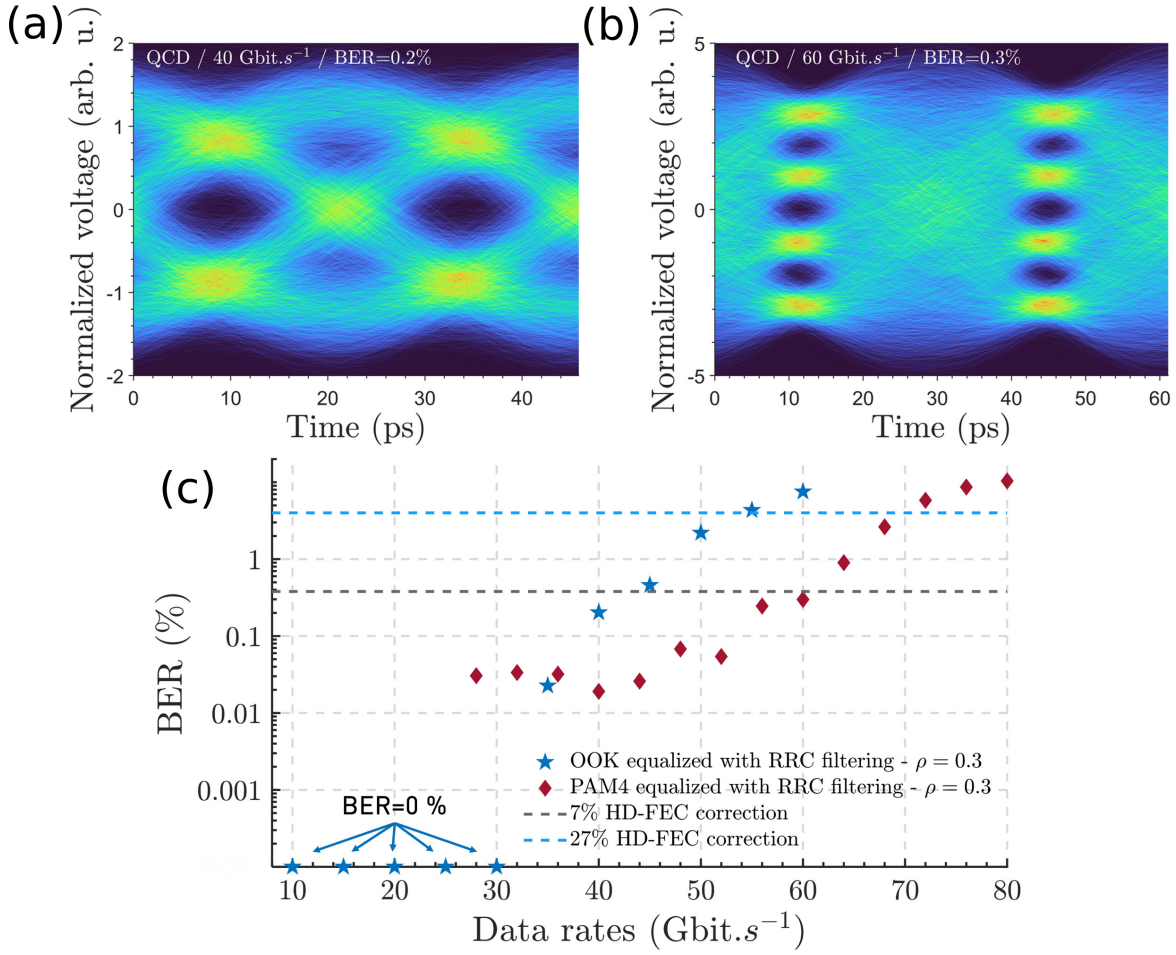

Fig. 4.42 *(a) Eye diagram for a 40 Gbit·s^{-1} OOK after equalization. (b) Eye diagram for a 60 Gbit·s^{-1} PAM-4 after equalization. (c) Summary of the BER for OOK and PAM-4 data transmission with the metamaterials.*

the message, higher bitrates are even possible, but the net bitrate after subtraction of the overhead is only marginally better, and introduces additional latency.

4.5 Conclusions

The introduction of metamaterials for improving the ISB devices proved relevant in the context of data transmission. We showed in this chapter significant gain of electrical bandwidth, offered by the miniaturization and improved optical confinement for both detectors and modulators. The use of 2D patch resonators have the potential to further increase the bandwidth (in recent work, QWIPs detecting 220 GHz signals were exhibited, having only four patches [125]), although reducing the device size can also reduce the fraction of light coupled in the resonators, thus reducing the responsivity for detectors or absorption for modulators. For QWIPs in particular, the reduction of the dark noise coming with the reduction of the surface of the device would also improve the overall performances.

The cavity effect was also already known from previous works for the improvement it brings to the responsivity of detectors [35]. In this chapter, we indeed verified the dramatic

improvement of the room temperature responsivity of our QCD with respect to the mesa, reaching a photovoltaic responsivity of 26 mA/W at room temperature and 10 µm. In the case of the quaternary QWIP, a record responsivity of 600 mA/W was observed at room temperature and 1.4 V bias, at 9.4 µm.

The metamaterial also brings the possibility to engineer the coupling of the QWs with light, making possible the observation of polaritons. The Stark modulator I fabricated takes advantage of this effect to increase the contrast obtained with applied bias. In QWIPs, the strong coupling regime does not improve of the performances, but we could observe in this work thermally activated photocurrent at the energy of the lower polariton.

Finally, we used the metamaterial Stark modulator and QCD to fabricate a second free-space optical link, which was able to transmit information up to 60 Gbit·s^{-1} with a PAM-4 signal encoded on a 10 µm QCL emission, which sets a new record for data transmission in the MIR.

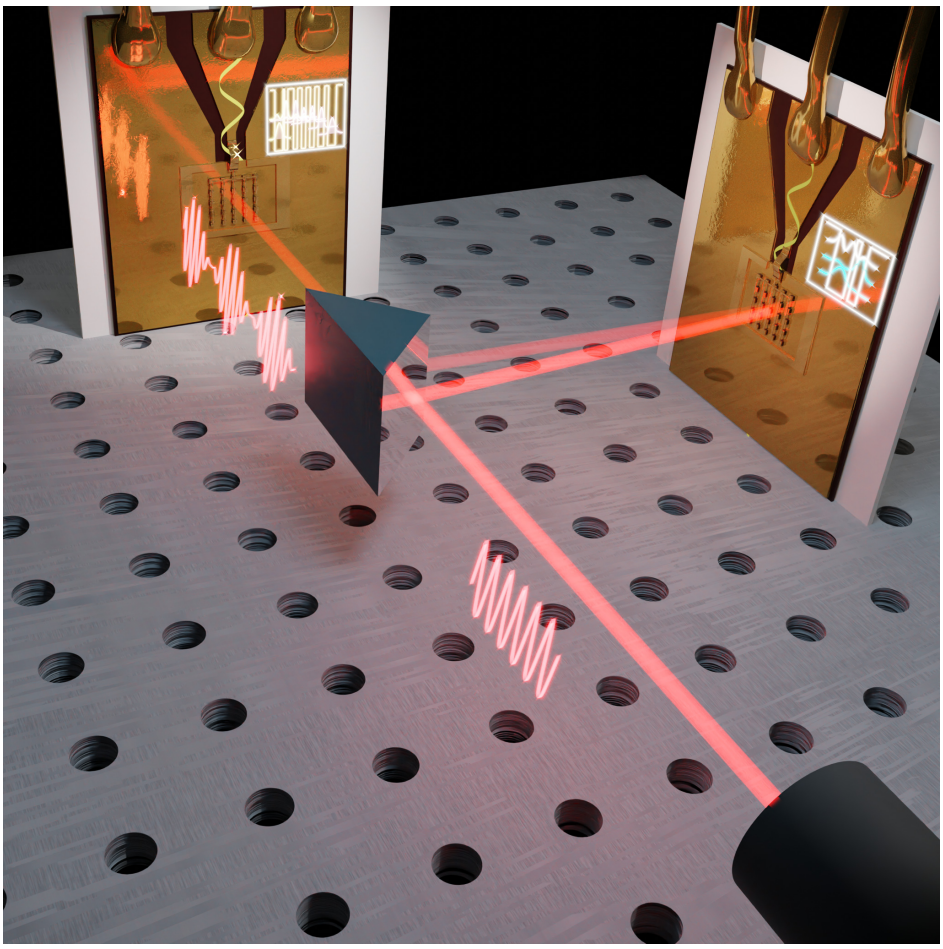

Conclusion

This work is centered around the creation of efficient optoelectronic devices for the MIR based on InP materials, with a specific aim towards free space optical communications. The main objective is to create a new type of high-speed MIR external modulator that could operate at room temperature, which is a crucial missing element needed to enable fast optical links.

After introducing in chapter 1 the basics of intersubband devices and the figures of merit of their performances, in chapter 2 I describe MIR modulators. In particular, I show that coupled asymmetric quantum wells are an adequate system to modulate the MIR light, taking advantage of quantum confined Stark effect. The amplitude modulation is obtained by shifting the absorption energy of two confined electronic states by applying an electric field: the difference in the localization of the first two wavefunctions in the quantum wells makes their energy difference sensitive to the electric field. We fabricated small mesas connected to coplanar waveguides with an air bridge to allow for high speed operation. Taking a close look at their electrical bandwidths, we inferred a lower bound on the maximal speed accessible for the modulator, estimated at 40 GHz. By exploiting a QCD processed in the same fashion and a commercial QCL, we demonstrated a free space optical link and transmit data with a bitrate as high as 10 Gbit$\cdot$s^{-1} without equalization of the received signal.
In Chapter 3, we show that the device performances can be improved by using patch antenna resonators to increase the light matter interaction with the active region while reducing the electrical area. We used the Coupled Mode Theory formalism to model the light-matter coupling occurring in those metamaterials and determine the relevant quantities for device optimization. A study on empty cavities gave us access to the typical losses of the resonators, the input parameters of the CMT. We then could draw guidelines for the design of both modulators and detectors based on patch antennas. A fabrication process was developed to fabricate these devices, taking into account the specificities of the resonators, high speed connections, and material characteristics.
In Chapter 4, we designed new active regions for modulator, QCD and QWIP on InP to be embedded in the metamaterials. We characterized each structure to determine the missing input parameters for the CMT related to the active regions, and optimized metamaterial devices were processed. The performance of the modulator was measured, in terms of modulation depth and electrical bandwidth: the metamaterial Stark modulator shows a 28 % modulation depth with insertion losses as low as 2 dB. Using a coherent detection setup with two heterodyne measurements, we also demonstrated that amplitude modulation is accom-

panied by a 12° phase modulation. Detectors also greatly benefited from the metamaterial architecture, increasing drastically the responsivity. The QCD displayed a responsivity of 26 mA/W at 10 μm and the QWIP a responsivity greater than 500 mA/W at 9.4 μm, at room temperature under 1.4 V bias. We observed that the microcavities affect the spectral response of the devices, which can be tuned by changing the geometrical parameters of the metamaterial array. By comparing the shape of the responsivity with that of the absorptivity of the devices, we were able to extract a transfer function, which only depends on the electronic transport. For QWIPs, we were also able to observe photocurrent in a very wide energy range, at energies well below that of the intersubband transition. This behaviour is associated with the existence a strong light-matter coupling regime between the ISB transition and the cavity mode. Finally, using the QCD and the modulator metamaterial devices, both with bandwidths exceeding 10 GHz, we were able to demonstrate a free space optical linkwith a significantly increased bitrate of 25 Gbit·s^{-1}. Furthermore, by implementing pulse shaping and equalization methods developed by the Telecom Paris, we were able to improve performance even further, achieving a record value of 60 Gbit·s^{-1} on a 10 μm carrier.

The throughputs achieved for a single channel using these metamaterials are in line with modern telecommunications standards. Improving these performances further without paradigmatic change is clearly still possible, by using 2D optical confinement to further increase the bandwidth. Beyond that, and following the development of telecommunication in other wavelengths, the next big step would be multiplexing (wavelength division multiplexing most likely), at the cost of a tremendous increase of the complexity of the implementation. In addition to increasing the bitrate, it is also necessary to demonstrate the ability to transmit optical signals over longer distances. While a 31-meter link has been achieved using this mesa modulator, it will be important to demonstrate the ability to transmit over much longer distances (e.g. kilometers) to establish the potential of MIR for optical communications over the shorter wavelengths currently in use.

Perspectives

Implementation of amplitude and phase modulation

It is possible to take advantage of the phase modulation to add channels for data transmission, encoding information both on the phase and on the amplitude. Using two modulators, one on each arm of a heterodyne set-up, could allow such data transmission scheme. Fig.4.43 qualitatively explains how it could be implemented, using two modulators with sizes slightly different (1.21 and 1.25 µm here for a 138 meV laser).

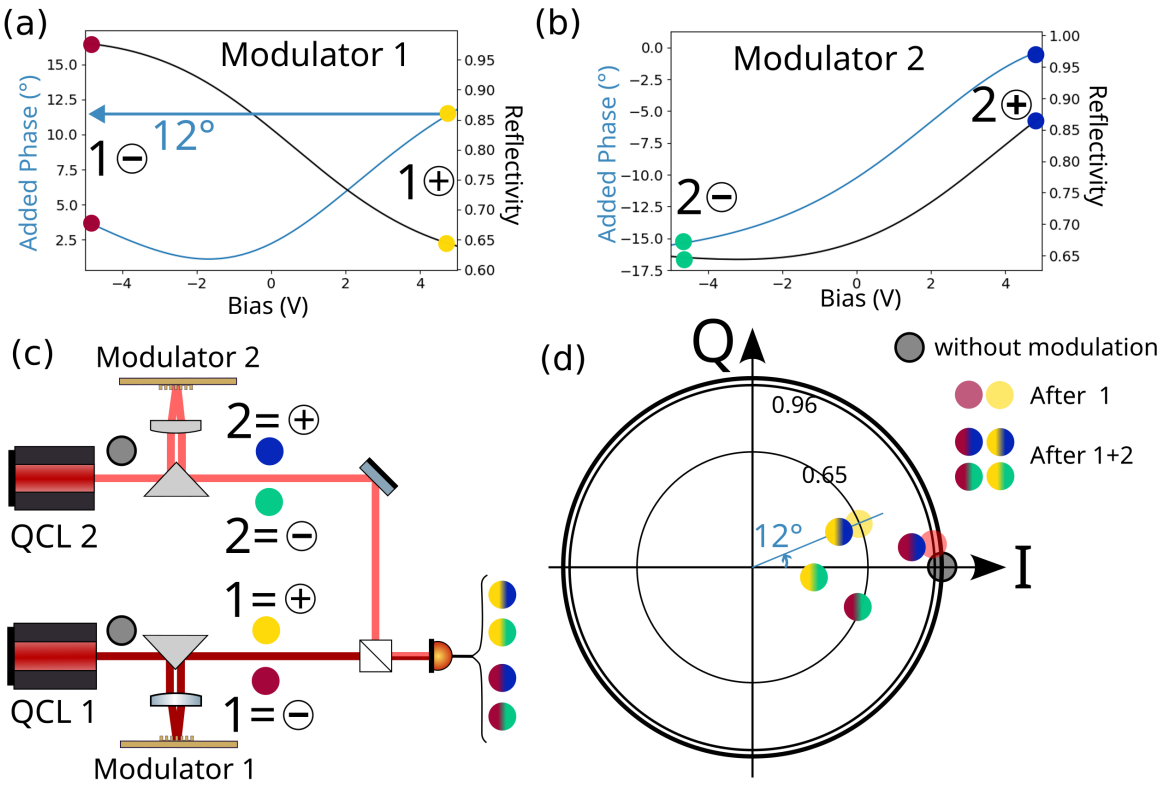

Fig. 4.43 *(a) Simulated phase and reflectivity modulation for a Stark modulator, s=1.21 µm. (b) Idem, but s=1.25 µm. (c) Possible experimental setup to observe amplitude and phase modulation. The stabilization part of the setup is omitted. (d) Simulated constellation diagram corresponding to the previous experiment. The final states are circled in blue while the states after the first modulator are circled in green.*

Fig.4.43 (a) and (b) show the simulated CMT phase and amplitude modulation as-

suming a signal of ±4.5 V. Each modulator is present on one arm of the heterodyne set-up. Each beam is modulated independently but at the same frequency. the set-up is sketched in panel (c). Along the first arm, after the modulator, the laser is in the state 1+ or 1- corresponding to the red and yellow dots in (a). Along the second arm after the modulator 2, two different states are possible, 2+ or 2- corresponding to the blue and green dots in (a). After recombination, the heterodyne current reads on the detector $I_{het}(t) = E_1(V_1)E_2(V_2)\cos(\Delta\omega t + \phi_{mod1}(V_1) + \phi_{mod1}(V_1))$ and states 1+2+, 1+2-, 1-2+ or 1-2- are possible at each sampling. Mixed colors of modulators 1 and 2 are associated to those states to describe them. The detectors and modulators need to share the same clock.

In (d), those colored dots are plotted on a polar IQ diagram (each axis is associated to a quadrature of the periodic signal). In this complex plane, the amplitude is the modulus of the point and the phase its argument. The thick black circle is the unity circle, corresponding to the unattenuated initial amplitude of the laser. Each state used for the transmission is represented by the colored dot associated with the state. As guides for the eyes, black circles corresponding to the amplitude after the first modulators in the state 1+ (0.65) and 1- (0.96), as well as the angle corresponding to the phase for the state 1+ are also represented. As in the eye diagrams for amplitude modulation, two states will be distinguishable if two points do not overlap. Their area in the plot would be related to noise on the phase and the amplitude. When only using amplitude modulation, the dots are restricted to the x-axis, limiting the number of level one can use, assuming constant SNR.

At the cost of added complexity, this is a way to increase the capacity of the link while using the same bandwidth. The other main possibility, with constant bandwidth, to increase the bit rate, is wavelength multiplexing since the modulator has a rather large optical bandwidth. Authors in [126] experimentally demonstrate wavelength-division-multiplexing along three optical carriers separated by 0.001 µm at 4 µm, and mode-division-multiplexing, with each wavelength carries two modulated orbital-angular-momentum beams, multiplying by 6 the capacity of their link. The authors actually produce the signal and the multiplexing in the microwave region before downconverting it to the MIR, transmitting in free space, upconverting it back to microwaves and detecting it. With our modulator working at high frequency in the MIR, it is now directly do the multiplexing and the modulation in the MIR, avoiding nonlinear processes and making the transmission more energy efficient.

Monolithic integration

Having the possibility to fabricate chips with multiple functions implemented would simplify greatly the operation, allowing the creation of compact objects and offering new possibilities with guided light, notably regarding nonlinear optics. This work was centered around InP-compatible devices with in mind a potential future integration since the light source, the QCL, is almost systematically grown on InP. Realizing wavelength multiplexing (on the transmitter side) and demultiplexing (on the receptor side) for instance would require such

implementation. Different path towards integration are possible.

The first possibility is to take advantage of silicon photonics with heterogeneous integration of III-V devices on Si platform [127, 128]: either with wafer bonding (BCB, SU8 [129], oxide [130, 131]), or grown over a buffer layer (Ge or strained superlattices to eventually have the lattice constants match) [132, 133]. Authors in [134, 135] showed SiGe waveguide modulators operating in the MIR for instance.

The second possibility, using simply III-V materials, is to have a single heterostructure doing the various function. The very invention of a QCD was with a QCL active region, simply used without bias as a photodetector [37]. This dual use of the active region has created some interest in creating on-chip laser and detectors : two ridges can be processed perfectly facing each other and separated by a few microns, and separately connected. One is biased for laser operation, the other used as a photovoltaic detector at the matching wavelength [136, 137]. For spectroscopy though, a need for some propagation in the gas is necessary for absorption. Plasmonic waveguides have been introduced to extend the distance between laser and detector to 100 µm while keeping satisfactory coupling [138]. Interestingly, the Stark modulator active region design is not far from the active wells of a diagonal QCD and the latter could maybe be used as a modulator.

Authors in [139] bypassed the complexity of having the same active region for QCL et QCD, and grew the two active regions stacked on each other with a contact layer in between: on half of the sample they remove the upper QCD heterostructure and designed the QCL ridge, and on the other half the design a facing QCD ridge, and showed an overlap between the QCL mode and the QCD ridge and could detect photocurrent despite the two ridges not being at the same height.

Finally, work is being carried out toward full InP photonic integration: the QCL can be grown on top of a cladded passive InGaAs layer that will serve as a waveguide [140]. The QCL is tapered to increase the coupling with the buried waveguide and can reach 90 % coupling. From there on can narrow waveguides be defined, as well as ring resonators for instance [113], allowing for nonlinear operations. A QCL working in comb operation combined with ring resonators can be used for wavelength multiplexing [141, 142]. The same group also showed the possibility of growing different heterostructures above the same waveguide layer by masking different regions at every growth. This make it possible to have multiple wavelengths on the same chip, and they were able to couple the beam together [143]. Modulator would have to be added on each arm before recombination and free space emission. On the receiver side, demultiplexing must be done, and can also be performed with ring resonators. Authors in [144] also showed (at 1.5 µm) a passive and compact wavelength demultiplexer, but that I believe could be scaled to the MIR.

Patch QCLD

The idea of having an active region able to lase or detect depending on the DC bias presented above can also be used with the patch geometry. Laser in the THz using this geometry have already been proposed [145]. One could design two adjacent metamaterials, the first designed for lasing the other second for detection. Used in pair with corner retroreflector this can serve as a gas sensing compact tool. At long distance, the retroreflector could also be switched for a patch modulator and mounted on a drone for instance (unable to carry a heavy laser source), allowing for optical telecommunication with it, only downloading data in that case.

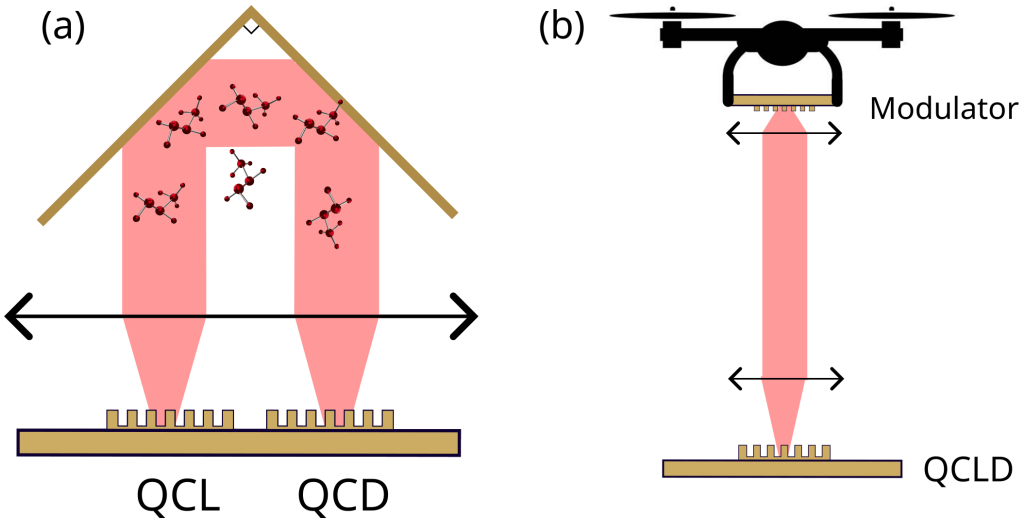

Fig. 4.44 *Patch QCLD with retroreflector.*

Using supplementary degrees of freedom to counteract feedback

One of the issues raised by the introduction of the normal incidence device is the feedback generated, detrimental to the laser operation. One way it could be tackled, else than optical isolators, could be by playing with the metamaterial parameter. It was observed numerically that devising a laser metamaterial with a linearly increasing periodicity over the sample makes it emit in a preferential non vertical direction. Conversely, optimal incidence angle for a detector with similar disposition would not be not 0° anymore and the specular reflection of non-coupled light would not go back to the laser.

Appendix A

Alloy composition and barrier height

The knowledge the conduction band offset for heterostructures is not a trivial task. [146] compiled the efforts made for various III-V semiconductors alloys. The bandgap, valence band offset as well as other parameters such as the effective mass are reported for the main binary and ternary alloys. Their approach to ternary alloys is to start from the binary alloys that are well investigated and to write that for a ternary alloy of the form $A_{1-x}B_xC$, the band related quantity G takes a quadratic form:

$$G_{ABC} = (1-x)G_A + xG_B - x(1-x)C_0 \tag{A.1}$$

where C_0 is called the bowing parameter. At room temperature for bandgaps for instance, the authors suggest $C_{0,InGaAs} = 0$ and $C_{0,InAlAs} = 0.7$ for an InP lattice-matched structure.

Quaternaries are generally of the form $A_xB_{1-x}C_yD_{1-y}$ with two group III and two group V elements.[147] suggested the following weighted sum for the quaternary, based on the ternary values:

$$G_{ABCD}(x,y) = \frac{x(1-x)\left[(1-y)G_{ABD}(x) + yG_{ABC}(x)\right] + y(1-y)\left[xG_{ACD}(y) + (1-x)G_{BCD}(y)\right]}{x(1-x) + y(1-y)} \tag{A.2}$$

Generally speaking, a given quaternary comprises a vast two-dimensional space of compositions (x,y). But in practice and in our case, x and y are linked since our structures are lattice matched to InP. Since the two constituents have identical lattice constants, the treatment is considerably simplified by the usual absence of any strong bowing of the band parameters for such an alloy. The quaternary will thus be considered represented as a mix of two constituents and treated as in Eq. A.1 .

The quaternary AlGaInAs actually combines two lattice-matched ternary alloys and can be written as $[Al_{0.48}In_{0.52}As]_z[Ga_{0.47}In_{0.53}As]_{1-z}$. The author of [146, 148] consider the room temperature bowing parameter for the alloy lattice matched to InP to be almost zero, meaning that we can simply interpolate the band parameters knowing the fraction of each ternary in the alloy.

Appendix B

Alternative fabrication strategies

In appendix section regarding clean room fabrication, I will present the variants of the previous processes that could be considered to avoid what I consider being the weaknesses of the process. First how to realize a hard mask for ICP, secondly how to avoid the only step that needs to be performed outside the lab, and finally how to realize InP 2D resonators.

B.1 Avoiding Ni masking

Finding a better solution for the ICP mask would be a welcome improvement to this process. I could try two different ways to manage the ICP with a hard mask and end up with gold on top afterward.

Three solutions, unequal in terms of steps or development required, are proposed:

- The most direct solution is to do two EBL: one positive for the gold deposition and one, realigned and negative, for the SiO patterning. (Use of HSQ resist, a negative resist that hardens upon e-beam insolation can make this step simpler). In this case some margin has to be anticipated to match the hard mask on the gold and a modification of the future cavity energy is bound to happen with respect to the expected energy using the metal as a mask.

- A second idea is to evaporate gold on the full sample first, then to deposit the SiO with a thickness necessary for the ICP plus the gold thickness. After patterning with a negative E-beam resist and RIE-etch the oxide, Ar^+ non selective milling could yield the desired result.

- Finally, a last possibility was quickly tested: performing the ICP with the HSQ mask without any gold, and then try to take advantage of the new topology to deposit the gold only on the top of the pillars. The goal is to planarize a resist decrease, it's thickness by plasma, such that it is lower than the top of the pillars and then to do the metal deposition. The main issue is that the resist is always conformal to a certain

degree: after spinning, it will be higher above the pillars than elsewhere, even after reflow. Using the thickest resist available (s1828, spun at 3000rpm $>$ 3µm thick) helps though.

Inspired by the nanoimprint lithography processes [149], I unsuccessfully tried to press on the sample above T_g with a piece of Silicon previously coated with fluor through silanization (thanks to Lola Ciapa at the SIMM, ESPCI) to make it non adhesive but it wasn't enough and a strong shear was still necessary to separate both pieces, resulting in damaged resist.

The idea then was to take advantage of the slow rehydration of the thick resist, necessary to make it photosensitive: immediately after spinning and baking the resist was exposed to UVs for 6 seconds (12 are necessary for usual development) and developed in MF319. Leftover resist, almost perfectly flat, was measured with the profilometer and the missing etch was done in RIE with oxygen plasma while measuring the speed with a red laser interferometer to reach the targeted thickness. The result is shown in Fig.B.1 (left). Regular TiAu evaporation and lift off yielded the metallized pillars in Fig.B.1 (right). Assuming this method can be scaled to a larger sample, this method

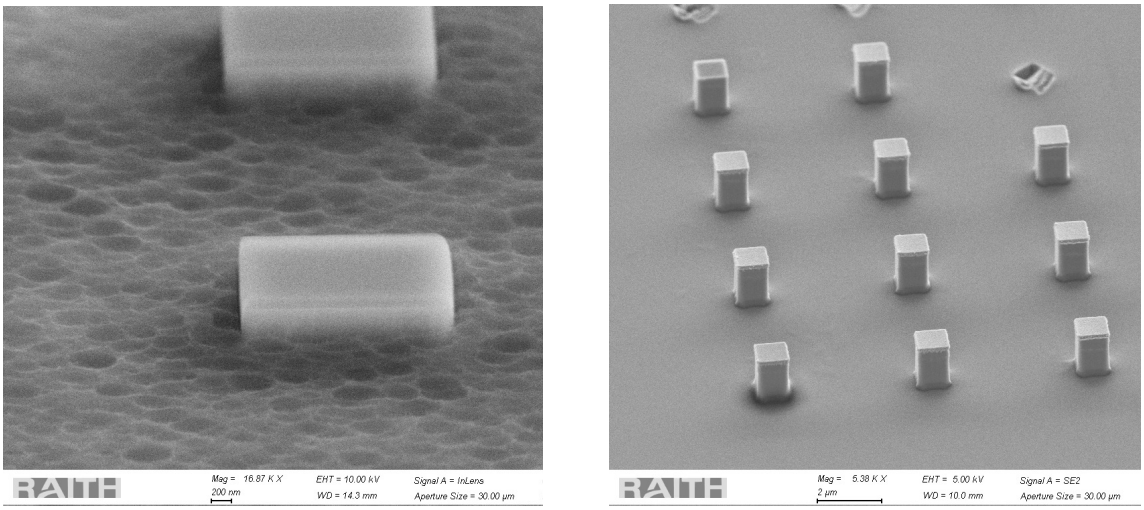

Fig. B.1 *(left) SEM image of planarized s1828 leaving just the top of the patched emerging.(right) Metallized pillars post etch. The top left pillar in the image is bare. Breaking of the top right pillar was not caused by steps related to the process.*

would provide a self-aligned metallization and make the sidewalls etching smoother.

B.2 Patch process for InP : suspended wires

The process to make self standing wires was developed though largely unused and is summarized in FigB.2. Inspired by [48], the idea is similar to the air bridge used to connect the waveguides to the devices: make a physical support layer to allow metal deposition on top of it before lifting it off altogether with the patterning resist.

Starting from the patterned resonators (a), the first step consists in planarizing an e-beam resist using reflow above the glass transition temperature (b), then lowering its surface to just

above the patches using O_2 RIE. We will then open the resist above each patch (c). The resist must be a positive resist otherwise it would be unreasonably long to write, hence the choice of PMMA. After development, the second step is to write the wires on top, but using again PMMA directly wouldn't work because the first layer would also be exposed and developed. To block this first support layer, we used the PMGI SF6 (d), compatible with the temperatures for PMMA baking, and insensitive to developer. It will act both as a chemical barrier for the second development of the wires and as an underetch (e). After metal deposition, a complete lift off of the three layers is performed using DMSO (f). After rinsing in IPA, it is recommended to flash dry the sample on a hotplate (200°C) because during evaporation the liquid risks pulling the wires down and breaking them. Large (400nm) and thick wires are less prone to breaking.

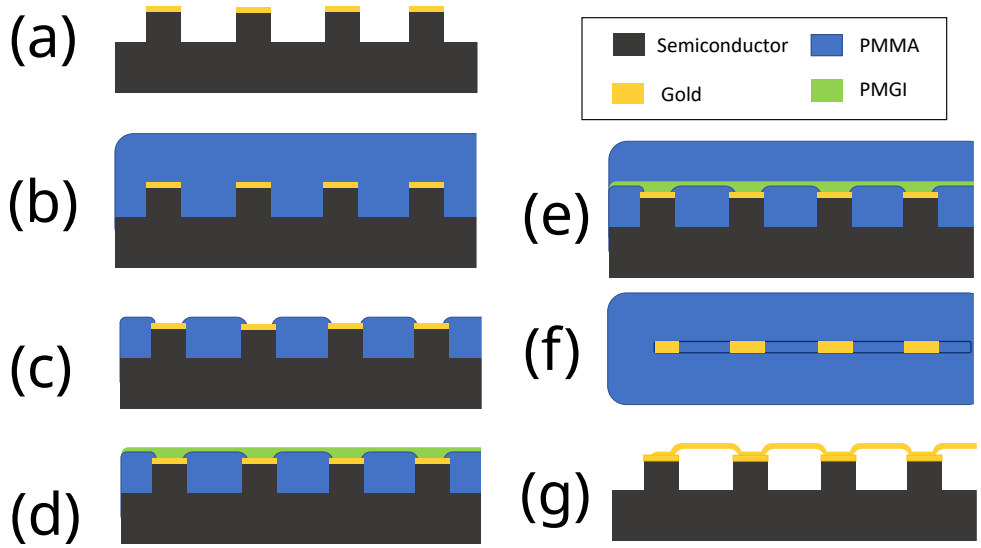

Fig. B.2 *Sketch of the process for self-standing wires between patch resonators.(a)Non connected patch resonators. (b) PMMA is spun. (c) PMMA is planarized, lowered, and opened above the patches. (d) PMGI is spun. (e) A second PMMA is spun above the PMGI (f) top view: wires are patterned in the top layer and the PGMI is unselectively removed under the opened area.(g) Metal deposition and lift off leave the wires suspended.*

An alternative to the PMGI compartmentalization is to use a thin metallic (Ti for instance) layer that can be removed after the second lithography in the opened areas via RIE.

B.3 MMA/PMMA Bilayer

The use of a PMGI/PMMA bilayer patterning process for Ni deposition in the main process was motivated by the development of the recipe in the context of the self standing wires. In terms of simplicity and toxicity of the resists and the solvents used, this bilayer could easily and advantageously be replaced by another more commonly bilayer: MMA/PMMA. The MMA is the monomer of the PMMA. With its much lower molecular weight, it is more sensitive to the electron dose than the PMMA. An e-beam lithography of the bilayer

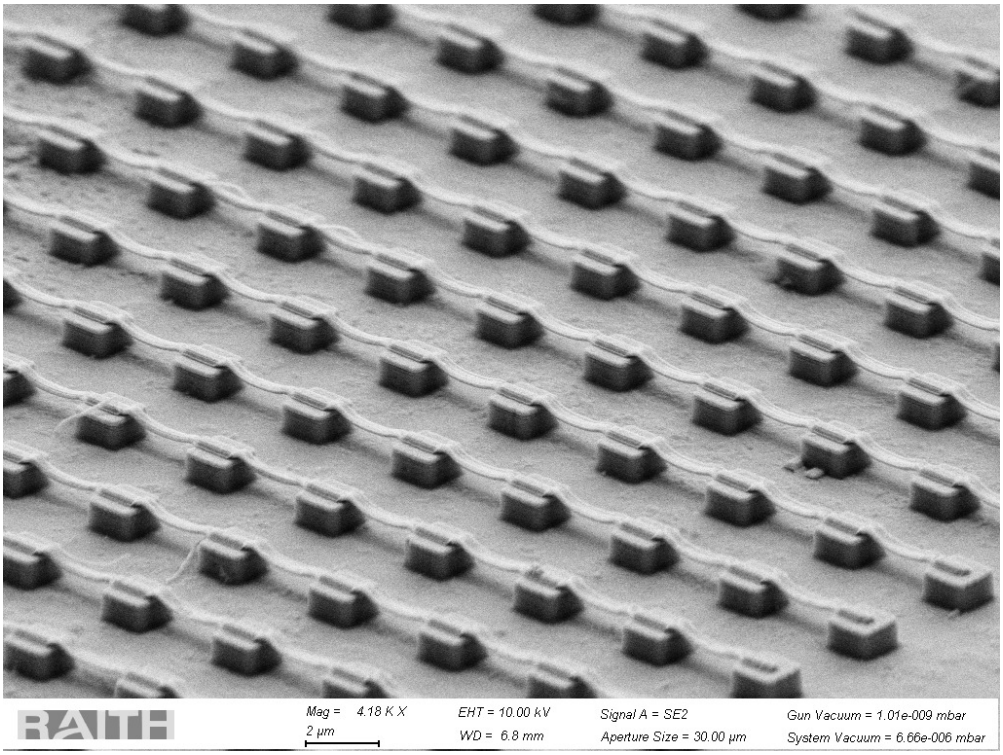

Fig. B.3 *Self standing wires connecting an array of patch resonators*

will produce slightly oversized patterns in the MMA layer underneath after development in MIBK:IPA, creating the underetch favorable for the lift-off without edge defects.

B.4 Epoxybonding and modified process

In order to avoid the one step that requires outsourcing, the waferbonding, an alternative process was developed, inspired by [150, 151]. To avoid the Au/Au thermocompression, 1.2x1.2 cm^2 pieces of the host GaAs wafer and of the active region covered in gold are glued together using an epoxy resin that can handle the high temperature of the ICP etching (EPOTEK 353ND).

Before the bonding of the structure, 300x150 μm^2 rectangles of gold are patterned on the active region and the active region is completely and selectively etched away from the InP, leaving only large mesa covered by gold. The resulting surface is then encapsulated in 1µm-thick SiN deposited in PECVD at 150°C as sketched in Fig.B.4 and is ready for bonding.

Special care before and during the curing was necessary to achieve a waferbonding thin enough to be cleaved in the end, that resists heating and vacuum. After mixing and before curing, each part was degassed at 10^{-2} mbar for 5 min. Deeper vacuums led to underwhelming results, maybe because the evaporation started and led to trapped bubbles in the resin.

The assembly of the active region and the host was made at 60°C, temperature at which the viscosity decreases steeply but reticulation doesn't start significantly. Continuous pressure was applied using a homemade press to minimize the final thickness (2µm thick layers were achieved). Temperature was slowly elevated to 250°C on a hot plate and cured for 20 min

before cooldown.
Next steps (substrate removal, resonator patterning, ICP) are identical to the normal process.

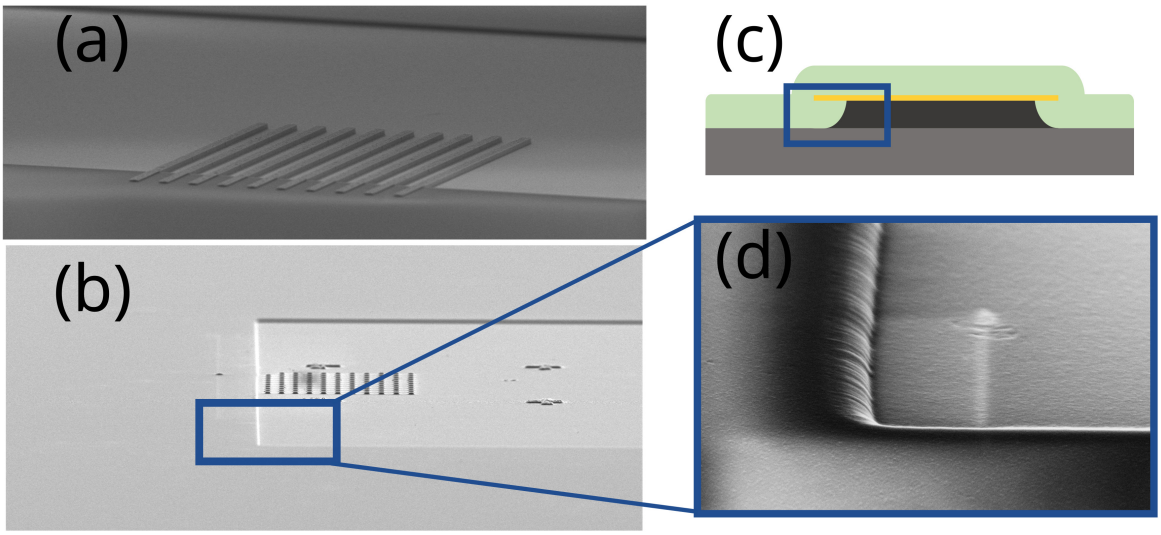

Fig. B.4 *(a),(b) SEM image of the Epoxybonding process of stripes and patches resonators after the ICP. On the zoom in (d), the edge of the SiN is visible and smoothly reaching the bottom gold contact. (c) shows the states of the sample after the encapsulation to explain the smooth slope at the edge of the SiN.*

The state of the sample is showed in Fig.B.4 (a) and (b). For stripes, the sample is ready for a CPW immediately: the end of the stripes reaches the SiN and can be connected, and the ground can be connected without further steps thanks to the advantageous profile of the SiN (Fig.B.4 (d)) inherited from the isotropic acid etching before encapsulation (Fig.B.4 (c)). For patches, self-standing wires are necessary.
Alternatively, gluebonding can be used to replace the Au/Au thermocompressive waferbonding without any other modification of the initial process.

Appendix C

Growth Sheets

C.1 Modulator V0351

Material	Doping (cm^{-3})	Thickness (nm)	
InGaAs	1×10^{18}	100	
InAlAs	–	20	x30 cycles
InGaAs	–	2.6	
InAlAs	–	1.4	
InGaAs	1×10^{18}	5.6	
InAlAs	-	20	
InGaAs	1×10^{18}	500	
InP Buffer			
InP:Fe semi-insulating wafer			

C.2 Modulator AC19

Material	Doping (cm^{-3})	Thickness (nm)	
InGaAs	1×10^{18}	50	
InAlAs	–	20	x20 cycles
InGaAs	–	2.6	
InAlAs	–	1.4	
InGaAs	2×10^{18}	5.6	
InAlAs	-	50	
InGaAs	1×10^{18}	100	
InP wafer			

C.3 Modulator AC715

Material	Doping (cm^{-3})	Thickness (nm)	
InGaAs	1×10^{18}	50	
InAlAs	–	20	x20 cycles
InGaAs	–	2.6	
InAlAs	–	1.4	
InGaAs	6×10^{18}	5.6	
InAlAs	-	50	
InGaAs	1×10^{18}	100	
InP:Fe wafer			

C.4 QWIP quaternary V0786

Material	Si Doping (cm^{-3})	Thickness (nm)	
InGaAs	1×10^{18}	50	
InGaAlAs	–	36.7	x13 cycles
InGaAs	–	0.5	
InGaAs	5×10^{17}	7	
InGaAs	–	0.5	
InGaAlAs	-	50	
InGaAs	1×10^{18}	100	
InP buffer			
InP:S wafer			

C.5 Diagonal QCD on GaAs L1604

Material	Doping (cm^{-3})	Thickness (nm)	
GaAs	6×10^{18}	50	
GaAs	-	8	
$Al_{0.35}Ga_{0.65}As$	–	5.2	
GaAs	–	2.3	
$Al_{0.35}Ga_{0.65}As$	–	5.8	
GaAs	–	1.7	
$Al_{0.35}Ga_{0.65}As$	–	5.5	
GaAs	–	1.4	
$Al_{0.35}Ga_{0.65}As$	–	1.4	
GaAs	–	0.5	
GaAs	1×10^{18}	3.4	
GaAs	–	0.5	
$Al_{0.35}Ga_{0.65}As$	–	4.8	x12 cycles
GaAs	–	3.0	
$Al_{0.35}Ga_{0.65}As$	–	5.2	
GaAs	–	2.3	
$Al_{0.35}Ga_{0.65}As$	–	5.8	
GaAs	–	1.7	
$Al_{0.35}Ga_{0.65}As$	–	5.5	
GaAs	–	1.4	
$Al_{0.35}Ga_{0.65}As$	–	1.4	
GaAs	–	0.5	
GaAs	1×10^{18}	3.4	
GaAs	–	0.5	
$Al_{0.35}Ga_{0.65}As$	-	8	
GaAs	-	8	
GaAs	6×10^{18}	40	
$Al_{0.35}Ga_{0.65}As$	-	400	etch stop
Semi insulating GaAs wafer			

C.6 Diagonal QCD on InP EU 2863

Material	Si Doping (cm^{-3})	Thickness (nm)	
InGaAs	1×10^{18}	50	
InGaAs	-	5	
InAlAs	–	3.4	
InGaAs	–	3.7	
InAlAs	–	3.5	
InGaAs	–	3.5	
InAlAs	–	3.5	
InGaAs	–	3.2	
InAlAs	–	4.9	
InGaAs	–	2.8	
InAlAs	–	1.1	
InGaAs	–	6.7	
InAlAs	–	3.3	x8 cycles
InGaAs	–	4.9	
InAlAs	–	3.4	
InGaAs	–	3.7	
InAlAs	–	3.5	
InGaAs	–	3.5	
InAlAs	–	3.5	
InGaAs	–	3.2	
InAlAs	–	4.9	
InGaAs	–	2.8	
InAlAs	–	1.1	
InGaAs	1×10^{18}	6.7	
InAlAs	-	3.3	
InGaAs	-	4.9	
InAlAs	-	6	
InGaAs	-	5	
InGaAs	1×10^{18}	100	
InP:Fe wafer			

List of Figures

Bibliography

[1] W. Patrick McCray. MBE deserves a place in the history books. *Nature Nanotechnology*, 2(5):259–261, May 2007.

[2] J. Faist, F. Capasso, D.L. Sivco, C. Sirtori, A.L. Hutchinson, and A.Y. Cho. Quantum Cascade Laser. *Science*, 264(5158):553–556, 1994.

[3] Stefan Menzel, Laurent Diehl, Christian Pflügl, Anish Goyal, Christine Wang, Antonio Sanchez, George Turner, and Federico Capasso. Quantum cascade laser master-oscillator power-amplifier with 15 W output power at 300 K. *Optics Express*, 19(17):16229, August 2011.

[4] E. Dupont, D. Delacourt, V. Berger, N. Vodjdani, and M. Papuchon. Phase and amplitude modulation based on intersubband transitions in electron transfer double quantum wells. *Applied Physics Letters*, 62(16):1907–1909, April 1993.

[5] Carlo Sirtori, Federico Capasso, Deborah L. Sivco, A. L. Hutchinson, and Alfred Y. Cho. Resonant Stark tuning of second-order susceptibility in coupled quantum wells. *Applied Physics Letters*, 60(2):151–153, January 1992.

[6] William Herschel. Investigation of the powers of the prismatic colours to heat and illuminate objects; with remarks, that prove the different refrangibility of radiant heat. To which is added, an inquiry into the method of viewing the sun advantageously, with telescopes of large apertures and high magnifying powers. *Philosophical Transactions of the Royal Society of London*, 90:255–283, December 1800.

[7] G. Kirchhoff. Ueber das Verhältniss zwischen dem Emissionsvermögen und dem Absorptionsvermögen der Körper für Wärme und Licht. *Annalen der Physik und Chemie*, 185(2):275–301, 1860.

[8] Willy Wien. On the division of energy in the emission-spectrum of a black body. *The London, Edinburgh, and Dublin Philosophical Magazine and Journal of Science*, 43(262):214–220, March 1897.

[9] Max Planck. Ueber das Gesetz der Energieverteilung im Normalspectrum. *Annalen der Physik*, 309(3):553–563, 1901.

[10] S. P. Langley. The Bolometer and Radiant Energy. *Proceedings of the American Academy of Arts and Sciences*, 16:342, 1880.

[11] M S Shur, A D Bykhovski, and R Gaska. PYROELECTRIC AND PIEZOELECTRIC PROPERTIES OF GAN-BASED MATERIALS.

[12] Roselyne Ishimwe, K. Abutaleb, and F. Ahmed. Applications of Thermal Imaging in Agriculture—A Review. *Advances in Remote Sensing*, 03(03):128–140, 2014.

[13] Alexandra Witze. Four revelations from the Webb telescope about distant galaxies. *Nature*, 608(7921):18–19, August 2022.

[14] GRAVITY+ Collaboration et al. The GRAVITY+ Project: Towards All-sky, Faint-Science, High-Contrast Near-Infrared Interferometry at the VLTI. *Published in The Messenger vol. 189*, pp. 17-22:6 pages, 2022. Artwork Size: 6 pages Medium: PDF Publisher: European Southern Observatory (ESO).

[15] Guillaume Bourdarot, Jean-Philippe Berger, and Hugues Guillet de Chatellus. Architecture of photonics correlation for infrared heterodyne interferometry: demonstration of amplitude-modulation based correlation. *Journal of the Optical Society of America B*, 38(10):3105, October 2021.

[16] Chloé Sauvage, Clélia Robert, Béatrice Sorrente, Frédéric Grillot, and Didier Erasme. Study of short and mid-wavelength infrared telecom links performance for different climatic conditions. In Karin U. Stein and Szymon Gladysz, editors, *Environmental Effects on Light Propagation and Adaptive Systems II*, page 18, Strasbourg, France, November 2019. SPIE.

[17] Abdulsalam Ghalib Alkholidi and Khaleel Saeed Altowij. Free Space Optical Communications — Theory and Practices. In Mutamed Khatib, editor, *Contemporary Issues in Wireless Communications*. InTech, November 2014.

[18] Paul Corrigan, Rainer Martini, Edward A. Whittaker, and Clyde Bethea. Quantum cascade lasers and the Kruse model in free space optical communication. *Optics Express*, 17(6):4355, March 2009.

[19] H. Hemmati. *Near-Earth Laser Communications, Second Edition*. Optical Science and Engineering. CRC Press, 2020.

[20] https://www.airbus.com/en/products-services/defence/connectivity/space-data highway. Space Data Highway.

[21] https://www.sda.mil/wp-content/uploads/2022/04/SDA-OCT-Standard-v3.0.pdf Space Development Agency. Optical Communications Terminal (OCT) Standard.

[22] Xiaodan Pang, Oskars Ozolins, Lu Zhang, Richard Schatz, Aleksejs Udalcovs, Xianbin Yu, Gunnar Jacobsen, Sergei Popov, Jiajia Chen, and Sebastian Lourdudoss. Free-Space Communications Enabled by Quantum Cascade Lasers. *physica status solidi (a)*, 218(3):2000407, February 2021.

[23] Gerald Bastard. Enveloppe function descritpion of heterostructure electronic states. In *Wave mechanics applied to semiconductor heterostructures*. Les Editions de Physique.

[24] Carlo Sirtori, Federico Capasso, Jérôme Faist, and Sandro Scandolo. Nonparabolicity and a sum rule associated with bound-to-bound and bound-to-continuum intersubband transitions in quantum wells. *Physical Review B*, 50(12):8663–8674, September 1994.

[25] Manfred Helm. The Basic Physics of Intersubband Transitions. In *Intersubband Transitions in Quantum Wells Physics and Device Applications I*, SEMICONDUCTORS AND SEMIMETALS. Academic Press, 2000.

[26] Yanko Todorov and Carlo Sirtori. Intersubband polaritons in the electrical dipole gauge. *Physical Review B*, 85(4):045304, January 2012.

[27] H. C. Liu and Federico Capasso. *Intersubband transitions in quantum wells: physics and device applications I*. Academic Press, San Diego, CA, 2000. OCLC: 289516980.

[28] F. Capasso, C. Sirtori, and A.Y. Cho. Coupled quantum well semiconductors with giant electric field tunable nonlinear optical properties in the infrared. *IEEE Journal of Quantum Electronics*, 30(5):1313–1326, May 1994.

[29] Jongwon Lee, Mykhailo Tymchenko, Christos Argyropoulos, Pai-Yen Chen, Feng Lu, Frederic Demmerle, Gerhard Boehm, Markus-Christian Amann, Andrea Alù, and Mikhail A. Belkin. Giant nonlinear response from plasmonic metasurfaces coupled to intersubband transitions. *Nature*, 511(7507):65–69, July 2014.

[30] RF Kazarinov and RA Suris. Electric and electromagnetic properties of semiconductors with a superlattice. *Sov. Phys. Semicond*, 6(1):120–131, 1972.

[31] B. F. Levine, K. K. Choi, C. G. Bethea, J. Walker, and R. J. Malik. New 10 μm infrared detector using intersubband absorption in resonant tunneling GaAlAs superlattices. *Applied Physics Letters*, 50(16):1092–1094, April 1987.

[32] H. C. Liu. Photoconductive gain mechanism of quantum-well intersubband infrared detectors. *Applied Physics Letters*, 60(12):1507–1509, March 1992.

[33] B. F. Levine, C. G. Bethea, K. K. Choi, J. Walker, and R. J. Malik. Bound-to-extended state absorption GaAs superlattice transport infrared detectors. *Journal of Applied Physics*, 64(3):1591–1593, August 1988.

[34] Steven K H Sim, H C Liu, A Shen, M Gao, Kevin F Lee, M Buchanan, Y Ohno, H Ohno, and E H Li. Effect of barrier width on the performance of quantum well infrared photodetector. *Infrared Physics*, page 7, 2001.

[35] Daniele Palaferri, Yanko Todorov, Azzurra Bigioli, Alireza Mottaghizadeh, Djamal Gacemi, Allegra Calabrese, Angela Vasanelli, Lianhe Li, A. Giles Davies, Edmund H.

Linfield, Filippos Kapsalidis, Mattias Beck, Jérôme Faist, and Carlo Sirtori. Room-temperature nine-μm-wavelength photodetectors and GHz-frequency heterodyne receivers. *Nature*, 556(7699):85–88, April 2018.

[36] A. Vasanelli, A. Leuliet, C. Sirtori, A. Wade, G. Fedorov, D. Smirnov, G. Bastard, B. Vinter, M. Giovannini, and J. Faist. Role of elastic scattering mechanisms in GaInAs/AlInAs quantum cascade lasers. *Applied Physics Letters*, 89(17):172120, October 2006.

[37] Daniel Hofstetter, Mattias Beck, and Jérôme Faist. Quantum-cascade-laser structures as photodetectors. *Applied Physics Letters*, 81(15):2683–2685, October 2002.

[38] Marcel Graf, Giacomo Scalari, Daniel Hofstetter, Jérôme Faist, Harvey Beere, Edmund Linfield, David Ritchie, and Giles Davies. Terahertz range quantum well infrared photodetector. *Applied Physics Letters*, 84(4):475–477, January 2004.

[39] Peter Reininger, Benedikt Schwarz, Hermann Detz, Don MacFarland, Tobias Zederbauer, Aaron Maxwell Andrews, Werner Schrenk, Oskar Baumgartner, Hans Kosina, and Gottfried Strasser. Diagonal-transition quantum cascade detector. *Applied Physics Letters*, 105(9):091108, September 2014.

[40] A. Delga. Quantum cascade detectors: A review. In *Mid-infrared optoelectronics: materials, devices, and applications*, Woodhead Publishing Series in Electronic and Optical Materials.

[41] A. Harrer, B. Schwarz, S. Schuler, P. Reininger, A. Wirthmüller, H. Detz, D. MacFarland, T. Zederbauer, A. M. Andrews, M. Rothermund, H. Oppermann, W. Schrenk, and G. Strasser. 43 µm quantum cascade detector in pixel configuration. *Optics Express*, 24(15):17041, July 2016.

[42] Mathurin Lagrée. Transport électronique en régime de couplage fort lumière-matière pour les dispositifs quantiques moyen-infrarouge. page 227.

[43] P. Harrison. The nature of the electron distribution functions in quantum cascade lasers. *Applied Physics Letters*, 75(18):2800–2802, November 1999.

[44] A. Buffaz, A. Gomez, M. Carras, L. Doyennette, and V. Berger. Role of subband occupancy on electronic transport in quantum cascade detectors. *Physical Review B*, 81(7):075304, February 2010.

[45] C. Sirtori, F. Capasso, J. Faist, A.L. Hutchinson, D.L. Sivco, and A.Y. Cho. Resonant tunneling in quantum cascade lasers. *IEEE Journal of Quantum Electronics*, 34(9):1722–1729, September 1998.

[46] Azzurra Bigioli, Giovanni Armaroli, Angela Vasanelli, Djamal Gacemi, Yanko Todorov, Daniele Palaferri, Lianhe Li, A. Giles Davies, Edmund H. Linfield, and Carlo Sirtori.

Long-wavelength infrared photovoltaic heterodyne receivers using patch-antenna quantum cascade detectors. *Applied Physics Letters*, 116(16):161101, April 2020.

[47] Hideki T. Miyazaki, Takaaki Mano, Takeshi Kasaya, Hirotaka Osato, Kazuhiro Watanabe, Yoshimasa Sugimoto, Takuya Kawazu, Yukinaga Arai, Akitsu Shigetou, Tetsuyuki Ochiai, Yoji Jimba, and Hiroshi Miyazaki. Synchronously wired infrared antennas for resonant single-quantum-well photodetection up to room temperature. *Nature Communications*, 11(1):565, January 2020.

[48] M Hakl, Q Y Lin, S Lepillet, J-F Lampin, S Pirotta, R Colombelli, J Wan, J C Cao, H Li, E Peytavit, and S Barbieri. Ultra-fast quantum-well infared photodetectors operating at 10μm with flat response up to 70GHz at room temperature. page 12.

[49] G. Quinchard, C. Mismer, M. Hakl, J. Pereira, Q. Lin, S. Lepillet, V. Trinité, A. Evirgen, E. Peytavit, J. L. Reverchon, J. F. Lampin, S. Barbieri, and A. Delga. High speed, antenna-enhanced 10.3 $\boldsymbol{\mu}$ m quantum cascade detector. *Applied Physics Letters*, 120(9):091108, February 2022.

[50] J. B. Johnson. Thermal Agitation of Electricity in Conductors. *Physical Review*, 32(1):97–109, July 1928.

[51] Tatsuo Dougakiuchi, Akio Ito, Masahiro Hitaka, Kazuue Fujita, and Masamichi Yamanishi. Ultimate response time in mid-infrared high-speed low-noise quantum cascade detectors. *Applied Physics Letters*, 118(4):041101, January 2021.

[52] Ayoub Bounab, Olivier Boulade, Cyril Cervera, Xavier De La Broïse, Cyrille Delisle, Quan Dong, Yong Jin, Adrien Lamoure, Lydie Mathieu, Vincent Moreau, and Patrick Mulet. LWIR quantum efficiency measurements using a calibrated MCT photodiode read by a cryo-HEMT-based amplifier. In Andrew D. Holland and James Beletic, editors, *X-Ray, Optical, and Infrared Detectors for Astronomy IX*, page 86, Online Only, United States, December 2020. SPIE.

[53] G. Marschick, M. David, E. Arigliani, N. Opačak, B. Schwarz, M. Giparakis, A. Delga, M. Lagree, T. Poletti, V. Trinite, A. Evirgen, B. Gerard, G. Ramer, R. Maulini, J. Butet, S. Blaser, A. M. Andrews, G. Strasser, and B. Hinkov. High-responsivity operation of quantum cascade detectors at 9 μm. *Optics Express*, 30(22):40188, October 2022.

[54] J. Y. Andersson and L. Lundqvist. Grating-coupled quantum-well infrared detectors: Theory and performance. *Journal of Applied Physics*, 71(7):3600–3610, April 1992.

[55] H Schneider, M Walther, C Schönbein, R Rehm, J Fleissner, W Pletschen, J Braunstein, P Koidl, G Weimann, J Ziegler, and W Cabanski. QWIP FPAs for high-performance thermal imaging. *Physica E: Low-dimensional Systems and Nanostructures*, 7(1-2):101–107, April 2000.

[56] B F Levine. Quantum-well infrared photodetectors. page 82.

[57] Y. Todorov, L. Tosetto, J. Teissier, A. M. Andrews, P. Klang, R. Colombelli, I. Sagnes, G. Strasser, and C. Sirtori. Optical properties of metal-dielectric-metal microcavities in the THz frequency range. *Optics Express*, 18(13):13886, June 2010.

[58] Mattias Beck, Daniel Hofstetter, Thierry Aellen, Jérôme Faist, Ursula Oesterle, Marc Ilegems, Emilio Gini, and Hans Melchior. Continuous Wave Operation of a Mid-Infrared Semiconductor Laser at Room Temperature. *Science*, 295(5553):301–305, January 2002.

[59] Mattias Beck, Daniel Hofstetter, Thierry Aellen, Jérôme Faist, Ursula Oesterle, Marc Ilegems, Emilio Gini, and Hans Melchior. Continuous Wave Operation of a Mid-Infrared Semiconductor Laser at Room Temperature. *Science*, 295(5553):301–305, January 2002.

[60] K. M. Oresick, J. D. Kirch, L. J. Mawst, and D. Botez. Highly efficient $\sim$8 μ m-emitting, step-taper active-region quantum cascade lasers. *AIP Advances*, 11(2):025004, February 2021.

[61] Manijeh Razeghi. High-performance InP-based midinfrared quantum cascade lasers at Northwestern University. *Optical Engineering*, 49(11):111103, November 2010.

[62] John E. Carroll, James Whiteaway, and Dick Plumb. *Distributed feedback semiconductor lasers*. Number 10 in IEE Circuits, devices and systems series. The Institution of Electrical Engineers : SPIE Optical Engineering Press, London, UK, 1998.

[63] P. L. T. Sow, S. Mejri, S. K. Tokunaga, O. Lopez, A. Goncharov, B. Argence, C. Chardonnet, A. Amy-Klein, C. Daussy, and B. Darquié. A widely tunable 10- μ m quantum cascade laser phase-locked to a state-of-the-art mid-infrared reference for precision molecular spectroscopy. *Applied Physics Letters*, 104(26):264101, June 2014.

[64] Tadao Nagatsuma, Guillaume Ducournau, and Cyril C. Renaud. Advances in terahertz communications accelerated by photonics. *Nature Photonics*, 10(6):371–379, June 2016.

[65] Chloé Sauvage, Clélia Robert, Béatrice Sorrente, Frédéric Grillot, and Didier Erasme. Study of short and mid-wavelength infrared telecom links performance for different climatic conditions. In Karin U. Stein and Szymon Gladysz, editors, *Environmental Effects on Light Propagation and Adaptive Systems II*, page 18, Strasbourg, France, November 2019. SPIE.

[66] N. Vodjdani, B. Vinter, V. Berger, E. Böckenhoff, and E. Costard. Tunneling assisted modulation of the intersubband absorption in double quantum wells. *Applied Physics Letters*, 59(5):555–557, July 1991.

[67] J. Y. Duboz, V. Berger, N. Laurent, D. Adam, and J. Nagle. Grating coupled infrared modulator at normal incidence based on intersubband transitions. *Applied Physics Letters*, 70(12):1569–1571, March 1997.

[68] Stefano Pirotta, Ngoc-Linh Tran, Giorgio Biasiol, Arnaud Jollivet, Paul Crozat, Jean-Michel Manceau, Adel Bousseksou, and Raffaele Colombelli. Ultra-fast amplitude modulation of mid-IR free-space beams at room-temperature. *Nature Communications*, 12(1):799, December 2021. arXiv: 2006.12215.

[69] J. Stark. Beobachtungen über den Effekt des elektrischen Feldes auf Spektrallinien. I. Quereffekt. *Annalen der Physik*, 348(7):965–982, 1914.

[70] Alex Harwit and J. S. Harris. Observation of Stark shifts in quantum well intersubband transitions. *Applied Physics Letters*, 50(11):685–687, March 1987.

[71] Alex Harwit, J. S. Harris, and A. Kapitulnik. Calculated quasieigenstates and quasieigenenergies of quantum well superlattices in an applied electric field. *Journal of Applied Physics*, 60(9):3211–3213, November 1986.

[72] I. Bar-Joseph, C. Klingshirn, D. A. B. Miller, D. S. Chemla, U. Koren, and B. I. Miller. Quantum-confined Stark effect in InGaAs/InP quantum wells grown by organometallic vapor phase epitaxy. *Applied Physics Letters*, 50(15):1010–1012, April 1987.

[73] D. C. S. Dumas, K. Gallacher, S. Rhead, M. Myronov, D. R. Leadley, and D. J. Paul. Ge/SiGe quantum confined Stark effect electro-absorption modulation with low voltage swing at 0xCE 0xBB = 1550 nm. *Optics Express*, 22(16):19284, August 2014.

[74] Dominique Delacourt and Michel Papuchon. Mid-Infrared Phase Modulation via Stark Effect on Intersubband Transitions in GaAdGaAlAs Quantum Wells. page 6.

[75] R.P.G. Karunasiri, Y.J. Mii, and K.L. Wang. Tunable infrared modulator and switch using Stark shift in step quantum wells. *IEEE Electron Device Letters*, 11(5):227–229, May 1990.

[76] Y. J. Mii, R. P. G. Karunasiri, K. L. Wang, M. Chen, and P. F. Yuh. Large Stark shifts of the local to global state intersubband transitions in step quantum wells. *Applied Physics Letters*, 56(20):1986–1988, May 1990.

[77] J. Teissier, S. Laurent, C. Manquest, C. Sirtori, A. Bousseksou, J. R. Coudevylle, R. Colombelli, G. Beaudoin, and I. Sagnes. Electrical modulation of the complex refractive index in mid-infrared quantum cascade lasers. *Optics Express*, 20(2):1172, January 2012.

[78] Jongwon Lee, Seungyong Jung, Pai-Yen Chen, Feng Lu, Frederic Demmerle, Gerhard Boehm, Markus-Christian Amann, Andrea Alù, and Mikhail A. Belkin. Ultrafast Electrically Tunable Polaritonic Metasurfaces. *Advanced Optical Materials*, 2(11):1057–1063, November 2014.

[79] Alexander Benz, Inès Montaño, John F. Klem, and Igal Brener. Tunable metamaterials based on voltage controlled strong coupling. *Applied Physics Letters*, 103(26):263116, December 2013.

[80] K. Pantzas and G. Patriarche. Experimental quantification of atomically-resolved HAADF-STEM images using EDX. *Ultramicroscopy*, 220:113152, January 2021.

[81] Konstantinos Pantzas, Grégoire Beaudoin, Gilles Patriarche, Ludovic Largeau, Olivia Mauguin, Giulia Pegolotti, Angela Vasanelli, Ariane Calvar, Maria Amanti, Carlo Sirtori, and Isabelle Sagnes. Sub-nanometrically resolved chemical mappings of quantum-cascade laser active regions. *Semiconductor Science and Technology*, 31(5):055017, May 2016.

[82] Esperanza Luna, Álvaro Guzmán, Achim Trampert, and Gabriel Álvarez. Critical Role of Two-Dimensional Island-Mediated Growth on the Formation of Semiconductor Heterointerfaces. *Physical Review Letters*, 109(12):126101, September 2012.

[83] T Roch, C Pflügl, A M Andrews, W Schrenk, and G Strasser. X-ray investigation of quantum well intermixing after postgrowth rapid thermal processing. *Journal of Physics D: Applied Physics*, 38(10A):A132–A136, May 2005.

[84] B. Knipfer, S. Xu, J.D. Kirch, D. Botez, and L.J. Mawst. Analysis of interface roughness in strained InGaAs/AlInAs quantum cascade laser structures (0xCE 0xBB $\sim$ 4.6 µm) by atom probe tomography. *Journal of Crystal Growth*, 583:126531, April 2022.

[85] Etienne Rodriguez, Alireza Mottaghizadeh, Djamal Gacemi, Daniele Palaferri, Zahra Asghari, Mathieu Jeannin, Angela Vasanelli, Azzurra Bigioli, Yanko Todorov, Mattias Beck, Jerome Faist, Qi Jie Wang, and Carlo Sirtori. Room-Temperature, Wide-Band, Quantum Well Infrared Photodetector for Microwave Optical Links at 4.9 µm Wavelength. *ACS Photonics*, 5(9):3689–3694, September 2018.

[86] Rainee N. Simons. *Coplanar Waveguide Circuits, Components, and Systems*. Wiley Series in Microwave and Optical Engineering. John Wiley & Sons, Inc., New York, USA, March 2001.

[87] Katrin Steinberg, Marc Scheffler, and Martin Dressel. Microwave inductance of thin metal strips. *Journal of Applied Physics*, 108(9):096102, November 2010.

[88] H.C. Liu, Jianmeng Li, M. Buchanan, and Z.R. Wasilewski. High-frequency quantum-well infrared photodetectors measured by microwave-rectification technique. *IEEE Journal of Quantum Electronics*, 32(6):1024–1028, June 1996.

[89] Tatsuo Dougakiuchi, Akio Ito, Masahiro Hitaka, Kazuue Fujita, and Masamichi Yamanishi. Ultimate response time in mid-infrared high-speed low-noise quantum cascade detectors. *Applied Physics Letters*, 118(4):041101, January 2021.

[90] Hamza Dely*, Thomas Bonazzi*, Olivier Spitz, Etienne Rodriguez, Djamal Gacemi, Yanko Todorov, Konstantinos Pantzas, Grégoire Beaudoin, Isabelle Sagnes, Lianhe Li, Alexander Giles Davies, Edmund H. Linfield, Frédéric Grillot, Angela Vasanelli, and Carlo Sirtori. 10 Gbit s−1 Free Space Data Transmission

at 9 μm Wavelength With Unipolar Quantum Optoelectronics (Laser Photonics Rev. 16(2)/2022). *Laser & Photonics Reviews*, 16(2):2270006, 2022. _eprint: https://onlinelibrary.wiley.com/doi/pdf/10.1002/lpor.202270006.

[91] Pierre Didier, Hamza Dely, Thomas Bonazzi, Olivier Spitz, Elie Awwad, Étienne Rodriguez, Angela Vasanelli, Carlo Sirtori, and Frédéric Grillot. High-capacity free-space optical link in the midinfrared thermal atmospheric windows using unipolar quantum devices. *Advanced Photonics*, 4(05), November 2022.

[92] Hamza Dely, Mahdieh Joharifar, Xiaodan Pang, Djamal Gacemi, Toms Salgals, Richard Schatz, Yan-Ting Sun, Thomas Bonazzi, Etienne Rodriguez, Yanko Todorov, Angela Vasanelli, Aleksejs Udalcovs, Sandis Spolitis, Vjaceslavs Bobrovs, Oskars Ozolins, Sergei Popov, and Carlo Sirtori. High bitrate data transmission in the 8-14 μmatmospheric window using external Stark-effectmodulator with digital equalization. *Optics Express*, December 2022.

[93] Li Tao, Zefeng Chen, Zhiyong Li, Jiaqi Wang, Xin Xu, and Jian-Bin Xu. Enhancing light-matter interaction in 2D materials by optical micro/nano architectures for high-performance optoelectronic devices. *InfoMat*, 3(1):36–60, January 2021.

[94] N Berkovitch, P Ginzburg, and M Orenstein. Nano-plasmonic antennas in the near infrared regime. *Journal of Physics: Condensed Matter*, 24(7):073202, February 2012.

[95] Byoungho Lee, Il-Min Lee, Seyoon Kim, Dong-Ho Oh, and Lambertus Hesselink. Review on subwavelength confinement of light with plasmonics. *Journal of Modern Optics*, 57(16):1479–1497, September 2010.

[96] CA Balanis. Antenna Theory: Analysis and Design, 2015.

[97] Mel F. Hainey, Takaaki Mano, Takeshi Kasaya, Tetsuyuki Ochiai, Hirotaka Osato, Kazuhiro Watanabe, Yoshimasa Sugimoto, Takuya Kawazu, Yukinaga Arai, Akitsu Shigetou, and Hideki T. Miyazaki. Systematic studies for improving device performance of quantum well infrared stripe photodetectors. *Nanophotonics*, 9(10):3373–3384, August 2020.

[98] Cheryl Feuillet-Palma, Yanko Todorov, Angela Vasanelli, and Carlo Sirtori. Strong near field enhancement in THz nano-antenna arrays. *Scientific Reports*, 3(1):1361, December 2013.

[99] Theodor Förster. Energy migration and fluorescence. *Journal of Biomedical Optics*, 17(1):011002, 2012.

[100] hermann a Haus. *Waves And Fields In Optoelectronics*. 1984.

[101] Etienne Rodriguez, Thomas Bonazzi, Hamza Dely, Konstantinos Pantzas, Isabelle Sagnes, Angela Vasanelli, and Carlo Sirtori. Metamaterial engineering for optimized photon absorption in unipolar quantum devices. page 17.

[102] T. Skauli, P. S. Kuo, K. L. Vodopyanov, T. J. Pinguet, O. Levi, L. A. Eyres, J. S. Harris, M. M. Fejer, B. Gerard, L. Becouarn, and E. Lallier. Improved dispersion relations for GaAs and applications to nonlinear optics. *Journal of Applied Physics*, 94(10):6447–6455, November 2003.

[103] P. Jouy, Y. Todorov, A. Vasanelli, R. Colombelli, I. Sagnes, and C. Sirtori. Coupling of a surface plasmon with localized subwavelength microcavity modes. *Applied Physics Letters*, 98(2):021105, January 2011.

[104] Mark A. Ordal, Robert J. Bell, Ralph W. Alexander, Larry L. Long, and Marvin R. Querry. Optical properties of Au, Ni, and Pb at submillimeter wavelengths. *Applied Optics*, 26(4):744, February 1987.

[105] Grégory Quinchard. *Détecteur infrarouge hétérodyne à cascade quantiques*. PhD thesis, Paris, 2021.

[106] Daniele Palaferri. *Antenna resonators for quantum infrared detectors and fast heterodyne receivers*. PhD thesis, Université Paris Diderot, Paris, 2018.

[107] Raffaele Colombelli, Robson Ferreira, François Julien, Xavier Letartre, Roland Teissier, and Jérôme Tignon. PHOTONIQUE POUR LES LASERS À CASCADE QUANTIQUE TÉRAHERTZ. page 252.

[108] M. Lagrée, M. Jeannin, G. Quinchard, O. Ouznali, A. Evirgen, V. Trinité, R. Colombelli, and A. Delga. Direct Polariton-To-Electron Tunneling in Quantum Cascade Detectors Operating in the Strong Light-Matter Coupling Regime. *Physical Review Applied*, 17(4):044021, April 2022.

[109] A.R Clawson. Guide to references on III–V semiconductor chemical etching. *Materials Science and Engineering: R: Reports*, 31(1-6):1–438, January 2001.

[110] Troels Markussen and Kurt Stokbro. Metal-InGaAs contact resistance calculations from first principles. In *2016 International Conference on Simulation of Semiconductor Processes and Devices (SISPAD)*, pages 373–376, Nuremberg, Germany, September 2016. IEEE.

[111] John S. Parker, Erik J. Norberg, Robert S. Guzzon, Steven C. Nicholes, and Larry A. Coldren. High verticality InP/InGaAsP etching in Cl2/H2/Ar inductively coupled plasma for photonic integrated circuits. *Journal of Vacuum Science & Technology B, Nanotechnology and Microelectronics: Materials, Processing, Measurement, and Phenomena*, 29(1):011016, January 2011.

[112] Fares Chouchane, Bassem Salem, Guillaume Gay, Mickael Martin, Erwine Pargon, Franck Bassani, Sandrine Arnaud, Sylvain David, Reynald Alcotte, Sébastien Labau, Jérémy Moeyart, and Thierry Baron. Sub-10 nm plasma nanopatterning of InGaAs with nearly vertical and smooth sidewalls for advanced n-fin field effect transistors on silicon.

Journal of Vacuum Science & Technology B, Nanotechnology and Microelectronics: Materials, Processing, Measurement, and Phenomena, 35(2):021206, March 2017.

[113] Kevin Zhang, Gerhard Böhm, and Mikhail A. Belkin. Mid-infrared microring resonators and optical waveguides on an InP platform. *Applied Physics Letters*, 120(6):061106, February 2022.

[114] S. Vicknesh and A. Ramam. Etching Characteristics of HBr-Based Chemistry on InP Using the ICP Technique. *Journal of The Electrochemical Society*, 151(12):C772–C780, December 2004.

[115] Hsin-Yi Chen and Harry E. Ruda. Inductively coupled plasma etching of InP using CH[sub 4]/H[sub 2] and CH[sub 4]/H[sub 2]/N[sub 2]. *Journal of Vacuum Science & Technology B: Microelectronics and Nanometer Structures*, 20(1):47, 2002.

[116] Benjamin Askenazi. Du Couplage Ultra-Fort Lumière-Matière pour de Nouveaux Métamatériaux Térahertz. page 218.

[117] Sean L Rommel, Jae-Hyung Jang, Wu Lu, Gabriel Cueva, Ling Zhou, Ilesanmi Adesida, Gary Pajer, Allen Lepore, Zane Schellanbarger, and Joseph H Abeles. Effect of H 2 on the etch profile of InP/InGaAsP alloys in Cl 2 / Ar / H 2 inductively coupled plasma reactive ion etching chemistries for photonic device fabrication. *J. Vac. Sci. Technol. B*, 20(4):5, 2002.

[118] https://wiki.nanotech.ucsb.edu/wiki/. UCSB wiki for nanofabrication.

[119] Mamadou Aliou Barry, Vincent Berthier, Bodo D. Wilts, Marie-Claire Cambourieux, Pauline Bennet, Rémi Pollès, Olivier Teytaud, Emmanuel Centeno, Nicolas Biais, and Antoine Moreau. Evolutionary algorithms converge towards evolved biological photonic structures. *Scientific Reports*, 10(1):12024, December 2020.

[120] A. Gajić, J. Radovanović, V. Milanović, D. Indjin, and Z. Ikonić. Genetic algorithm applied to the optimization of quantum cascade lasers with second harmonic generation. *Journal of Applied Physics*, 115(5):053712, February 2014.

[121] Simon Huppert, Angela Vasanelli, Thibault Laurent, Yanko Todorov, Giulia Pegolotti, Grégoire Beaudoin, Isabelle Sagnes, and Carlo Sirtori. Radiatively Broadened Incandescent Sources. *ACS Photonics*, 2(12):1663–1668, December 2015.

[122] Badreddine Smiri, Faouzi Saidi, Adnen Mlayah, and Hassen Maaref. Effect of substrate polarity on the optical and vibrational properties of (311)A and (311) B oriented InAlAs/InP heterostructures. *Physica E: Low-dimensional Systems and Nanostructures*, 112:121–127, August 2019.

[123] A. Milekhin, A. Kalagin, A. Vasilenko, A. Toropov, N. Surovtsev, D. R. T. Zahn, Marília Caldas, and Nelson Studart. Optical Phonons In InAlAs Thin Layers: Raman And IR Study. pages 43–44, Rio de Janeiro (Brazil), 2010.

[124] John G. Proakis and Masoud Salehi. *Digital communications*. McGraw-Hill, Boston, 5th ed edition, 2008.

[125] Quyang Lin, Michael Hakl, Jean-François Lampin, Wenjian Wan, J. C. Cao, Hua Li, Emilien Peytavit, and Stefano Barbieri. Frequency response of patch-array QWIP photodetectors up to 220 GHz via mid-infrared photomixing. In Manijeh Razeghi, Giti A. Khodaparast, and Miriam S. Vitiello, editors, *Quantum Sensing and Nano Electronics and Photonics XIX*, page 43, San Francisco, United States, March 2023. SPIE.

[126] Kaiheng Zou, Kai Pang, Hao Song, Jintao Fan, Zhe Zhao, Haoqian Song, Runzhou Zhang, Huibin Zhou, Amir Minoofar, Cong Liu, Xinzhou Su, Nanzhe Hu, Andrew McClung, Mahsa Torfeh, Amir Arbabi, Moshe Tur, and Alan E. Willner. High-capacity free-space optical communications using wavelength- and mode-division-multiplexing in the mid-infrared region. *Nature Communications*, 13(1):7662, December 2022.

[127] John E. Bowers, Tin Komljenovic, Michael Davenport, Jared Hulme, Alan Y. Liu, Christos T. Santis, Alexander Spott, Sudharsanan Srinivasan, Eric J. Stanton, and Chong Zhang. Recent advances in silicon photonic integrated circuits. page 977402, San Francisco, California, United States, February 2016.

[128] Eric Tournié, Laura Monge Bartolome, Marta Rio Calvo, Zeineb Loghmari, Daniel A. Díaz-Thomas, Roland Teissier, Alexei N. Baranov, Laurent Cerutti, and Jean-Baptiste Rodriguez. Mid-infrared III–V semiconductor lasers epitaxially grown on Si substrates. *Light: Science & Applications*, 11(1):165, June 2022.

[129] Seungyong Jung, Jeremy Kirch, Jae Hyun Kim, Luke J. Mawst, Dan Botez, and Mikhail A. Belkin. Quantum cascade lasers transfer-printed on silicon-on-sapphire. *Applied Physics Letters*, 111(21):211102, November 2017.

[130] Alexander Spott, Jon Peters, Michael L. Davenport, Eric J. Stanton, Charles D. Merritt, William W. Bewley, Igor Vurgaftman, Chul Soo Kim, Jerry R. Meyer, Jeremy Kirch, Luke J. Mawst, Dan Botez, and John E. Bowers. Quantum cascade laser on silicon. *Optica*, 3(5):545, May 2016.

[131] J. G Coutard, M. Brun, M. Fournier, O. Lartigue, F. Fedeli, G. Maisons, J. M Fedeli, S. Nicoletti, M. Carras, and L. Duraffourg. Volume Fabrication of Quantum Cascade Lasers on 200 mm-CMOS pilot line. *Scientific Reports*, 10(1):6185, April 2020.

[132] Hoang Nguyen-Van, Alexei N. Baranov, Zeineb Loghmari, Laurent Cerutti, Jean-Baptiste Rodriguez, Julie Tournet, Gregoire Narcy, Guilhem Boissier, Gilles Patriarche, Michael Bahriz, Eric Tournié, and Roland Teissier. Quantum cascade lasers grown on silicon. *Scientific Reports*, 8(1):7206, May 2018.

[133] Rowel Go, H. Krysiak, M. Fetters, Pedro Figueiredo, Matthew Suttinger, X. M. Fang, A. Eisenbach, J. M. Fastenau, D. Lubyshev, A. W. K. Liu, N. G. Huy, A. O. Morgan,

S. A. Edwards, M. J. Furlong, and Arkadiy Lyakh. InP-based quantum cascade lasers monolithically integrated onto silicon. *Optics Express*, 26(17):22389, August 2018.

[134] Miguel Montesinos-Ballester, Vladyslav Vakarin, Joan Manel Ramirez, Qiankun Liu, Carlos Alonso-Ramos, Xavier Le Roux, Jacopo Frigerio, Andrea Ballabio, Andrea Barzaghi, Lucas Deniel, David Bouville, Laurent Vivien, Giovanni Isella, and Delphine Marris-Morini. Optical modulation in Ge-rich SiGe waveguides in the mid-infrared wavelength range up to 11 μm. *Communications Materials*, 1(1):6, February 2020.

[135] Tiantian Li, Milos Nedeljkovic, Nannicha Hattasan, Wei Cao, Zhibo Qu, Callum G. Littlejohns, Jordi Soler Penades, Lorenzo Mastronardi, Vinita Mittal, Daniel Benedikovic, David J. Thomson, Frederic Y. Gardes, Hequan Wu, Zhiping Zhou, and Goran Z. Mashanovich. Ge-on-Si modulators operating at mid-infrared wavelengths up to 8 µm. *Photonics Research*, 7(8):828, August 2019.

[136] Benedikt Schwarz, Peter Reininger, Hermann Detz, Tobias Zederbauer, Aaron Maxwell Andrews, Stefan Kalchmair, Werner Schrenk, Oskar Baumgartner, Hans Kosina, and Gottfried Strasser. A bi-functional quantum cascade device for same-frequency lasing and detection. *Applied Physics Letters*, 101(19):191109, November 2012.

[137] Benedikt Schwarz, Christine A. Wang, Leo Missaggia, Tobias S. Mansuripur, Paul Chevalier, Michael K. Connors, Daniel McNulty, Jeffrey Cederberg, Gottfried Strasser, and Federico Capasso. Watt-Level Continuous-Wave Emission from a Bifunctional Quantum Cascade Laser/Detector. *ACS Photonics*, 4(5):1225–1231, May 2017.

[138] Benedikt Schwarz, Peter Reininger, Daniela Ristanić, Hermann Detz, Aaron Maxwell Andrews, Werner Schrenk, and Gottfried Strasser. Monolithically integrated mid-infrared lab-on-a-chip using plasmonics and quantum cascade structures. *Nature Communications*, 5(1):4085, June 2014.

[139] Masahiro Hitaka, Tatsuo Dougakiuchi, Akio Ito, Kazuue Fujita, and Tadataka Edamura. Stacked quantum cascade laser and detector structure for a monolithic mid-infrared sensing device. *Applied Physics Letters*, 115(16):161102, October 2019.

[140] Kevin Zhang, Dominik Burghart, Edoardo De Toma, Rudolf Mayer, Alexander Gardanow, Gerhard Boehm, and Mikhail A. Belkin. Mid-infrared photonic integration on InP. In Alexey A. Belyanin and Peter M. Smowton, editors, *Novel In-Plane Semiconductor Lasers XXII*, page 34, San Francisco, United States, March 2023. SPIE.

[141] Po Dong, Wei Qian, Hong Liang, Roshanak Shafiiha, Xin Wang, Dazeng Feng, Guoliang Li, John E. Cunningham, Ashok V. Krishnamoorthy, and Mehdi Asghari. 1x4 reconfigurable demultiplexing filter based on free-standing silicon racetrack resonators. *Optics Express*, 18(24):24504, November 2010.

[142] Xuezhe Zheng, Ivan Shubin, Guoliang Li, Thierry Pinguet, Attila Mekis, Jin Yao, Hiren Thacker, Ying Luo, Joey Costa, Kannan Raj, John E. Cunningham, and Ashok V. Krishnamoorthy. A tunable 1x4 silicon CMOS photonic wavelength multiplexer/demultiplexer for dense optical interconnects. *Optics Express*, 18(5):5151, March 2010.

[143] Dominik Burghart, Kevin Zhang, Gerhard Boehm, and Mikhail A. Belkin. Multiplexed quantum cascade laser sources for multi-species gas sensing using photonic integration. In Alexey A. Belyanin and Peter M. Smowton, editors, *Novel In-Plane Semiconductor Lasers XXII*, page 55, San Francisco, United States, March 2023. SPIE.

[144] Alexander Y. Piggott, Jesse Lu, Konstantinos G. Lagoudakis, Jan Petykiewicz, Thomas M. Babinec, and Jelena Vučković. Inverse design and demonstration of a compact and broadband on-chip wavelength demultiplexer. *Nature Photonics*, 9(6):374–377, June 2015.

[145] Joel Pérez-Urquizo, Yanko Todorov, Lianhe Li, Alexander G. Davies, Edmund H. Linfield, Carlo Sirtori, Julien Madéo, and Keshav M. Dani. Monolithic Patch-Antenna THz Lasers with Extremely Low Beam Divergence and Polarization Control. *ACS Photonics*, 8(2):412–417, February 2021.

[146] I. Vurgaftman, J. R. Meyer, and L. R. Ram-Mohan. Band parameters for III–V compound semiconductors and their alloys. *Journal of Applied Physics*, 89(11):5815–5875, June 2001.

[147] T. H. Glisson, J. R. Hauser, M. A. Littlejohn, and C. K. Williams. Energy bandgap and lattice constant contours of iii–v quaternary alloys. *Journal of Electronic Materials*, 7(1):1–16, January 1978.

[148] R. F. Kopf, H. P. Wei, A. P. Perley, and G. Livescu. Electron effective mass and bandgap dependence on alloy composition of Al $_{y}$ Ga $_{x}$ In $_{1-y-x}$ As, lattice matched to InP. *Applied Physics Letters*, 60(19):2386–2388, May 1992.

[149] Sophie Garidel, Marc Zelsmann, Nicolas Chaix, Pauline Voisin, Jumana Boussey, Arnaud Beaurain, and Bernard Pelissier. Improved release strategy for UV nanoimprint lithography. *Journal of Vacuum Science & Technology B: Microelectronics and Nanometer Structures*, 25(6):2430, 2007.

[150] Mathieu Jeannin, Thomas Bonazzi, Djamal Gacemi, Angela Vasanelli, Stéphan Suffit, Lianhe Li, Alexander Giles Davies, Edmund Linfield, Carlo Sirtori, and Yanko Todorov. High temperature metamaterial terahertz quantum detector. *Applied Physics Letters*, 117(25):251102, December 2020.

[151] Mario Malerba, Mathieu Jeannin, Stefano Pirotta, Lianhe Li, Alexander Giles Davies, Edmund Linfield, Adel Bousseksou, Jean-Michel Manceau, and Raffaele Colombelli.

A “Janus” double sided mid-IR photodetector based on a MIM architecture. *Applied Physics Letters*, 119(18):181102, November 2021.